Characterisation of MIMO radio propagation channels

Razavi-Ghods, Nima

How to cite:

Razavi-Ghods, Nima (2007) *Characterisation of MIMO radio propagation channels*, Durham theses, Durham University. Available at Durham E-Theses Online: http://etheses.dur.ac.uk/2526/

Characterisation of MIMO Radio Propagation Channels

By

Nima Razavi-Ghods, BEng (Hons.)

A thesis submitted to the
University of Durham for the degree of Doctor of Philosophy

2007

School of Engineering, University of Durham,
Durham, United Kingdom

Abstract

Due to the incessant requirement for higher performance radio systems, wireless designers have been constantly seeking ways to improve spectrum efficiency, link reliability, service quality, and radio network coverage. During the past few years, space-time technology which employs multiple antennas along with suitable signalling schemes and receiver architectures has been seen as a powerful tool for the implementation of the aforementioned requirements. In particular, the concept of communications via Multiple-Input Multiple-Output (MIMO) links has emerged as one of the major contending ideas for next generation ad-hoc and cellular systems. This is inherently due to the capacities expected when multiple antennas are employed at both ends of the radio link. Such a mobile radio propagation channel constitutes a MIMO system.

Multiple antenna technologies and in particular MIMO signalling are envisaged for a number of standards such as the next generation of Wireless Local Area Network (WLAN) technology known as 802.11n and the development of the Worldwide Interoperability for Microwave Access (WiMAX) project, such as the 802.16e. For the efficient design, performance evaluation and deployment of such multiple antenna (space-time) systems, it becomes increasingly important to understand the characteristics of the spatial radio channel. This criterion has led to the development of new sounding systems, which can measure both spatial and temporal channel information. In this thesis, a novel semi-sequential wideband MIMO sounder is presented, which is suitable for high-resolution radio channel measurements. The sounder produces a frequency modulated continuous wave (FMCW) or chirp signal with variable bandwidth, centre frequency and waveform repetition rate. It has programmable bandwidth up to 300 MHz and waveform repetition rates up to 300 Hz, and could be used to measure conventional high-resolution delay/Doppler information as well as spatial channel information such as Direction of Arrival (DOA) and Direction of Departure (DOD). Notably the knowledge of the angular information at the link ends could be used to properly design and develop systems such as smart antennas.

This thesis examines the theory of multiple antenna propagation channels, the sounding architecture required for the measurement of such spatial channel information and the signal processing which is used to quantify and analyse such measurement data. Over 700 measurement files were collected corresponding to over 175,000 impulse responses with different sounder and antenna array configurations. These included measurements in the Universal Mobile Telecommunication Systems Frequency Division Duplex (UMTS-FDD) uplink band, the 2.25 GHz and 5.8 GHz bands allocated for studio broadcast MIMO video links, and the 2.4 GHz and 5.8 GHz ISM bands allocated for Wireless Local Area Network (WLAN) activity as well as for a wide range of future systems defined in the WiMAX project. The measurements were collected predominantly for indoor and some outdoor multiple antenna channels using sounding signals with 60 MHz, 96 MHz and 240 MHz bandwidth. A wide range of different MIMO antenna array configurations are examined in this thesis with varying space, time and frequency resolutions. Measurements can be generally subdivided into three main categories, namely measurements at different locations in the environment (static), measurements while moving at regular intervals step by step (spatial), and measurements while the receiver (or transmitter) is on the move (dynamic). High-scattering as well as time-varying MIMO channels are examined for different antenna array structures.

Declaration

No portion of the work referred to in this report has been submitted in support of an application for another degree or qualification at this or any other university, or institution of learning.

Acknowledgements

I would like to thank my supervisor, Professor Sana Salous for her help and guidance throughout the course of my PhD. I would also like to express my gratitude to the members of the radio systems research laboratory, including Roger Lewenz, Stuart Feeney and Moustafa Abdalla who provided me with constructive discussions about the research project. I am also very grateful to the mechanical workshop for their help in cutting the inter-digital filters and making a number of antenna brackets.

Furthermore, I would like to give my thanks to the EPSRC and Ofcom (formerly the Radiocommunications Agency) for funding my studies and giving me the opportunity to undertake research in such a fascinating field. My special thanks also go to Mr. Dave Eden (Ofcom and later QinetiQ) for his support of my project.

Last but certainly not least I would like to thank my family for their unflinching love and support throughout the period of this project.

To my parents, Mehrdad and Sima

Abbreviations and Acronyms

3G	Third Generation
3GPP	3rd Generation Partnership Plan
3GPP2	3rd Generation Partnership Plan 2
4G	Fourth Generation
ABF	Average Bandwidth of Fades
ADC	Analogue to Digital Converter
AFD	Average Fade Duration
AGC	Automatic Gain Control
AMPS	Advanced Mobile Phone Service
ARMA	Auto-Regressive Moving Average
AWGN	Additive White Gaussian Noise
BLAST	Bell Laboratories Layered Space-Time Architecture
BPF	Band-pass Filter
BPSK	Binary Phase Shift-Keying
BRAN	Broadband Radio Access Network
BS	Base Station
CDF	Cumulative Distribution Function
CDMA	Code Division Multiple Access
COST	COoperation in the field of Scientific and Technical research
CPM	Critical Path Method
CRB	Cramér Rao bound
CSI	Channel State Information
CUBA	Circular Uniform Beam Array
CW	Continuous Wave
DAC	Digital to Analogue Converter
DAU	Data Acquisition Unit
DCS	Digital Communication System
DDFS	Direct Digital Frequency Synthesiser
DECT	Digital European Cordless Telephone
DFT	Discrete Fourier Transform
DGUS	Deterministic Gaussian Uncorrelated Scattering
DML	Deterministic Maximum Likelihood
DOA	Direction of Arrival (also referred to as Angle of Arrival)
DOD	Direction of Departure (also referred to as Angle of Departure)

DS	Delay Spread
EDGE	Enhanced Data Rates for GSM Evolution
ENBW	Effective Noise Bandwidth
ESPRIT	Estimation of Signal Parameters via Rotational Invariance Techniques
ETACS	European Total Access Cellular System
FB	Forward-Backward
FDD	Frequency Division Duplex
FDM	Frequency Division Multiplexing
FDMA	Frequency Division Multiple Access
FFT	Fast Fourier Transform
FM	Frequency Modulation
FMCW	Frequency Modulated Continuous Wave
FPGA	Field Programmable Gate Array
FSO	Free-Space Optics
GPRS	General Packet Radio Service
GPS	Global Positioning Satellite
GSM	Global System for Mobile Communications (Groupe Spécial Mobile)
GUI	Graphical User Interface
HSCSD	High Speed Circuit Switched Data
IF	Intermediate Frequency
IFFT	Inverse Fast Fourier Transform
IID	Independent Identically Distributed
IMT-2000	International Mobile Telecommunications-2000
IQML	Iterative Quadratic Maximum Likelihood
IS	Interim Standard
ISI	Intersymbol Interference
ISM	Industrial, Scientific, and Medical
IST	Information Societies Technologies
ITU	International Telecommunications Union
JADE	Joint Angle-Delay Estimation
LCR	Level Crossing Rate
LCR_f	Frequency Level Crossing Rate
LMDS	Local Multipoint Distribution Service
LNA	Low Noise Amplifier
LOS	Line of Sight
LPF	Low-pass Filter
LS	Least Squares

LSB	Least Significant Bit
METRA	Multielement Transmit-Receive Antennas
MIMO	Multiple Input, Multiple Output
MIMO-OFDM	MIMO - Orthogonal Frequency Division Multiplexing
MIMO-OFDMA	MIMO - Orthogonal Frequency Division Multiple Access
MISO	Multiple Input, Single Output
ML	Maximum Likelihood
MMAC	Multimedia Mobile Access Communication
MMDS	Multi-Channel Multipoint Distribution Service
MRC	Maximum Ratio Combining
MS	Mobile Station
MSB	Most Significant Bit
MUSIC	Multiple Signal Classification
MVDR	Minimum Variance Distortionless Response
NIST	National Institute of Standards and Technology
NMT	Nordic Mobile Telephone
NSF	Noise Subspace Fitting
NTT	Nippon Telephone and Telegraph company
OLOS	Obstructed Line of Sight
PACS	Personal Access Communication System
PCA	Principle Component Analysis
PCB	Printed Circuit Board
PDA	Personal Digital Assistants
PDC	Pacific Digital Cellular
PDF	Probability Density Function
PDP	Power Delay Profile
PHS	Personal Handyphone System
PLL	Phase Locked Loop
PN	Pseudo Noise
PSD	Power Spectral Density
QAM	Quadrature Amplitude Modulation
RF	Radio Frequency
RMS	Root Mean Square
ROM	Read-Only Memory
SAGE	Space Alternating Generalised Expectation Maximisation
SATURN	Smart Antenna Technology in Universal Broadband Wireless Networks
SAW	Surface Acoustic Wave

SF	Subspace Fitting
SIMO	Single-Input Multiple-Output
SINR	Signal to Interference + Noise Ratio
SISO	Single Input, Single Output
SML	Stochastic Maximum Likelihood
SNR	Signal to Noise Ratio
SoE	School of Engineering (Durham University)
SRF	Sweep Repetition Frequency
SSB	Single Sideband
SSF	Signal Subspace Fitting
ST	Space-Time
STDCC	Swept-Time Delay Cross-Correlation
SUI	Stanford University Interim
SVD	Singular Value Decomposition
TDD	Time Division Duplex
TDM	Time Division Multiplexing
TDMA	Time Division Multiple Access
TDOA	Time Delay of Arrival
TD-SCDMA	Time Division Synchronous Code Division Multiple Access
TF	Transfer Function
TLS	Total Least Squares
TOA	Time of Arrival (i.e., multipath time-delay)
TWDP	Two Wave with Diffuse Power
UCA	Universal Circular Array
ULA	Universal Linear Array
UMTS	Universal Mobile Telecommunications System
UMTS-FDD	UMTS Frequency Division Duplex
UMTS-TDD	UMTS Time Division Duplex
US	Uncorrelated Scattering
USDC	United States Digital Cellular
UWC	Universal Wireless Communications
VNA	Vector Network Analyser
VPDCPA	Vertically Polarised Directional Circular Patch Array
VPDLPA	Vertically Polarised Directional Linear Patch Array
VPULDA	Vertically Polarised Uniform Linear Dipole Array
WARC	World Administrative Radio Conference
W-CDMA	Wideband Code Division Multiple Access

Wi-Fi	Wireless Fidelity
WiMAX	Worldwide Interoperability for Microwave Access
WLAN	Wireless Local Area Network
WLL	Wireless Local Loop
WPAN	Wireless Personal Area Network
WRF	Waveform Repetition Frequency (or SRF for Chirp Technique)
WSS	Wide Sense Stationary
WSSUS	Wide Sense Stationary Uncorrelated Scattering
WSSUS-HO	Wide Sense Stationary Uncorrelated Scattering - Homogenous
WWiSE	World-Wide Spectrum Efficiency
XPC	Cross Polarisation Coupling
XPD	Cross Polarisation Discrimination
ZMCSCG	Zero Mean Circularly Symmetric Complex Gaussian

Table of Contents

Chapter 1

Introduction

1.1 Introduction

The past two decades has seen an increasing demand for faster and more spectrally efficient mobile radio services for voice, data and multimedia applications. This requirement has been the main catalyst for driving radio systems research, and as a consequence has led to the development of many new wireless systems and standards across the world. Modern radio communication systems have been able to only partially fulfil the requirement for higher data rates and better qualities of service for nomadic users. It is predicted that in order to provide better channel throughputs via radio links, multiple antennas have to be employed at both transmit and receive sites, thus creating a Multiple-Input Multiple-Output (MIMO) system.

Multi-antenna array technologies can significantly enhance the performance of radio systems. MIMO signalling techniques in particular can offer a combination of diversity and multiplexing gains to provide considerably higher channel throughputs as compared to conventional Single-Input Single-Output (SISO) systems [1]. These systems have been studied quite extensively so far and have shown great potential in terms of MIMO space-time processing [2, 3]. Although to date more emphasis has been placed on the system's aspect, it is important to note that whilst space-time coding and MIMO signal processing are essential to the implementation of MIMO technologies, it is often the radio propagation channel along with the antenna array type and geometry that proves to be the major restriction in utilising this technology. The propagation characteristics of a typical MIMO channel can often show quite significant deviation from the standard Independent and Identically Distributed (IID) assumption. The time varying nature of the channel can also provide a major problem in realistically predicting the performance of such systems. Therefore the experimental characterisation of such propagation channels is vital to the future development of MIMO technologies which are intended for both ad-hoc and cellular systems. Over the years this has led to the development of a number of channel characterisation systems known as sounders for radio propagation studies [4]. The majority of the sounders developed in the past have focused on measuring temporal channel parameters such as power vs. delay information. However, the requirement to employ multiple antennas at both ends of the link provides the challenge of measuring spatial channel parameters such as Direction of Arrival (DOA) and Direction of Departure (DOD), to aid with system design.

The following sections provide the background to the evolution of mobile radio systems from first generation analogue systems to second generation and third generation digital systems. The reasons for developing multi-antenna communication systems are given, and the issues concerning channel characterisation are discussed. Finally, there is a brief review of all chapter contents.

1.2 Evolution of Mobile Radio Systems

The first generation cellular radio systems were all based on analogue technology, and used Frequency Modulation (FM) with Frequency Division Multiple Access (FDMA) as the air interface technology. These included the worlds first cellular system, which was implemented by Nippon Telephone and Telegraph company (NTT) in Japan (1979), Advanced Mobile Phone Service (AMPS) in United States (1983), Nordic Mobile Telephone System (NMT 450) followed by European Total Access Cellular System (ETACS) in Europe (1985) and cellular standard 450 (C-450) in Germany (1985). ETACS was virtually identical to AMPS with the exception that it employed smaller bandwidth channels.

The incompatibility and low coverage capability of first generation analogue systems led to the development of second generation digital systems. The second generation cellular mobile radio systems employed digital modulation and advanced call processing capabilities. Amongst these were, Groupe Spécial Mobile (GSM) in Europe (1990), US Digital Cellular (USDC: IS-54 and IS-136) in United States (1991), Pacific Digital Cellular (PDC) in Japan (1993) and Interim Standard 95 (IS-95) in United States (1993). During this period, several successful cordless telephone standards were also developed, including Second Generation Cordless Telephone (CT2) in Europe (1989), Digital European Cordless Telephone (DECT) in Europe (1993), Personal Handyphone System (PHS) in Japan (1993), Personal Access Communication System (PACS) in United States (1994) and Digital Communication

System (DCS-1800) in Europe (1993). Most of these standards used Time Division Multiple Access (TDMA) and FDMA air interface technologies with the exception of IS-95, which used Code Division Multiple Access (CDMA). Currently the most successful of all of these standards is the Pan European Digital Cellular Standard GSM [5].

Several Enhancements have been made to second generation systems in order to provide new services and better speech quality. They come under the name: enhanced second generation systems or 2.5G. These include Interim standard 95B (IS-95B) in the United States, and in Europe, General Packet Radio Service (GPRS), High Speed Circuit Switched Data (HSCSD) and Enhanced Data Rates for GSM Evolution (EDGE).

Due to the capacity limitations of second generation systems for data and multi-media applications, there has been enormous work towards the development of third generation technologies. In 1992 the World Administrative Radio Conference (WARC) defined the frequency spectrum for third generation systems to support advanced services for data and multimedia applications. International Mobile Telecommunications-2000 (IMT-2000) was the International Telecommunication Union's (ITU) effort to develop a rigorous definition for 3G. Although the original intent of a worldwide standard for 3G was the Universal Mobile Telecommunications System (UMTS), the reality of economics, competition and other factors forced the development of competing and incompatible systems. The 3GPP developed the UMTS Frequency Division Duplex (UMTS-FDD) and UMTS Time Division Duplex (UMTS-TDD) standards [6], while the 3GPP2 produced cdma2000 (including 1xEV-DO/DV, 1xRTT, 3xRTT) [7]. The 1x prefix specifies that it is 1 times the spreading rate of standard IS-95 (1.2288 Mcps). In china, the development of IMT-2000 is underway based on Time Division-Synchronous Code Division Multiple Access (TD-SCDMA). There are many other IMT-2000 Candidate standards such as Universal Wireless Communications Consortium (UWC-136), Enhanced DECT and CDMA I. All the IMT-2000 3G standards are based on CDMA air interface technologies. While cdma2000 is an evolution of the original IS-95 standard with 1.25 MHz channel bandwidth, UMTS (W-CDMA) is an entirely new standard, which uses 5 MHz channel bandwidth CDMA air interface [5].

Amongst the evolution of mobile cellular systems, there have been enormous developments for fixed broadband microwave links used to create a Wireless Local

Loop (WLL). A vast array of new services and applications has been proposed and are in the various stages of commercialisation. These services include Local MultiPoint Distribution Service (LMDS) and Multi-channel Multipoint Distribution Service (MMDS). In the United States, the standardisation committee for the US LMDS/MMDS is IEEE 802.16, while in Europe the committee for Broadband Radio Access Networks (BRAN) has developed the HIPERACCESS and HIPERLINK standards. Enormous progress has also been made in Free-Space Optics (FSO) and Millimetric wave Technologies. There are products commercially available which support transfer rates of several Gbits/s (Gigabit Ethernet).

In parallel to the growth of fixed wireless broadband, there have been tremendous developments of the so-called Wi-Fi (Wireless Fidelity) era. In the United States, the IEEE 802.11 standards is fast becoming a global standard, while in Europe HIPERLAN/2 has emerged as the next generation Wireless Local Area Network (WLAN) standard. It is widely believed that the IEEE 802.11 standards have already occupied the niche that HIPERLAN was designed for, albeit with lower performance. In Japan, Multimedia Mobile Access Communication system (MMAC) has been developed as the WLAN standard. All of these WLAN standards have been implemented to work in the 2.4 GHz and 5.8 GHz Industrial, Scientific, and Medical (ISM) frequency bands with the exception of HIPERLAN, which will work at 5.2 GHz and 5.6 GHz. The IEEE 802.15 standards committee have also formed to provide an international forum for developing Bluetooth and other Wireless Personal Area Networks (WPANs) that interconnect pocket PCs, personal digital assistants (PDAs), cellphones, light projectors, and other appliances. These licence free networks provide an interesting dichotomy in the radio systems market since; high data rate ad-hoc networks are being deployed by individuals within buildings without a licence, whereas cellular operators have focused on providing outdoor voice coverage and have been slow in providing reliable in-building coverage and high data rate services to their cellular subscribers [5]. Emerging standards include the Worldwide Interoperability for Microwave Access (WiMAX) project, which is defined under the IEEE 802.16 working group. It is very similar in concept to Wi-Fi, but has certain improvements that are aimed at enhancing performance and should permit usage over much greater distances.

Although the current achievements in mobile radio technology have been monumental, there are inevitably more requirements placed for future generation systems. Ideally in the long term, high capacity terminals should become 'go anywhere' personal ones. The so-called fourth generation mobile radio systems have the criterion to produce higher capacity links for nomadic users [8, 9]. In order to achieve higher channel throughputs, different types of technologies may need to be combined and some of the current research suggestions for future generation radio systems are IP-based core ad-hoc networks, employing broadband technology and/or multi-antenna systems. In general, it is difficult to predict the future of wireless technology, and in particular, the future of mobile radio systems. However, with the knowledge of current systems, it is believed that the key to providing reliable high data rate communications lies in designing systems that allow maximum possible reconfigurability and global roaming [10, 11].

It is predicted that MIMO and smart antenna technologies will have a central role for future generation systems. This is due to the inherent Shannon capacity gains provided when multiple antennas are employed at the transmitter and/or receiver sites. Currently multiple antennas are employed to achieve simple space-time diversity for third generation systems, which is mainly for the 3GPP's specifications of the W-CDMA systems. The use of Alamouti space-time coding has been extremely effective for 3G scenarios, particularly when two antennas are employed at the base station and only one antenna at the mobile terminal [12].

1.3 Development Towards Multi-Antenna Communications

The actual concept of MIMO signalling was first introduced by Jack Winters in 1987 [13]. This work examined the capacity of multi-antenna systems for two different scenarios. The first case inspected the communications link between a multiple antenna base station and several single antenna mobile terminals and the second case inspected the communications link between two mobile terminals both with multiple antennas. This provided a basic understanding of MIMO channels and the capacities available when using multiple antennas. However, it was not until the mid 1990s that the groundbreaking work by Telatar and Foschini [1, 14] paved the way for future research on MIMO. Gerald Foschini showed through his conceptual analysis of MIMO, that there would be an almost linear increase in the channel capacity as the number of antennas at both ends of the system increased. The potential of MIMO signalling was shown, when the Bell Labs Layered Space-Time

Architecture (BLAST) 8 × 8 system demonstrated a capacity of 42 b/s/Hz at 1% outage and 21 dB average SNR at each receiving element [1]. This performance was realised based on a number of assumptions, which included, a Rayleigh flat-fading environment, uncorrelated antenna signals and equal power sub-channels. However, the potential capacity of MIMO channels is still said to exist even in relatively poor scattering environments.

The realisation of MIMO signalling is certainly not trivial and numerous factors can hinder system performance. The primary limiting factor in a practical MIMO environment is the correlation of the received antenna signals. This infers that in order to achieve higher channel capacities, a rich scattering environment is required, which can permit uncorrelated signals at the receiver array. Research studies undertaken do show that the capacity of MIMO radio links can be significantly degraded if a LOS situation is present. By using channel training sequences [15] and appropriate space-time coding schemes [16], it is possible to approach the information theoretic capacity limit of MIMO channels.

Although MIMO techniques are often more complicated to implement than conventional systems, their inherent ability to allow faster data rates is a real incentive to system developers and operators. So far, most of the systems developed use Orthogonal Frequency Division Multiplexing (OFDM/OFDMA) as the air interface technology. Such systems are currently being developed for a number of ongoing wireless standards for adhoc systems such as 802.11n and 802.16e. Currently, the latest MIMO-oriented version of the IEEE 802.11n standard has seen two competing approaches being proposed. The TGn Sync proposal is a 2 × 2 MIMO system, which can expand up to a 4 × 4 array and is backed by Intel, Agere, Atheros, and some others. The World-Wide Spectrum Efficiency (WWiSE) proposal is mostly a 4 × 4 MIMO solution backed by Broadcom, Motorola, Airgo, and others. So far, it seems that the simpler 2 × 2 version will prevail, however the likely solution is a compromise between the two groups. There is clearly a greater cost associated with having more antennas on the end user terminal. It is interesting to observe that there are currently hardware products available for the 802.11n market and these are classified as 'Pre-N' systems. The MIMO concepts are also being used in the IEEE 802.16 standard for WiMAX.

MIMO is also being examined for cellular systems defined as super 3G and/or 4G technologies. A number of companies have already invested in MIMO for cellular, such a Nortel, Nokia, and others. However, MIMO cellular clearly presents a number of further complications as compared to point to point links. If dealing with cellular handsets, there are such requirement as smaller antenna arrays, as well as less computational complexity for the processing (i.e. battery life), although the latter presents a much greater challenge for MIMO signalling. Despite these challenges various communities, industrial and otherwise are investigating the development of MIMO for cellular. With the developments made thus far, it is reasonable to predict that multi-antenna technologies will, in general, play a critical role in the future of wireless communications. So far, numerous research studies have been undertaken in the areas of information theory, channel modelling, signal processing and system design relating particularly to the MIMO concept. The aim is to develop faster and more spectrally efficient radio communication systems whether using pure diversity techniques or spatial multiplexing. Figure 1.1 shows the prospects of MIMO, Single-Input Multiple-Output (SIMO), and Multiple-Input Single-Output (MISO) technologies for future generation systems in relation to current European radio communication systems.

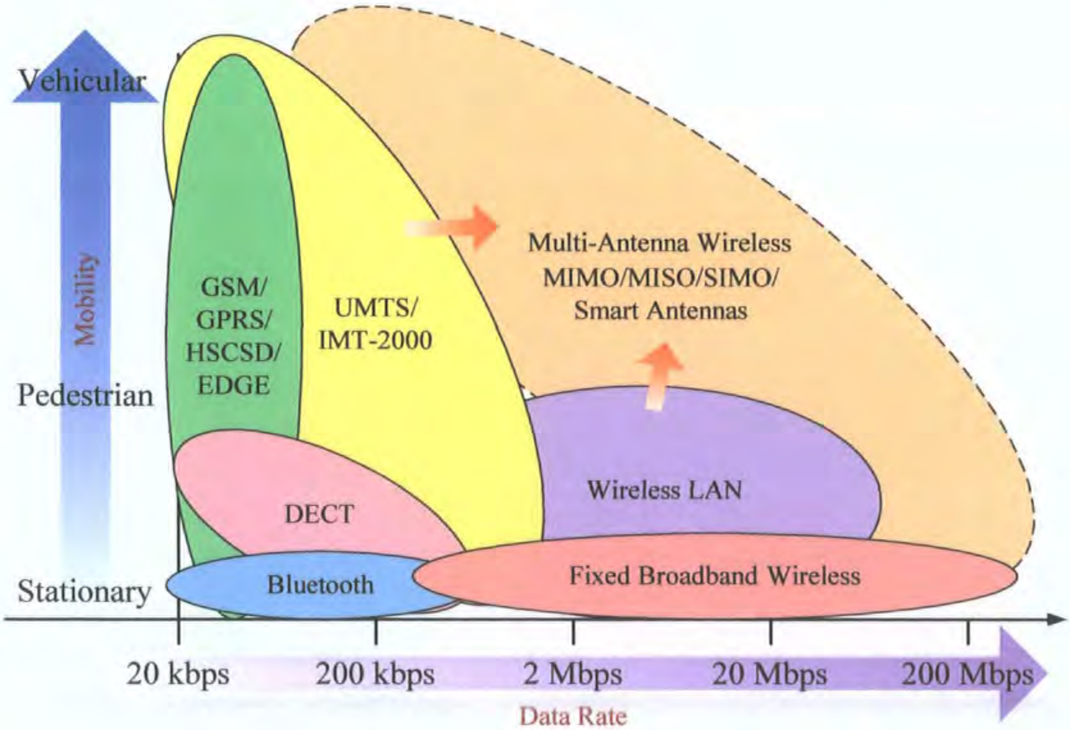

Figure 1.1: Mobility versus throughput for current and future wireless systems.

1.4 Challenges for Mobile Radio Propagation

Clearly, the fundamental limitation of all radio communication systems is the propagation channel. The radio link between the transmitter and receiver can vary significantly from a simple Line-of-Site (LOS) scenario to a complex non line-of-site one, which is severely obstructed by buildings, mountains and foliage. Unlike wire-line communications, where the characteristics of the link (e.g. Coax, Fibre) are well known, radio channels are described as being extremely complex and random in nature. The numerous different propagation mechanisms including reflection, refraction, diffraction, and scattering, all attribute to the complexity of radio wave propagation.

Radio channels can be characterised into two generally different propagation environments. Large-scale path loss describes the mechanism behind long distance electromagnetic wave propagation and is mainly a function of reflection, diffraction, and scattering. Small-scale fading is described as the rapid fluctuations experienced over very short travel distances and is usually described by rapid changes in the receiver signal level. This is affected by the varying Doppler shifts and multipath propagation delays experienced in the channel environment. The factors that influence this include velocity of the mobile, velocity of surrounding objects and the transmission bandwidth [5].

Characterisation of MIMO propagation channels are even more complex, since additional variables are introduced in the analysis, namely the number of antennas at the transmitter and at the receiver with their spatial locations. Multiple antennas at both ends of the radio link create a matrix channel and the advantage of this is the possibility of transmitting data on several spatial data pipes over the same frequency-time slot. Having a high scattering radio channel actually helps MIMO signalling, since each spatial sub-channel will be different. A straight LOS link, will in general degrade channel performance, however this is not trivial to characterise. Every MIMO channel presents a different set of spatial characteristics which have significant impact on the performance of the system.

To date there have been numerous simulation studies on MIMO channels, however, only a limited number of studies have been carried out on actual wideband MIMO propagation focusing on the physical channel itself and even fewer studies on time-variant channels. Time-variation being a case where either objects in the physical channel are moving and/or the transmitter and receiver units are moving in space. Most of the research conduced so far shows that the physical channel plays a vital role in the overall channel throughput.

Clearly, there is an overwhelming requirement to study the various types of channel environments for different system and antenna configurations. In order to perform measurements for various types of MIMO links, the parallel chirp sounder previously developed for SIMO measurements was upgraded to a wider bandwidth semi-sequential MIMO architecture. The inherent merits of this approach are discussed in the thesis. This project has involved the design and development of various RF and digital circuits, and the development of many MATLAB algorithms for data processing. More than 175,000 MIMO channel impulse responses have been measured and analysed for different environments. The results include channel capacity, spatial channel characterisation and time-variability amongst other parameters. Capacity results in particular give direct insight into the performance of a MIMO radio system when present in a real-world environment.

1.5 Review of Chapter Contents

Chapter 2 describes the fundamental principles of wireless channels with emphasis on the small-scale fading characteristics. The mechanisms of multipath propagation are explained in some detail with a brief review of wideband channel modelling. Important channel parameters are described such as power delay profiles, delay spread, Doppler spread, scattering functions, coherence time and coherent bandwidth and data fitting with probability distribution functions.

Chapter 3 extends the theory of wireless channels to take into account a MIMO propagation environment. The underlying theory of MIMO signalling is the ability to separate channels in multipath and this is described in some detail. The general topics of discussion in this chapter include, channel capacity limits, signal correlation, practical MIMO signalling, physical and non-physical channel modelling, and spatial channel parameters. This chapter provides a literature review of the previous MIMO models and measurement campaigns.

In order to measure directional (or double-directional) channel information, it is necessary to apply the knowledge of array signal processing. Therefore, chapter 4 reviews the various direction finding algorithms, from the overly simple beamforming techniques to the complex yet resourceful Space-Alternating Generalized Expectation-Maximization (SAGE) algorithm. Due to their resolution capabilities, more emphasis will be placed on parametric estimation techniques than spectral-based methods.

In chapter 5, the various different wideband channel sounding techniques are discussed, which includes the chirp sounding method. The advantages and disadvantages of such methods are described in detail, as well as the FFT data processing.

Chapter 6 describes the MIMO chirp sounder architecture at the systems level. The concept of the semi-sequential chirp sounder system is given along with the sounder calibration results, which include back-to-back tests, two-tone tests, and ambiguity functions. Furthermore, calibration results are presented for two antenna arrays.

In chapter 7, the spatial parameters of the multiple antenna radio channel are examined. A range of spatio-temporal results are presented, such as DOA and DOD. Particular emphasis is placed on the concept of a double-directional radio channel. This chapter also includes the practical implementation of the array signal processing algorithms, such as SAGE. Along with the measured data, there will be some descriptions of the MIMO or SIMO environments surveyed.

In chapter 8, the characterisation of numerous ‘typical’ indoor (and some outdoor) MIMO links are examined. A broad spectrum of channel statistics are presented including Cumulative Distribution Functions (CDFs) of link capacity. Time-variant analysis is performed on various channel environments. The results are typically associated with an allocated frequency band, such as that for MIMO-OFDM studio video links (BBC) in the 2.25 GHz band. Many MIMO statistics are presented for different frequency bands including those simultaneously collected in two bands.

Chapter 9 is the conclusions section of the thesis. It describes the work accomplished thus far and the requirements needed in order to perform further measurements and analysis.

1.6 References

1. G. J. Foschini, "Layered Space-Time Architecture for Wireless Communication in a Fading Environment When using Multi-Element Antennas," *Bell Labs Technical Journal*, vol. 1, pp. 41-59, 1996.
2. D. Gesbert, M. Shafi, D. Shiu, P. J. Smith, A. Naguib, "From Theory to Practice: An Overview of MIMO Space-Time Coded Wireless Systems," *IEEE Journal on Selected Areas in Communications*, vol. 21, pp. 281-302, 2003.
3. M. A. Jenson, J. W. Wallace, "A Review of Antennas and Propagation for MIMO Wireless Communications," *IEEE Transactions on Antennas and Propagation*, vol. 52, pp. 2810-2824, 2004.
4. J. D. Parsons, *The Mobile Radio Propagation Channel*, 2 ed: John Wiley & Sons Ltd, 2000.
5. T. S. Rappaport, *Wireless Communications: Principles and Practice*, 2 ed: Prentice Hall PTR, 2002.
6. 3G Project Initiative: "3rd Generation Partnership Plan (3GPP)," http://www.3gpp.org/.
7. 3G Project Initiative: "3rd Generation Partnership Plan 2 (3GPP2)," http://www.3gpp2.org/.
8. W. Mohr, "Developing Mobile Communications Systems beyond Third Generation," *Wireless Personal Communications (Kluwer)*, vol. 17, pp. 191-207, 2001.
9. A. Bria, F. Gessler, O. Queseth, R. Stridh, M. Unbehaun, J. Wu, J. Zander, M. Flament, "4th-Generation Wireless Infrastructures: Scenarios and Research Challenges," *IEEE Personal Communications*, vol. 8, pp. 25-31, 2001.
10. M. Frodigh, S. Parkvall, C. Roobol, P. Johansson, P. Larsson, "Future Generation Wireless Networks," *IEEE Personal Communications*, vol. 8, pp. 10-17, 2001.
11. T. Otsu, N. Umeda, Y. Yamao, "System Architecture for Mobile Communications Systems Beyond IMT-2000," GLOBECOM 2001 - IEEE Global Telecommunications Conference, 2001.
12. S. M. Alamouti, "A Simple Transmit Diversity Technique for Wireless Communications," *IEEE Journal on Selected Areas in Communications*, vol. 16, pp. 1451-1458, 1998.

13. J. H. Winters, "On the Capacity of Radio Communication Systems with Diversity in a Rayleigh Fading Environment," *IEEE Journal on Selected Areas in Communications*, vol. 5, pp. 871-878, 1987.
14. I. E. Telatar, "Capacity of Multi-antenna Gaussian Channels," *European Transactions on Telecommunications*, vol. 10, pp. 585–595, 1999.
15. B. Hassibi, B. M. Hochwald, "How Much Training is Needed in Multiple-Antenna Wireless Links?," *IEEE Transactions on Information Theory*, vol. 49, pp. 951-964, 2003.
16. A. F. Naguib, V. Tarokh, N. Seshadri, A. R. Calderbank, "A Space-Time Coding Modem for High-Data-Rate Wireless Communications," *IEEE Journal on Selected Areas in Communications*, vol. 16, pp. 1459-1478, 1998.

Chapter 2

Mobile Radio Propagation

2.1 Introduction

In a radio link, the most basic channel propagation characteristics are the signal attenuation over ideal free space. The model of free space treats the region between the transmitter and receiver as being free of all objects that might absorb or reflect Radio Frequency (RF) energy. It also assumes that the channel behaves as a perfectly uniform and non-absorbent medium and that there are no reflected components other than the LOS. The free space equation or the *Friis* equation [1] is a well-known ideal model, which assumes that the attenuation of RF energy between the transmitter and receiver behaves according to an inverse square power law.

For most practical channels, where signal propagation takes place in the atmosphere and near the ground, the free space model is inadequate to describe the channel characteristics and predict system performance. In a mobile radio communication system, a signal can travel from transmitter to receiver over multiple reflective paths and this phenomenon is referred to as multipath propagation. The effect can cause fluctuations in the received signal's amplitude, phase and angle of arrival, giving rise to the terminology multipath fading. The fading channel manifestations can be categorised into two types: large-scale and small-scale fading. Large-scale fading represents the average signal power attenuation or path loss due to motion over large areas. It is affected by the land undulations and prominent terrain contours such as hills, forests, buildings, etc, between the transmitter and the receiver. The statistics of large-scale fading provides a way of computing an estimate of path loss as a function of distance. This is usually specified in terms of mean path loss (1/n power law) and a log-normally distributed variation about the mean [2]. Small-scale fading refers to the fluctuations in signal amplitude and phase due to small changes in the spatial separation between the transmitter and receiver, which can be as low as half a wavelength. Small-scale fading can be described by two mechanisms, namely, time-spreading of the signal, also known as signal dispersion and time-variant behaviour of the channel. The channel is considered to be time-variant because motion between the transmitter and receiver results in propagation path changes [2]. The rate of change of these propagation conditions accounts for the rapidity of the fading. In a mobile radio channel, both types of fading are prominent such that, small-scale fading is superimposed on large-scale fading. It must be noted however, that the term fading is usually applied when referring to small-scale signal fluctuations. Figure 2.1 illustrates small-scale fading and large-scale fading for a received signal level as a function of position.

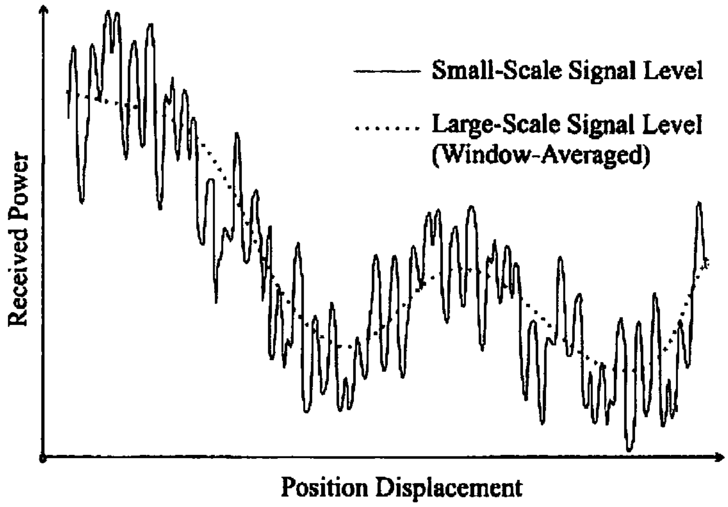

Figure 2.1: Small-scale and large-scale spatial channel fading.

There are three main mechanisms of propagation in a mobile radio channel. They are reflection, diffraction and scattering. Reflection occurs when a signal impinges on a smooth surface that has a larger dimension than the signal wavelength. Diffraction occurs when the radio path between the transmitter and receiver is obstructed by a dense body with larger dimensions than the signal wavelength. Scattering occurs when a radio signal impinges on a rough surface or any surface whose dimensions are on the order of the signal wavelength or less, causing the reflected energy to spread out in all directions. Diffraction is the main propagation mechanism for most mobile radio communication systems, since in most cases there is no LOS path between the transmitter and the receiver. This is often referred to as shadowing, since the diffracted signal can reach the receiver, even when it is shadowed by an impenetrable obstruction such as a building. The following sections will describe these propagation mechanisms in more detail, with emphasis on the small-scale fading characteristics of the radio channel.

2.2 Small-Scale Fading and Multipath

Fading is caused by interference between two or more versions of the transmitted signal, which arrive at the receiver at slightly different times. These multipath waves, combine at the receiver antenna to give a resultant signal, which can vary in amplitude and phase, depending on the distribution of signal intensity, relative propagation time of the waves, and transmission bandwidth of the signal. The three main factors that affect fading are: fluctuations in the signal level over a period of time or travel distance, random frequency modulation due to varying Doppler shifts on different multipath signals, and time dispersion or echoes caused by multipath propagation delays.

2.2.1 Multipath Propagation

The signal received at the mobile terminal at any point in space, may consist of a large number of plane waves with randomly distributed amplitudes, phases and angles of arrival. These so called *multipath signals* are then combined vectorially at the receiver, and can cause the resultant received signal to fade or distort. If the mobile terminal is stationary, then the received signal may fade due to movement of the surrounding objects in the channel [3]. If the channel environment is static, and movement is considered to be only due to the mobile, then fading can be considered as a purely spatial phenomenon. The spatial variations of the resulting signal are perceived as temporal variations by the receiver as it moves in space. As the receiver moves in the multipath field, it can go through several deep fades. Maintaining a 'good' communications link during such fades can be extremely difficult, hence leading to the deployment of various multipath mitigation techniques. Antenna diversity techniques can be extremely useful in improving link quality. Some popular antenna diversity techniques include space, polarisation, and pattern diversity.

2.2.2 Physical Basis for Fading

Many physical factors can influence small-scale fading in the mobile radio channel. Figure 2.2 illustrates a typical mobile radio propagation environment in which, multipath signals, speed of surrounding objects, speed of the mobile, and transmission bandwidth all attribute concurrently to fades in the resultant received signal.

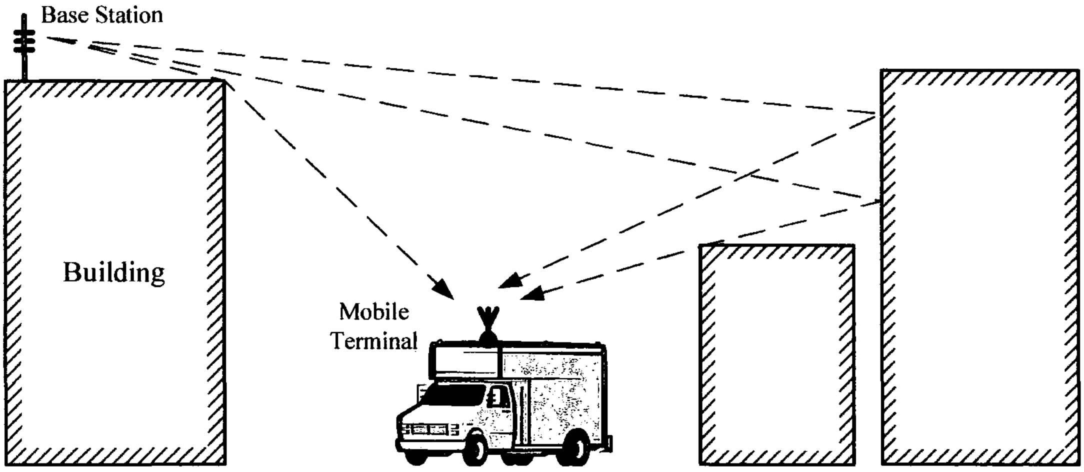

Figure 2.2: Multipath signals arriving at the mobile radio receiver antenna.

Multipath signals result from reflective objects and scatterers in the radio channel environment. Often multipath propagation lengthens the time required for the signal to reach the receiver, and this can result in signal smearing due to Intersymbol Interference (ISI). The speed of the mobile terminal results in random frequency modulation due to different Doppler shifts affecting each multipath component. The polarity of the Doppler shift is dependant on whether the mobile receiver is moving towards or away from the base station. Doppler shift directly impacts the time-variability of the channel, which is defined by the *coherence time*. The speed of surrounding objects in the channel can result in a time varying Doppler shift on each of the multipath components. If the surrounding objects are moving at a faster rate than the mobile receiver, then this effect can dominate the fading in the channel [2]. Otherwise, the surrounding objects can be ignored and only the movement of the mobile terminal can be considered.

The transmission bandwidth is also an important factor in influencing fading. If the signal transmission bandwidth is greater than the channel bandwidth, the received signal will be distorted, but the small-scale fading will not be significant. The channel bandwidth is quantified by the *coherence bandwidth*, and this will be discussed in the following sections.

2.2.3 Doppler Shift

Due to the relative motion between the mobile terminal and the base station, each multipath wave undergoes a shift in frequency. This shift in the received signal frequency is referred to as the Doppler shift, and is directly proportional to the velocity of the mobile with respect to the direction of arrival of the received multipath signal. Figure 2.3 illustrates the Doppler shift experienced by a mobile moving at constant velocity *v*, along a path of length *d* (between points *A* and *B*), while receiving signals from source *S*.

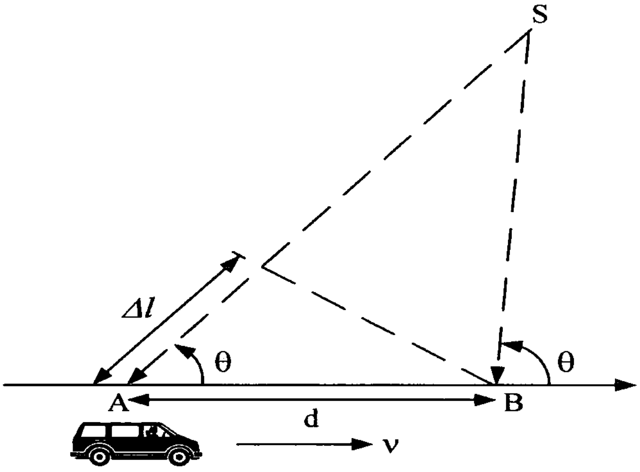

Figure 2.3: Illustration of Doppler effect.

The difference in path lengths travelled by the signal from source *S* to the mobile at points *A* and *B* is $\Delta l = d\cos(\theta) = v\Delta t\cos(\theta)$. Where Δt is the time required for the mobile to travel from *A* to *B*. The phase change in the received signal due to the difference in path length is given by equation (2.1).

$$\Delta\phi = \frac{2\pi\Delta l}{\lambda} = \frac{2\pi v\Delta t}{\lambda}\cos\theta \qquad (2.1)$$

The Doppler shift is then given by

$$f_d = \frac{1}{2\pi}\cdot\frac{\Delta\phi}{\Delta t} = \frac{v}{\lambda}\cos\theta \qquad (2.2)$$

It can be observed from equation (2.2) that the Doppler shift is positive if the mobile is moving toward the direction of arrival of the signal and negative if the mobile is moving away from the direction of arrival of the signal.

In most radio channels, the scatterers that contribute the most power are likely to have the smallest Doppler frequencies. This is usually referred to as the big-slow rule and states that bigger objects scatter more power but are less likely to move. The meaning and implications of Doppler spectra are discussed in section 2.6.2.2 when describing Clarke's model.

2.3 Channel Impulse Response

The wideband multipath channel can be fully characterised by its impulse response. This contains all the necessary information required to simulate, analyse and predict any type of radio transmission through the channel. The mobile radio channel can be modelled as a linear filter with a time varying impulse response [3]. The time variation is due to the movement of the receiver in space and/or the environment. For a case where the mobile receiver is moving along the ground at a constant velocity v, the impulse response varies as a function of receiver position d.

Assuming that v is constant over short time or distance intervals, the impulse response of the multipath radio channel is denoted as $h(t, \tau)$. The variable t represents the time variations due to motion and τ represents the multipath delay for a particular t. The received signal can now be expressed as a convolution of the transmitted signal $x(t)$ and the channel impulse response $h(t, \tau)$.

$$y(t) = \int_{-\infty}^{\infty} x(t-\tau)h(t,\tau)d\tau = x(t) * h(t,\tau) \tag{2.3}$$

The impulse response shown in equation (2.3) is derived for a bandlimited passband channel, however it can be expressed equivalently as a complex baseband impulse response $h_b(t, \tau)$. The use of representing passband radio systems at baseband is discussed in section 2.4.1.1. Using baseband notation, the complex received signal envelope can be written as

$$y_b(t) = x_b(t) * \frac{1}{2} h_b(t,\tau) \tag{2.4}$$

where $y_b(t)$ and $x_b(t)$ are the complex envelopes of $y(t)$ and $x(t)$, respectively. The ½ factor in equation (2.4) is due to baseband signals having twice as much signal power as their passband counterparts. This fits in with conventional baseband signal theory and analysis (described in section 2.4.1.1).

2.3.1 Discrete Temporal Models

It is useful to divide the multipath delay axis τ of the impulse response into equally spaced time delay segments called excess delay bins, with each bin having a time delay width of $\Delta\tau$, i.e. $\tau_i = i\Delta\tau$ with $i = 0$ to N-1 for a maximum excess delay of $N\Delta\tau$. It is important to note that, depending on the choice of $\Delta\tau$ and the radio channel environment, there may be more than one multipath signal arriving within an excess delay bin. In such a scenario the individual components are unresolved, but do combine vectorially to yield a single multipath component. Such situations can cause the signal level to fade within an excess delay bin, however this is usually not significant over the local area [3].

The multipath channel consists of a series of attenuated, time-delayed, phase-shifted replicas of the transmitted signal. Therefore the baseband impulse response of the channel can be expressed as

$$h_b(t,\tau) = \sum_{i=0}^{N-1} a_i(t,\tau)\cdot e^{j(2\pi f_c \tau_i(t) + \phi_i(t,\tau))}\delta(\tau - \tau_i(t)) \tag{2.5}$$

where $a_i(t,\tau)$ and $\tau_i(t)$ are the real amplitudes and excess delays, respectively, of the i^{th} multipath component in time t. The phase term $e^{j(2\pi f_c \tau_i(t) + \phi_i(t,\tau))}$ in equation (2.5) represents the phase shift, due to the propagation of the i^{th} multipath component in the radio channel and any additional phase shifts encountered along the different propagation paths. The symbol $\delta(\cdot)$, denotes the unit impulse function, which is often used by engineers to represent a set of individual delayed and weighted signal components (in this case; multipath radio components at time t with excess delays τ_i). Figure 2.4 gives an example of the time varying discrete impulse response model for a multipath radio channel. In general, discrete temporal channel models are useful, not only because the digitisation of channel information is made relatively easy, but also because it is made possible to simulate the convolution of packet data with the channel impulse response [4].

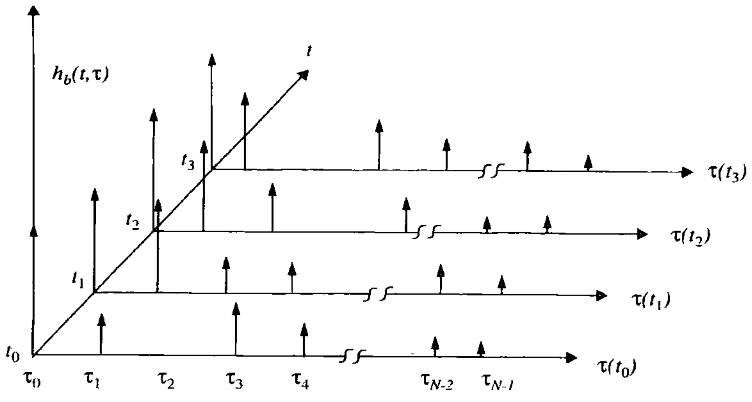

Figure 2.4: Time varying impulse response [3].

It is possible to assume a static channel environment over a local area if the time delay resolution of the channel impulse response resolves every multipath component over that area accurately. The term local area is often used when describing small-scale channel environments. By definition a local area is the largest volume of free space about a specified point in the radio channel, which can be modelled accurately as a sum of uniform plane waves (homogenous waves). With the aforementioned time-invariant channel assumption, equation (2.5) simplifies to

$$h_b(\tau)=\sum_{i=0}^{N-1} a_i(\tau)\cdot e^{j(2\pi f_c\tau_i+\phi_i(\tau))}\delta(\tau-\tau_i) \tag{2.6}$$

In general, the motion of scatterers in the radio channel introduces two components, which attribute to the overall channel impulse response; the non-fluctuating component $h_b(\tau)$, which describes the static channel and the fluctuating component $\delta h_b(t,\tau)$, which describes the transient channel. This is mathematically expressed as

$$h_b(t,\tau)=h_b(\tau)+\delta h_b(t,\tau) \tag{2.7}$$

In temporal channel modelling, the transient behaviour of the channel is of greater importance, since it is directly related to the motion of radio scatterers. When the radio channel is considered to be time invariant, only $h_b(\tau)$ is considered (as described by equation (2.6)).

The past literature has shown the developments of many new channel impulse response models, some of which take into account the spatial channel parameters (for multi-antenna systems), such as direction of arrival and/or direction of departure [6]. This is usually formulated by extending equations (2.5/2.6) to take into account directional channel information. Such models are often referred to as directional or double-directional channel models and have significant importance in characterising the spatial radio channel. Many of the developments in double-directional parametric channel modelling have come from the research programmes undertaken at the Technical Universities of Vienna (Austria) and Ilmenau (Germany) [7-12]. Some of these will be discussed in the following chapter.

It should be noted that the propagation physics of the mobile radio medium is described by the physical laws of small-scale fading formulated by Maxwell's equations (Maxwellian basis). Several publications explain this formulation including [13-15].

2.3.2 Power Delay Profile

In order to measure or statistically model the channel impulse response, a probing signal is often required to sound the radio channel (see chapter 5). Mobile radio channel sounding can be classified as being either direct pulse measurements, spread spectrum sliding correlator measurements, or swept frequency measurements. If a continuous pulse is used to sound the channel, it is possible to directly determine $h_b(t, \tau)$, since a pulse can approximate a delta function $\delta(t-\tau)$. For small-scale channel modelling, the power delay profile of the channel is found by taking the spatial average of $|h_b(t, \tau)|^2$ over a local area. By taking several local area measurements of $|h_b(t, \tau)|^2$ in different locations, it is possible to build an ensemble of different power delay profiles, each representing a small scale channel state [3]. When sounding the radio channel, the actual measured power is found by summing up the multipath powers resolved in the instantaneous power delay profile $|h_b(t, \tau)|^2$ of the channel and is equal to the energy received over the time duration of the total multipath delay divided by the maximum measured excess delay. Therefore small-scale received power is simply the sum of the average power received in each multipath component. The average time invariant power delay profile is given as

$$P(\tau) = \left\langle k \cdot \left| h_b(t, \tau) \right|^2 \right\rangle \tag{2.8}$$

Where $\langle \cdot \rangle$ denotes statistical expectation and k represents the total channel gain.

2.4 Mobile Radio Channel parameters

Various channel parameters can be derived from the power delay profiles of the channel, which are often represented as plots of relative received power as a function of excess delay (with a fixed time delay reference). The Doppler spectrum is equally important in describing the characteristics of the mobile radio channel with respect to the motion in the channel. However, these parameters can only be discussed if the fundamentals of stochastic radio channel modelling are revised.

2.4.1 Basic Stochastic Modelling Parameters

It is well known that the mobile radio propagation channel is a random process medium, which can only be modelled effectively by some measure of channel correlation. In general probability theory, correlation is a measure of conditional predictability, usually made between two observations of a random event. In stochastic channel modelling, the relationship between sample correlation and sample separation provides the starting point for characterising the behaviour of random process evolution. This type of analysis is based on the autocorrelation function of a particular channel parameter.

2.4.1.1 Baseband-Passband Representations

Although not directly relevant to the subject of stochastic modelling, baseband-passband transformations are very important in the notation used to represent signals. The development of baseband representation for modulated signals can be considered to be the cornerstone of channel modelling and analysis. A baseband representation essentially removes the dependence of a passband radio channel from its carrier frequency. This intern generalises and simplifies channel modelling. The following sections of this report will instinctively use this notation.

In order to understand such transformations, figure 2.5 illustrates both types of representation in the time and frequency domains [15]. The outer sketches show the process of modulation-demodulation for a baseband signal in the frequency domain, while the block diagram shows the same process in the time domain.

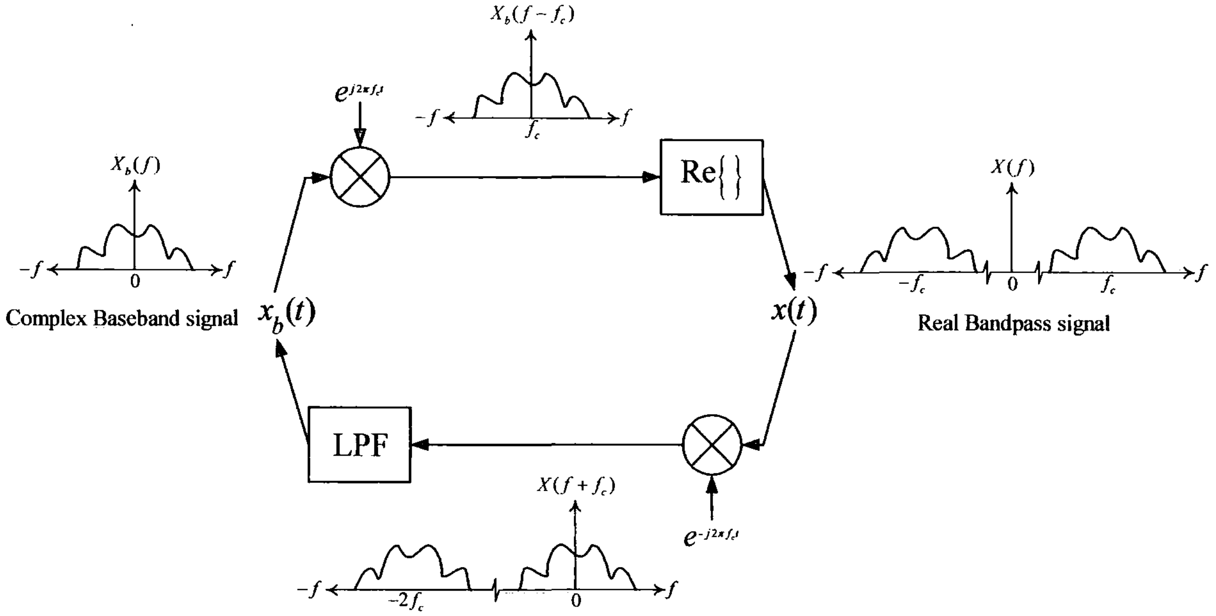

Figure 2.5: Baseband-passband transformations.

The subscript *b* denotes that the signal is in the baseband domain, hence $X_b(f)$ and $x_b(t)$ represent the baseband signal in the frequency and time domains, respectively. The passband signal represented in the time and frequency domains is denoted by $x(t)$ and $X(f)$, respectively. The passband signal is given by

$$x(t) = \mathrm{M}\left\{x_b(t)\right\} = \mathrm{Re}\left\{x_b(t)e^{j2\pi f_c t}\right\} \tag{2.9}$$

where $\mathrm{M}\{\cdot\}$ denotes the modulation operator and $\mathrm{Re}\{\cdot\}$ denotes the real part of a function. Using the identity $\mathrm{Re}\{\beta\} = \frac{1}{2}(\beta + \beta^*)$ in equation (2.9) yields

$$x(t) = \frac{1}{2}\left[\left(x_b(t)e^{j2\pi f_c t}\right) + \left(x_b(t)e^{j2\pi f_c t}\right)^*\right] \tag{2.10}$$

In order to demodulate the passband signal, the following can be derived

$$x_b(t) = \mathrm{M}^{-1}\left\{x(t)\right\} = \underbrace{\left[x(t)e^{-j2\pi f_c t}\right]}_{\text{frequency shift}} * \underbrace{\left[2k_B \mathrm{sinc}\left(k_B t\right)\right]}_{\text{low-pass filter}}$$

$$= 2k_B \int_{-\infty}^{\infty} x(\tau) e^{-j2\pi f_c \tau} \cdot \mathrm{sinc}\left(k_B \left[t-\tau\right]\right) d\tau \tag{2.11}$$

In equation (2.11), the first term denotes the frequency shift and the second term represents the low pass filter (LPF) response, with k_B as the filter bandwidth. The convolution of these two terms removes the high frequency mirror image so that only $X_b(f)$ remains.

The spectrum of the passband signal can be equivalently derived in the frequency domain using the Fourier transform.

$$\begin{aligned} X(f) &= \int_{-\infty}^{\infty} x(t) e^{-j2\pi f t} dt \\ &= \int_{-\infty}^{\infty} \left[\mathrm{Re}\left\{x_b(t) e^{j2\pi f_c t}\right\}\right] e^{-j2\pi f t} dt \\ &= \frac{1}{2} \int_{-\infty}^{\infty} \left[x_b(t) e^{j2\pi f_c t} + x_b^*(t) e^{-j2\pi f_c t}\right] e^{-j2\pi f t} dt \\ &= \frac{1}{2}\left[X_b(f-f_c) + X_b^*(-f-f_c)\right] \end{aligned} \tag{2.12}$$

2.4.1.2 Autocorrelation Relationships

A stochastic process is usually described by an ensemble of different random functions or realisations. The most common way to characterise a stochastic process is by calculating the autocorrelation function of that process. Taking the example of a time-varying stochastic channel $h_b(t)$, it is possible to derive its autocorrelation function as

$$R_{h_b}(t_1, t_2) = E\left\{h_b(t_1) h_b^*(t_2)\right\} \tag{2.13}$$

where $E\{\cdot\}$ denotes the ensemble average of all possible realisations. Equation (2.13) quantifies the time evolution of $h_b(t)$ by averaging the products of all samples in the random process ensemble at two different points in time, t_1 and t_2. Therefore, the autocorrelation function provides a snapshot of the typical correlation behaviour for a random channel. In order to simplify matters, it is possible to assume a Wide-Sense

Stationary (WSS) stochastic process, which infers that the time difference in the autocorrelation function is invariant of absolute time [15]. By this assumption the time difference $t_2 - t_1$, can be defined as a stationary variable Δt. Hence equation (2.13) can be expressed as

$$R_{h_b}(\Delta t) = E\left\{h_b(t_1)h_b^*(t_1 + \Delta t)\right\} \tag{2.14}$$

Also for a WSS process the mean $\mathrm{E}\{h_b(t)\}$ must not be a function of time. The WSS assumption is often not true in real life stochastic processes, but rather a simplifying assumption for channel characterisation.

There are various different definitions of autocorrelation function including autocovariance and unit autocovariance. If a stochastic process does not have a zero mean, then the autocovariance definition is used which removes the mean value. This is defined by

$$\begin{aligned}\bar{R}_{h_b}(\Delta t) &= E\left\{\left[h_b(t_1) - \mu\right]\left[h_b^*(t_1 + \Delta t) - \mu^*\right]\right\} \\ &= R_{h_b}(\Delta t) - |\mu|^2\end{aligned} \tag{2.15}$$

where μ is the random process mean and equal to $\mu = \mathrm{E}\{h_b(t)\}$.

The unit autocovariance is an autocovariance function that has been normalised against the mean power of the random process. It is dimensionless and therefore extremely useful in measuring correlation on a scale of 0 to1. In a time-varying stochastic channel the mean power is equal to the autocorrelation function evaluated at $\Delta t = 0$:

$$R_{h_b}(0) = E\left\{h_b(t)h_b^*(t)\right\} = E\left\{\left|h_b(t)\right|^2\right\} \tag{2.16}$$

Therefore, the unit autocovariance is defined as

$$\bar{r}_{h_b}(\Delta t) = \frac{R_{h_b}(\Delta t) - |\mu|^2}{R_{h_b}(0) - |\mu|^2} \tag{2.17}$$

With the autocorrelation function defined, it is possible to derive a definition for Power Spectral Density (PSD). PSD arises from the Wiener-Khintchine relationship, which states that the PSD and the autocorrelation of a WSS random process are Fourier Transform pairs. The Wiener-Khintchine theorem principally states that studying the autocorrelation properties in the base domain is equivalent to studying average signal power in the spectral domain. This relationship between autocorrelation and PSD is useful for joint channel statistics (described in section 2.7), as well as single dependency statistics. With this definition, a random process is only WSS if its spectral components are uncorrelated. This is inherently understood and is often referred to as Uncorrelated Scatterings (US) in the spectral domain [17].

For radio channel parameters, the spectral domain of time is the Doppler frequency domain, the spectral domain of frequency is the time delay domain, and the spectral domain of position is the wavenumber domain. Using these definitions, it is possible to note that by taking the Fourier transform of the autocorrelation function in time, the Doppler spectrum can be obtained. This duality is equivalently true for all other spectral representations. Using the example of channel autocorrelation in time, the Doppler spectrum is defined as

$$P_{h_b}(\nu) = \mathbb{F}\left\{R_{h_b}(\Delta t)\right\} = \int_{-\infty}^{\infty} R_{h_b}(\Delta t)\cdot e^{-j\nu\Delta t}\, d\Delta t \tag{2.18}$$

where $\mathrm{F}\{\cdot\}$ denotes the Fourier transform, and ν represents the Doppler frequency variable. The autocorrelation function in time can be derived using the inverse Fourier transform

$$R_{h_b}(\Delta t) = \mathbb{F}^{-1}\left\{P_{h_b}(\nu)\right\} = \frac{1}{2\pi}\int_{-\infty}^{\infty} P_{h_b}(\nu)\cdot e^{j\nu\Delta t}\, d\nu \tag{2.19}$$

2.4.2 Time Dispersion Parameters

Various multipath channel parameters can be derived from the power delay profile. The time dispersion properties of the wideband channel are often described by their mean excess delay ($\bar{\tau}$) and rms delay spread (σ_τ). The mean excess delay is the first moment of the power delay profile and is defined as

$$\bar{\tau} = \frac{\sum_k a_k^2 \tau_k}{\sum_k a_k^2} = \frac{\sum_k P(\tau_k)\tau_k}{\sum_k P(\tau_k)} \tag{2.20}$$

As previously mentioned, the power delay profile can be defined as the combined powers of k resolvable multipath components (up to resolvable τ_{max}) with amplitudes a_k. The rms (root mean square) delay spread is the square root of the second central moment of the power delay profile, and is defined as

$$\sigma_\tau = \sqrt{\overline{\tau^2} - (\bar{\tau})^2} \tag{2.21}$$

where

$$\overline{\tau^2} = \frac{\sum_k a_k^2 \tau_k^2}{\sum_k a_k^2} = \frac{\sum_k P(\tau_k)\tau_k^2}{\sum_k P(\tau_k)} \tag{2.22}$$

These delays are measured relative to the first resolved signal arriving at the receiver at $\tau_0 = 0$. Equations (2.21)-(2.22), only rely on the relative amplitudes of the multipath components within $P(\tau)$, and not the absolute power level. Typical values of rms delay spread are on the order of microseconds for outdoor mobile radio channels and on the order of nanoseconds for indoor radio channels. The statistics of delay spread are often studied to determine the time dispersion parameters of a small-scale channel environment. Intuitively, the rms delay spread can be defined in terms of the measured width of the delay PSD. This gives insight into the coherence of the channel since; as PSD widens, the autocorrelation becomes narrower and the coherence decreases.

The maximum excess delay (X dB) of the power delay profile is defined as the time delay during which multipath energy falls to X dB below the maximum. Figure 2.6 shows an example of the power delay profile for an indoor radio channel with a maximum excess delay defined for multipath signals within 20 dB of the maximum.

The measured channel delay parameters illustrated in figure 2.6, depend on the choice of noise floor used to process $P(\tau)$. The noise floor is the level, which differentiates between the resolvable multipath signals and thermal noise. If the noise threshold is set too low, then noise will be processed as multipath, therefore giving rise to delay parameters that are artificially too high.

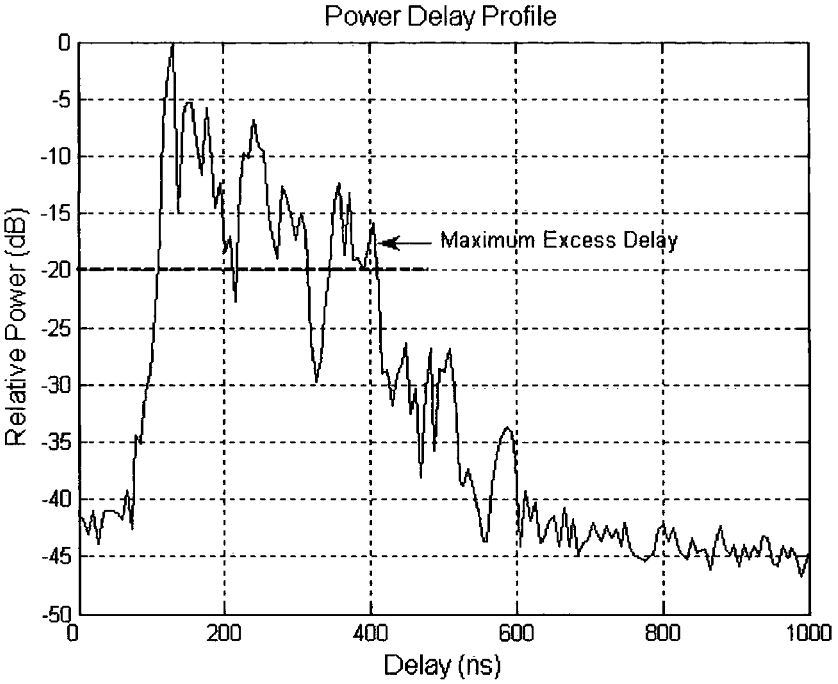

Figure 2.6: Indoor power delay profile with defined delay parameters.

2.4.3 Coherence Bandwidth

Delay spread is a natural phenomenon caused by reflection and scattering in the radio channel and the coherence bandwidth, B_c, is a defined relationship derived from the rms delay spread. Coherence bandwidth is simply a statistical measure of the range of frequencies over which the channel can be considered to pass all spectral components with approximately equal gain and linear phase. It is generally known as the range of frequencies over which spectral components have a strong potential for amplitude correlation. Two spectral components with a greater separation than the coherence bandwidth will behave quite differently. If the coherence bandwidth is defined as the bandwidth over which the frequency correlation function is greater than 0.9 [18], then this can be approximated as

$$B_c \approx \frac{1}{50\sigma_\tau} \tag{2.23}$$

However, the common rule of thumb for coherence bandwidth is defined so that the frequency correlation function is greater than 0.5. This gives an approximate coherence bandwidth of

$$B_c \approx \frac{1}{5\sigma_\tau} \tag{2.24}$$

The above definitions are only rough estimates of coherence bandwidth and therefore cannot determine the exact impact of time-varying channels on multipath signals [3]. This implies that more rigorous models have to be developed for more accurate radio channel characterisation.

2.4.4 Frequency Dispersion Parameters

The delay spread and coherence bandwidth do not provide information on the time varying nature of the channel caused by either the movement of objects in the channel or the relative motion between the mobile terminal and base station. Doppler spread and coherence time provide a description of this time varying nature of the channel.

Doppler spread, B_d, is a measure of the spectral widening caused by the time rate of change of the channel and is fundamentally defined as the frequency range over which the received Doppler spectrum is non-zero [3]. Hence, if a CW signal is transmitted at frequency f_0, the received signal spectrum (also defined as the Doppler spectrum), will have spectral components in the range of $f_0 - f_d$ to $f_0 + f_d$, where f_d is the Doppler shift defined earlier. If the spectrum of the transmitted baseband signal is much greater than B_d, the effects of Doppler spread can be neglected. This is usually termed slow fading. Using traditional definitions, the rms Doppler spread, σ_ν, which is a measure of the width of the Doppler spectrum, $P(\nu)$, can be defined as

$$\sigma_\nu = \sqrt{\overline{\nu^2} - (\overline{\nu})^2} \tag{2.25}$$

where the n^{th} central moment of the Doppler spectrum is given by

$$\overline{\nu^n} = \frac{\sum_F \nu_F^n P(\nu_F)}{\sum_F P(\nu_F)} \tag{2.26}$$

here F denotes the total interval of the Doppler spectrum. When $n = 1$, equation (2.26) denotes the mean Doppler, $\overline{\nu}$.

2.4.5 Coherence Time

Coherence time, T_c, is the time domain dual of the Doppler spread and is used to characterise the time varying nature of the frequency dispersive channel (in the time domain). The Doppler spread and coherence time are inversely proportional to one another and this can be expressed as

$$T_c \approx \frac{1}{f_m} \tag{2.27}$$

where f_m is the maximum Doppler shift derived from equation (2.2) and given by $f_m = v/\lambda$. Analogous to the definition of coherence bandwidth defined earlier, the coherence time can be defined as the maximum time separation over which received signals have a strong potential for amplitude correlation. In essence, coherence time is a statistical measure of the time duration over which the channel impulse response is time invariant, which is used to quantify the similarity of the channel response at different times. If the inverse of the transmitted signal bandwidth ($1/B_s$) is greater than the coherence time of the channel, then there will be channel variations during transmission causing the received signal to distort. As in the case of coherence bandwidth, there are also various slightly different expressions for coherence time. By assuming coherence time is defined as the time over which the time correlation function is above 0.5, T_c can be approximately expressed as [18]

$$T_c \approx \frac{9}{16\pi f_m} \tag{2.28}$$

However, a popular rule of thumb defines the coherence time as a geometric mean of equations (2.27) and (2.28). This is expressed as

$$T_c \approx \sqrt{\frac{9}{16\pi f_m^2}} = \frac{0.423}{f_m} \tag{2.29}$$

2.4.6 Time and Frequency Selective Fading

In Summary of the above, time dispersion and frequency selective fading are both manifestations of multipath propagation with delay spread, and as noted previously, they are both intuitively related to one another. Time dispersion causes a signal to stretch in time so that the duration of the received signal is greater than the duration of the transmitted signal. In general, time dispersion is a result of signals taking different times to cross the channel via different propagation paths and is quantified by the delay spread. Frequency selective fading on the other hand, filters the transmitted signal, attenuating certain frequencies more than others. It occurs because the electrical length ($l_e = \tau/c$) of each propagation path can be expressed as a function of frequency and this is measured by the coherence bandwidth [18].

Frequency dispersion and time selective fading both represent the time varying nature of the channel. Frequency dispersion results in the signal bandwidth being stretched so that the received signal's bandwidth is different (greater or less) from that of the transmitted signal. The frequency dispersion of the channel is measured by the Doppler spread. Time selective fading represents the frequency dispersion characteristics of the channel in the time domain and can cause distortion because the channel characteristics may change while the signal is in flight. Time selective fading is expressed in terms of coherence time and has a reciprocal relationship with Doppler spread.

2.4.7 Angle Spectrum and Space Selective Fading

The concept of delay spectrum is quite intuitive and can be described as multipath power arriving at the receiver with different propagation delays due to the relative electrical lengths of the propagation paths in the channel, thus causing a smear of the received signal power as a function of time delay. The Doppler spectrum is equally intuitive, since the movement of objects in the channel and the relative motion between the transmitter and receiver introduces nonzero Doppler frequencies on selected multipath components, causing frequency dispersion of the received signal. However, the concept of wavenumber (or wavevector) spectrum is not so intuitive, since scientists and engineers do not often work in the spectral domain of space. Since the motion of objects in space and the temporal variations of the channel are related by $d = vt$, often a space-varying channel is converted into a time varying channel.

The concept of angle spectrum is quite intuitive (as oppose to wavenumber) and attempts to define the spatial fading of the channel in terms of the Direction of Arrival (DOA) of incoming multipath power typically only in the azimuth plane. Angle spread at the receiver refers to the spread in the DOA of the multipath components at the receive array for a multi-antenna system. Similarly, angle spread at the transmitter refers to the spread in the Direction of Departure (DOD) of the multipath signals that finally reach the receiver. It is possible to define the rms angle spread, σ_θ, as

$$\sigma_\theta = \sqrt{\overline{\theta^2} - \left(\overline{\theta}\right)^2} \tag{2.30}$$

where the n^{th} central moment of the angle spectrum, $P(\theta)$, is given by

$$\overline{\theta^n} = \frac{\sum_{i=-\pi}^{\pi} \theta_i^n P(\theta_i)}{\sum_{i=-\pi}^{\pi} P(\theta_i)} \tag{2.31}$$

when $n = 1$, equation (2.31) defines the mean DOA ($\overline{\theta}$).

Angle Spread causes space selective fading, meaning that the signal amplitude varies with the spatial position of the antenna. Space selective fading is characterised by coherence distance, D_c, which is inherently defined by a reciprocal relationship with rms angle spread, given as

$$D_c \propto \frac{1}{\sigma_\theta} \tag{2.32}$$

The exact constant in the relationship depends on the spatial environment. The coherence distance is often used to classify an environment as being either small-scale or large scale [15].

2.5 Types of Channel Fading

As described in the previous section, the type of fading experienced by a signal propagating in the channel depends on the characteristics of the radio channel and that of the transmitted signal. In general, different signals transmitted through the channel will undergo different types of fading, depending on the relationships between signal characteristics such as bandwidth and symbol period, and channel parameters such as delay spread and Doppler spread. The time and frequency dispersion mechanisms in the channel lead to four distinctly different effects, which are manifested based on signal and channel characteristics. It is quite apparent from the channel parameters, that the delay spread leads to time dispersion and frequency selective fading, whereas the Doppler spread leads to frequency dispersion and time selective fading. These time and frequency dispersion mechanisms are independent of one another and are described below.

2.5.1 Multipath Fading Caused by Delay spread

Time dispersion due to multipath propagation causes signal fading, which can be classified as either frequency flat fading or frequency selective fading [2].

2.5.1.1 Frequency Flat Fading

If the radio channel has a constant gain and linear phase over a bandwidth, which is greater than the transmitted signal bandwidth, then the received signal will undergo frequency flat fading, or simply flat fading. The channel multipath structure in a flat fading environment is such that the transmitted signal spectra is preserved at the receiver. However, the receiver signal changes over time due to the variations of the channel gain caused by multipath. In a flat fading channel, the reciprocal bandwidth of the transmitted signal is much larger than the channel multipath delay spread and $h_b(t, \tau)$ can be approximately described as having no excess delay. Flat fading channels are also referred to as amplitude varying channels (in time), and since the bandwidth of such channels are inherently narrow, the term narrowband fading is also applied. In general, flat fading channels cause deep signal fades and are often described by a Rayleigh distribution. A signal undergoes flat fading if

$$B_s << B_c \tag{2.33}$$

where B_s and B_c denote the transmission bandwidth and the channel coherence bandwidth, respectively. Due to the reciprocal relationship, this can be expressed as

$$T_s = \frac{1}{B_s} >> \sigma_\tau \tag{2.34}$$

where T_s is the reciprocal bandwidth (i.e. for digital data this is the symbol period) and σ_τ is the rms delay spread.

2.5.1.2 Frequency Selective Fading

If the radio channel has a constant gain and linear phase over a bandwidth, which is smaller than the transmitted signal bandwidth, then the received signal will experience frequency selective fading. In such a fading environment, the channel impulse response has a delay spread which is greater than the reciprocal bandwidth of the transmitted signal. Such a channel by its nature induces intersymbol interference. Since the signal bandwidth is considered to be larger than the coherence bandwidth, certain frequency components in the received signal spectrum have greater gain than others.

In the analysis of flat fading channels, the impulse response was approximately modelled by a single delta function. However, this is no longer the case with frequency selective fading channels, since each multipath component must be described and the channel should be considered as a linear filter. This makes it extremely difficult to model frequency selective channels, and it is for this reason that wideband channel measurements are made, and models are developed from these measurements. Several models have been developed so far to characterise the wideband multipath channel, such as the statistical two-ray Rayleigh fading model, which considers the channel impulse response to be constructed from two delta functions (see section 2.6.2.3).

Frequency selective fading is caused by multipath delays, which approach or exceed the symbol period of the transmitted symbol [3]. The term ‘wideband channels’ are often used to describe frequency selective fading channels, since the bandwidth of the transmitted signal is considered to be wider than the channel coherence bandwidth. As time varies, the channel changes in gain and phase across the transmitted signal spectrum, causing time varying distortion in the received signal. In summary a signal undergoes frequency selective fading if

$$B_s > B_c \tag{2.35}$$

and

$$T_s = \frac{1}{B_s} < \sigma_\tau \tag{2.36}$$

A rule of thumb, which is often used to distinguish between the types of channel fading caused by delay spread is that a channel is flat fading if $T_s \geq 10\sigma_\tau$, and is frequency selective fading if $T_s < 10\sigma_\tau$. Figure 2.7 illustrates the types of channel fading by comparing the signal spectrum to the channel coherence bandwidth.

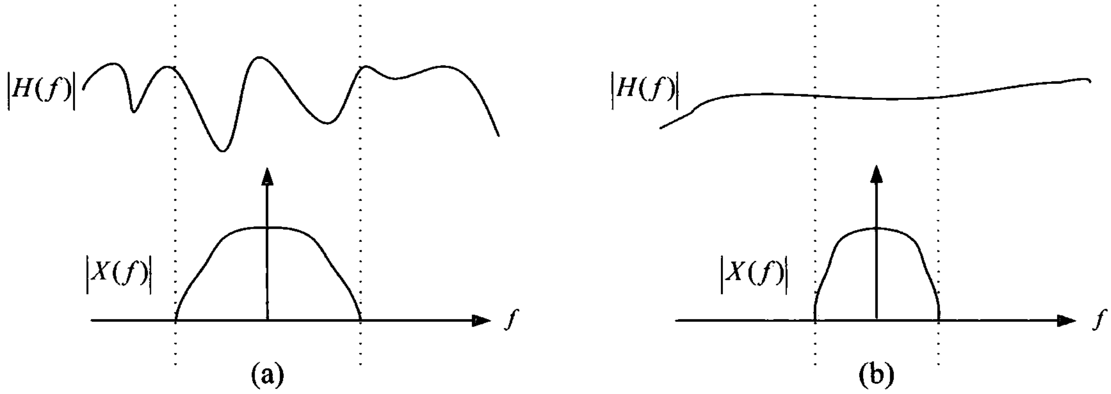

(a) (b)

Figure 2.7: (a) Frequency selective fading, and (b) flat fading for a transmitted signal of spectrum $X(f)$ as compared to the channel spectrum $H(f)$.

2.5.2 Multipath Fading Caused by Doppler Spread

Frequency dispersion due to the time variant nature of the channel causes signal fading, which can be classified as either fast fading or slow fading.

2.5.2.1 Fast Fading

The rate of change of the transmitted baseband signal as compared to the rate of change of channel determines the type of fading caused by Doppler spread. In a fast fading channel, the impulse response changes rapidly within the symbol duration and the symbol period of the transmitted signal is considered to be larger than the coherence time of the channel. The Doppler spreading of the channel causes frequency dispersion, which distorts the signal by introducing Doppler frequencies to the various multipath components. In summary, a signal experiences fast fading if

$$T_s = \frac{1}{B_s} > T_c \tag{2.37}$$

and

$$B_s < \sigma_v \tag{2.38}$$

where T_c and σ_v are the coherence time and Doppler spread, respectively.

It must be noted that the term fast fading and slow fading only refer to the rate of change of the channel due to motion and do not specify the frequency selectivity of the radio channel. When dealing with flat fading channels, the impulse response can be approximated by a single delta function since there is effectively no excess delay. Hence a flat fading, fast fading channel is a channel where the amplitude of the delta function varies faster than the rate of change of the transmitted signal [3]. In the case of a frequency selective fading, fast fading channel, the amplitudes, phases and delays of any of the multipath components varies faster than the rate of change of the transmitted signal. In real systems, fast fading only occurs if the data rate is very low.

2.5.2.2 Slow Fading

In a slow fading channel, the rate of change of the channel impulse response is much slower than the rate of change of the transmitted signal and the channel may be assumed static over one or several symbol periods. This infers that the Doppler spread of the channel is much smaller that the bandwidth of the baseband signal in the frequency domain. Therefore, a signal undergoes slow fading if

$$T_s = \frac{1}{B_s} << T_c \tag{2.39}$$

and

$$B_s >> \sigma_v \tag{2.40}$$

The velocity of the mobile and the velocity of the surrounding objects in the channel determine whether the transmitted signal experiences fast or slow fading. Figure 2.8 illustrates the type of channel fading caused by Doppler spread for simple transmitted square pulse symbols for both fast and slow fading.

Figure 2.9 illustrates the relationship between multipath channel parameters and the type of fading experienced by the transmitted signal in matrix form. Both matrix tables are equivalent to one another, and are related by a reciprocal relationship [3]. Fast fading and slow fading deal with the relationship between the time rate of change in the channel and the transmitted signal, and therefore should not be confused with the terms large-scale and small-scale fading, since these are defined by the measure of spatial channel coherence and spatial selectivity.

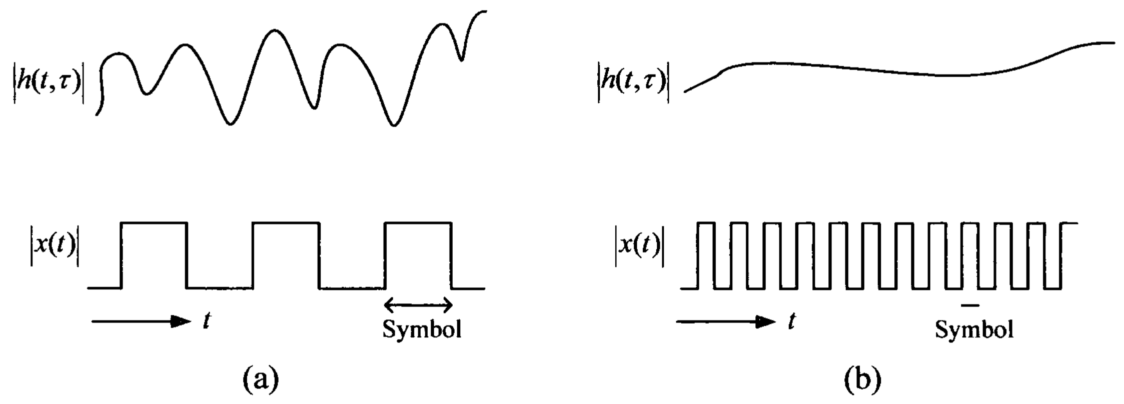

(a) (b)

Figure 2.8: (a) Fast fading, and (b) slow fading for a transmitted signal of square pulses, where *x(t)* and $h_b(t,\tau)$, denote the transmitted baseband signal and the channel impulse response, respectively.

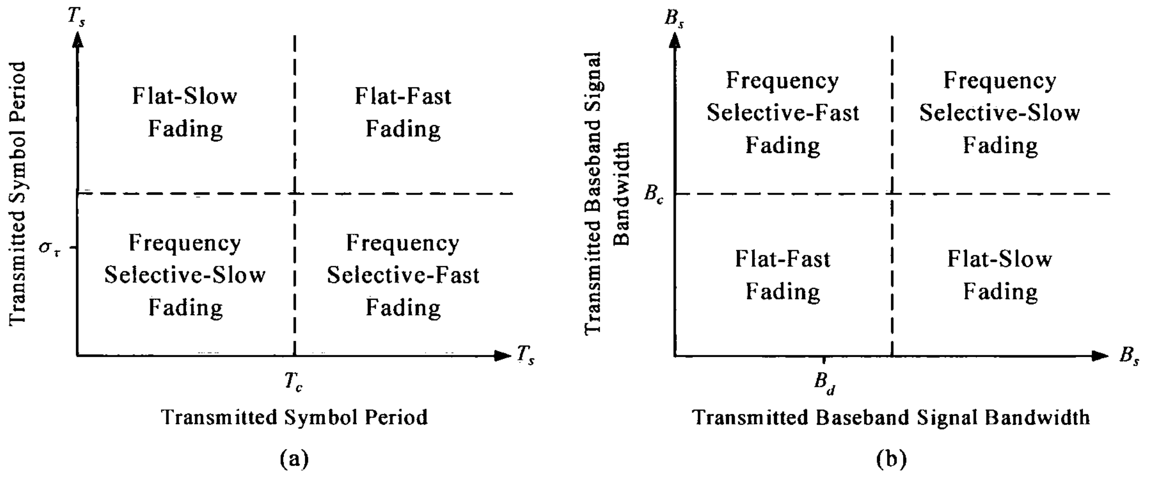

(a) (b)

Figure 2.9: Types of fading experienced by a signal as (a) a function of transmitted symbol period, and (b) a function of transmitted baseband signal bandwidth.

2.6 Statistics of Fading

The mobile radio channel can be analysed by its first order and second order statistics. The following describes the probability distribution functions used to describe the envelope fading characteristics of signals in the channel. The distribution functions used to describe small-scale signal variations (rapid signal variations) include Rayleigh, Rician and Nakagami. Several statistical models, which describe the multipath fading in the channel, are also discussed. Furthermore, the second order statistics of the channel are described such as level crossing rate and duration of fades.

2.6.1 Fading Distributions for Received Signal Envelope

2.6.1.1 Rayleigh Fading Distribution

The Rayleigh distribution is often used to describe the time varying nature of the received envelope of a flat fading signal, or the envelope of an individual multipath component in a non-LOS environment. The Pythagorean sum of two quadrature Gaussian noise signals follows a Rayleigh distribution. The Rayleigh distribution has a Probability Density Function (PDF), which is given by

$$p(r)=\frac{r}{\sigma^2}\cdot e^{-\left(\frac{r^2}{2\sigma^2}\right)}, \qquad r\geq 0 \tag{2.41}$$

where r is the signal strength in linear units, $r^2/2$ is the short term signal power, and σ is the rms value of the received voltage signal [19]. The probability that the received signal envelope does not exceed a particular value R, is given by the Cumulative Distribution Function (CDF)

$$\Pr\left[r\leq R\right]=\int_0^R p(r)dr=1-e^{-\left(\frac{R^2}{2\sigma^2}\right)} \tag{2.42}$$

The mean value r_{mean} and the variance σ_r^2 of the Rayleigh distribution is given by

$$r_{mean}=E\{r\}=\int_0^\infty r\cdot p(r)dr=\sqrt{\frac{\pi}{2}}\sigma=1.2533\sigma \tag{2.43}$$

and

$$\sigma_r^2 = E\{r^2\} - (E\{r\})^2 = \int_0^\infty r^2 \cdot p(r)dr - \frac{\pi}{2}\sigma^2$$

$$= \left(2 - \frac{\pi}{2}\right)\sigma^2 = 0.4292\sigma^2 \tag{2.44}$$

Furthermore, the median r_{median} of the distribution is found by solving

$$0.5 = \int_0^{r_{median}} p(r)dr \tag{2.45}$$

therefore,

$$r_{median} = 1.77\sigma \tag{2.46}$$

The term Rayleigh fading actually describes an environment in which all the received signal power is non-specular in nature. In other words, the received signal power does not have any LOS (specular) components present.

2.6.1.2 Rician Fading Distribution

When there is a dominant specular non-fading signal component present in the channel (such as for a LOS path), the fading envelope distribution is described to be Rician. In such a scenario, random multipath signal components are superimposed on a dominant stationary (non-fading) signal. At the output of the envelope detector, this is manifested by adding a dc component to the random multipath. As the dominant signal becomes weaker, the composite signal starts resembling a noise signal which has a Rayleigh envelope. Hence, the Rician distribution collapses to a Rayleigh distribution, when the dominant signal fades away. The Rician PDF is given by

$$p(r) = \frac{r}{\sigma^2} \cdot e^{-\left(\frac{r^2+V_p^2}{2\sigma^2}\right)} I_0\left(\frac{V_p r}{\sigma^2}\right), \quad V_p \geq 0,\ r \geq 0 \tag{2.47}$$

where the parameter V_p, denotes the peak amplitude of the dominant signal and $I_0(\cdot)$ is the zero-order modified Bessel function of the first kind.

A parameter called the K-factor is very important in describing the Rician distribution. The Rician K-factor describes the ratio of specular power, V_p^2, to the remaining non-specular multipath power, $2\sigma^2$. In the literature, the K-factor is often given in dB value

$$K_{dB} = 10\log_{10}\left(\frac{V_p^2}{2\sigma^2}\right) \tag{2.48}$$

As $V_p \to 0$; $K \to -\infty$ dB, therefore the Rician Distribution degenerates to a Rayleigh distribution. This is illustrated in the PDF and CDF plots in figure 2.10 [20].

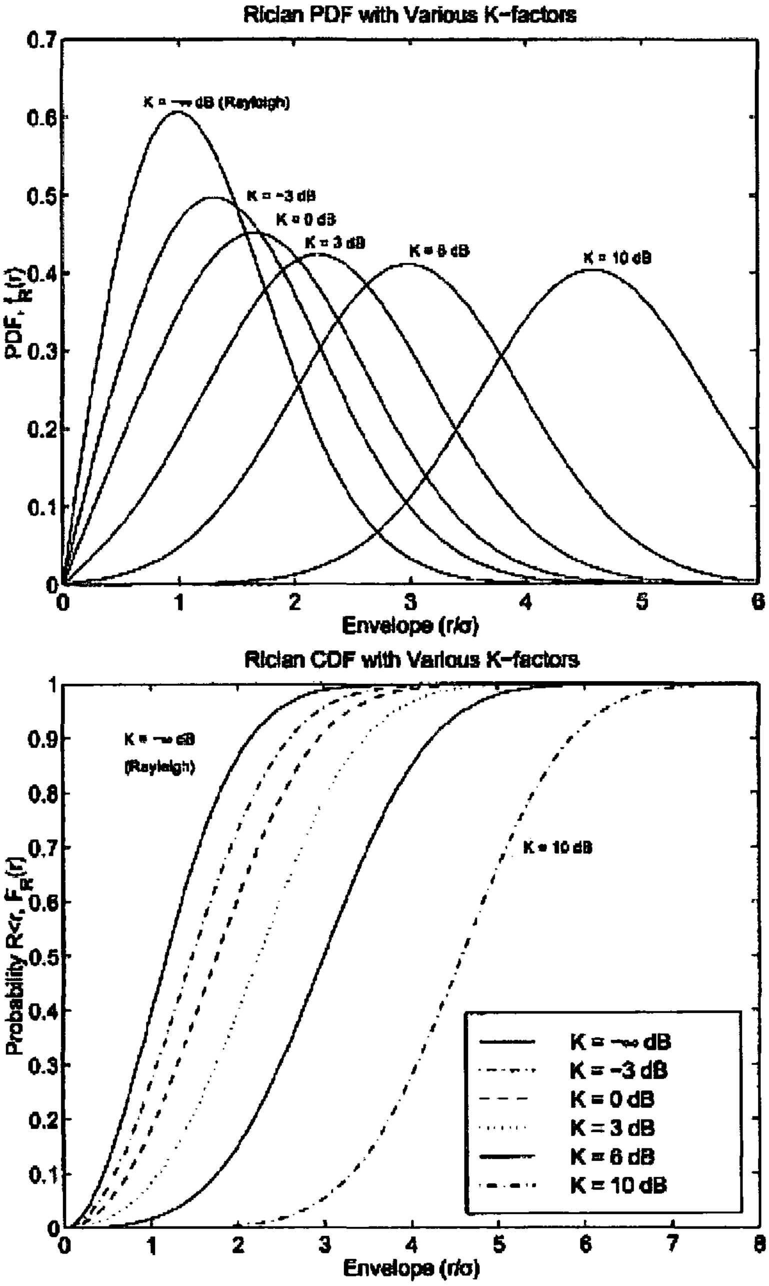

Figure 2.10: Rician PDF ($f_R(\rho)$) and CDF ($F_R(\rho)$) as the dominant multipath signal component increases [20].

The Rician CDF is given by

$$\Pr\left[r \le R\right] = \frac{1}{2} + \frac{1}{2} erf\left(\frac{R - V_p}{\sqrt{2}}\right) - \frac{1}{\sqrt{8\pi V_p}}\left(1 - \frac{R - V_p}{4V_p} + \frac{1 + \left(R - V_p\right)^2}{8V_p^2}\right) \cdot e^{-\frac{\left(R - V_p\right)^2}{2}} \tag{2.49}$$

where the error function, erf(·), is defined as

$$erf(x) = \frac{2}{\pi}\int_0^x e^{-t^2} dt \tag{2.50}$$

2.6.1.3 Nakagami Fading Distribution

The Nakagami distribution is useful in modelling mobile radio channels, which are either more, or less severe than the Rayleigh channels. The distribution is modelled by a single parameter, m, which corresponds to the amount of fading in the channel [19].

$$p(r) = \frac{2}{\Gamma(m)}\left(\frac{m}{R}\right)^m r^{(2m-1)} e^{-\left(\frac{mr^2}{R}\right)}, \quad r \ge 0 \tag{2.51}$$

where m is mathematically expressed as the ratio of moments (inverse normalised variance of envelope, r^2), and $R = \overline{r^2}$. The m parameter is given by

$$m = \frac{R^2}{\left(r^2 - R\right)^2}, \quad m \ge 0.5 \tag{2.52}$$

The Nakagami distribution is very useful in approximating other distributions. For example, m = 0.5 gives the one-sided Gaussian distribution, and m = 1 gives the Rayleigh distribution. In equation (2.51), Γ(·) denotes the Gamma function, which is given by [21]

$$\Gamma(x) = \int_0^\infty t^{x-1} e^{-t} dt \tag{2.53}$$

The Nakagami CDF is given

$$\Pr\left[r \le S\right] = 1 - \frac{m^m}{\Gamma(m)} \int_{\frac{2}{m}(S-f_0)}^{\infty} e^{m\left(x-e^x\right)} dx \qquad (2.54)$$

There are many other statistical distributions which describe the fading experienced in a mobile radio channel, including the log-normal distribution, which is useful for urban channel characterisation, and the Suzuki distribution, which combines short-term Rayleigh fading with long-term log-normal fading. There have also been recent developments of fading distributions, which are based on the physical descriptions of multipath signals [20]. Such fading distributions include, the Two-Wave with Diffuse Power (TWDP) PDF, which extends the Rician model to include two dominant specular non-fading multipath components rather than one.

2.6.2 Statistical Models for Multipath Fading

A number of models are presented here, which describe the statistical nature of the mobile radio channel. The first model that attempted to describe the multipath channel statistics, was Ossana's model, which was based on the interference of waves incident and reflected from the flat sides of randomly located buildings [1]. Ossana's model made certain assumptions, including the requirement for a LOS path, which restricted it from being applied to cluttered radio channels, in which no direct signal would be available from the transmitter to the receiver. A model based on scattering was much more appropriate, and the most widely quoted is Clarke's model [22]. The Doppler power spectra derived from Clarke's model is famous in its shape and used widely in channel characterisation. Clarke's model is a two dimensional signal model, meaning that incoming waves that travel vectorially are restricted to the azimuth plane [22]. An extended three dimensional signal model based on Clarke's work was made available by Aulin, in order to alleviate such problems [1]. The following describes Clarke's model as well as some other important channel models, which statistically describe multipath fading.

2.6.2.1 Clarke's Flat Fading Model

Clarke developed a model based on channel scattering, which provided the statistical characteristics of the electromagnetic waves received at the mobile terminal. The model assumes a fixed transmitter with a vertically polarised antenna. The received field is assumed to be in the azimuthal plane, and comprises of N equal amplitude plane waves, with arbitrary carrier phases and azimuthal angles of arrival. The received waves are assumed to be of equal amplitude, since in the absence of a LOS path, the received (scattered) components will experience similar channel attenuations over small-scale distances. Figure 2.11, illustrates a typical Azimuthal nth component wave arriving at the mobile receiver.

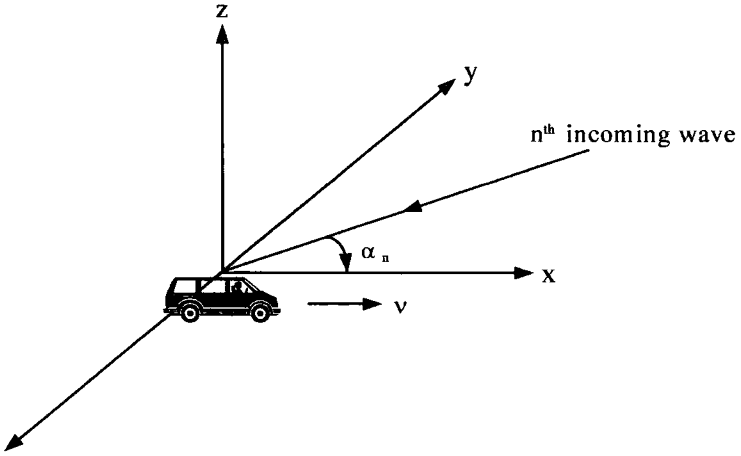

Figure 2.11: Illustrating the nth component wave incident on a mobile receiver travelling at velocity v, in the x-direction. The angle of arrival of the nth component wave is given in the azimuthal x-y plane, and denoted by α_n.

Every wave incident on the mobile terminal experiences a Doppler shift (defined in equation (2.2)) due to the motion of the receiver, and arrives at the receiver at the same time. This inherently infers that there is no excess delay for any of the incoming component waves (i.e. flat fading assumption). The Doppler shift for the nth component wave arriving at an angle of α_n with reference to the x-axis is given by

$$f_n = \frac{v}{\lambda}\cos\alpha_n \tag{2.55}$$

If the transmitted signal is vertically polarised, the E and H field components seen at the mobile receiver are given by [22]

$$E_z = E_0 \sum_{n=1}^{N} C_n \cos(2\pi f_c t + \theta_n) \tag{2.56}$$

$$H_x = -\frac{E_0}{\eta}\sum_{n=1}^{N} C_n \sin\alpha_n \cos(2\pi f_c t + \theta_n) \tag{2.57}$$

$$H_y = \frac{E_0}{\eta}\sum_{n=1}^{N} C_n \cos\alpha_n \cos(2\pi f_c t + \theta_n) \tag{2.58}$$

where

$$\theta_n = 2\pi f_n t + \phi_n \tag{2.59}$$

In the above equations, f_c is the carrier frequency of the transmitted signal, η is the intrinsic free space wave impedance ($120\pi \approx 377\Omega$), E_0 defines the amplitude of the average E-field (assumed locally constant), and C_n is a real variable representing the amplitudes of individual waves. Together, E_0C_n denotes the amplitude of the nth wave in the E_z field. The θ_n parameter denotes the random phase angle of the nth arriving component (ϕ_n is uniformly distributed between 0 and 2π).

The amplitudes of the E and H fields are normalised such that

$$E\left\{\sum_{n=1}^{N} C_n^2\right\} = 1 \tag{2.60}$$

The three field components may be modelled as narrowband random processes, since the experienced Doppler shift is small compared to the carrier frequency. Furthermore, as a consequence of the central limit theorem, for large values of N, the three field components can be approximately modelled as Gaussian random variables. Based on the analysis by Rice, the E-field can be expressed in an in-phase and quadrature form [22]

$$E_z(t) = T_c(t)\cos(2\pi f_c t) - T_s(t)\sin(2\pi f_c t) \tag{2.61}$$

where

$$T_c(t) = E_0\sum_{n=1}^{N} C_n \cos(2\pi f_n t + \phi_n) \tag{2.62}$$

and

$$T_s(t) = E_0\sum_{n=1}^{N} C_n \sin(2\pi f_n t + \phi_n) \tag{2.63}$$

Both $T_c(t)$ and $T_s(t)$ are Gaussian random processes, corresponding to the in-phase and quadrature components of E_z, and are denoted by T_c and T_s (for a fixed t), respectively. They have zero mean and equal variance, and are denoted by

$$E\left\{T_c^2\right\} = E\left\{T_s^2\right\} = \frac{E_0^2}{2} = E\left\{\left|E_z\right|^2\right\} \tag{2.64}$$

It must be noted that T_c and T_s are independent:

$$E\left\{T_c T_s\right\} = 0 \tag{2.65}$$

Since $T_c(t)$ and $T_s(t)$ are Gaussian random variables, the envelope of the received E-field ($|E(t)|^2$) follows a Rayleigh distribution (proof is derived via the Jacobean transformation) [22].

2.6.2.2 Doppler Spectra Derived From Clarke's Model

So far it is assumed that the field may be represented by the sum of N component waves (equation (2.56)). As N→ ∞, it would be expected that the incident power included in an angle between α and $\alpha + d\alpha$ would approach a continuous, instead of discrete, distribution [3]. Let $p(\alpha)d\alpha$ denote this fraction of the total incoming power within $d\alpha$ of the angle of α, and also assume that the receiver antenna is directive in the azimuthal plane with power gain pattern $G(\alpha)$. Thus it is possible to express the total received power as

$$P_r = \int_0^{2\pi} AG(\alpha)p(\alpha)d\alpha \tag{2.66}$$

where A denotes the average received power with respect to an isotropic antenna, and $AG(\alpha)p(\alpha)d\alpha$ is the differential variation of the received power with angle [3]. This differential variation of the received power can be expressed in terms of frequency [22]. If the scattered signal is a CW signal of frequency f_c, then the instantaneous frequency of the received signal component arriving at angle α is defined as

$$f(\alpha) = f = f_m \cos\alpha + f_c \tag{2.67}$$

where f_m is the maximum Doppler shift ($f_m = v/\lambda$) and $f(\alpha)$ is an even function of α. Since $f(\alpha) = f(-\alpha)$, the differential variation of power with frequency may be expressed as

$$S(f)|df| = A\left[p(\alpha)G(\alpha) + P(-\alpha)G(-\alpha)\right]|d\alpha| \tag{2.68}$$

where $S(f)$ is the power spectrum of the received signal. Using the differentiation of equation (2.67), it is possible to derive

$$|df| = |d\alpha||-\sin\alpha|f_m \tag{2.69}$$

since α can be expressed in terms of f, such that

$$\alpha = \cos^{-1}\left(\frac{f - f_c}{f_m}\right) \tag{2.70}$$

therefore

$$\sin\alpha = \sqrt{1 - \left(\frac{f - f_c}{f_m}\right)^2} \tag{2.71}$$

substituting equation (2.69) and (2.71) into (2.68), thus gives the power spectrum of the output of a receiving antenna

$$S(f) = \frac{A\left[p(\alpha)G(\alpha) + P(-\alpha)G(-\alpha)\right]}{f_m\sqrt{1 - \left(\frac{f - f_c}{f_m}\right)^2}} \tag{2.72}$$

where

$$S(f) = 0, \qquad \text{for } |f - f_c| > f_m \tag{2.73}$$

The above spectrum is centred on the carrier frequency and is zero outside the limits of $f_c \pm f_m$. Each of the arriving waves has a carrier frequency, which due to the direction of arrival, is slightly offset from the centre frequency. This power spectrum depends on the antenna gain pattern and differs from the power spectrum of the field components. It is possible to assume from the present model, that there are antennas that respond to the field directly. For example, if the transmitted signal is assumed to be vertically polarised, the electric field will be in the z-direction. This infers that the field may be sensed by a vertical $\lambda/4$ antenna (with $G(\alpha) = 1.5$). Substituting this into equation (2.72) and assuming that $p(\alpha)$ is uniformly distributed over the interval of 0 to 2π (i.e., $p(\alpha) = 1/2\pi$) gives

$$S_{E_z}(f) = \frac{1.5}{\pi f_m \sqrt{1 - \left(\frac{f - f_c}{f_m}\right)^2}} \tag{2.74}$$

Antennas may likewise be used to sense the magnetic field along the x-axis (H_x) and along the y-axis (H_y) in order to derive the magnetic field power spectra ($S_{Hx}(f)$ and $S_{Hy}(f)$).

In equation (2.74), the power spectrum at $f = f_c \pm f_m$ is infinite, meaning that the Doppler components arriving at 0° and 180° have an infinite power spectrum. This is not a problem since α is continuously distributed and the probability of components arriving at exactly these angles is zero [3]. Figure 2.12 illustrates the Doppler power spectral density for an unmodulated CW signal. The spectrum analysis for Clarke's model was developed by Gans [22].

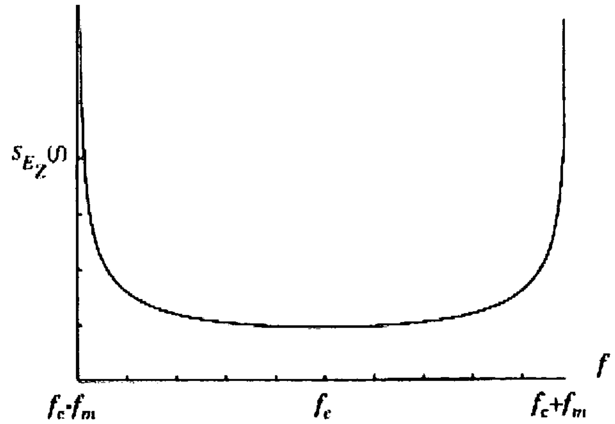

Figure 2.12: Doppler power spectra derived from Clare's model.

The Doppler spectra derived from Aulin's model gives an RF spectrum, which does not tend to infinity at $f = f_c \pm f_m$, and is therefore a better fit for the Doppler experienced in the channel. Parson's Model gives an even better fit to this spectrum and is derived in [1].

Following the envelope detection of the Doppler-shifted signal at the receiver, the baseband power spectrum has a maximum frequency of $2f_m$. It is shown from Jakes [22] that the electric field produces a baseband power spectral density given by

$$S_{bbE_z}(f)=\frac{1}{8\pi f_m}K\left[\sqrt{1-\left(\frac{f}{2f_m}\right)^2}\right] \tag{2.75}$$

where K[·] is the complete elliptic integral of the first kind. This is a result of the temporal correlation of the received signal when passed through a nonlinear detector [3]. Also, the complete elliptic integral of the first kind is defined as [21]

$$K(m)=\int_0^{\pi/2}\left(1-m\sin^2\theta\right)^{1/2}d\theta \tag{2.76}$$

In reality, the Doppler spectrum can show considerable variation from this model. In fixed wireless applications the Doppler spectrum is approximately exponential in its shape [23]. Clarke's model conveniently produces analytical statistics that are unrealistically identical regardless of the direction of travel (omnidirectional). Many measurement campaigns have shown that the arriving multipath in a local area bears little resemblance to this omnidirectional propagation assumption. In general, an approximately omnidirectional model does not accurately describe fading statistics if directional or smart antenna systems are used.

Recently a powerful method of using shape factors [24] has been presented which allows the quantative analysis of any distribution of non-omnidirectional multipath components in a local area. Three shape factors are defined; angular spread, angular constriction and azimuth direction of maximum fading, which describes the distribution of the arriving multipath energy. Basic second order small-scale statistics such as level crossing rate, average fade duration, autocovariance and coherence distance, may be described in terms of multipath shape factors. These are well documented in [15, 24].

2.6.2.3 Two-Ray Rayleigh Fading Model

Clarke's model and the statistics of Rayleigh fading are for flat fading conditions and therefore do not consider multipath delay. Modelling the effect of multipath delay spread has become essential for high data rate communication systems [3]. A simple model which can be useful in modelling the multipath in a channel is the two-ray independent Rayleigh fading model. The impulse response of the model is given by

$$h_b(t) = \alpha_1 e^{j\phi_1}\delta(t) + \alpha_2 e^{j\phi_2}\delta(t-\tau) \tag{2.77}$$

where α_1 and α_2 are independent and Rayleigh distributed, ϕ_1 and ϕ_2 are independent and uniformly distributed over the interval of 0 to 2π, and τ is the time delay separation between the two rays. By varying τ, it is possible to examine a wide variety of frequency selective fading effects.

2.6.2.4 Saleh-Valenzuela Model

The Saleh-Valenzuela Model [25] is a popular indoor statistical multipath channel model based on measurement results. Here, it is reported that the measurement results were obtained by using 10ns radar-like pulses. The method involved averaging the square law detected pulse response while sweeping the frequency of the transmitted signal.

The Saleh-Valenzuela Model is based on the assumption that the rays of the received signal arrive in clusters. The received ray amplitudes are independent Rayleigh random variables with variances that decay exponentially with cluster delay as well as with ray delay within a cluster. The corresponding phase angles are independent uniform random variables over the interval of 0 to 2π. The clusters, as well as the rays within a cluster, form Poisson arrival processes with different, but fixed rates. Equivalently, the clusters and the rays have exponentially distributed inter-arrival times. The formation of the cluster is related to the building superstructure, while the rays within a cluster are formed by multiple reflections from objects in the vicinity of the transmitter and the receiver.

The analysis of the model carried out to produce a channel impulse response can be presented as follows. Let the gain of the k^{th} ray of the l^{th} cluster be denoted by β_{kl}, and its phase by θ_{kl}. Thus, the complex low-pass impulse response of the channel is given by

$$h(t)=\sum_{l=0}^{\infty}\sum_{k=0}^{\infty}\beta_{kl}e^{j\theta_{kl}}\delta(t-T_l-\tau_{kl}) \tag{2.78}$$

where T_l is the arrival time of the l^{th} cluster ($l = 0,1,2, \ldots$) and τ_{kl} is the arrival time of the k^{th} ray measured from the beginning of the l^{th} cluster ($k = 0,1,2, \ldots$). By definition, for the first cluster, $T_l = 0$, and for the first ray within the l^{th} cluster, $\tau_{0l} = 0$. Thus, according to this model T_l and τ_{kl} are described by independent inter-arrival exponential PDFs.

2.6.3 Level Crossing Rate and Average Fade Duration

Rice computed joint statistics for a mathematical problem which was similar to Clarke's fading model. This provided simple expressions for computing the Level Crossing Rate (LCR) of the signal and the Average Fade Duration (AFD) of the signal. The LCR and AFD are two important second-order statistics which are useful for designing error control codes and diversity schemes to be used in mobile communication systems. The LCR is defined as the expected rate at which the normalised Rayleigh fading signal envelope crosses a specified level, R, in a positive direction, and is defined as

$$N_t=\int_0^{\infty}\dot{r}p(R,\dot{r})d\dot{r}=\sqrt{2\pi}f_m\rho e^{-\rho^2} \tag{2.79}$$

where $\dot{r}$ is the time derivative of the received signal, $p(R,\dot{r})$ is the joint PDF of r and $\dot{r}$ at $\dot{r}=R$, f_m is the maximum Doppler shift, and $\rho = R/R_{rms}$ is the value of the specified level R, normalised to the local rms amplitude of the fading signal envelope [22]. Usually the signal envelope undergoes frequent shallow fades and occasional deep fades.

The AFD is defined as the average period of time for which the received signal is below a specified level R. For a Rayleigh fading signal, this is defined as

$$\bar{t} = \frac{1}{N_t}\Pr\left[r \le R\right] = \frac{1}{N_t}\int_0^R p(r)dr = \frac{1-e^{-\rho^2}}{N_t} \tag{2.80}$$

substituting equation (2.79) into (2.80) gives

$$\bar{t} = \frac{e^{\rho^2}-1}{\rho f_m\sqrt{2\pi}} \tag{2.81}$$

The AFD is very useful in indicating the most likely number of signalling bits lost during the fade. The manner in which LCR and AFD are related is shown in figure 2.13, where the LCR is the average number of positive going crossings per second and the AFD is the average of τ_1, τ_2, τ_3, ..., τ_n.

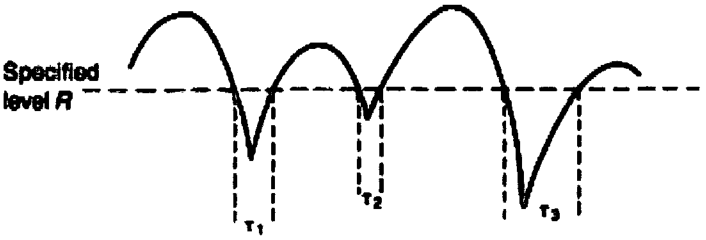

Figure 2.13: The relation between LCR and AFD [1].

2.7 Wideband Channel Characterisation

The characterisation of frequency-selective mobile radio channels can be developed from the general description of linear time-variant filters (figure 2.14). The channel can be described in terms of system functions, which give insight into the physical mechanisms that dominate channel behaviour. This so-called 'systems' approach to linear time-variant channels was formally and rigorously developed by Bello [17], based on the original work done by Zadeh on linear time-variant filters [1]. In a seminal paper, Bello proposed four system functions, which individually provided full knowledge of the channel in the time and frequency domains. The symmetrical relationships between these system functions via the frequency and time duality principle meant that the full knowledge of one function would allow the direct calculation of any other function.

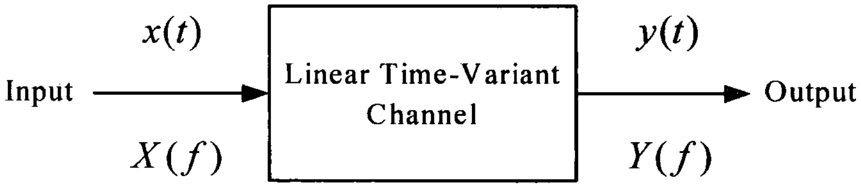

Figure 2.14: A linear time-variant channel with input ($x(t) \leftrightarrow X(f)$) and output ($y(t) \leftrightarrow Y(f)$) described in the time and frequency domains, respectively.

Mobile radio channels have propagation characteristics that are seen to vary randomly with the location of the mobile and relative motion of objects in the channel. Bello system functions provide a description of deterministic channels, which can then be transformed to random variables used to describe randomly time-variant linear channels.

2.7.1 Bello System Functions

A set of four system functions are denoted by Bello as; input delay-spread function $h(t, \tau)$, time-variant transfer function $T(f, t)$, output Doppler-spread function $H(f, \nu)$, and delay-Doppler-spread function $S(\tau, \nu)$. The following briefly describes each function.

- **Input Delay-Spread Function, $h(t, \tau)$**

The input delay-spread function relates the input signal $x(t)$ to the output signal $y(t)$ by the convolution relationship, as previously expressed in equation (2.3)

$$y(t) = \int_{-\infty}^{\infty} x(t-\tau)h(t,\tau)d\tau \qquad (2.82)$$

where $h(t, \tau)$ is the time-variant channel impulse response. In the discrete time delay and using the causality principle, equation (2.82) can be expressed as

$$y(t) = \sum_{n=1}^{N} x(t-n\Delta\tau)h(t,n\Delta\tau)\Delta\tau \qquad (2.83)$$

which can be realised in the form of a tapped delay line, composed of N delay elements, N modulators and N adders (figure 2.15). This provides a time domain description of the channel, where delay is associated with the channel input.

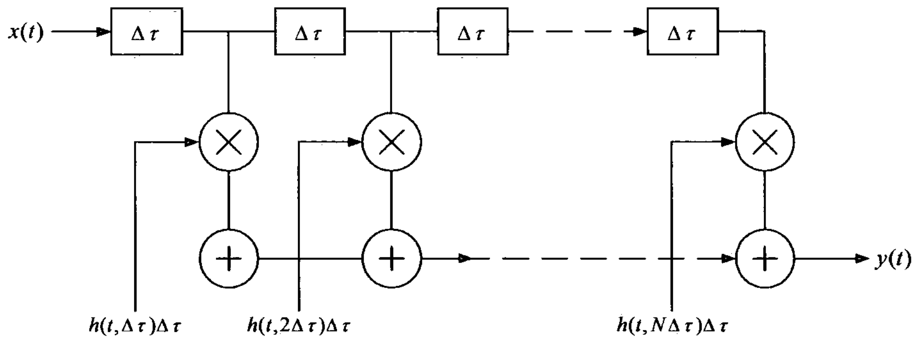

Figure 2.15: Tapped delay line model of a multipath channel.

The time-variant impulse response is measured directly by time domain wideband sounders, which either use a wideband RF pulse, or its equivalent. The tapped delay line model is often used in system simulations [4, 26].

- **Time-Variant Transfer Function, *T(f,t)***

The time-variant transfer function is found by taking the Fourier transform of the time-variant impulse response, with respect to τ. This provides the relationship between input spectrum $X(f)$ and the output time function $y(t)$. This is expressed as

$$y(t) = \int_{-\infty}^{\infty} X(f)T(f,t)e^{j2\pi ft}df \tag{2.84}$$

where

$$Y(f,t) = X(f,t) \cdot T(f,t) \tag{2.85}$$

and $X(f,t)$ and $Y(f,t)$ are the short term spectra of the input and output signals, respectively, and are only valid if the channel is varying slowly with time, i.e. time-invariant assumption [27].

For narrowband (frequency-flat) channels, the transfer function is obtained by means of a single tone (unmodulated CW carrier) sounder. For wideband (frequency-selective) channels, a multi tone sounder can be used which transmits several simultaneous spaced CW tones, which are then received individually via a narrowband receiver [28]. This gives a direct measure of the coherence bandwidth of the channel (chapter 5). An alternative and far more efficient technique in the frequency/time domain is to use a swept CW carrier, i.e. a chirp signal.

- **Output Doppler-Spread Function, $H(f, \nu)$**

The Fourier transform of the transfer function with respect to time t, gives the output Doppler-spread function, which relates the output spectrum $Y(f)$ to the input spectrum $X(f)$ in an identical manner to the way in which $h(t, \tau)$ relates the input/output time functions. The interpretation of this function is that the channel output spectrum is represented as the superposition of elemental Doppler-shifted and filtered replicas of the input spectrum. This is described in terms of frequency, f, and Doppler shift, ν, given by

$$Y(f) = \int_{-\infty}^{\infty} X(f-\nu)H(f-\nu,\nu)d\nu \tag{2.86}$$

Analogous to the tapped delay line model, it is possible to realise the physical model of the channel based on $H(f, \nu)$ in the form of dense frequency conversion chains which represent the positive and negative Doppler frequency shifts on the input signal spectrum. This model is realised in figure 2.16, using a differential circuit representation of equation (2.86), which uses a bank of filters with transfer functions $H(f, \nu)\Delta\nu$, followed by Doppler shifting frequency converters. The output Doppler-spread function can be directly measured by frequency domain wideband sounders and can be used for simulation of the channel as an alternative to $h(t, \tau)$ [18].

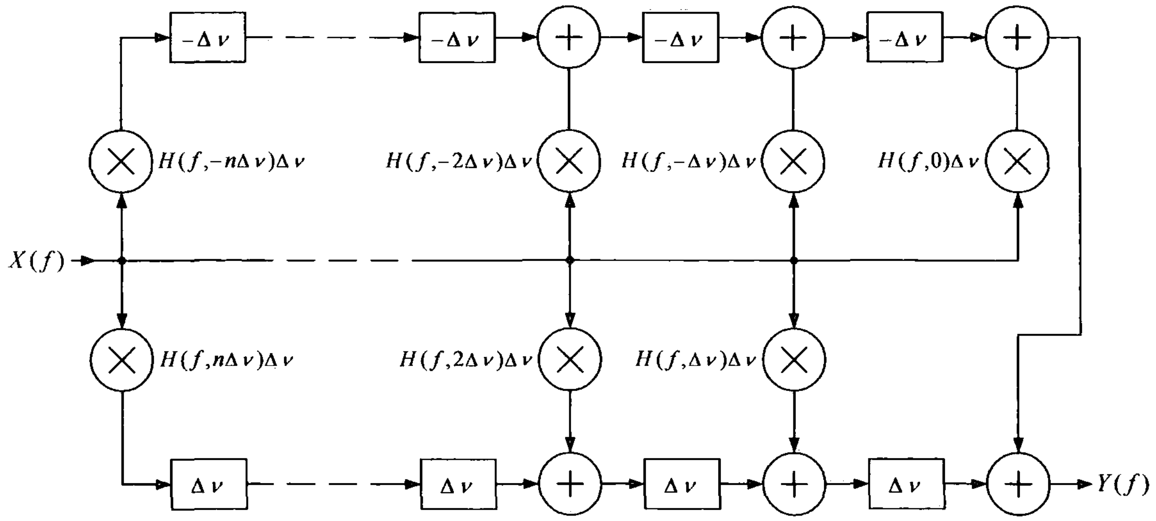

Figure 2.16: Tapped frequency conversion chain model. This provides a frequency domain description of the channel, where Doppler is associated with the output port of the channel.

- **Delay-Doppler-Spread Function, $S(\tau,\nu)$**

A Fourier transform of $h(t,\tau)$ with respect to t yields a function $S(\tau,\nu)$, which is denoted as the delay-Doppler-spread function, or simply the scattering function. Unlike either $h(t,\tau)$ or $H(f,\nu)$, which provide an explicit description of only one aspect of the channel's dispersive behaviour (either delay or Doppler), the scattering function provides a description of both the delay and Doppler characteristics of the channel. This represents a channel, which has the time-delay operation at the input and the Doppler-shift operation on the output. The output signal $y(t)$ is the sum of delayed and Doppler shifted replicas of the input signal $x(t)$, weighted by $S(\tau,\nu)$, which can thus be interpreted as the gain of infinitesimal point scatterers. Using the obvious definition of

$$h(t,\tau)=\int_{-\infty}^{\infty}S(\tau,\nu)e^{j2\pi\nu\tau}d\nu \tag{2.87}$$

the input-output relationship can be defined as

$$y(t)=\int_{-\infty}^{\infty}\int_{-\infty}^{\infty}x(t-\tau)S(\tau,\nu)e^{j2\pi\nu\tau}d\nu d\tau \tag{2.88}$$

2.7.2 Bello Dual Set Functions

Bello system functions have a dual set denoted as output delay-spread function $g(t,\tau)$, frequency-dependent modulation function $M(t,f)$, input Doppler-spread function $G(f,\nu)$ and Doppler-delay-spread function $V(\nu,\tau)$. These equivalent functions are referred to as sister functions since they describe the channel in the same domain, therefore it is common to employ only the first set of system functions.

2.7.3 Relationships Between System Functions

It is inherently understood from Bello that the system variables f and ν are orthogonal to each another in the same way that the variables t and τ are orthogonal. The duality of system variables defined by Bello is illustrated in figure 2.17, with $\mathbb{F}$ and $\mathbb{F}^{-1}$ denoting the forward Fourier transform and the inverse Fourier transform, respectively, with respect to a system variable. In figure 2.17, the standard convention is applied; therefore when converting from a time variable to a frequency variable, the Fourier transform is used, whereas the inverse Fourier transform is used when converting from a frequency variable to a time variable. The Relationships between the Bello system functions can be illustrated using this convention (figure 2.18).

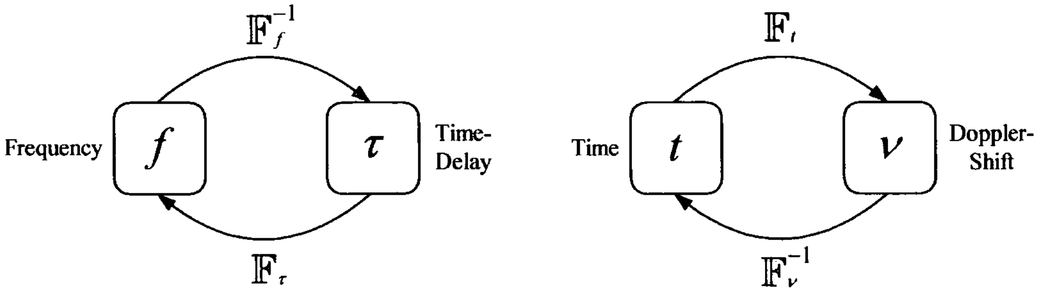

Figure 2.17: Relationship between system variables.

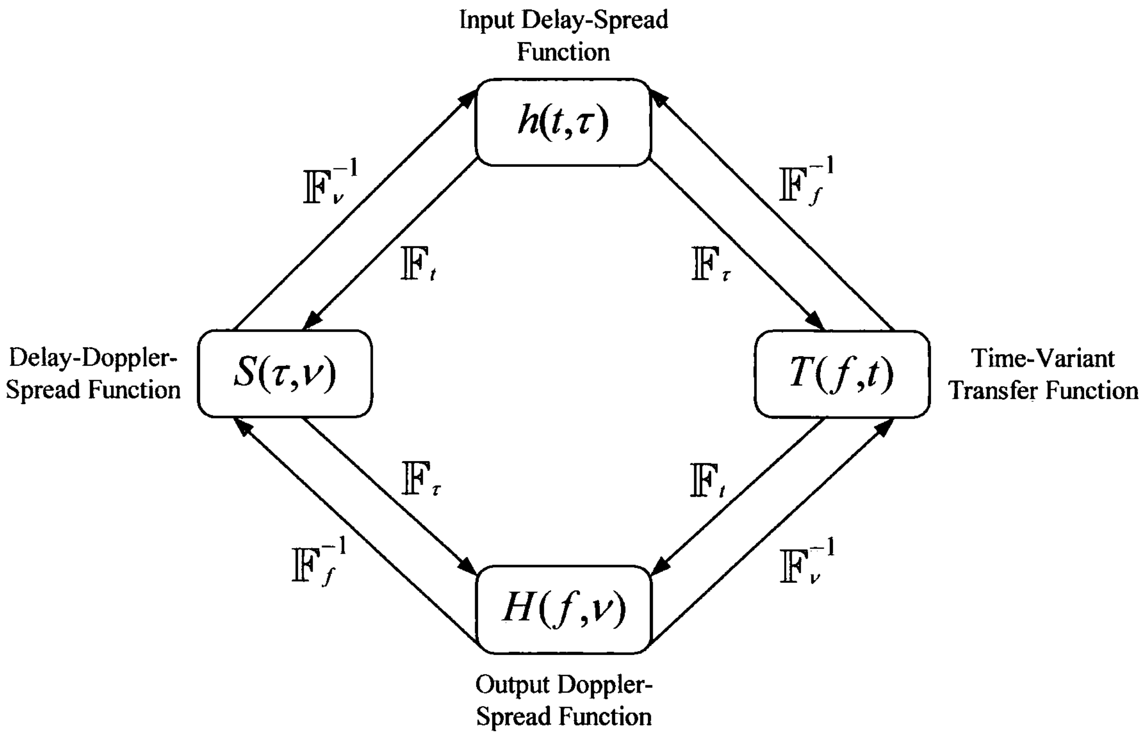

Figure 2.18: Fourier Transform Relationships between Bello System functions.

2.7.4 Randomly Time-Variant Linear Channels

Having established the various descriptions of the channels deterministic behaviour (using Bello functions), it is now possible to extend the analysis to a discussion of real radio channels, which are randomly time-variant in nature. For a complete stochastic description of the channel, it is necessary to have a multidimensional joint PDF of the impulse response, or an equivalent system function. Since this is too complicated in practice, Bello suggested that the characterisation of these channels be done using just the autocorrelation of the impulse response or one of its Fourier transforms. Noting the definition of autocorrelation defined in section 2.4.1.2, it is possible to describe the purely random channel using the autocorrelation definition of the four system functions described earlier. This is formulated as

$$R_h(t,t';\tau,\tau') = E\{h(t,\tau)h^*(t',\tau')\} \tag{2.89a}$$

$$R_T(f,f';t,t') = E\{T(f,t)T^*(f',t')\} \tag{2.89b}$$

$$R_H(f,f';\nu,\nu') = E\{H(f,\nu)H^*(f',\nu')\} \tag{2.89c}$$

$$R_S(\tau,\tau';\nu,\nu') = E\{S(\tau,\nu)S^*(\tau',\nu')\} \tag{2.89d}$$

where t and t' are time variables, τ and τ' are time-delay variables, f and f' are frequency variables and ν and ν' are Doppler-shift variables.

In the same way that the Bello system functions were related by the Fourier transform, the system autocorrelation functions are also related by an inherent Fourier relationship. However, since there are two pairs of each variable, the double Fourier transform has to be employed [17]. This is denoted by DF and DF^{-1}, which represents double forward Fourier transform and double inverse Fourier transform, respectively. However, it must be noted that when transforming from a time variable to a frequency variable, a positive exponent is used to connect the first variables in each pair and a negative exponent to connect the second variables (e.g. from R$_h$ to R$_T$, use $e^{j2\pi f\tau}$ and $e^{-j2\pi f'\tau'}$). When transforming from a pair of frequency variables to a pair of time variables, an opposite signing procedure is used (e.g. from R$_T$ to R$_h$, use $e^{-j2\pi\tau f}$ and $e^{j2\pi\tau' f'}$). Using this convention, the relationships of the system autocorrelation functions are illustrated in figure 2.19.

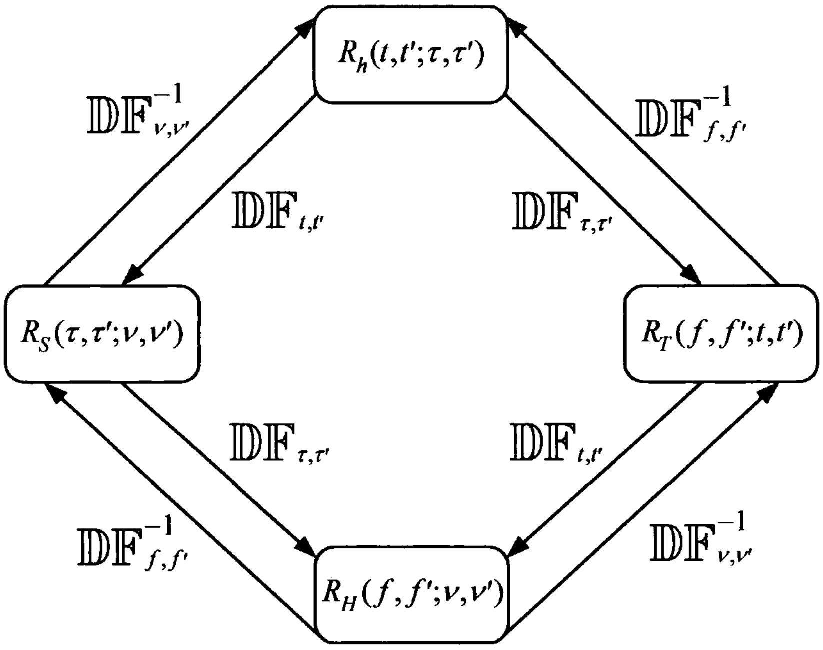

Figure 2.19: Relationships between system autocorrelation functions.

If the statistics of the channel are zero-mean Gaussian, then the autocorrelation functions are sufficient to completely characterise the channel. If they are not zero-mean, then the mean values are required in order to use the autocovariance definition. Only non-Gaussian statistics require higher-order statistics [27].

2.7.5 Description of Practical Channels

Even the Autocorrelation function is too complicated for a practical description of the channel, since it is dependent on four variables, e.g., *t*, *t'*, τ, τ' (or its equivalent). The Wide-Sense Stationary Uncorrelated Scattering (WSSUS) assumption allows a further simplification (as noted in section 2.4.1.2).

2.7.5.1 Wide-Sense Stationarity (WSS)

As noted previously, a channel is wide-sense stationary if its autocorrelation function does not depend on *t* and *t'*, but only on the difference $\Delta t = t' - t$. This is denoted by

$$R_h(t,t';\tau,\tau') = R_h(t,t+\Delta t;\tau,\tau') = R_h(\Delta t;\tau,\tau') \tag{2.90}$$

and

$$R_T(f,f';t,t') = R_T(f,f';t,t+\Delta t) = R_T(f,f';\Delta t) \tag{2.91}$$

The physical interpretation of this is that the second-order statistics of the channel remain the same over time (strict sense stationarity would mean that the higher-order statistics would not change over time) [27]. The equivalent narrowband case would be a Rayleigh fading amplitude (equation (2.41)), where σ^2 stays the same over time.

A further interpretation of the WSS condition is given by the spreading function $S(\tau, \nu)$ and its Fourier relationship

$$R_S(\tau,\tau';\nu,\nu') = \int_{-\infty}^{\infty}\int_{-\infty}^{\infty} R_h(t,t';\tau,\tau')e^{j2\pi(\nu t-\nu' t')}dtdt' \tag{2.92}$$

Inserting equation (2.90) into (2.92) gives

$$R_S(\tau,\tau';\nu,\nu') = \int_{-\infty}^{\infty} e^{j2\pi(\nu-\nu')t}dt \cdot \int_{-\infty}^{\infty} R_h(\Delta t;\tau,\tau')e^{-j2\pi\nu'\Delta t}d\Delta t \tag{2.93}$$

The first integral in equation (2.93) is just a delta Dirac function $\delta(\nu-\nu')$, therefore

$$R_S(\tau,\tau';\nu,\nu')=\tilde{P}_S(\tau,\tau';\nu)\delta(\nu-\nu') \tag{2.94}$$

In the general notation used, $P\{\cdot\}$ represents the PSD, which is derived by taking the Fourier transform of the autocorrelation functions. In equation (2.94), $\tilde{P}_S(\tau,\tau';\nu)$ is the delay-Doppler cross power, denoted by the second integral in equation (2.93). Thus, the WSS assumption implies that the contributions of the different scatterers are uncorrelated if they give different Doppler shifts. In a similar way

$$R_H(f,f';\nu,\nu')=P_H(f,f';\nu)\delta(\nu-\nu') \tag{2.95}$$

In terms of circuit model representation, this implies that the transfer functions of the random filters associated with different Doppler shifts (figure 2.16) are uncorrelated.

2.7.5.2 Uncorrelated Scattering (US)

The Uncorrelated Scattering (US) assumption is defined as the contributions of scatterers with different delays being uncorrelated. This implies

$$R_h(t,t';\tau,\tau')=P_h(t,t';\tau)\delta(\tau-\tau') \tag{2.96}$$

For R_S, the US condition means

$$R_S(\tau,\tau';\nu,\nu')=\tilde{\tilde{P}}_S(\tau;\nu,\nu')\delta(\tau-\tau') \tag{2.97}$$

Physically, the US assumption implies that one echo gives no information about another echo with a different delay. The US is regarded as the dual of the WSS assumption in the frequency domain, such that the autocorrelation functions will only depend on the frequency difference between the variables, i.e. $\Delta f=f'-f$. This implies

$$R_H(f,f';\nu,\nu')=R_H(f,f+\Delta f;\nu,\nu')=R_H(\Delta f;\nu,\nu') \tag{2.98}$$

and

$$R_T(f,f';t,t')=R_T(f,f+\Delta f;t,t')=R_T(\Delta f;t,t') \tag{2.99}$$

Thus equations (2.98) and (2.99) only depend on the frequency difference, and not the absolute frequency.

2.7.5.3 The WSSUS channel

It is an obvious step to combine the WSS and US conditions to form the WSSUS assumption. As a result a WSSUS channel exhibits WSS with respect to the time and time-delay variables and US with respect to the frequency and Doppler-shift variables. The WSSUS assumption provides the simplest type of randomly time-variant linear channel description. This is accomplished via the WSSUS channel correlation functions, described as

$$R_h(t,t+\Delta t;\tau,\tau')=\delta(\tau-\tau')P_h(\Delta t;\tau) \tag{1.100a}$$

$$R_T(f,f+\Delta f;t,t+\Delta t)=R_T(\Delta f;\Delta t) \tag{1.100b}$$

$$R_S(\tau,\tau';\nu,\nu')=\delta(\tau-\tau')\delta(\nu-\nu')P_S(\tau;\nu) \tag{1.100c}$$

$$R_H(f,f+\Delta f;\nu,\nu')=\delta(\nu-\nu')P_H(\Delta f;\nu) \tag{1.100d}$$

The functions on the right depend now on only two variables, which clearly simplifies the formulation and computations of the channel characteristics. The name and Fourier relationships of these correlation functions are shown in figure 2.20.

The WSSUS assumption provides many inaccuracies, however it is a simple model for the channel that has proved to be very useful in the characterisation of scattering radio environments. The ergodicity assumption (with respect to t and f) leads directly to the WSSUS channel. However, the US assumption is only fulfilled for certain types of environments. For particular indoor channels and other special environments such as corridors and tunnels, scatterers are not uncorrelated [29].

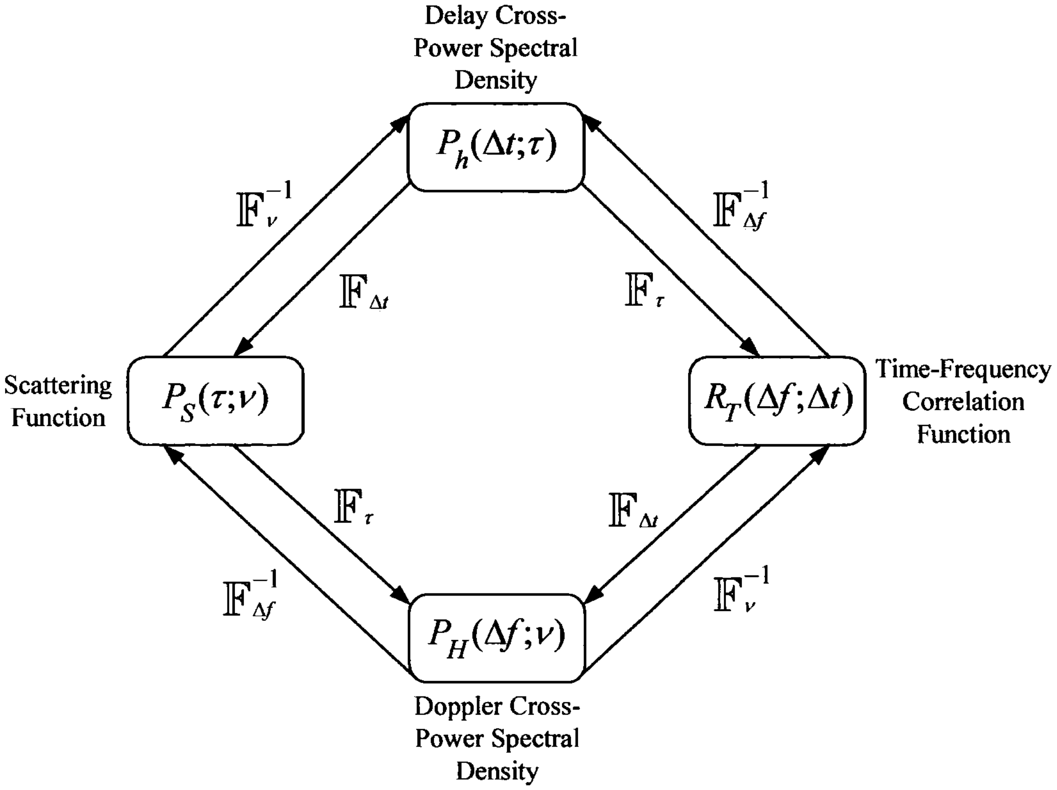

Figure 2.20: Relationships between correlation functions in the WSSUS channel.

Many channel parameters can be derived from the correlation functions shown above, including power delay profile $P(\tau)$, Doppler spectrum $P(\nu)$, frequency correlation function $R_T(\Delta f)$ and time correlation function $R_T(\Delta t)$. In turn these parameters lead to the computations of many other parameters, such as coherence time, coherence bandwidth, delay spread and Doppler spread. The most useful correlation function is the scattering function, since it can lead directly to the power delay profile and the Doppler spectrum [30]. The link between the channel parameters used for WSSUS channels is shown in figure 2.21.

In general, many models have been developed from the WSSUS assumption [31] and in the literature the simplified channel correlation functions have been extended to include spatial parameters. One example is the WSSUS Homogenous channel (WSSUS-HO) model [23]. Furthermore, Deterministic Gaussian Uncorrelated Scattering (DGUS) models have been developed to form an analogous relationship to the WSSUS model [29, 32].

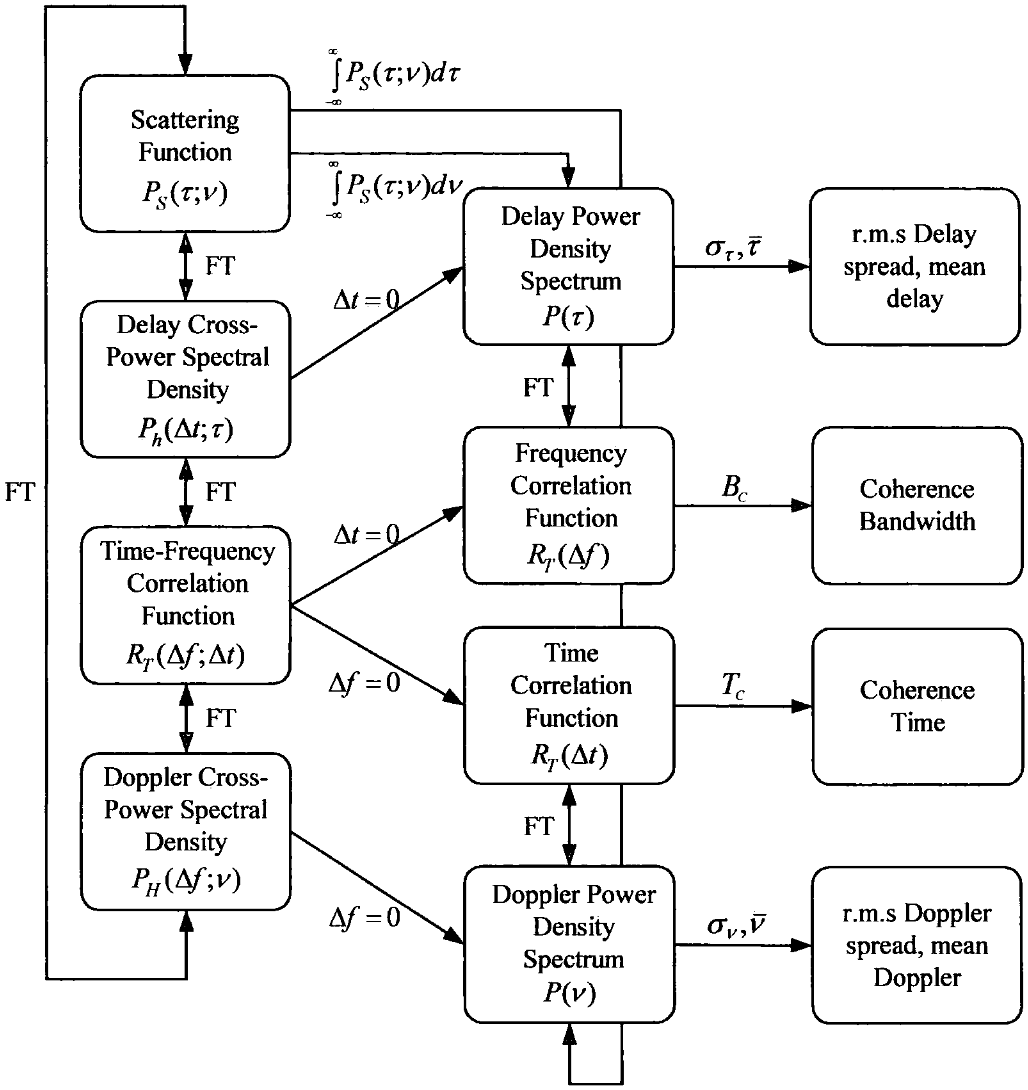

Figure 2.21: Special cases for WSSUS channels, which lead to important channel parameters. The arrows labelled FT, represent the relevant Fourier transforms.

2.8 Summary and Conclusions

Thus far, the fundamental principles of mobile radio channels have been presented. These include the effects of time dispersion and frequency selective fading, which were defined as manifestations of multipath propagation, giving rise to the terms delay spread and coherence bandwidth. The effects of frequency dispersion and time selective fading were also described, as being the result of the time-varying nature of the channel, giving rise to the terms Doppler spread and coherence time. Angle spectrum and angular spread were also defined with the fundamental definition of coherence distance. Furthermore, the basic statistics of channel fading were discussed, including Clarke's model, which resulted in the well-known U-shape Doppler power spectra. Finally, a description of the Bello system functions was presented. These functions could be used to characterise randomly time-variant linear channels, and could lead to a description of practical radio channels via the simplified WSSUS assumption. To date, these definitions are widely used to process and analyse a broad range of mobile radio propagation channels.

2.9 References

1. J. D. Parsons, *The Mobile Radio Propagation Channel*, 2 ed: John Wiley & Sons Ltd, 2000.
2. B. Sklar, "Rayleigh Fading Channels in Mobile Digital Communication Systems (Pt I & II)," *IEEE Communications Magazine*, vol. 35, pp. 90-109, 1997.
3. T. S. Rappaport, *Wireless Communications: Principles and Practice*, 2 ed: Prentice Hall PTR, 2002.
4. H. Hashemi, "Impulse Response Modeling of Indoor Radio Propagation Channels," *IEEE Journal on Selected Areas in Communications*, vol. 11, pp. 967-978, 1993.
5. W. H. Tranter, K. Shanmugan, T. S. Rappaport, K. Kosbar, *Computer-Aided Design and Analysis of Communication Systems with Wireless Applications*: Prentice Hall PTR, 2002.
6. R. B. Ertel, P. Cardieri, K. W. Sowerby, T. S. Rappaport, J. Reed, "Overview of Spatial Channel Models for Antenna Array Communication Systems," *IEEE Personal Communications*, vol. 5, pp. 10-22, 1998.
7. M. Steinbauer, A. F. Molisch, E. Bonek, "The Double-Directional Mobile Radio Channel," *IEEE Antennas and Propagation Magazine*, vol. 43, pp. 51-63, 2001.
8. A. F. Molisch, "A Generic Model for MIMO Wireless Propagation Channels," IEEE International Conference on Communications, New York, 2002.
9. E. Bonek, H. Hofstetter, C. F. Mecklenbrauker, M. Steinbauer, "Double Directional Superresolution Radio Channel Measurements," 39th Annual Allerton Conference on Communication, Control, and Computing, Urbana, Illinois, USA, 2001.
10. E. Bonek, M. Steinbauer, H. Hofstetter, C. F. Mecklenbrauker, "Double-Directional Radio Channel Measurements - What We Can Derive from Them,"

International Symposium on Signals, Systems, and Electronics, Tokyo, Japan, 2001.

11. R. S. Thomä, D. Hampicke, M. Landmann, G. Sommerkorn, A. Richter, "MIMO Measurement for Double-Directional Channel Modelling," IEE Technical Seminar on MIMO Communication Systems, 2001.
12. R. S. Thomä, D. Hampicke, M. Landmann, C. Schneider, G. Sommerkorn, A. Richter, "MIMO Channel Sounding and Double-Directional Modelling," XXXVIIth URSI-GA, 2002.
13. M. Born, E. Wolf, *Principles of Optics: Electromagnetic Theory of Propagation, Interference, and Diffraction of Light*, 6 ed: Purgamon Press, 1980.
14. H. L. Bertoni, *Radio Propagation for Modern Wireless Systems*: Prentice Hall PTR, 2000.
15. G. D. Durgin, *Space-Time Wireless Channels*: Prentice Hall PTR, 2003.
16. R. Vauhgan, J. B. Anderson, *Channels, Propagation and Antennas for Mobile Communications*: IEE Press, 2003.
17. P. A. Bello, "Characterization of Randomly Time-Variant Linear Channels," *IEEE Transactions on Communications Systems*, vol. 11, pp. 360-393, 1963.
18. R. Steel (ed.), L. Hanzo (ed.), *Mobile Radio Communications: Second and Third Generation Cellular and WATM Systems*, 2 ed: John Wiley & Sons Ltd, 1999.
19. T. K. Sarkar, Z. Ji, K. Kim, A. Medouri, M. Salazar-Palma, "A Survey of Various Propagation Models for Mobile Communication," *IEEE Antennas and Propagation Magazine*, vol. 45, pp. 51-82, 2003.
20. G. D. Durgin, T. S. Rappaport, D. A. de Wolf, "New Analytical Models and Probability Density Functions for Fading in Wireless Communications," *IEEE Transactions on Communications*, vol. 50, pp. 1005-1015, 2002.
21. M. Abramowitz (ed.), I. A. Stegun (ed.), *Handbook of Mathematical Functions*, 9 ed: Dover Publications, 1970.
22. W. C. Jakes Jr. (ed.), *Microwave Mobile Communications*, 2 ed: IEEE Press & Wiley-Interscience Reissue, 1974.
23. A. Paulraj, R. Nabar, D. Gore, *Introduction to Space-Time Wireless Communications*: Cambridge University Press, 2003.
24. G. D. Durgin, T. S. Rappaport, "Theory of Multipath Shape Factors for Small-Scale Fading Wireless Channels," *IEEE Transactions on Antennas and Propagation*, vol. 48, pp. 682-693, 2000.

25. A. A. M. Saleh, R. A. Valenzuela, "A Statistical Model for Indoor Multipath Propagation," *IEEE Journal on Selected Areas in Communications*, vol. 5, pp. 128-137, 1987.
26. D. Cassioli, M. Z. Win, A. F. Molisch, "The Ultra-Wide Bandwidth Indoor Channel: From Statistical Model to Simulations," *IEEE Journal on Selected Areas in Communications*, vol. 20, pp. 1247-1257, 2002.
27. A. F. Molisch (ed.), *Wideband Wireless Digital Communications*: Prentice Hall PTR, 2001.
28. J. D. Parsons, J. G. Gardiner, *Mobile Communication Systems*: Blackie & Son Ltd, 1989.
29. M. Pätzold, *Mobile Fading Channels*: John Wiley & Sons Ltd, 2002.
30. J. K. Cavers, *Mobile Channel Characteristics*: Kluwer Academic Publishers, 2000.
31. L. M. Correia, *Wireless Flexible Personalised Communications*: John Wiley & Sons Ltd, 2001.
32. M. Pätzold, "Spatial Deterministic Gaussian Uncorrelated Scattering Processes - Theory and Applications," 2nd International Workshop on Research Directions in Mobile Communications and Services, Grimstad, Norway, 2002.

Chapter 3

MIMO Radio Channels

3.1 Introduction

The desire for higher capacity links for mobile radio systems has led to the development of multi-antenna technologies. To date, multiple antenna systems have been used widely for diversity enhancement relative to single antenna systems. The deployment of multiple antennas at both sides of the radio link constitutes a Multiple-Input Multiple-Output (MIMO) system. Such systems can be employed not only to provide diversity gains through appropriate space-time (ST) coding strategies but can also allow parallel data streams to be transmitted in order to provide multiplexing gain [1, 2]. The fundamental aims of employing MIMO space-time wireless systems are not only to improve spectrum efficiency (bits/s/Hz) but also quality of service and radio network coverage. Figure 3.1 illustrates a typical MIMO communication system with n_T transmit antennas and n_R receive antennas.

There has been considerable effort by various research communities around the world to study and develop MIMO technologies, although most of the research studies undertaken thus far have been restricted to narrowband (flat fading) channels. Recently the performance of frequency selective channels has drawn more attention and in particular the combination of OFDM with MIMO systems (MIMO-OFDM) is being proposed for next generation adhoc and cellular systems as well as MIMO spread spectrum and MIMO multi-user technologies [3, 4]. Although the MIMO system concept is relatively new and presents a number of practical challenges such as multiple antenna integration and signal processing, it is nevertheless anticipated that a great deal of progress could be made in this field over the coming years.

In this chapter, the different types of multi-antenna systems are reviewed and the channel capacities available when communicating via MIMO links are described. Furthermore, a literature survey is provided on the various MIMO channel models and reported measurement campaigns undertaken thus far. Finally, some of the issues concerning practical MIMO signalling are defined, with a basic description of systems such as the Bell Labs Layered Space-Time Architecture (BLAST) [5].

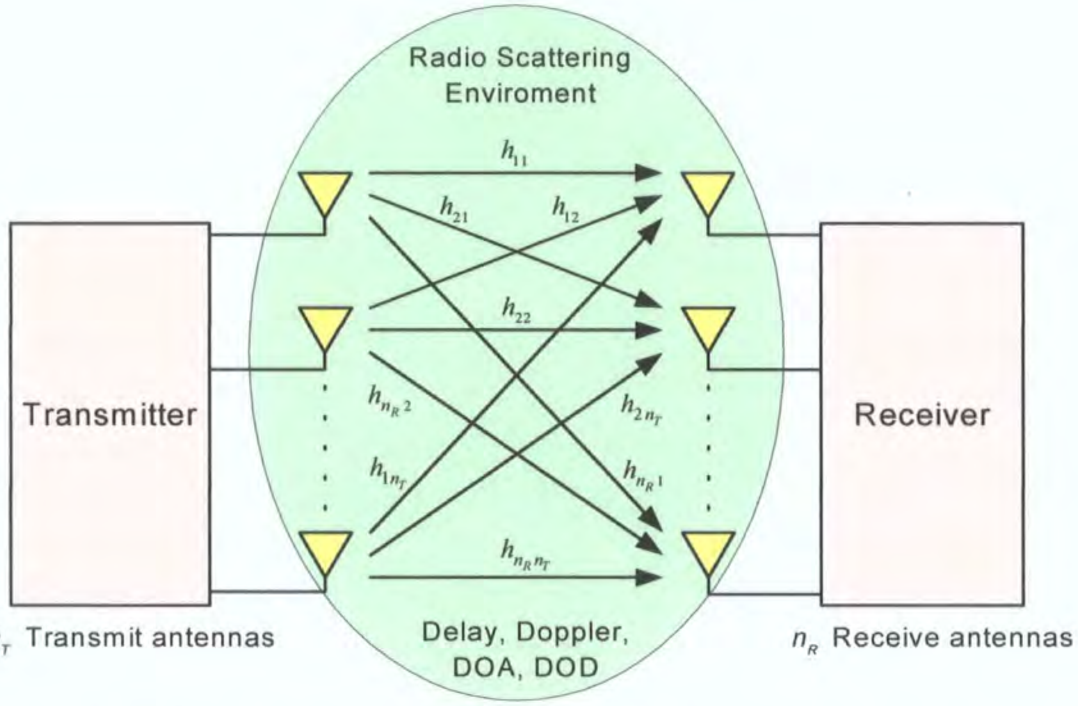

Figure 3.1: A MIMO system with a channel matrix of size $n_R \times n_T$.

3.2 Multiple Antenna Diversity Schemes

In general, the majority of conventional radio communication systems are termed SISO, since only single antennas are used at the transmit and at the receive sites. The impulse response of such channels was described in detail in chapter 2.

In a simple SISO system, the transmitted signal power is denoted by P_T and at the receiver, the average Signal to Noise Ratio (SNR) is denoted by ρ_0. The estimate for the theoretic Shannon limit of a SISO communication system is given by

$$C_{SISO} = B\log_2(1+\rho_0) \tag{3.1}$$

Equation (3.1) provides an upper bound on the channel capacity because it assumes a perfectly flat, distortion-less and interference-free communication link, with the noise taking the form of Additive White Gaussian Noise (AWGN).

For a SIMO (Single Input Multiple Output) system with n_R antennas and a MISO (Multiple Input Single Output) system with n_T antennas, the received signal strength is enhanced by n_R or n_T, respectively. Since the noise adds incoherently, and assuming coherent addition of the signal components, an increase in channel capacity is achieved, given by [6]

$$C_{SIMO} \approx B\log_2(1+n_R\rho_0) \tag{3.2}$$

and

$$C_{MISO} \approx B\log_2(1+n_T\rho_0) \tag{3.3}$$

A MIMO communication system employs n_T transmit antennas and n_R receive antennas and hence for coherent addition this enhances the received signal strength by n_Tn_R times, giving a capacity

$$C_{MIMO} \approx B\log_2(1+n_Tn_R\rho_0) \tag{3.4}$$

3.3 MIMO Spatial Multiplexing

The diversity MIMO capacity given in equation (3.4) can be further increased by spatial multiplexing, i.e. transmitting independent data streams on the different antennas over independently faded channels. This is discussed in section 3.4.

For MIMO systems, the time-variant impulse response between the j^{th} transmit antenna and the i^{th} receive antenna is given by $h_{ij}(t,\tau)$ and denoted by a $n_R \times n_T$ matrix, $\mathbf{H}(t,\tau)$, defined in [9] as

$$\mathbf{H}(t,\tau)=\begin{bmatrix} h_{11}(t,\tau) & h_{12}(t,\tau) & \cdots & h_{1n_T}(t,\tau) \\ h_{21}(t,\tau) & h_{22}(t,\tau) & \cdots & h_{2n_T}(t,\tau) \\ \vdots & \vdots & \ddots & \vdots \\ h_{n_R1}(t,\tau) & h_{n_R2}(t,\tau) & \cdots & h_{n_Rn_T}(t,\tau) \end{bmatrix} \tag{3.5}$$

Therefore, for a signal $x_j(t)$ transmitted from the j^{th} antenna, the signal received at the i^{th} antenna, $y_i(t)$, is given by

$$y_i(t)=\sum_{j=1}^{n_T} h_{ij}(t,\tau)*x_j(t), \qquad i=1,2,\ldots,n_R \tag{3.6}$$

and in matrix notation

$$\mathbf{y}(t) = \mathbf{H}(t,\tau) * \mathbf{x}(t) \tag{3.7}$$

where

$$\mathbf{x}(t) = \begin{bmatrix} x_1(t) & x_2(t) & \cdots & x_{n_T}(t) \end{bmatrix}^T \tag{3.8}$$

and

$$\mathbf{y}(t) = \begin{bmatrix} y_1(t) & y_2(t) & \cdots & y_{n_R}(t) \end{bmatrix}^T \tag{3.9}$$

The time-varying channel matrix is normally simplified for the static narrowband case expressed as

$$\mathbf{H} = \begin{bmatrix} h_{11} & h_{12} & \cdots & h_{1n_T} \\ h_{21} & h_{22} & \cdots & h_{2n_T} \\ \vdots & \vdots & \ddots & \vdots \\ h_{n_R 1} & h_{n_R 2} & \cdots & h_{n_R n_T} \end{bmatrix} \tag{3.10}$$

consequently

$$\mathbf{y}(t) = \mathbf{H}\mathbf{x}(t) \tag{3.11}$$

If the elements of **H** are independent Zero-Mean Circularly Symmetric Complex Gaussian (ZMCSCG) random variables with unit variance [8, 9], this leads to the Independent and Identically Distributed (IID) spatially white assumption of MIMO channels i.e. $\mathbf{H} = \mathbf{H}_w$. This basic model is often used for MIMO system simulations and is defined as a reference for many capacity calculations. For the case that $n_T = n_R = n$ and $\mathbf{H} = \mathbf{H}_w$, a central result is achieved via the strong law of large numbers [9, 17]

$$\frac{1}{n}\mathbf{H}_w\mathbf{H}_w^H \rightarrow \mathbf{I}_n \quad \text{as} \quad n \rightarrow \infty \tag{3.12}$$

$$\therefore \; C \rightarrow n \cdot B\log_2(1+\rho) \tag{3.13}$$

Equation (3.13) implies an n fold increase in channel capacity, over that of the SISO case.

In reality, **H** can deviate significantly from $\mathbf{H}_w$ for a variety of different reasons. These include inadequate antenna spacing causing spatial correlation, the presence of a LOS link (Rician fading), gain imbalances between the channel elements through the use of polarised antennas, or channel rank deficiency caused by keyhole channels [11-14]. Many of these are discussed in [9].

There are various properties of the $n_R \times n_T$ MIMO channel matrix which should be analysed before proceeding. Channel decomposition is particularly important for analysis of systems where channel knowledge is available at the transmitter as well as at the receiver. Using Singular Value Decomposition (SVD), any $n_R \times n_T$ channel matrix, **H**, can be written as

$$\mathbf{H} = \mathbf{U}\mathbf{D}\mathbf{V}^H \tag{3.14}$$

Where **D** is the diagonal matrix containing the non-negative singular values, and **U** and **V** are the $n_R \times r$ and $n_T \times r$ unitary matrices, respectively, where r is the rank of the channel matrix and is limited by the smallest array size (either at the transmit site or at the receive site). The diagonal values of **D** are the square roots of the eigenvalues of matrix $\mathbf{HH}^{\mathrm{H}}$ denoted by λ.

In defining the MIMO channel matrix, there is often reference to the squared Frobenius norm of **H**, $\|\mathbf{H}\|_F^2$, which is given by

$$\|\mathbf{H}\|_F^2 = \sum_{i=1}^{n_R}\sum_{j=1}^{n_T}\left|h_{ij}\right|^2 \tag{3.15}$$

This norm typically represents the overall power gain of the channel. The squared Frobenius norm is important in the normalisation of channel capacity results since it represents the overall matrix gain. This is practically described in chapter 8 and MATLAB programs for channel normalisation are provided on the accompanying CD-ROM.

3.4 Capacity of MIMO Channels

The input-output relationship of a MIMO system is given by

$$\mathbf{y} = \sqrt{\frac{E_s}{n_T}}\mathbf{Hx} + \mathbf{n} \tag{3.16}$$

where **x** is the transmit signal vector ($n_T \times 1$), **y** is the receive signal vector ($n_R \times 1$), **H** is the $n_R \times n_T$ channel matrix and **n** is the noise vector ($n_R \times 1$). Here, E_s is the total average energy available at the transmitter over a symbol period. The transmit signal covariance matrix, $\mathbf{R}_{\mathbf{xx}} = E\{\mathbf{xx}^H\}$, must satisfy the condition $\mathrm{Tr}(\mathbf{R}_{\mathbf{xx}}) = n_T$ to limit the total average energy transmitted over a symbol period [9]. Noting that E_s / N_0 represents the signal to noise ratio denoted by ρ, the generic capacity of a MIMO channel can be expressed as [9]

$$C_{MIMO} = \max_{\mathrm{Tr}(\mathbf{R}_{\mathbf{xx}})=n_T} \log_2 \det\left(\mathbf{I}_{n_R} + \frac{\rho}{n_T}\mathbf{H}\mathbf{R}_{\mathbf{xx}}\mathbf{H}^H\right) \quad \text{bits/s/Hz} \qquad (3.17)$$

Equation (3.17) is the fundamental capacity equation from which various expressions can be derived. Assuming the channel is completely unknown to the transmitter but known to the receiver, then the input vector, **x**, may be chosen to be non-preferential (i.e. $\mathbf{R}_{\mathbf{xx}} = \mathbf{I}_{n_T}$). This means transmitting the same power on all the antennas, thus giving a capacity

$$C = \log_2 \det\left(\mathbf{I}_{n_R} + \frac{\rho}{n_T}\mathbf{H}\mathbf{H}^H\right) \qquad (3.18)$$

A higher capacity can be achieved when the channel is known at the transmitter. In this case it is possible to increase the channel capacity through adaptive power allocation also referred to as waterfilling [16]. This is achieved by the modal decomposition of the **H** matrix into r (where r is the rank of the channel) parallel spatial sub-channels, each with gain $\sqrt{\lambda_i}$. Figure 3.2 provides a simple illustration of the parallel sub-channels or "data pipes".

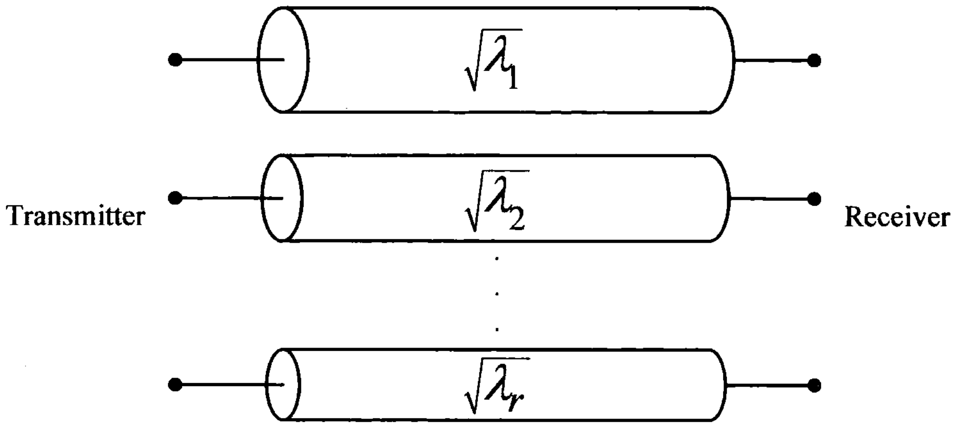

Figure 3.2: Representation of *r* spatial data pipes between transmitter and receiver.

This can be understood simply by representing the MIMO capacity equation given earlier as the sum of *r* SISO channels, each having power gain λ_i

$$C = \sum_{i=1}^{r} \log_2\left(1 + \frac{\rho}{n_T}\lambda_i\right) \tag{3.19}$$

With channel state information (CSI), the transmitter now has the potential of allocating variable energy across each of the spatial sub-channels, given as

$$C = \sum_{i=1}^{r} \log_2\left(1 + \varepsilon_i \frac{\rho}{n_T}\lambda_i\right) \tag{3.20}$$

where ε_i represents the transmit allocated energy in the i^{th} sub-channel and satisfies $\sum_{i=1}^{r} \varepsilon_i = n_T$.

In general, CSI at the transmitter could be obtained either through some type of feedback link from the receiver or via the reciprocity principle in a duplex system. In the case of feedback, the channel information is sent from the receiver to the transmitter. This feedback will inherently involve some delay period (for the time of flight), therefore it must be ensured that this delay time is much smaller than the coherence time of the channel to avoid considerable temporal variations. Feedback could potentially provide a large overhead on the reverse link. An alternative is to only feedback partial information, which will reduce this overhead.

The reciprocity principle could be examined for Time Division Duplexing (TDD) and Frequency Division Duplexing (FDD) systems. For TDD channels, the forward and reverse links can only be equated if the time delay (i.e. the time difference between the forward and reverse link) is small compared to the coherence time of the channel. In FDD links, the forward and reverse channel can only be equated if the duplexing frequency difference is small compared to the coherence bandwidth of the channel. Due to limits on the filters separating these two bands, the frequency difference is not smaller than the coherence bandwidth, meaning that in practice the reciprocity principle cannot be used in FDD links [9].

Channel capacity where no CSI is available at either end of the radio link (i.e. blind channel estimation) is still an ongoing research area and is not discussed here.

3.4.1 Wideband Channel Capacity

So far the capacity equations have been defined for narrowband links. It is also possible to calculate the capacity of a wideband fading MIMO channel by dividing the frequency band into N narrower frequency-flat channels, each with a bandwidth of $1/N$ Hz [9]. By denoting the i^{th} frequency flat channel as $\mathbf{H}_i$ ($i = 1,2,\ldots,N$), the input-output relationship can now expressed as

$$\mathbf{y}_i = \sqrt{\frac{E_s}{n_T}}\mathbf{H}_i\mathbf{x}_i + \mathbf{n}_i \tag{3.21}$$

where as before, $\mathbf{y}_i$ is the $n_R \times 1$ received vector, $\mathbf{x}_i$ is the $n_T \times 1$ transmit vector and $\mathbf{n}_i$ is the $n_R \times 1$ noise vector for each i^{th} sub-channel. The total input-output relationship can then be written as

$$\underbrace{\begin{bmatrix}\mathbf{y}_1\\ \mathbf{y}_2\\ \vdots\\ \mathbf{y}_N\end{bmatrix}}_{\mathbf{Y}_{WB}} = \sqrt{\frac{E_s}{n_T}}\underbrace{\begin{bmatrix}\mathbf{H}_1 & 0 & \cdots & 0\\ 0 & \mathbf{H}_2 & \cdots & 0\\ \vdots & \vdots & \ddots & \vdots\\ 0 & 0 & \cdots & \mathbf{H}_N\end{bmatrix}}_{\mathbf{H}_{WB}}\underbrace{\begin{bmatrix}\mathbf{x}_1\\ \mathbf{x}_2\\ \vdots\\ \mathbf{x}_N\end{bmatrix}}_{\mathbf{X}_{WB}} + \underbrace{\begin{bmatrix}\mathbf{n}_1\\ \mathbf{n}_2\\ \vdots\\ \mathbf{n}_N\end{bmatrix}}_{\mathbf{N}_{WB}} \tag{3.22}$$

where the subscript WB here denotes a wideband channel, hence $\mathbf{Y}_{WB}$ is $n_RN \times 1$, $\mathbf{X}_{WB}$ is $n_TN \times 1$, $\mathbf{N}_{WB}$ is $n_RN \times 1$, and $\mathbf{H}_{WB}$ is an $n_RN \times n_TN$ matrix whose diagonal elements represent the narrowband sub-channels $\mathbf{H}_i$. As in the case of narrowband channels, when the channel is unknown to the transmitter, equal power is allocated to each transmit antenna (i.e. $\mathbf{R}_{\mathbf{XX}} = \mathbf{I}_{n_T N}$) giving a capacity defined as [9]

$$C_{WB} \approx \frac{1}{N}\sum_{i=1}^{N} \log_2 \det\left(\mathbf{I}_{n_R} + \frac{\rho}{n_T}\mathbf{H}_i\mathbf{H}_i^H\right) \quad \text{bits/s/Hz} \qquad (3.23)$$

If all the elements $\mathbf{H}_i$ are IID, then by the strong law of large numbers [17], the capacity of one sample realisation of the wideband channel approaches a fixed value.

In most of the literature, the frequency-selective capacity is similarly defined by integrating over all frequencies [19], and is expressed as

$$C_{WB} = \frac{1}{B}\int_B \log_2 \det\left(\mathbf{I}_{n_R} + \frac{\rho}{n_T}\mathbf{H}(f)\mathbf{H}^H(f)\right) df \quad \text{bits/s/Hz} \qquad (3.24)$$

where $\mathbf{H}(f)$ is the frequency-selective transfer function and B denotes the bandwidth of interest.

For random channel capacity, a practical measure which is often used, is the outage capacity. This gives the channel capacity that is guaranteed with a defined level of reliability. The q% outage capacity is defined as the information rate that is guaranteed for (100-q)% of the channel realisations. This definition of link throughput is used in chapter 8.

3.4.2 Degradation of MIMO Channels

Various factors influence the degradation of MIMO channels from the ideal IID channel model, $\mathbf{H}_w$. These include spatial correlation caused by the antenna spacing or scattering, different polarised antennas leading to gain imbalances between the elements of $\mathbf{H}$, the presence of a LOS component leading to Rician fading as well as antenna coupling, the effects of interferers in the channel, and high Doppler frequencies, which are not reviewed in this section.

Some of these effects can be reasonably examined by substituting the various extended channel models in the literature into the capacity equations. For the case of spatial correlation, the Rayleigh flat-fading channel can be modelled by

$$\mathbf{H} = \mathbf{R}_r^{1/2}\mathbf{H}_w\mathbf{R}_t^{1/2} \qquad (3.25)$$

where $\mathbf{R}_t$ and $\mathbf{R}_r$ represent the positive definite Hermitian matrices for transmit and receive correlation, respectively. Therefore, substituting this into the capacity equation for a MIMO channel without CSI at the transmitter, gives [8]

$$C = \log_2 \det\left(\mathbf{I}_{n_R} + \frac{\rho}{n_T}\mathbf{R}_r^{1/2}\mathbf{H}_w\mathbf{R}_t\mathbf{H}_w^H\mathbf{R}_r^{H/2}\right) \qquad (3.26)$$

3.5 MIMO Propagation Models

The desire to develop future wireless systems which offer higher data rates and better qualities of service has driven an overwhelming number of researchers to investigate a variety of MIMO space-time systems. In the past few years, researchers have developed a number of MIMO channel models, mostly while assuming a comparatively benign temporal environment. Some of the more significant channel models are reviewed in the following.

There are various ways of classifying MIMO channel models. In the literature some classify channel models by the effective system bandwidth, and these are termed narrowband or wideband models. A more popular classification is by whether the models are stochastic or deterministic in nature. Stochastic models essentially refer to parametric methods, geometrically-based methods and correlation-based methods. Deterministic models on the other hand refer to Ray-tracing methods and recorded impulse response models. In the following, the MIMO channel models are divided into physical and non-physical models.

In general, the physical models use some physical parameters to describe the MIMO propagation channel. Some typical parameters include Direction of Arrival (DOA), Direction of Departure (DOD) and time delay. Non-physical models on the other hand are based on channel statistical characteristics using non-physical parameters. Non-physical models are easy to simulate and provide accurate characterisation of the channel for the scenarios under investigation, although they only give limited insight into the channel and are primarily limited by the channel measurement equipment used [20]. Physical models are less restrictive, but still prone to the same prejudice in relation to the conditions under which the models are identified. The following briefly describes both categories of channel models.

3.5.1 Non-Physical Channel Models

3.5.1.1 IST METRA Project

The European Union IST METRA (Information Society Technologies Multielement Transmit-Receive Antennas) project [21-23] was initiated to carry out an extensive indoor measurement campaign in Aalborg (Denmark) at a carrier frequency of 2.05 GHz. The aim of the project was to develop a simple stochastic MIMO radio channel model (with its implementation in COSSAP® simulation software) using correlation matrices at the transmitter and at the receiver.

Assuming M number of transmit antennas and N number of receive antennas, the wideband channel model (excluding noise) was given by

$$\mathbf{H}(\tau)=\sum_{l=1}^{L}\mathbf{A}_l\delta(\tau-\tau_l) \tag{3.27}$$

where $\mathbf{H}(\tau)$ is the $N \times M$ matrix of impulse responses and $\mathbf{A}_l$ is a matrix of complex transmission coefficients, which describe the linear transformation between the transmit and receive antenna arrays at delays τ_l. $\mathbf{A}_l$ is given by

$$\mathbf{A}_l=\begin{bmatrix}\alpha_{11}^{(l)} & \alpha_{12}^{(l)} & \cdots & \alpha_{1M}^{(l)}\\ \alpha_{21}^{(l)} & \alpha_{22}^{(l)} & \cdots & \alpha_{2M}^{(l)}\\ \vdots & \vdots & \ddots & \vdots\\ \alpha_{N1}^{(l)} & \alpha_{N2}^{(l)} & \cdots & \alpha_{NM}^{(l)}\end{bmatrix} \tag{3.28}$$

where the coefficients $\alpha_{nm}^{(l)}$ (for the m^{th} transmit antenna and the n^{th} receive antenna) are assumed to be zero-mean complex Gaussian with the same average power, P_l.

In order to construct this MIMO channel model, the correlation between the different pairs of transmission coefficients needed to be determined. The correlation coefficients between different transmit antennas (m_1 and m_2) and different receive antennas (n_1 and n_2) are denoted by

$$\rho_{m_1 m_2}^{Tx} = \left\langle \left|\alpha_{m_1 n}^{(l)}\right|^2, \left|\alpha_{m_2 n}^{(l)}\right|^2 \right\rangle \tag{3.29}$$

$$\rho_{n_1 n_2}^{Rx} = \left\langle \left|\alpha_{m n_1}^{(l)}\right|^2, \left|\alpha_{m n_2}^{(l)}\right|^2 \right\rangle \tag{3.30}$$

where it is assumed that the spatial correlation on one side of the radio link is quite independent of antenna elements on the opposite side. However, the cross correlation of the two transmission coefficients connecting two different sets of antennas (for $n_1 \neq n_2$ and $m_1 \neq m_2$) can also be defined, and this is given by

$$\rho_{n_2 m_2}^{n_1 m_1} = \left\langle \left|\alpha_{m_1 n_1}^{(l)}\right|^2, \left|\alpha_{m_2 n_2}^{(l)}\right|^2 \right\rangle = \rho_{m_1 m_2}^{Tx} \rho_{n_1 n_2}^{Rx} \tag{3.31}$$

where this equation represents a theoretical result [23]. It is also possible to denote equation (3.31) in terms of symmetrical complex correlation matrices $\mathbf{R}^{Tx} = [\rho_{pq}^{Tx}]_{M \times M}$ and $\mathbf{R}^{Rx} = [\rho_{pq}^{Rx}]_{N \times N}$, given by

$$\mathbf{R}_{MIMO} = \mathbf{R}^{Tx} \otimes \mathbf{R}^{Rx} \tag{3.32}$$

Following the approach in [24], the correlated transmission matrix can be simulated according to

$$\tilde{\mathbf{A}}_l = \text{vec}(\mathbf{A}_l) = \sqrt{P_l}\mathbf{C}\mathbf{a}_l \tag{3.33}$$

where vec(·) denotes the operator to stack the columns of the correlated transmission matrix $\mathbf{A}_l$ into a column vector $\tilde{\mathbf{A}}_l$, and $\mathbf{a}_l$ is a column vector with IID elements ($MN \times 1$). Here, **C** denotes the symmetrical mapping matrix, which is a direct result of the standard Cholesky factorisation [10] of the matrix $\mathbf{R}_{MIMO} = \mathbf{C}\mathbf{C}^T$ [22].

In the IST METRA Project, narrowband MIMO channels were simulated via the above model and compared with measured data by means of the Cumulative Distribution Function (CDF) of the eigenvalues. The results showed agreement between the simulated channel and the measured channel.

The METRA Channel characterisation model only reproduces the correlation matrices and the fast fading characteristics of the channel, while the phase information across the antenna arrays is not necessarily reflected correctly in the model. An improvement for this was to employ a phase steering matrix to provide the average phase-shift information with respect to the first element [22].

3.5.1.2 IST SATURN Project

The European Union IST SATURN (Information Society Technologies - Smart Antenna Technology in Universal bRoadband wireless Networks) project was a significant effort by the European community to investigate smart antenna technologies, primarily for UMTS and HIPERLAN systems [25]. Various measurement campaigns (both wideband and narrowband) were undertaken by two of the partners of the IST SATURN project in the aim to develop a correlation model for the channel. The measurement campaigns were conducted by; the University of Bristol using the MEDAV RUSK BRI Vector Channel Sounder, and France Telecom R&D using the new AMERICC (Appareil de Mesure de la Réponse Impulsionnelle pour la Caractérisation du Canal) sounder. The outcome of the project led to a justification that the channel covariance matrix could be modelled by the Kronecker product ⊗ of the covariance matrices at both ends of the radio link, that is

$$\mathbf{R}_{\mathbf{H}}^{k} = E\left\{\operatorname{vec}\left(\mathbf{H}^{k}\right)\operatorname{vec}\left(\mathbf{H}^{k}\right)^{H}\right\} = \left(\mathbf{R}_{\mathbf{H},Tx}^{k}\right)^{H} \otimes \left(\mathbf{R}_{\mathbf{H},Rx}^{k}\right) \tag{3.34}$$

where $\mathbf{R}_{\mathbf{H}}^{k}$ denotes the channel covariance matrix of the k^{th} tap (from a tapped delay line analogy) of the MIMO channel impulse response [25], and $\mathbf{R}_{\mathbf{H},Tx}^{k}$ and $\mathbf{R}_{\mathbf{H},Rx}^{k}$ denote the covariance matrices of the k^{th} tap seen from the transmitter and receiver, respectively. For a narrowband channel model, $\mathbf{R}_{\mathbf{H}} = (\mathbf{R}_{\mathbf{H},Tx})^{H} \otimes (\mathbf{R}_{\mathbf{H},Rx})$.

Assuming that the taps are independent zero-mean complex Gaussian, the k^{th} tap of the wideband MIMO channel impulse response can be modelled as

$$\mathbf{H}_{k} = \left(\mathbf{R}_{\mathbf{H},Rx}^{k}\right)^{1/2} \mathbf{G}_{k} \left(\mathbf{R}_{\mathbf{H},Tx}^{k}\right)^{1/2} \tag{3.35}$$

where $\mathbf{H}_{k}$ is the k^{th} tap of the MIMO channel impulse response, $\mathbf{H}$, and $\mathbf{G}_{l}$ is a random matrix with IID elements.

For measured narrowband data, the relative error between the estimated MIMO covariance matrix and the Kronecker product of the estimated receive and transmit covariance matrices were shown to be less than 1% for a 2 × 2 antenna system and less than 5% for a 3 × 3 antenna system. In the case of the wideband channel model, separate channel covariance matrices were estimated for each channel tap, $\mathbf{H}_k$. Again, the product structure in equation (3.35) showed very good agreement with the measured data, with a relative error of less than 10% for each tap. The accuracy of the estimated covariance matrices were worse in this case, since no averaging was possible over frequency [25].

3.5.2 Physical Channel Models

3.5.2.1 Distributed Scattering Model

This effective narrowband channel model was presented in [8] for describing outdoor MIMO propagation. It is assumed again for this model that there is an $N \times M$ MIMO propagation channel and a distributed scattering environment between the transmitter and the receiver. By assuming that there are enough scatterers (denoted by S) between the transmitter and the receiver to cause random fading in the channel, the scatterers at the receive end could be seen as a virtual array between the two ends of the radio link. Consequently, the channel transfer function can be represented as [8]

$$\mathbf{H} = \frac{1}{\sqrt{S}} \mathbf{R}^{1/2}_{\theta_r, d_r} \mathbf{G}_r \mathbf{R}^{1/2}_{\theta_S, 2D_r/S} \mathbf{G}_t \mathbf{R}^{1/2}_{\theta_t, d_t} \tag{3.36}$$

In equation (3.36), the $1/\sqrt{S}$ term represents the normalisation factor and $\mathbf{R}^{1/2}_{\theta_r, d_r}$, $\mathbf{R}^{1/2}_{\theta_S, 2D_r/S}$, $\mathbf{R}^{1/2}_{\theta_t, d_t}$ are the correlation matrices seen from the transmitter, the virtual array, and the receiver, respectively. Here, $\mathbf{G}_t$ and $\mathbf{G}_r$ are random matrices with IID elements which denote the scatterers by the transmitter and receiver, respectively. There is a detailed description of the distributed scattering model and its parameters in [8, 27].

Various outdoor channel environments could be examined by determining the rank of the channel matrix (influenced by $\mathbf{R}^{1/2}_{\theta_r, d_r}$, $\mathbf{R}^{1/2}_{\theta_S, 2D_r/S}$, $\mathbf{R}^{1/2}_{\theta_t, d_t}$). This includes the study of true keyhole channels where the rank of the channel matrix is effectively singular.

3.5.2.2 Multidimensional Parametric Channel Model

The *k*-dimensional parametric channel model is a powerful deterministic representation of the channel proposed by the collective research studies of the technical universities of Ilmenau (Germany) and Vienna (Austria) [30-40]. This model is formed from the multipath parameters derived from measured results, with the fundamental assumption that the propagation signal is a finite sum of discrete, locally planar waves. It is further assumed that the relative bandwidth is small enough so that the time delay of the impinging waves simply transforms to a phase shift between individual antennas in the arrays, and the array aperture is small enough so that there is no observable magnitude variation of any single wave received at the different array elements [30, 31]. Furthermore, the channel parameters are assumed to be time-invariant during a measurement snapshot time period. Based on the above assumptions, the multidimensional wave propagation model can be expressed as

$$\begin{aligned}\mathbf{h}\left(\nu,\tau,\psi_{Rx},\vartheta_{Rx},\psi_{Tx},\vartheta_{Tx}\right)=\sum_{p=1}^{P}\gamma_p\cdot\delta\left(\nu-\nu_p\right)\delta\left(\tau-\tau_p\right)\\ \cdot\delta\left(\psi_{Rx}-\psi_{Rx,p}\right)\delta\left(\vartheta_{Rx}-\vartheta_{Rx,p}\right)\\ \cdot\delta\left(\psi_{Tx}-\psi_{Tx,p}\right)\delta\left(\vartheta_{Tx}-\vartheta_{Tx,p}\right)\end{aligned} \tag{3.37}$$

where γ_p represents the 2 × 2 path weight matrix describing the two polarisation responses of the receive and transmit antennas, respectively. The parameters τ, ν denote the time delay and Doppler shift, respectively, while the DOA and DOD (in azimuth and elevation angles) are represented by ψ_{Rx}, ϑ_{Rx} and ψ_{Tx}, ϑ_{Tx}, respectively. Equation (3.37) denotes the complex channel impulse response described by P dominant paths and resolved in six dimensions for time delay, doppler shift, and both directions seen from the transmitter and receiver [30]. In equation (3.37), the path weight matrix is given by

$$\gamma_p=\begin{bmatrix}\gamma_{\psi\psi_p} & \gamma_{\psi\vartheta_p}\\ \gamma_{\vartheta\psi_p} & \gamma_{\vartheta\vartheta_p}\end{bmatrix} \tag{3.38}$$

With appropriate arrays deployed at the BS and the MS, the data model in equation (3.37), transforms into a multidimensional harmonic retrieval problem, given by

$$\begin{aligned}\mathbf{H}\left(t,f,n_{Rx},m_{Rx},n_{Tx},m_{Tx}\right)=\sum_{p=1}^{P}\gamma_p e^{-j2\pi\nu_p t}e^{-j2\pi f\tau_p}\\ \cdot e^{-j2\pi n_{Rx}\psi_{Rx,p}}e^{-j2\pi m_{Rx}\vartheta_{Rx,p}}\\ \cdot e^{-j2\pi n_{Tx}\psi_{Tx,p}}e^{-j2\pi m_{Tx}\vartheta_{Tx,p}}\end{aligned} \quad (3.39)$$

where the variables m and n represent the corresponding spatial aperture domains at the receiver and transmitter antennas, respectively. The harmonic retrieval problem could be solved using a k-dimensional parameter estimation based on the ESPRIT algorithm, which is a search-free method based on the SVD of the signal subspace, and is widely used for DOA estimation. This algorithm can be considered as a superresolution algorithm since it results in parameter resolution, which is better than the Fourier method [31]. The resolution achievable by the ESPRIT algorithm is limited in terms of SNR, incorrect model assumption, and limited measurement accuracy such as calibration errors, etc. In most cases, the Unitary ESPRIT algorithm is used because of its computational efficiency.

A collection of real time measurement data in various typical radio environments are used in [30-35] to provide a deterministic characterisation of the radio channel by resolving individual multipath parameters. Based on the full set of estimated multipath parameters, $\{\gamma_p,\nu_p,\tau_p,\vartheta_{Rx,p},\psi_{Rx,p}\vartheta_{Tx,p}\psi_{Tx,p}\}$, which describe the discrete path model, it is possible to locally construct the electromagnetic field in the distinct vicinity of the receive and transmit antennas, in both time and frequency. The basic principle of parametric channel modelling based on high-resolution MIMO measurements is illustrated in figure 3.3. It should be noted that although this model provides a very useful step for parametric MIMO channel modelling, it does ultimately make a number of restrictive assumptions about the channel which can result in erroneous estimates. Some of these issues will be addressed in the following chapters. One example is the use of delta functions as opposed to finite pulses (limited by system bandwidth) to model each channel parameter.

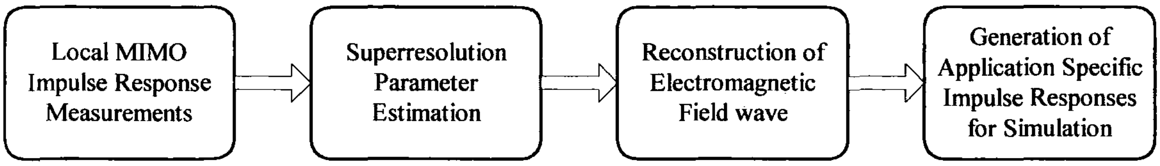

Figure 3.3: Principle of multidimensional parametric channel modelling.

A number of other physical MIMO channel models have been proposed over the past few years, including the virtual array channel model which separates the MIMO channel into K parallel virtual channels, and the Electromagnetic scattering model which is based on the electromagnetic properties of the channel and the antenna arrays at both link ends.

3.5.2.3 Other Physical Channel Models

A widely referenced MIMO channel model is the one-ring model [26] which was initially developed in order to give a physical description of the narrowband MIMO channel. In the one-ring model, the base station (BS) is assumed to be elevated well above ground so that it is not obstructed by local scatterers, while the mobile station (MS) is surrounded by scatterers [20]. For this model, no direct LOS path is assumed to be present between the transmitter and the receiver. Here, each ray is assumed to be reflected once and all the received rays are assumed to have the same power. This provides a rudimentary physical description of the channel coefficients. It is possible to extend the one-ring model, so that the BS is also surrounded by scatterers. For this case, each ray is reflected twice and the channel coefficients can be derived [26].

In [29] a directional model was developed by the European cooperative research initiative COST 259 (COoperation in the field of Scientific and Technical research). This model aimed to define the double directional channel impulse response using the analogy of L impinging plane waves at the receiver.

Another key model was the MIMO extended Saleh-Valenzuela model which was a double-directional narrowband version of the original model presented in chapter 2. This model assumes that the multipath at the receiver arrive in clusters [28].

Whilst the physical channel models provide some analytical description of the channel, they often fall short of providing an accurate description of the multipath environment.

3.6 MIMO Channel Measurements

In section 3.5, a brief description of a number of MIMO channel models were given and some of these were often based on or verified using measurement data. It is difficult to keep a full account of all the past MIMO measurements due to the sheer quantity of publications so far and the continuing research studies in this field, however in this section, some of the more significant measurement campaigns are examined.

The majority of the MIMO measurement campaigns so far have focused on the 1.9-2.5 GHz band (predominantly for outdoor systems) and the 5.2-5.8 GHz band (typically for indoor systems). Principally, these measurements have been used to examine practical channel capacity and multi-antenna channel parameters, such as angular spread, correlation coefficients, channel rank deficiency, etc. A brief description of some of these measurement campaigns is given in the following.

3.6.1 Lucent Technologies: BLAST Measurements

A laboratory prototype of the Vertical BLAST (V-BLAST) system was constructed for the purpose of demonstrating the feasibility of the BLAST approach [7, 41, 42]. The prototype operated at a carrier frequency of 1.9 GHz, and a symbol rate of 24.3 ksymbols/s, in a bandwidth of 30 kHz. The MIMO system consisted of 8 transmit antennas ($M = 8$) and 12 receive antennas ($N = 12$). The antenna arrays were $\lambda/2$ wire dipoles mounted in various arrangements, with ~$\lambda/2$ inter-element spacing.

The measurement environments were indoor offices and laboratories, with transmitter-receiver separations of up to about 12 meters. The environments under test were particularly benign, since the delay spread was considered negligible, the fading rates were low, and there was significant near-field scattering from nearby equipment and office furniture.

Measurements were made using this architecture, with transmission bursts of 100 symbols, 20 of which were used for training. In the experiment, the 8 transmit antenna sub-streams utilised uncoded 16 level Quadrature Amplitude Modulation (16-QAM). At SNRs of 24-34 dB, spectral efficiencies of 20-40 bits/s/Hz were demonstrated under real indoor conditions [41-43].

A number of other Lucent measurement campaigns have been undertaken thus far, in which a 5-tone transmission signal with separations of 1 kHz or a 16-tone transmission signal with separations of 2 kHz were used for channel measurements [44-47]. The results showed that for a LOS scenario with 84 meter separation, a 5 × 7 ($M = 5$, $N = 7$) system at 22 dB SNR gave spectral efficiencies of around 20 bits/s/Hz, while for suburban environments, 60% of the IID capacity was achieved for a 5 × 4 system, and 50% for a 5 × 7 system. For outdoor BLAST measurements at 2.44 GHz [46], the initial results indicated above 38 bits/s/Hz for 20% of the measured locations and above 24 bits/s/Hz for 50% of the measurement locations.

In [47], a narrowband MIMO measurement campaign was carried out in Manhattan (under Lucent) using a 16 × 16 system. Measured median capacities of the full 16 × 16 arrays were found to be 35 bits/s/Hz at 10 dB SNR, which was 80% of the IID channel capacity. Subarray capacities for a 2 × 2 and 4 × 4 system were found to be 5.5 and 10 bits/s/Hz, respectively, which was 90% of the IID capacity. The measurement setup was based on a 16-tone transmission signal with separations of 2 kHz, centred at 2.11 GHz.

A wideband 16 × 16 BLAST array measurement campaign was reported in [48]. These measurements were conducted using the National Institute of Standards and Technology (NIST) open area test site. Using the **H** matrix, capacity results were computed and showed less than 5% error when compared to theoretical calculations.

3.6.2 Multidimensional Measurements

Although the term ‘multidimensional measurements’ can be somewhat generic, this section just groups together the publications which have focused on multi-parameter channel estimation, some of which were described in section 3.5.2.5. To date, various MIMO measurement campaigns have been conducted and in the majority of these cases, some version of the MEDAV RUSK vector sounder has been used. Thereafter, parameters such as DOA, DOD, capacity, etc, have been determined for a particular channel environment, typically for WLAN type systems in the ISM bands [19, 30-40, 49-54]. In some cases, capacity results were estimated and often compared to a Kronecker-type (or Weichselberger [55]) channel model. The following describes some of these papers.

The work presented in [30-34] by the Technical University of Ilmenau investigates the steps required for performing deterministic parametric channel modelling based on general measured data. Here the focus is on parametrically estimating DOA, DOD, and Time Delay of Arrival (TDOA) for specific antenna arrangements (see figure 3.15). For these measurements, the RUSK (ATM) sounder was used at 5.2 GHz with 120 MHz of system bandwidth (which is the maximum bandwidth available for the MEDAV RUSK sounder). Measurements were performed by using a Uniform Linear Array (ULA) at the receiver and a Uniform Rectangular Array (URA) or Uniform Circular Array (UCA) at the transmitter. Channel parameters were often estimated using the ESPRIT algorithm (see chapter 4). The measurement system employed here (RUSK sounder) is based on an arbitrary waveform generator, which is used to generate a periodic multi-tone signal. The advantages and disadvantages of such a technique are described in chapter 5.

Paper [50] uses the same techniques as described in [30-35], however in this case, channel capacity is estimated from synthesised impulse responses (using measurement data) for a minimum SNR of 16 dB. Measurements were conducted for an 8 × 8 array configuration, where a ULA was employed at the transmitter and a UCA was employed at the receiver.

The concept of a double-directional radio channel was formally described in [36] by the Technical University of Vienna. Such a principle was born out of certain MIMO channel assumptions, which are further explored in the forthcoming chapters. In [36], a number of multipath scenarios were explored using the RUSK (ATM) sounder with 120 MHz bandwidth at 5.2 GHz. The measurements were typically conducted for a 16 × 8 antenna configuration. At the transmitter a virtual array was used (the array is formed by a dipole being moved by a computer controlled step motor), while at the receiver, a simple linear patch array was used with a fast RF switch. This technique was employed for many channel measurements, described in [36, 38, 40, 51, 52].

The measurements reported in [40], examine the spatial characteristics of the double-directional channel in the 2 GHz band at high mobile speeds. The measurements were conducted on a race track for a 15 × 8 configuration, where a UCA (0.43λ spacing) was used at the transmitter and a ULA (0.5λ spacing) was used at the receiver. For these measurements, the transmitter was mounted on a moving vehicle. Each measurement took 0.25 s, with each impulse response being 3.2 μs in duration. Results such as DOA and DOD were estimated using a conditional maximum likelihood algorithm.

In paper [38], the same measurement setup is employed as described in [36], however measurements are also performed at 5.2 GHz using the same synthetic array. Here the Unitary ESPRIT algorithm is used to identify and estimate DOAs and DODs. Papers [51, 52] follow on from [38], where measurements are performed using the RUSK (ATM) sounder with 120 MHz at 5.2 GHz. In [51], indoor office channel capacity results are presented for 2 × 2, 4 × 4, and 8 × 8 array configurations. Here, the receiver employed an 8-element ULA (0.4λ spacing), while at the transmitter a 2D virtual array was used. This utilised the same x-y positioning system which formed a grid with 20 x positions and 10 y positions, and λ/2 inter-element spacings. This system took 10 minutes to record one full channel measurement file, therefore the measurements were performed at night to ensure stationarity [51]. The results showed that for the larger array configurations, such as 8 × 8, the system suffered particularly from high correlation.

The measurements described in [52] were performed using the same system setup as [51]. Here, however, the focus was on BER analysis and modelling for 4 × 4 and 6 × 8 MIMO systems. The results showed that the popular Kronecker model was not the best choice of channel representation. The paper concludes that the newly introduced Weichselberger model was a more suitable choice [55].

In [19, 49], a powerful method for measuring channel capacity was described. This method was used to calculate the CDF of the channel capacity from a single measurement snapshot. The method is based on the extraction of multipath parameters (as in the case of *k*-dimensional parametric methods), and thereafter applying a synthetic phase variation in order to obtain an ensemble of different channel capacities. Capacity results were presented for frequency-flat and frequency-selective channels. Here, the studies concluded that the estimated capacities were up to 30% lower than what would be expected from a simple model.

Paper [53] examines MIMO data for 5.2 GHz channels in order to analyse the statistical properties of the channel matrix, particularly for correlated radio environments. For these measurements, the same RUSK system was used. The results show that in cases where there was particular correlation between transmitter and receiver, the Kronecker model was simply inadequate for channel estimation. In this paper, the Weichselberger model [55] was shown to provide a better fit for measured channel capacity.

In [54], capacity results are presented for several 4 × 4 subarrays of a full 16 × 16 array system. Here, the MEDAV RUSK (BRI) system was employed at 5.2 GHz and good agreement was shown between measured and estimated channel capacity results.

Multi-parameter channel measurements have also been conducted using a basic Vector Network Analyser (VNA) [56, 57]. Such a measurement technique is further described in chapter 5. In [56], measurements are performed using an Agilent E8358A VNA. Here, virtual array results for DOA and DOD are collected at 5.25 GHz with a measurement bandwidth of 200 MHz.

3.6.2.1 Measurements for the IST METRA Project

The IST METRA project [21] was described in section 3.5.1.1. For this project, numerous measurement campaigns were carried out in Aalborg, Denmark at a carrier frequency of 2.05 GHz, for a 4 × 4 and a 2 × 4 system, while moving the antenna elements at the transmitter. Two measurement setups were considered and these differed in transmitter antenna motion and array topology. The aim of the project was to develop a stochastic MIMO radio channel model with experimental validation.

The results for picocell environments showed capacities within 14 bits/s/Hz and 16 bits/s/Hz in 80% of the cases for a 4 × 4 antenna system which implemented waterfilling at 20 dB SNR. In [58], measurements for a 4 × 4 system showed that 0.4λ separation between the elements of the antenna array were sufficient to get decorrelated channels even in a LOS scenario. Moreover, it was concluded that a gain of 18 dB at 10% outage could be achieved using this set-up. The stochastic model derived from these measurement results was fed into a COSSAP® block for implementation [21].

3.6.2.2 Measurements for the IST SATURN Project

For the SATURN project, the majority of the measurements were carried out using the MEDAV RUSK (BRI) vector sounder, which has an eight-element omnidirectional ULA at the transmit side and an eight-element ULA with 120° beamwidth at the receive side, i.e. an 8 × 8 antenna configuration. The measurements were centred at 5.2 GHz with a bandwidth of 120 MHz. The Kronecker structure of the channel was examined as well as the capacity for several antenna configurations.

3.6.3 Other Measurement Campaigns

Other measurements include the Stanford University measurements for 2 × 2 MIMO channels in the time and frequency domains for fixed wireless applications [59-62]. The parameters extracted from these measurements included path loss, Rician K-factor, fading signal correlations, delay spread, Doppler spread, cross-polarisation discrimination (CPD), second order statistics, as well as link capacity. The measurements were carried out with a discrete frequency swept signal with RF bandwidth of 4 MHz at an operating frequency of 2.48 GHz (for the ISM band).

Path loss results in [61] showed that blockage due to buildings or foliage caused an excess loss of 35.45 dB compared to free-space propagation at a distance of 1 km. In [62], a generalised 2 × 2 channel model is described based on the correlation properties between path loss, co-polarised K-factor, and CPD distribution of the constant and scattered signal components. The work presented here was used to develop the Stanford University Interim (SUI) models for space-time wireless channels [9].

A number of notable channel measurement campaigns were conducted by Wallace *et al.* [63-66]. In [63, 65], MIMO measurements are presented in the nominal 2.45 GHz frequency band for 4 × 4 and 10 × 10 antenna arrays, as well as for 2 × 2 in [64]. The system architecture used is narrowband, where the system generates and receives a binary phase shift-keyed (BPSK) signal [65]. The measured data presented allows assessment of the channel statistical behaviour including transfer matrix PDFs and temporal-spatial correlation. In addition to this, the impact of polarisation, directivity, and number of array elements on the channel capacity were demonstrated.

Paper [67] presents a statistical narrowband model for the obstructed LOS indoor MIMO channels based on the channel covariance structure. Indoor MIMO capacity results were examined in the 5.8 GHz ISM band and the effect of inter-element spacing on the channel capacity was studied. The investigation showed that the envelope of the channel coefficients for this obstructed LOS scenario was approximately Rayleigh distributed.

The work presented in [68] by Martin *et al.* (originally at AT&T Labs Research) examines MIMO capacity for 4 × 4 channels. The experimental data were collected at 1.9 GHz with a bandwidth of 30 kHz, as for IS-136 systems. The results showed the degradation in capacity due to correlation.

In [69], an experimental MIMO study was carried out in the metro tunnels of Paris. Data files were collected for a single-track and a double-track tunnel with a transmitter-receiver distance of a few hundred meters. It was shown that at 10 dB SNR, the maximum mean data rate increased from 3 bits/s/Hz for a single antenna (SISO) channel to 8 bits/s/Hz using a 4 × 4 array system. The experimental arrangement is described in [69].

Experimental investigations into keyhole channels were carried out in [70]. The measurements used a waveguide, a small hole without a waveguide, and a hole of 300 × 300 mm size as the only paths between the two rich scattering environments. For the small hole, there was a loss in capacity compared to the ideal case, but for the large hole, the capacity was almost near the theoretic MIMO limit.

Paper [71] presented temporal channel results for a 2 × 2 MIMO-OFDM configuration at a centre frequency of 3.676 GHz with a channel bandwidth of 18.775 MHz. The system consisted of 751 sub-carriers spaced 25 kHz apart. The study involved data analysis for impulse response measurements, such as path loss and fading statistics. Most of the measurement locations showed moderate delay spread although this varied between 0 and 5 μs rms. The results indicated that locations further from the base would experience a range of path loss values, with higher path loss corresponding to higher delay spread.

The work presented in [72], describes channel measurements and analysis for wideband (100 MHz) indoor MIMO links at 5.25 GHz. The measurements were performed using the Elektrobit Multidimensional channel sounder [73]. The results showed that dual-polarised antennas provide a good solution for MIMO multiplexing.

It should be noted that the measurement campaigns described thus far provide only a representative sample of the work carried out to date. By and large, the majority of the MIMO capacity studies have focused on measuring the channel matrix, **H**, and comparing its statistics to that of a basic channel model, such as the Rayleigh IID channel. In most of the studies, only narrowband time-invariant MIMO channels have been considered, even though in recent years there has been more interest in wideband MIMO links, particularly for OFDM systems. The effects of Doppler on MIMO system performance have seldom been examined and the convenient 'quasi-static' assumption has been made in many of the propagation studies. In order to realise MIMO space-time architectures, some of these systematic deficiencies must be addressed. A comprehensive review of some of the aforementioned measurement campaigns are presented in [74]. There are also a substantial number of measurement results presented in the COST 273 action [75].

3.7 Practical MIMO Signalling

Even though there are only a few recognised MIMO systems in existence such as the BLAST system reported by Lucent, it should be noted that vast progress has been made in the field of MIMO space-time signalling. These technologies are envisaged not only for future generation systems but also for current standards (UMTS).

In general, the principle argument in the design of any space-time system is the inherent trade-off between diversity gain and spatial multiplexing. The reported MIMO channel capacities can only be achieved through the latter. This section describes two basic space-time architectural structures for a wireless link with multiple transmitters and multiple receivers.

The realisation of MIMO signalling can be achieved through the BLAST architecture in one of two ways [5, 7, 41, 42, 76]. The two proposed space-time architectures employed for practical MIMO signalling are classified as either vertical BLAST (V-BLAST) or Diagonal BLAST (D-BLAST). For the V-BLAST architecture, data are demultiplexed into parallel substreams, each going to a different antenna, i.e., independent data transmission. The data substreams may or may not be of equal data rate. Figure 3.4 illustrates this architecture.

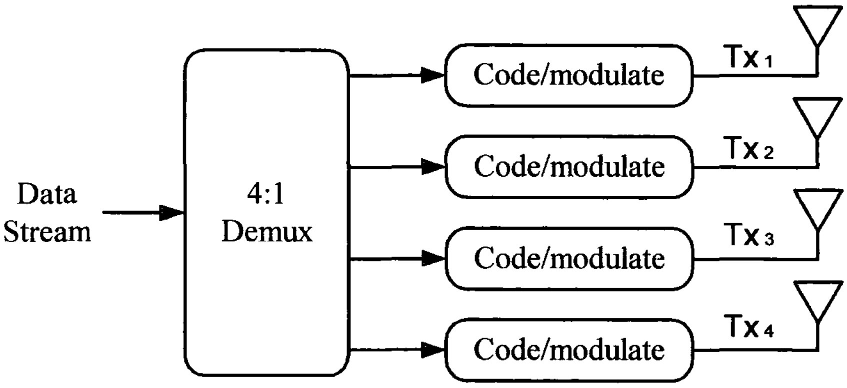

Figure 3.4: V-BLAST wireless transmission of four data substreams.

In an ideal scattering environment, the V-BLAST architecture can provide very high channel capacity. However, it must be noted that this architecture is not very practical, since if any transmit antenna is in a fade, the corresponding data substream will be lost. A more practical MIMO system architecture is that of the D-BLAST system, where the data substreams are diagonally layered in space-time so that each layer is transmitted sequentially on every transmit antenna, as illustrated in figure 3.5. This provides a more reliable system for communication, since if any of the transmit antennas are individually or collectively in a fade, the corresponding data layer will not be lost. The D-BLAST architecture is based on data redundancy with the data substreams being of equal data rate, therefore it is not as efficient as the V-BLAST system. However, in a practical radio environment it is unlikely that the V-BLAST system would be able to provide a reliable high capacity communication link [76]. It should be noted that the MIMO architectures described thus far have been based on burst mode data transmission as described for the BLAST system.

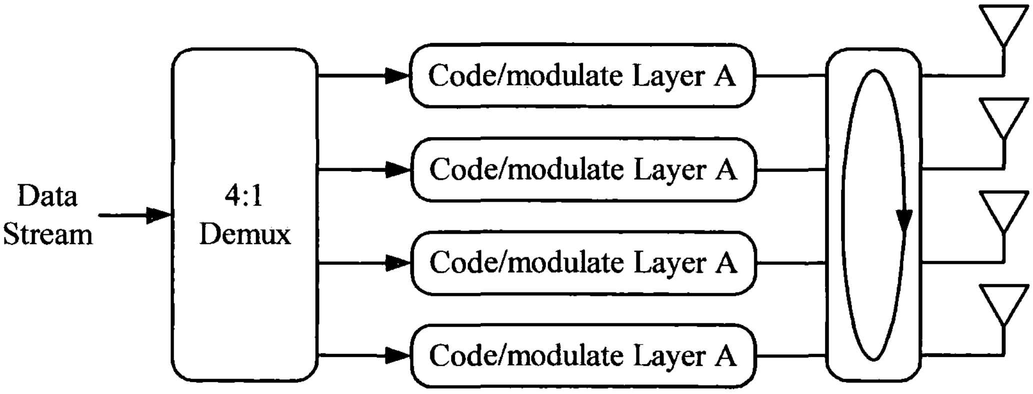

Figure 3.5: D-BLAST wireless transmission of four data substreams.

In recent years, a number of different MIMO system architectures have been investigated. These include simple linear receiver systems such as the Zero-Forcing (ZF) receiver to the more complex but optimal Maximum Likelihood (ML) receiver. Many of the practical issues concerning MIMO signalling techniques are discussed in [2, 4, 9, 76-80]. The implementation of MIMO was at the outset only reported by Lucent Technologies with the BLAST chip, which was capable of supporting communications for a 2 × 2 and a 4 × 4 link. However, at present there are a number of companies which manufacture MIMO chipsets. For the pre-N LAN market alone, chipmakers include Atheros, Airgo, and Ruckus.

3.8 Summary and Conclusions

In this chapter the basic principles of MIMO radio links were discussed. It was shown that the ideal environment for a MIMO channel is one with rich scattering, which permits uncorrelated signals at the receive array. The fundamental capacity formula for MIMO channels was given, with a discussion of channel state knowledge at the transmitter. Furthermore, the effects that diminish this capacity were specified as being caused by spatial correlation, LOS paths, cross polarised antennas as well as other perhaps less significant factors such as antenna coupling, user interference, self interference (limited by number of transmit antennas) and high Doppler frequencies. A number of MIMO channel models were described and a literature review of recent MIMO measurements was presented. Finally, two very basic MIMO signalling techniques were discussed.

3.9 References

1. A. F. Naguib, V. Tarokh, N. Seshadri, A. R. Calderbank, "A Space-Time Coding Modem for High-Data-Rate Wireless Communications," *IEEE Journal on Selected Areas in Communications*, vol. 16, pp. 1459-1478, 1998.
2. B. Vucetic, J. Yuan, *Space-Time Coding*: John Wiley & Sons Ltd, 2003.
3. T. Matsumoto, J. Ylitalo, M. Juntti, "Overview and Recent Challenges of MIMO Systems," *IEEE Vehicular Technology Society News*, vol. 50, pp. 4-9, 2003.

4. D. Gesbert, M. Shafi, D. Shiu, P. J. Smith, A. Naguib, "From Theory to Practice: An Overview of MIMO Space-Time Coded Wireless Systems," *IEEE Journal on Selected Areas in Communications*, vol. 21, pp. 281-302, 2003.
5. G. J. Foschini, "Layered Space-Time Architecture for Wireless Communication in a Fading Environment When using Multi-Element Antennas," *Bell Labs Technical Journal*, vol. 1, pp. 41-59, 1996.
6. G. D. Durgin, *Space-Time Wireless Channels*: Prentice Hall PTR, 2003.
7. G. J. Foschini, M. J. Gans, "On Limits of Wireless Communication in a Fading Environment when using Multiple Antennas," *Wireless Personal Communications (Kluwer)*, vol. 6, pp. 311, 1998.
8. D. Gesbert, H. Bölcskei, D. A. Gore, A. J. Paulraj, "MIMO Wireless Channels: Capacity and Performance Prediction," IEEE GLOBECOM 2000, San Francisco, CA.
9. A. Paulraj, Nabar, R., Gore, D., *Introduction to Space-Time Wireless Communications*: Cambridge University Press, 2003.
10. G. Strange, *Linear Algebra and Its Applications*, 3 ed: Thomson Learning Inc, 1988.
11. F. R. Farrokhi, A. Lozano, G. J. Foschini, R. A. Valenzuela, "Spectral Efficiency of Wireless Systems with Multiple Transmit and Receive Antennas," IEEE International Symposium on PIMRC, London, UK, 2000.
12. R. Nabar, H. Bölcskei, V. Erceg, D. Gesbert, A. J. Paulraj, "Performance of Multi-Antenna Signalling Techniques in the Presence of Polarization Diversity," *IEEE Transactions on Signal Processing*, vol. 50, pp. 2553-2562, 2002.
13. R. Vauhgan, J. B. Anderson, *Channels, Propagation and Antennas for Mobile Communications*: IEE Press, 2003.
14. D. Chizhik, G. J. Foschini, M. J. Gans, and R. A. Valenzuela, "Keyholes, Correlations, and Capacities of Multielement Transmit and Receive Antennas," *IEEE Transactions on Wireless Communications*, vol. 1, pp. 361-368, 2002.
15. I. E. Telatar, “Capacity of Multi-antenna Gaussian Channels,” *European Transactions on Telecommunications*, vol. 10, pp. 585–595, 1999. Originally a Bell Laboratories, Lucent Technologies, Technical Report, 1995.
16. T. M. Cover, J. A. Thomas, *Elements of Information Theory*, 2 ed: John Wiley & Sons Ltd, 1991.

17. A. Papoulis, S. U. Pillai, *Probability, Random Variables and Stochastic Processes*, 4 ed: McGraw Hill, 2002.
18. A. Paulraj, *Class Reader for EE492m - Space-Time Wireless Communications*. Stanford University, Stanford, CA, 2002.
19. A. F. Molisch, M. Steinbauer, M. Toeltsch, E. Bonek, R. S. Thomä, "Measurement of the Capacity of MIMO Systems in Frequency-Selective Channels," IEEE VTC Spring, Rhodes, Greece, 2001.
20. K. Yu, B. Ottersten, "Models for MIMO Propagation Channels: A Review," *Wireless Communications and Mobile Computing*, vol. 2, pp. 653-666, 2002.
21. L. Schumacher, J. P. Kermoal, F. Frederiksen, K. I. Pedersen, A. Algans, P. E. Mogensen, "The METRA Project: MIMO Channel Characterisation," *Report: IST-1999-11729*, 2001.
22. J. P. Kermoal, L. Schumacher, K. I. Pedersen, P. E. Mogensen, F. Frederiksen, "A Stochastic MIMO Radio Channel Model with Experimental Validation," *IEEE Journal on Selected Areas in Communications*, vol. 20, pp. 1211-1226, 2002.
23. K. I. Pedersen, J. B. Anderson, J. P. Kermoal, P. E. Mogensen, "A Stochastic Multiple-Input-Multiple-Output Radio Channel Model for Evaluation of Space-Time Coding Algorithms," IEEE VTC-Fall, Rhodes, Greece, 2000.
24. T. Klingenbrunn, P. E. Mogensen, "Modelling Frequency Correlation of Fast Fading in Frequency Hopping GSM Link Simulations," IEEE VTC-Fall, Amsterdam, Netherlands, 1999.
25. O. Gasparini, E. de Marinis, M. Beach, A. Nix, J. Vidal, S. Barbarossa, J. Thibault, J. Douris, B. Ottersten, M. Bengtsson, "The SATURN Project: Final Report," *Report: IST-1999-10322*, 2003.
26. D. Shiu, *Wireless Communication Using Dual Antenna Arrays*: Kluwer Academic Publishers, 2000.
27. R. B. Ertel, P. Cardieri, K. W. Sowerby, T. S. Rappaport, J. Reed, "Overview of Spatial Channel Models for Antenna Array Communication Systems," *IEEE Personal Communications*, vol. 5, pp. 10-22, 1998.
28. A. A. M. Saleh, R. A. Valenzuela, "A Statistical Model for Indoor Multipath Propagation," *IEEE Journal on Selected Areas in Communications*, vol. 5, pp. 128-137, 1987.

29. L. M. Correia, *Wireless Flexible Personalised Communications*: John Wiley & Sons Ltd, 2001.
30. R. S. Thomä, D. Hampicke, A. Richter, G. Sommerkorn, U. Trautwein, "MIMO Vector Channel Sounder Measurement for Smart Antenna System Evaluation," *European Transaction on Telecommunications*, vol. 12, pp. 427-438, 2001.
31 R. S. Thomä, D. Hampicke, M. Landmann, G. Sommerkorn, A. Richter, "MIMO Measurement for Double-Directional Channel Modelling," IEE Technical Seminar on MIMO Communication Systems, London, 2001.
32. R. S. Thomä, D. Hampicke, M. Landmann, C. Schneider, G. Sommerkorn, A. Richter, "MIMO Channel Sounding and Double-Directional Modelling," XXXVIIth URSI-GA, Maastricht, NL, 2002.
33. W. Wirnitzer, D. Bruckner, R. S. Thomä, G. Sommerkorn, D. Hampicke, "Broadband Vector Channel Sounder for MIMO Channel Measurement," IEE Seminar: MIMO - Communication Systems from Concept to Implementation, London, 2001.
34. A. Richter, D. Hampicke, G. Sommerkorn, R. S. Thomä,, "MIMO Measurement and Joint M-D Parameter Estimation of Mobile Radio Channels," IEEE VTC-Spring, Rhodes, Greece, 2001.
35. G. Sommerkorn, A. Richter, R. S. Thomä, W. Wirnitzer, "Antenna Multiplexing & Time Alignment for MIMO Channel Sounding," XXXVIIth URSI-GA, Maastricht, NL, 2002.
36. M. Steinbauer, A. F. Molisch, E. Bonek, "The Double-Directional Mobile Radio Channel," *IEEE Antennas and Propagation Magazine*, vol. 43, pp. 51-63, 2001.
37. A. F. Molisch, "A Generic Model for MIMO Wireless Propagation Channels," IEEE International Conference on Communications, New York, 2002.
38. E. Bonek, H. Hofstetter, C. F. Mecklenbrauker, M. Steinbauer, "Double Directional Superresolution Radio Channel Measurements," 39th Annual Allerton Conference on Communication, Control, and Computing, Urbana, Illinois, USA, 2001.
39. E. Bonek, M. Steinbauer, H. Hofstetter, C. F. Mecklenbrauker, "Double-Directional Radio Channel Measurements - What We Can Derive from Them," International Symposium on Signals, Systems, and Electronics, Tokyo, Japan, 2001.

40. H. Hofstetter, M. Steinbauer, C. F. Mecklenbrauker, "Double-Directional Radio Channel Estimation at 2 GHz for High Speed Vehicular Mobiles - Experimental Results," 4th International Symposium on Wireless Personal Multimedia Communications, Aalborg, Denmark, 2001.
41. P. W. Wolniansky, G. J. Foschini, G. D. Golden, R. A. Valenzuela, "V-BLAST: An Architecture for Realizing Very High Data Rates Over the Rich-Scattering Wireless Channel," ISSSE, Pisa, Italy, 1998.
42. G. D. Golden, G. J. Foschini, P. W. Wolniansky, R. A. Valenzuela, "V-BLAST: A High Capacity Space-Time Architecture for the Rich-Scattering Wireless Channel," International Symposium on Advanced Radio Technologies, Boulder, CO, 1998.
43. G. D. Golden, G. J. Foschini, R. A. Valenzuela, P. W. Wolniansky, "Detection Algorithm and Initial Laboratory Results using the V-BLAST Space-Time Communication Architecture," *Electronic Letters*, vol. 35, pp. 14-15, 1999.
44. H. Xu, M. J. Gans, N. Amitay, R. A. Valenzuela, "Experimental Verification of MTMR System Capacity in Controlled Propagation Environment," *Electronic Letters*, vol. 37, pp. 936-937, 2001.
45. H. Xu, M. Gans, N. Amitay, R. A. Valenzuela, T. Sizer, R. Storz, D. Taylor, M. McDonald, C. Tran, "MIMO Channel Capacity for Fixed Wireless: Measurements and Models," IEEE VTC-Fall, Atlantic City, 2001.
46. M. J. Gans, N. Amitay, Y. S. A. Yeh, H. Xu, T. C. Damen, R. A. Valenzuela, T. Sizer, R. Storz, D. Taylor, W. M. MacDonald, C. Tran, A. Adamiecki, "Outdoor BLAST Measurement System at 2.44 GHz: Calibration and Initial Results," *IEEE Journal on Selected Areas in Communications*, vol. 20, pp. 570-583, 2002.
47. D. Chizhik, J. Ling, P. W. Wolniansky, R. A. Valenzuela, N. Costa, K. Huber, "Multiple Input-Multiple Output Measurements and Modeling in Manhattan," *IEEE Journal on Selected Areas in Communications*, vol. 21, pp. 321-331, 2003.
48. P. B. Papazian, Y. Lo, J. J. Lemmon, M. J. Gans, "Measurements of Channel Transfer Functions and Capacity Calculations for a 16x16 BLAST Array over a Ground Plane," *U.S. Departments of Commerce: NTIA Report TR-03-403*, 2003.
49. A. F. Molisch, M. Steinbauer, M. Toeltsch, E. Bonek, R. S. Thomä, "Capacity of MIMO systems based on measured wireless channels," *IEEE Journal on Selected Areas in Communications*, vol. 20, pp. 561-569, 2002.

50 D. Hampicke, M. Landmann, C. Schneider, G. Sommerkorn, R. Thomä, T. Fügen, J. Maurer, W. Wiesbeck, "MIMO Capacities for Different Antenna Array Structures Based on Double Directional Wide-Band Channel Measurements," IEEE VTC-Fall, Vancouver, Canada, 2002.

51. H. Ozcelik, M. Herdin, H. Hofstetter, E. Bonek, "Capacity of Different MIMO Systems Based on Indoor Measurements at 5.2 GHz," 5th European Personal Mobile Communications Conference, Glasgow, Scotland, 2003.

52. M. Herdin, G. Gritsch, B. Badic, E. Bonek, "The Influence of Channel Models on Simulated MIMO Performance," IEEE VTC-Spring, Milan, Italy, 2004.

53. S. Wyne, A. F. Molisch, P. Almers, G. Eriksson, J. Karedal, F. Tufvesson, "Statistical Evaluation of Outdoor-to-Indoor Office MIMO Measurements at 5.2 GHz," IEEE VTC-Spring, Stockholm, Sweden, 2005.

54. A. Pal, C. M. Tan, M. A. Beach, "Comparison of MIMO Channels From Multipath Parameter Extraction and Direct Channel Measurements," 15th IEEE International Personal, Indoor and Mobile Radio Communications (PIMRC 2004), Barcelona, Spain, 2004.

55. W. Weichselberger, M. Herdin, H. ¨Ozcelik, E. Bonek, "A Novel Stochastic MIMO Channel Model and its Physical Interpretation," International Symposium on Wireless Personal Multimedia Communications, Yokosuka, Japan, 2003.

56. K. Haneda, J. Takada, "High-Resolution Estimation of NLOS Indoor MIMO Channel with Network analyzer Based System," 14th IEEE International Personal, Indoor and Mobile Radio Communications (PIMRC 2003), Beijing, China, 2003.

57. J. Medbo, J. Berg, H. Asplund, M. Riback, "MIMO Channel Characteristics in a Small Macrocell Measured at 5.25 GHz and 200 MHz Bandwidth," IEEE VTC-Fall, Dallas, USA, 2005.

58. J. P. Kermoal, L. Schumacher, P. E. Mogensen, K. I. Pedersen, F. Frederiksen, "METRA: Experimental Investigation of MIMO Radio Channels for Indoor Picocell Scenarios," IST Mobile Communication Summit 2000, Galway, Ireland, 2000.

59. D. S. Baum, D. Gore, R. Nabar, S. Panchanathan, K. V. S. Hari, V. Erceg, A. J. Paulraj, "Measurement and Characterization of Broadband MIMO Fixed Wireless Channels at 2.5 GHz," IEEE International Conference on Personal Wireless Communications, Hyderabad, India, 2000.

60. V. Erceg, P. Soma, D. S. Baum, A. J. Paulraj, "Capacity Obtained from Multiple-Input Multiple-Output Channel Measurements in Fixed Wireless Environments at 2.5 GHz," IEEE International Conference on Communications, New York, USA, 2002.
61. P. Soma, D. S. Baum, V. Erceg, R. Krishnamoorthy, A. J. Paulraj, "Analysis and Modeling of Multiple-Input Multiple-Output (MIMO) Radio Channel Based on Outdoor Measurements Conducted at 2.5 GHz for Fixed BWA Applications," IEEE International Conference on Communications, New York, USA, 2002.
62. V. Erceg, P. Soma, P., D. S. Baum, S. Catreux, "Multiple-Input Multiple-Output Fixed Wireless Radio Channel Measurements and Modeling Using Dual-Polarized Antennas at 2.5 GHz," *IEEE Transactions on Wireless Communications*, vol. 3, pp. 2288 - 2298, 2004.
63. J. W. Wallace, M. A. Jensen, "Characteristics of Measured 4×4 and 10×10 MIMO Wireless Channel Data at 2.4-GHz," IEEE Antennas and Propagation Society International Symposium, San Antonio, Texas, USA, 2001.
64. J. W. Wallace, M. A. Jensen, "Modeling the Indoor MIMO Wireless Channel," *IEEE Transactions on Antennas and Propagation*, vol. 50, pp. 591 - 599, 2002.
65. J. W. Wallace, M. A. Jensen, A. L. Swindlehurst, B. D. Jeffs, "Experimental Characterization of the MIMO Wireless Channel: Data Acquisition and Analysis," *IEEE Transactions on Wireless Communications*, vol. 2, pp. 335-343, 2003.
66. B. T. Maharaj, W. Wallace, L. P. Linde, M. A. Jensen, "Frequency Scaling of Spatial Correlation from Co-located 2.4 and 5.2 GHz Wideband Indoor MIMO Channel Measurements," *IEE Electronics Letters*, vol. 41, pp. 336 - 337, 2005.
67. R. Stridh, K. Yu, B. Ottersten, P. Karlsson, "MIMO Channel Capacity and Modeling Issues on a Measured Indoor Radio Channel at 5.8 GHz," *IEEE Transactions on Antennas and Propagation*, vol. 4, pp. 895 - 903, 2005.
68. C. C. Martin, J. H. Winters, N. R. Sollenberger, "Multiple-Input Multiple-Output (MIMO) Radio Channel Measurements," IEEE VTC-Fall, Boston, MA, USA, 2000.
69. M. Lienard, P. Degauque, J. Baudet, D. Degardin, "Investigation on MIMO Channels in Subway Tunnels," *IEEE Journal on Selected Areas in Communications*, vol. 21, pp. 332-339, 2003.

70. P. Almers, F. Tufvesson, A. F. Molisch, "Measurement of Keyhole Effect in a Wireless Multiple-Input Multiple-Output (MIMO) Channel," *IEEE Communications Letters*, vol. 7, pp. 373-375, 2003.
71. M. D. Batariere, T. K. Blankenship, J. F. Kepler, T. P. Krauss, I. Lisica, S. Mukthavaram, J. W. Porter, T. A. Thomas, F. W. Vook, "Wideband MIMO Mobile Impulse Response Measurements at 3.7 GHz," IEEE VTC-Spring, Birmingham, Alabama, USA, 2002.
72. J. Hamalainen, R. Wichman, J.-P. Nuutinen, J. Ylitalo, T. Jamsa, "Analysis and Measurements for Indoor Polarization MIMO in 5.25 GHz Band," IEEE VTC-Spring, Stockholm, Sweden, 2005.
73. Elektrobit Ltd., "Propsound Multidimensional channel sounder," http://www.propsim.net/.
74. S. Salous, "The Provision of an Initial Study of Multiple In Multiple Out Technology - Section 2: Literature Search," *DTI Contract AY 4252 (510010100)*, 2003.
75. COST 273 Action, “Towards Mobile Broadband Multimedia Networks," www.lx.it.pt/cost273/.
76. G. J. Foschini, D. Chizhik, M. J. Gans, C. B. Papadias, R. A. Valenzuela, "Analysis and Performance of Some Basic Space-Time Architectures," *IEEE Journal on Selected Areas in Communications*, vol. 21, pp. 303-320, 2003.
77. A. B. Gershman, N. D. Sidiropoulos, *Space-Time Processing for MIMO Communications*. Chichester: John Wiley & Sons Ltd, 2005.
78. H. Bölcskei, D. Gesbert, C. Papadias, A. J. van der Veen, *Space-Time Wireless Systems: From Array Processing to MIMO Communications*. Cambridge: Cambridge University Press, 2005.
79. J. D. Gibson, Ed., *The Mobile Communications Handbook*, 2 ed: Springer-Verlag Berlin and Heidelberg GmbH & Co., 1999.
80. M. A. Jenson, J. W. Wallace, "Invited Paper: A Review of Antennas and Propagation for MIMO Wireless Communications," *IEEE Transactions on Antennas and Propagation*, vol. 52, pp. 2810-2824, 2004.

Chapter 4

Spatial Array Signal Processing

4.1 Introduction

Over the past two decades, there has been growing interest in spatial array signal processing, which is primarily concerned with estimating temporal and spatial channel parameters using the data collected from array sensors. The estimation problem depends on parameters such as array geometry, sensor characteristics and signal properties. For mobile radio communications, the extraction of signal parameters such as complex amplitudes, DOA, DOD, time delays and Doppler shifts from the antenna array are critical in measuring, analysing and modelling directional and double-directional radio channels.

This chapter provides a brief overview of the various methods available for estimating the DOA of a signal using an antenna array (the estimation of departure angles is based on the same principles). The array based DOA estimation techniques considered in this chapter are classified into three main branches: spectral-based techniques, parametric techniques and joint parametric techniques. Spectral-based methods are often used in order to form some spectrum-like function of the parameter(s) of interest, such as DOA estimates. Parametric methods on the other hand, require a simultaneous search for all parameters of interest. This often results in more accurate estimates, albeit at the expense of increased computational complexity. Maximum Likelihood (ML) type methods are an important category of parametric methods and are optimal techniques which perform well even under low SNR conditions. However, these techniques are often very computationally expensive. In this chapter, special emphasis is placed on parametric techniques, in particular ESPRIT (Estimation of Signal Parameters via Rotational Invariance Techniques) and SAGE (Space Alternating Generalised Expectation maximisation), which is especially suitable for high-resolution DOA estimation.

4.2 DOA Problem Formulation and Assumptions

In order to examine the various DOA estimation techniques, it is essential to first define the spatial data model and formulate the DOA estimation problem. Estimating the DOA of a wave emanating from a point source is by far the most analysed channel parameter estimation scenario. The difficulty in estimating DOAs is simplified by assuming that each source results in a single wave arriving from a specific direction θ. This assumption is referred to as the point source assumption, and is generally applicable to the majority of radio environments (far-field). However, in cases where the sources are not accurately modelled as point sources, such as close range environments, a rather more complicated approach is adopted based on spread source models [2]. In this chapter, the point source scenario is generally assumed.

The point source scenario implies that the classical spatial data model in which P waves are incident on a receiver array of N elements is appropriate and thus can be expressed as

$$\mathbf{x}(t) = \sum_{i=1}^{P} \mathbf{a}(\theta_i)\mathbf{s}_i(t) + \mathbf{n}(t) = \mathbf{A}(\theta)\mathbf{s}(t) + \mathbf{n}(t) \tag{4.1}$$

where $\mathbf{x}(t)$ is the $N \times 1$ measured voltage signal vector, $\mathbf{s}(t)$ is the $P \times 1$ source signal vector ($\mathbf{s}(t) = [s_1(t) \quad s_2(t) \quad \cdots \quad s_P(t)]^T$) and $\mathbf{n}(t)$ is the $N \times 1$ noise vector (assuming a AWGN model). $\mathbf{A}(\theta)$ is the $N \times P$ array manifold, defined as a set of P array steering vectors, $\mathbf{a}(\theta_i)$, each of dimension $N \times 1$, which model the spatial response of the array due to an incident plane wave from the azimuth direction θ. Thus, if P waves impinge on an N-element antenna array from distinct DOAs θ_1 to θ_P, the array manifold $\mathbf{A}(\theta)$ can be expressed as

$$\mathbf{A}(\theta) = \left[\mathbf{a}(\theta_1) \quad \mathbf{a}(\theta_2) \quad \cdots \quad \mathbf{a}(\theta_P)\right] \tag{4.2}$$

The physical (Maxwellian) modelling of the array antennas and the spatial data model can be found in a variety of publications, including [1-6]. It should be noted that there is a fundamentally analogous relationship between the signal model defined in equation (4.1) and the MIMO system model described in chapter 3.

In equation (4.2), each of the array steering vectors, $\mathbf{a}(\theta_i)$, represent the array response vector for a direction θ_i. In general, the steering vectors are dependent on the assumed data model, the array geometry, the carrier frequency and obviously the DOA. Different antenna array geometries give different expressions for the steering vectors. The most common array geometries are the Uniform Linear Array (ULA) and the Uniform Circular Array (UCA) geometries. These are illustrated in figure 4.1(a) and 4.1(b), respectively.

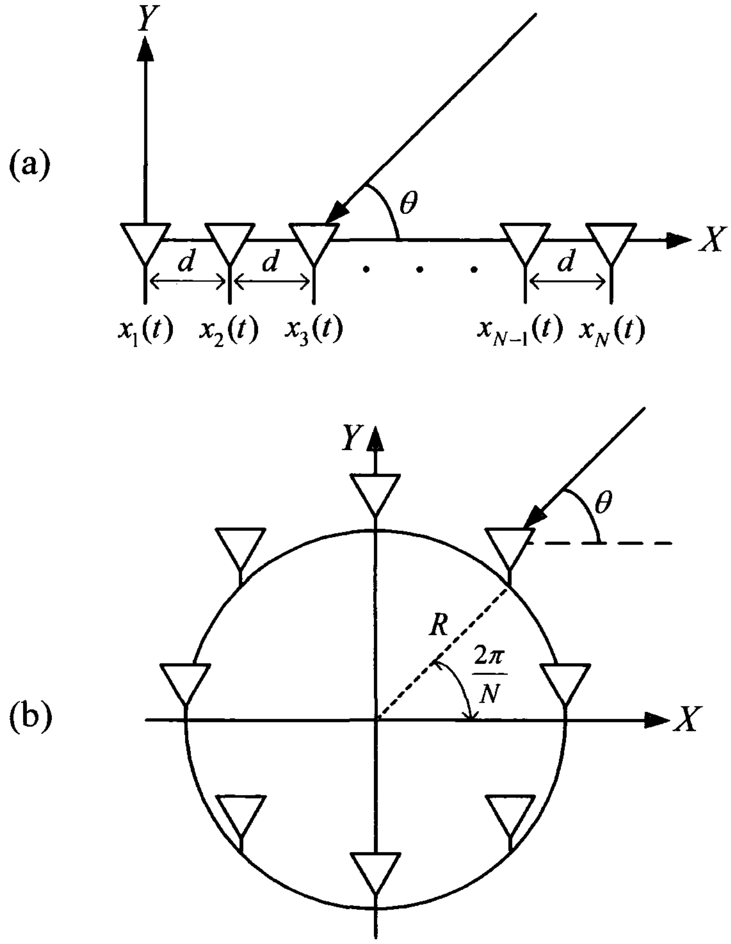

Figure 4.1: Illustration of (a) ULA with N antenna elements and (b) UCA with N antenna elements.

The steering vector, $\mathbf{a}(\theta)$, for direction θ using a ULA or a UCA can be mathematically expressed as

$$\mathbf{a}_{ULA}(\theta) = g(\theta)\begin{bmatrix}1 & e^{-jkd\cos(\theta)} & \cdots & e^{-j(N-1)kd\cos(\theta)}\end{bmatrix}^T \qquad (4.3)$$

and

$$\mathbf{a}_{UCA}(\theta) = g(\theta)\left[e^{jkR\cos(\theta)} \quad e^{jkR\cos\left(\theta - \frac{2\pi}{N}\right)} \quad \cdots \quad e^{jkR\cos\left(\theta - \frac{2\pi}{N}(N-1)\right)} \right]^T \tag{4.4}$$

where $g(\theta)$ is a singular complex antenna gain based on the assumption that $g_1(\theta) = g_2(\theta) = \cdots = g_N(\theta) = g(\theta)$. Since all elements are assumed to have the same directivity, it is common to drop the gain factor $g(\theta)$ from the above expression. In the above equations, $k = 2\pi/\lambda$ and is defined as the wavenumber (often expressed as ω_c/c). The inter-element spacing for the ULA is denoted by d, and for the UCA, the angular distance between 2 elements in an N-element array is clearly given by $2\pi/N$. In equation (4.4), R denotes the radius of the circle formed by the array antennas.

It is assumed in the signal model defined in equation (4.1), that $N > P$, i.e. there are more antenna elements than signals. Furthermore, it is assumed that the array manifold (or steering matrix), $\mathbf{A}(\theta)$, is of full rank and that the signal and noise vectors are zero-mean complex Gaussian and uncorrelated. In addition to this, it is assumed that there is no antenna coupling between elements and perfect calibration of the array antennas.

It is important to note that most of the DOA estimation techniques described in the following sections exploit the properties of the signal covariance matrix (as described in chapter 3). Using the aforementioned assumptions, the covariance matrix of the measured voltage signals can be expressed as

$$\mathbf{R} = E\left\{\mathbf{x}(t)\mathbf{x}^H(t)\right\} = \mathbf{A}E\left\{\mathbf{s}(t)\mathbf{s}^H(t)\right\}\mathbf{A}^H + E\left\{\mathbf{n}(t)\mathbf{n}^H(t)\right\} \tag{4.5}$$

where $\mathbf{A} = \mathbf{A}(\theta)$. It should be clear from equation (4.5) that the cross-correlation terms vanish, since it is assumed that the signal and the noise are uncorrelated. By denoting the source covariance matrix as $\mathbf{P}$ and the noise covariance matrix as $\sigma^2\mathbf{I}$ (it is assumed that noise has a common variance amongst all sensors and is also uncorrelated amongst all sensors), the following can be defined

$$\mathbf{R} = \mathbf{A}\mathbf{P}\mathbf{A}^H + \sigma^2\mathbf{I} \tag{4.6}$$

Assuming that there is one vector, $\mathbf{z}$, that is orthogonal to the steering matrix, $\mathbf{A}$, such that $\mathbf{A}^H\mathbf{z} = 0$, then $\mathbf{Rz} = \sigma^2\mathbf{z}$, meaning that $\mathbf{z}$ is an eigenvector of $\mathbf{R}$ with corresponding eigenvalue σ^2 [7]. Since the steering matrix, **A**, is full rank with dimension $N \times P$, there are N - P linearly independent vectors of **z** that are perpendicular to **A**. Thus, any vector orthogonal to **A** is an eigenvector of **R** with eigenvalue σ^2. The spatial covariance matrix **R** can be eigendecomposed as

$$\mathbf{R} = \mathbf{E}\Lambda\mathbf{E}^H \tag{4.7}$$

where $\Lambda = \mathrm{diag}\{\lambda_1, \lambda_2, \ldots, \lambda_N\}$ is a diagonal matrix of the real eigenvalues ordered such that $\lambda_1 \geq \lambda_2 \geq \cdots \geq \lambda_N$. **E** is the unitary matrix.

Many DOA estimation techniques presented in this chapter rely on the eigendecomposition of the covariance matrix, **R**, which can be written as a sum of two parts, one part corresponding to the noise eigenvectors and a second part relating to the signal eigenvectors. This is given by

$$\mathbf{R} = \mathbf{E}_s\Lambda_s\mathbf{E}_s^H + \sigma^2\mathbf{E}_n\mathbf{E}_n^H \tag{4.8}$$

where $\mathbf{E}_s = [e_1, \ldots, e_P]$ denotes the signal eigenvectors corresponding to the eigenvalues $\lambda_1 \geq \cdots \geq \lambda_P > \sigma^2$, and $\Lambda_s = \mathrm{diag}\{\lambda_1, \lambda_2, \ldots, \lambda_P\}$ denotes the signal eigenvalues. $\mathbf{E}_n = [e_{P+1}, \ldots, e_n]$ denotes the noise eigenvectors corresponding to the remaining eigenvalues $\lambda_{M+1} = \cdots = \lambda_N = \sigma^2$ (i.e., $\Lambda_n = \mathrm{diag}\{\sigma^2, \sigma^2, \ldots, \sigma^2\}$). This decomposition is sometimes referred to as spectral factorisation, and is used extensively when dealing with subspace-based DOA estimation (discussed in the following sections) [2].

Since all the noise eigenvectors are orthogonal to **A**, the columns of $\mathbf{E}_s$ must span the range space of **A** whereas those of $\mathbf{E}_n$ must span its orthogonal complement called the nullspace of $\mathbf{A}^H$. Thus by exploiting this orthonormality of the eigenvectors

$$\mathbf{E}_s\mathbf{E}_s^H + \mathbf{E}_n\mathbf{E}_n^H = \mathbf{I} \tag{4.9}$$

Following on from this, the covariance matrix can be written as

$$\mathbf{R} = \mathbf{E}_s\left(\Lambda_s - \sigma^2\mathbf{I}\right)\mathbf{E}_s^H + \sigma^2\mathbf{I} = \mathbf{E}_s\tilde{\Lambda}_s\mathbf{E}_s^H + \sigma^2\mathbf{I} \tag{4.10}$$

Comparing equations (4.10) and (4.6), indicates that the subspace spanned by the columns of $\mathbf{E}_s$ must be equal to the subspace spanned by the columns of **AP**. The subspace spanned by $\mathbf{E}_s$ is usually called the signal subspace and the corresponding space spanned by $\mathbf{E}_n$ is therefore called the noise subspace [2]. These spaces are orthogonal due to the orthogonality of the eigenvectors.

Almost all the DOA estimation techniques discussed in the following section exploit the properties of the covariance matrix of the measured voltages. However, since the induced voltages, $\mathbf{x}(t)$, are measured (as a finite number of measurement snapshots, N_0) and not the covariance matrix; $\mathbf{R}$ must often be approximated by the ML estimate of the covariance matrix in equation (4.5), which is defined by

$$\hat{\mathbf{R}} = \frac{1}{N_0} \sum_{t=1}^{N_0} \mathbf{x}(t)\mathbf{x}^H(t) \tag{4.11}$$

where N_0 represents the total number of array measurement snapshots. A spectral representation similar to that of equation (4.8) could be given by

$$\hat{\mathbf{R}} = \hat{\mathbf{E}}_s \hat{\mathbf{\Lambda}}_s \hat{\mathbf{E}}_s^H + \sigma^2 \hat{\mathbf{E}}_n \hat{\mathbf{E}}_n^H \tag{4.12}$$

4.3 Spectral-Based Techniques

Spectral-based estimation techniques were the first to be developed and the least complicated to apply. In general, they rely on calculating a spatial spectrum, and finding the DOA's by the location of the peaks in the spectrum. The most widely used DOA estimation technique based on spectral-based methods is beamforming [8]. Using this method, the received energy is focused in one direction (or beam) at a time. This is defined as

$$\mathbf{y}(t) = \mathbf{w}^H \mathbf{x}(t) \tag{4.13}$$

where the weighting vector, $\mathbf{w}$, can be considered as a spatial filter that emphasises one particular direction. Given samples y(1), y(2), ..., y(N_0), the output power is measured by

$$P(\mathbf{w}) = \frac{1}{N_0} \sum_{t=1}^{N_0} |y(t)|^2 = \frac{1}{N_0} \sum_{t=1}^{N_0} \mathbf{w}^H \mathbf{x}(t)\mathbf{x}^H(t)\mathbf{w} = \mathbf{w}^H \hat{\mathbf{R}} \mathbf{w} \tag{4.14}$$

where $\hat{\mathbf{R}}$ is the estimated spatial covariance matrix given in the previous section. Different weighting vectors, $\mathbf{w}$, result in different properties of the beamforming schemes [9].

4.3.1 Bartlett Beamformer

Following on from equation (4.14), if the weighting vector is chosen to maximise the received power in a particular direction θ, then $\mathbf{w}$ is given by [8]

$$\mathbf{w}_{BF} = \frac{\mathbf{a}(\theta)}{\sqrt{\mathbf{a}^H(\theta)\mathbf{a}(\theta)}} \tag{4.15}$$

Inserting equation (4.15) into (4.14) gives the classic spatial spectrum, denoted by

$$P_{BF}(\theta) = \frac{\mathbf{a}^H(\theta)\hat{\mathbf{R}}\mathbf{a}(\theta)}{\mathbf{a}^H(\theta)\mathbf{a}(\theta)} \tag{4.16}$$

This spatial spectrum is often referred to as the conventional (or Bartlett) beamformer, since it is a natural extension of the classical Fourier method only with different window functions. If a ULA is used (with omnidirectional elements), then the above spatial spectrum is analogous to the classic periodogram in time series analysis [6]. As with the periodogram, the spatial spectrum in equation (4.16) has a resolution threshold. Using this method, waves arriving with electrical angle separation (given by $kd\cos\theta$) less than $2\pi/N$ cannot be resolved. This poor resolution capability led to other choices of weighting vectors, $\mathbf{w}$, which could result in lower resolution thresholds.

4.3.2 Capon Beamformer

In an attempt to alleviate some of the limitations of the conventional beamformer, in particular the poor resolution capability, a better technique was proposed by Capon. This well-known beamformer [2] attempts to minimise the power contributed by noise and any signals coming from directions other than the direction of interest (θ), while maintaining a fixed gain in the direction of interest. In the literature, Capon's beamformer is also referred to as Minimum Variance Distortionless Response (MVDR) filter, and its weighting vector is given by

$$\mathbf{w}_{CAP} = \frac{\hat{\mathbf{R}}^{-1}\mathbf{a}(\theta)}{\mathbf{a}^H(\theta)\hat{\mathbf{R}}^{-1}\mathbf{a}(\theta)} \tag{4.17}$$

Inserting equation (4.17) into (4.14) gives the MVDR spatial spectrum, denoted by

$$P_{CAP}(\theta)=\frac{1}{\mathbf{a}^H(\theta)\hat{\mathbf{R}}^{-1}\mathbf{a}(\theta)} \tag{4.18}$$

Although this method is more complex, it does give a significantly lower resolution threshold than the conventional beamformer. The lower resolution threshold is achieved at the cost of reduced noise suppression capability. This resolution threshold when assuming a perfect $\hat{\mathbf{R}}$ can be expressed as [6]

$$\Delta_{Capon}=8.71\left(\frac{1}{N^5\rho}\right)^{1/4} \tag{4.19}$$

where ρ denotes the SNR. This is obviously lower than the $2\pi/N$ resolution threshold given by classic beamforming. It must be noted that both of the beamforming techniques presented thus far require a 1-D search for the DOA estimates and are incapable of dealing with coherent signals, which are signals that are scaled and delayed versions of each other. Even though many other beamforming methods have been presented in the literature, the resolution threshold for beamforming methods in general is still relatively high. This was one of the motivations for developing the so-called subspace-based methods such as MUSIC (Multiple Signal Classification).

4.3.3 Multiple Signal Classification

As discussed previously, subspace-based methods rely on the observations regarding the eigendecomposition of the covariance matrix, $\hat{\mathbf{R}}$, into signal subspace and noise subspace, as in equation (4.12). The concept of subspace is fully described in [7]. One of the most important subspace-based methods is the MUSIC estimation technique, which is in essence based on the observation that the noise eigenvectors, $\mathbf{E}_n$, are perpendicular to the steering matrix, $\mathbf{A}$, or the signal subspace, $\mathbf{E}_s$ [1]. The MUSIC algorithm calculates the noise subspace by using the eigendecomposition of the estimated covariance matrix given in equation (4.12). It should be noted that the noise eigenvectors can also be found by taking the Singular Value Decomposition (SVD) of the data matrix. The estimates of the DOAs are then taken as those θ that give the lowest value of $\mathbf{a}^H(\theta)\hat{\mathbf{E}}_n$, i.e., the values that result in a steering vector farthest away from the noise subspace. This is often formed by finding the P largest peaks in the MUSIC spatial spectrum [10], defined by

$$P_{MU}(\theta) = \frac{1}{\mathbf{a}^H(\theta)\hat{\mathbf{E}}_n\hat{\mathbf{E}}_n^H\mathbf{a}(\theta)} \tag{4.20}$$

In general, the movement towards subspace methods was mainly motivated by the improvement in the resolution capability over that of the beamforming techniques. The formula for the resolution threshold of MUSIC is rather complex and depends on a number of parameters including the number of samples N_0, the number of antenna elements N, and the SNR. Whilst the MUSIC technique is an improvement over the beamforming methods, there are extensions of MUSIC, which perform better than the basic algorithm. One in particular is weighted MUSIC which takes into account a weighting factor $\mathbf{w}$ and gives a better resolution capability.

4.4 Parametric Techniques

As mentioned in the previous section, spectral-based methods are computationally attractive and easy to apply, however they do not always provide sufficient accuracy, especially in propagation environments with highly correlated (or even coherent) signals. Therefore an alternative is to employ parametric techniques, which estimate the DOAs without initially calculating a spatial spectrum. Parametric techniques yield a far better performance in terms of accuracy and resolution by fully exploiting the underlying data model, thus resulting in greater efficiency and robustness. However, this is at the cost of increased complexity and computations, since a multidimensional search for estimates is required. Because parametric techniques do not calculate a spectrum like function, parameters such as bandwidth and resolution threshold become less significant. Thus, in order to evaluate the performance of such techniques, two statistical properties of the DOA estimates are usually defined [2]. These two measures are consistency and statistical efficiency. Consistency is a measure of whether an estimate converges to the true value when the amount of data tends to infinity. Whilst, statistical efficiency is a measure of whether an estimate asymptotically attains the Cramér Rao bound (CRB), which is a lower bound on the covariance matrix of any unbiased estimator [1]. Since all methods presented in the following are consistent, the statistical efficiency is a more important parameter for performance evaluation.

In the following sections several important parametric estimation techniques are discussed, including ML, Root-MUSIC, ESPRIT and unitary-ESPRIT. Furthermore, the description of the ESPRIT and unitary ESPRIT algorithms is extended to UCAs.

4.4.1 Maximum Likelihood

The ML method is possibly the most well-known and frequently used model-based estimation technique in array signal processing. The technique presented here assumes a statistical structure for data generation and uses the model assumptions stated in section 4.2. In the literature, this method is usually referred to as Stochastic Maximum Likelihood (SML) and is obtained by modelling the signal waveforms as complex Gaussian processes [2]. By using the signal model in equation (4.1), and the previous assumptions, a negative log likelihood function to be minimised can be defined as

$$l_{SML}\left(\theta,\mathbf{P},\sigma^2\right)=\log|\mathbf{R}|+\mathrm{Tr}\left(\mathbf{R}^{-1}\hat{\mathbf{R}}\right) \tag{4.21}$$

where the expressions for $\mathbf{R}$ and $\hat{\mathbf{R}}$ were defined earlier in the chapter. For a fixed θ, the minimising values of $\mathbf{P}$ and σ^2 can be expressed as [6]

$$\hat{\sigma}^2_{SML}(\theta)=\frac{1}{N-P}\mathrm{Tr}(\mathbf{P}_A^{\perp}\hat{\mathbf{R}}) \tag{4.22}$$

$$\hat{\mathbf{P}}_{SML}(\theta)=\mathbf{A}^{\dagger}\left(\hat{\mathbf{R}}-\hat{\sigma}^2_{SML}(\theta)\mathbf{I}\right)\mathbf{A}^{\dagger H} \tag{4.23}$$

where $\mathbf{A}^{\dagger}$ denotes the Moore-Penrose Pseudoinverse of $\mathbf{A}$ (i.e., $\mathbf{A}^{\dagger}=(\mathbf{A}^H\mathbf{A})^{-1}\mathbf{A}^H$). Inserting equations (4.22) and (4.23) into (4.21), gives the concentrated negative log likelihood function, defined by

$$\hat{\theta}_{SML}=\arg\min_{\theta}\left(\log\left|\mathbf{A}\hat{\mathbf{P}}_{SML}(\theta)\mathbf{A}^H+\hat{\sigma}^2_{SML}(\theta)\mathbf{I}\right|\right) \tag{4.24}$$

Therefore, the DOA estimates are found by the minimising argument. Note that the SML method is statistically efficient, since the variance of the DOA estimates attains the CRB. The MUSIC method only attains the CRB if signals are uncorrelated and there are a large number of measurement snapshots with high SNR. It is mainly for this reason that the SML method is chosen over MUSIC. However, compared to MUSIC, the SML technique is more complicated since it requires a numerical search due to the complicated nature of equation (4.24). Therefore, less computationally intensive techniques such as subspace methods and in particular MUSIC are still used for DOA estimation even though they are not statistically efficient [2].

So far, two different ML techniques have appeared in the signal processing literature, both of which make different assumptions about the nature of the signals. The ML method presented here is described as SML, and it models the signals as being complex Gaussian (note that this method is still applicable even if data is not considered to be Gaussian). However, there is another method which models the signals as being deterministic. This alternative method leads to a non-linear least squares (LS) fit to the data model and is often referred to as Deterministic Maximum Likelihood (DML). This method, although similar to SML, does yield DOA estimates that usually have a higher variance [2]. It should be noted, however, that in almost all practical scenarios the difference in performance between SML and DML is negligible.

Another class of subspace methods, which have attracted a great deal of attention, are Subspace Fitting (SF) techniques. These methods are efficient and have properties that are very similar to SML, however with a lower computational burden. There are mainly two versions of subspace fittings, one based on Signal Subspace (SSF) and the other based on Noise Subspace (NSF) [2]. The SSF method is based on the observations that the signal eigenvectors are equal to a linear combination of the steering vectors, while the NSF method is based on the same observation as in MUSIC, namely, that the columns of **A** are orthogonal to the noise subspace.

4.4.2 Root-MUSIC

The MUSIC method can be applied to any antenna array. However if the antennas form a ULA, then an efficient and simplified technique can be used where the elements of the steering vector in equation (4.3) and the MUSIC spectrum in equation (4.20) can be defined as a polynomial with respect to z, where $z = e^{-jkd\cos\theta}$. This essentially removes the DOA search required in the MUSIC method. Instead, the DOA estimates are found by finding the $2(m\text{-}1)$ roots of the symmetrical polynomial defined by

$$f(z) = \mathbf{a}^T(z^{-1})\hat{\mathbf{E}}_n\hat{\mathbf{E}}_n^H a(z) \tag{4.25}$$

Therefore by employing this technique, the DOAs are determined by finding the P largest roots of the polynomial and solving $\arg\{z_i\}$ (refer to [1, 2]). There are various other estimation techniques, where the numerical search can be avoided by exploiting the structure of the array. One in particular is the Iterative Quadratic Maximum Likelihood (IQML) technique, which is an iterative procedure for minimising the DML criterion for a ULA [2].

4.4.3 ESPRIT

The ESPRIT method is another subspace-based technique, which relies on the type of array structure. Although in this section the emphasis is placed on ULAs, it must be noted that in general this method can be applied to any array that has a so-called shift structure, which only exists if the array can be divided into two identical arrays displaced by a known translation δ. In this case the DOAs are defined relative to the normal of this translation [6]. For this technique, no information concerning the two subarrays is required, other than that they should be identical. In general, this implies that the majority of problems with calibration may be avoided by using this technique. The output vectors of the two subarrays can be defined as

$$\mathbf{x}_1(t) = \mathbf{A}_1\mathbf{s}(t) + \mathbf{n}_1(t) \tag{4.26}$$

$$\mathbf{x}_2(t) = \mathbf{A}_2\mathbf{s}(t) + \mathbf{n}_2(t) \tag{4.27}$$

The configuration of each subarray can be described by a pair of selection matrices, $\mathbf{J}_1$ and $\mathbf{J}_2$, which merely select the corresponding elements of the snapshots for each array. Thus, by using these selection matrices, the whole output array can be described as

$$\begin{bmatrix}\mathbf{J}_1\\ \mathbf{J}_2\end{bmatrix}\mathbf{x}(t)=\begin{bmatrix}\mathbf{J}_1\\ \mathbf{J}_2\end{bmatrix}\mathbf{A}\mathbf{s}(t)+\mathbf{n}(t)=\mathbf{A}_s\mathbf{s}(t)+\mathbf{n}(t) \tag{4.28}$$

The ESPRIT method relies on the principle that the steering matrix of the two arrays be formed so that

$$\mathbf{A}_s=\begin{bmatrix}\mathbf{A}_1\\ \mathbf{A}_2\end{bmatrix}=\begin{bmatrix}\mathbf{A}_1\\ \mathbf{A}_1\mathbf{\Phi}\end{bmatrix} \tag{4.29}$$

where $\mathbf{A}_l$ is an $l \times P$ steering matrix and Φ is a $P \times P$ diagonal matrix with elements

$$[\mathbf{\Phi}]_{ii}=e^{-jk\delta\sin\theta_i} \tag{4.30}$$

Although not all arrays have this shift structure, a ULA or a UCA with an even number of elements can be divided into two identical subarrays. However, it should be noted that the application of the ESPRIT method for UCAs is somewhat more difficult. The ESPRIT method exploits the shift structure of the array and also the fact that the subspace spanned by the columns of $\mathbf{E}_s$ must equal those spanned by the columns of $\mathbf{A}$ (assuming that the signal covariance matrix is of full rank). Therefore, it can be stated that

$$\mathbf{E}_s=\mathbf{A}_s\mathbf{T} \tag{4.31}$$

where $\mathbf{T}$ is a unique non-singular matrix. The basic idea is therefore to find those θs that best fit the relation in equation (4.31). The signal subspace matrix $\mathbf{E}_s$ may be partitioned so that

$$\mathbf{E}_s=\begin{bmatrix}\mathbf{E}_{s1}\\ \mathbf{E}_{s2}\end{bmatrix}=\begin{bmatrix}\mathbf{E}_{s1}\\ \mathbf{E}_{s1}\mathbf{\Psi}\end{bmatrix} \tag{4.32}$$

where $\Psi = \mathbf{T}^{-1}\,\Phi\mathbf{T}$ (assuming $\mathbf{A}$ is full rank) [6]. Due to the relationship between Φ and Ψ, both matrices share the same eigenvalues, which are denoted by $e^{-jk\delta\sin\theta_i}$ for $i = 1, .., P$. Given an estimate $\hat{\mathbf{E}}_S$, the submatrices $\hat{\mathbf{E}}_{S1}$ and $\hat{\mathbf{E}}_{S2}$ do not exactly share the same range space, therefore an approximation of Ψ is found by the relationship

$$\hat{\mathbf{E}}_{s2}\approx\hat{\mathbf{E}}_{s1}\mathbf{\Psi} \tag{4.33}$$

Solving the above equation in a LS sense or a Total Least Square (TLS) sense gives the solution, although in general the TLS method is more natural [1]. The TLS ESPRIT estimates are obtained through the eigendecomposition of the partitioned eigenvectors $\hat{\mathbf{E}}_{s1}$ and $\hat{\mathbf{E}}_{s2}$, that is

$$\begin{bmatrix} \hat{\mathbf{E}}_{s1}^{H} \\ \hat{\mathbf{E}}_{s2}^{H} \end{bmatrix} \begin{bmatrix} \hat{\mathbf{E}}_{s1} & \hat{\mathbf{E}}_{s2} \end{bmatrix} = \begin{bmatrix} V_{11} & V_{12} \\ V_{21} & V_{22} \end{bmatrix} \mathbf{L} \begin{bmatrix} V_{11}^{H} & V_{12}^{H} \\ V_{21}^{H} & V_{22}^{H} \end{bmatrix} \tag{4.34}$$

Where $\mathbf{L}$ is a diagonal matrix given by eigendecomposition. Solving equation (4.33) by the TLS method yields

$$\hat{\mathbf{\Psi}}_{TLS} = -V_{12}V_{22}^{-1} \tag{4.35}$$

Thus, the i^{th} DOA estimate is given by

$$\hat{\theta}_i = \sin^{-1}\left[\frac{\arg(\lambda_i)}{2\pi\delta}\right] \tag{4.36}$$

where λ_i is the i^{th} eigenvalue of the solution matrix in equation (4.35). The ESPRIT algorithm can be summarised as follows:

1. Compute the eigendecomposition of the array covariance matrix $\hat{\mathbf{R}}$ (or compute the SVD of the complete array data matrix $\mathbf{X} \in \mathbf{C}^{N \times N_0}$)
2. Form $\hat{\mathbf{E}}_{s1}$ and $\hat{\mathbf{E}}_{s2}$ from the N principle eigenvectors (i.e., split the signal subspace into two subspaces corresponding to $\mathbf{J}_1$ and $\mathbf{J}_2$).
3. Solve the relation $\hat{\mathbf{E}}_{s2} \approx \hat{\mathbf{E}}_{s1}\mathbf{\Psi}$, in either a LS sense or a TLS sense.
4. Obtain the DOA estimates by computing the eigenvalues of $\mathbf{\Psi}$ and substituting then into equation (4.36).

The main advantage of the ESPRIT method is that it offers high accuracy at a small computational cost, since no numerical search is required and the final solution is in closed form. In order to apply the ESPRIT algorithm, the two subarrays are required to be identical and due to practical constrains, the ESPRIT method is prone to more estimation errors than ML and SF, which inherently exploit the full antenna model and not just the translation. In the literature, there are several possible strategies for forming the two subarrays, especially in the case of ULAs, where a maximum overlapping structure is common, i.e. the first *N*-1 elements overlap with the last *N*-1 elements [1].

Various research studies have been carried out to improve on the performance of ESPRIT by applying row weighting and/or Forward-Backward (FB) averaging, as well as spatial smoothing for coherent environments. In particular, Unitary-ESPRIT [11] has been proposed as an intelligent way of incorporating FB averaging in order to reduce complexity and improve the estimation efficiency. While the ESPRIT method is not exclusively for ULAs, most of the research studies have focussed on linear array geometries. However, in order to achieve a 360° estimation of DOAs, it is common to employ UCAs. This introduces new difficulties in applying the ESPRIT algorithm. The procedure given in [12], presents a technique for using the ESPRIT method for UCAs by transforming the element space manifold into a beam space manifold via the phase mode excitation of the array. Similar efforts have been made in order to apply the MUSIC technique to UCAs. As in the case of many algorithms, the ESPRIT method can be applied for 2-D angle estimation to find both azimuth and elevation angles of arrival [1, 12].

4.4.4 Unitary-ESPRIT

The Unitary-ESPRIT method [11] was proposed in order to reduce the computational complexity apparent in the ESPRIT algorithm. It was also proposed based on the notion that it would improve the estimation accuracy. The main feature of this algorithm is that it employs FB averaging, which is simply a technique that is applied for handling coherent signals. In basic terms, FB averaging manipulates the array covariance matrix, **R**, to get

$$\mathbf{R}_{FB} = \frac{1}{2}\left(\mathbf{R} + \mathbf{\Pi}\mathbf{R}^{*}\mathbf{\Pi}\right) = \mathbf{A}\tilde{\mathbf{P}}\mathbf{A}^{H} + \sigma^{2}\mathbf{I} \qquad (4.37)$$

where $\mathbf{\Pi}$ is an exchange matrix with ones in its anti-diagonal and zeros elsewhere.

In essence, the Unitary-ESPRIT algorithm transforms the input data matrix $\mathbf{X} \in \mathbf{C}^{N \times N_0}$ into a real-valued representation so that all computations are real-valued. This transformation $T(\cdot)$ is applicable to any centro-symmetric antenna configuration (where the antenna elements are symmetric with respect to the centroid), and by this transformation, **X** becomes centro-hermitian. With the help of the so-called left Π-real transformation matrices, **Q**, the real-valued data matrix can be written as

$$T(\mathbf{X}) = \mathbf{Q}_N^H \left[\mathbf{X} \quad \mathbf{\Pi}_N \mathbf{X}^* \mathbf{\Pi}_{N_0} \right] \mathbf{Q}_{2N_0} \tag{4.38}$$

where $T(\mathbf{X}) \in \mathbf{R}^{N \times 2N_0}$ and $\mathbf{\Pi}_N$ is an $N \times N$ ($\mathbf{\Pi}_{N_0}$ is an $N_0 \times N_0$) exchange matrix with ones in its anti-diagonal and zeros elsewhere. Also

$$\mathbf{Q}_{2n} = \frac{1}{\sqrt{2}} \begin{bmatrix} \mathbf{I}_n & j\mathbf{I}_n \\ \mathbf{\Pi}_n & -j\mathbf{\Pi}_n \end{bmatrix} \tag{4.39}$$

and

$$\mathbf{Q}_{2n+1} = \frac{1}{\sqrt{2}} \begin{bmatrix} \mathbf{I}_n & 0 & j\mathbf{I}_n \\ 0 & \sqrt{2} & 0 \\ \mathbf{\Pi}_n & 0 & -j\mathbf{\Pi}_n \end{bmatrix} \tag{4.40}$$

are unitary matrices and $\mathbf{I}_n$ is an $n \times n$ identity matrix. Furthermore, the incorporated FB averaging used here effectively doubles the number of columns in equation (4.38), thus improving the resolution capability. As a result, coherent signals or very highly correlated signals can be resolved. In a similar way to the standard ESPRIT method, the real-valued signal subspace can be computed via an eigendecomposition of the real-valued covariance matrix estimate [13]. Therefore, $\mathbf{E}_s \in \mathbf{R}^{N \times P}$ denotes the P principle eigenvectors of

$$T(\mathbf{X})T(\mathbf{X})^H \in \mathbf{R}^{N \times N} \tag{4.41}$$

The Unitary-ESPRIT algorithm provides a solution for the real-valued representation of the invariance equation, given by

$$\mathbf{K}_1 \mathbf{E}_s \mathbf{Y} \approx \mathbf{K}_2 \mathbf{E}_s \tag{4.42}$$

This must be solved in a LS sense or a TLS sense [13]. $\mathbf{K}_1$ and $\mathbf{K}_2$ are selection matrices, which are analogous to matrices $\mathbf{J}_1$ and $\mathbf{J}_2$ for the standard ESPRIT method. The two selection matrices defined for the standard ESPRIT algorithm are chosen in this case to be centro-symetric with respect to each other, so that $\mathbf{J}_2 = \Pi\,\mathbf{J}_1\,\Pi$. Hence, $\mathbf{K}_1$ and $\mathbf{K}_2$ can be defined as

$$\mathbf{K}_1 = \mathbf{Q}_n^H\left(\mathbf{J}_1 + \mathbf{J}_2\right)\mathbf{Q}_N = \mathbf{Q}_n^H\left(\mathbf{J}_1 + \mathbf{\Pi}_n\mathbf{J}_1\mathbf{\Pi}_N\right)\mathbf{Q}_N \tag{4.43}$$

$$\mathbf{K}_2 = \mathbf{Q}_n^H\left(\mathbf{J}_1 - \mathbf{J}_2\right)\mathbf{Q}_N = \mathbf{Q}_n^H\left(\mathbf{J}_1 - \mathbf{\Pi}_n\mathbf{J}_1\mathbf{\Pi}_N\right)\mathbf{Q}_N \tag{4.44}$$

The eigendecomposition of the observed real-valued matrix, $\mathbf{Y}$, can therefore be defined as

$$\mathbf{Y} = \mathbf{T}\mathbf{\Omega}\mathbf{T}^{-1} \in \mathbf{R}^{P\times P} \tag{4.45}$$

where Ω is the $P \times P$ diagonal matrix of the eigenvalues, given by

$$\Omega = \text{diag}\left\{\omega_i\right\}_{i=1}^{P} \tag{4.46}$$

The estimated DOAs can be obtained by

$$\hat{\theta}_i = \sin^{-1}\left[\frac{2\tan^{-1}(\omega_i)}{2\pi\delta}\right] \tag{4.47}$$

Because of the relation between $\mathbf{Y}$ and Ω (defined in equation (4.45)), the DOAs can be computed in a straightforward manner by computing the eigenvalues of $\mathbf{Y}$. The Unitary-ESPRIT algorithm can be summarised as follows:

1. Compute the eigendecomposition of the matrix $T(\mathbf{X})T(\mathbf{X})^H$ (or compute the SVD of the complete array data matrix $T(\mathbf{X}) \in \mathbf{R}^{N\times 2N_0}$), and estimate $\mathbf{E}_s$.
2. Solve the relation $\mathbf{K}_1\mathbf{E}_s\mathbf{Y} \approx \mathbf{K}_2\mathbf{E}_s$, in either a LS sense or a TLS sense.
3. Obtain the DOA estimates by computing the eigenvalues of $\mathbf{Y}$ and substituting them into equation (4.47).

It should be noted that both ESPRIT and Unitary-ESPRIT methods presented so far have been based on 1-D estimation. However, there are multi-dimensional methods that can for example offer 2-D estimation of the DOAs. In the following section, both techniques are practically applied to UCAs.

4.4.5 CUBA-ESPRIT

So far, the ESPRIT and Unitary-ESPRIT methods have been discussed with respect to ULAs, which in principle have a maximum coverage range of 180°. However, as noted previously, UCAs have to be employed if full 360° area coverage is required for the impinging array signals. Here, a very effective method is described based on the CUBA (Circular Uniform Beam Array) [14], where it is assumed that the circular array is composed of uniform multi-beam antennas (sectorised antennas). The idealised antenna pattern for a CUBA is illustrated in figure 4.2

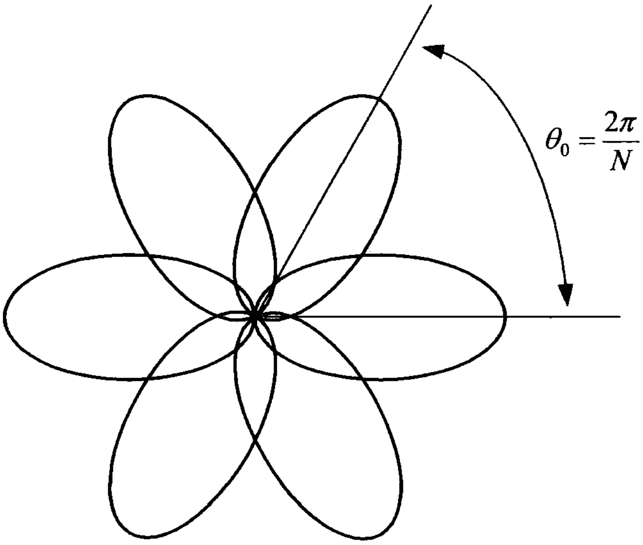

Figure 4.2: Illustration of the beam patterns for a 6-element CUBA.

A CUBA consists of N antennas with circular symmetric beam patterns $b_0(\theta)$, where the main directions of two adjacent elements are rotated by $\theta_0 = 2\pi/N$. It must be noted that CUBA configurations can be formed in a variety of different ways, including a bi-conical multi-beam array which has a zero phase reference, an array of microstrip patch antenna elements, or even an array of horn antennas. The antenna array designs are described in texts such as [15-18].

In the following, a method is described for applying the ESPRIT algorithm to CUBAs, with the capability to handle coherent sources. Given a narrowband signal impinging on a CUBA with angle θ_p, the output signals of the N array elements can be described by means of a sampled beam pattern, given by [14].

$$b_p(n\theta_0) = \gamma_p b_0(n\theta_0 - \theta_p) \tag{4.48}$$

where $\theta_0 = 2\pi/N$ and $n = 0, \ldots, (N\text{-}1)$. γ_p denotes the complex path weights.

Since the beam patterns of the antenna elements are periodic with respect to 2π, a DFT (discrete Fourier transform) can be used to transform this beamspace into a so-called virtual aperture space, which also holds the shift invariance property. The virtual aperture space (or function) corresponding to equation (4.48) is given by

$$g_0\left(\frac{l}{2\pi}\right) = \sum_{n=0}^{N-1} b_0(n\theta_0) e^{-j2\pi\frac{nl}{N}} \tag{4.49}$$

where $l = 0, \ldots, (L\text{-}1)$. The aperture space dimension L is defined as the number of DFT bins for which the virtual aperture has a finite support on (if $N \geq L$). This can be defined as

$$g_0(m) = \begin{cases} \neq 0 & \text{if } |m| \leq \dfrac{L-1}{2} \\ = 0 & \text{if } |m| > \dfrac{L-1}{2} \end{cases} \tag{4.50}$$

consequently, in the virtual aperture domain the signal source response with respect to equation (4.49) is given by

$$g_p\left(\frac{l}{2\pi}\right) = \gamma_0 g_0\left(\frac{l}{2\pi}\right) e^{-jl\theta_p} \tag{4.51}$$

and for P sources with complex weights, γ_p, the virtual aperture function of the array output can be described by [14]

$$g\left(\frac{l}{2\pi}\right) = g_0\left(\frac{l}{2\pi}\right) \sum_{p=1}^{P} \gamma_p e^{-jl\theta_p} \tag{4.52}$$

Equation (4.52) represents the virtual aperture vector of the whole array and in matrix format, this is defined as

$$\mathbf{g} = \mathbf{G}_0 \mathbf{A} \boldsymbol{\gamma} \tag{4.53}$$

where $\mathbf{G}_0 = \text{diag}\{g_0(0), \ldots, g_0((N\text{-}1)/2\pi)\}$ is a diagonal matrix containing virtual aperture functions. $\mathbf{A} = [\mathbf{a}(\theta_1), \ldots, \mathbf{a}(\theta_P)]$ is the steering matrix that is composed of the complex exponential vectors relating to P source directions, which are defined by $\mathbf{a}(\theta_p) = [1, \exp(-j\theta_p), ..., \exp(-j\theta_p(N-1))]^T$. γ is a vector containing the complex path weights. Since the array output signal is given by samples of the beam patterns, $b_0(n\theta_0)$, the Nyquist sampling criterion has to be considered. i.e., the virtual aperture function contains the required rotational invariance structure only if the Fourier transform of $b_0(\theta)$ has finite support in $L/2\pi$ and if $N \geq L$.

The virtual output aperture vector is calculated from the DFT of the received data $\mathbf{b} = \mathbf{B}\gamma$, where $\mathbf{B} = [\mathbf{b}(\theta_1), ..., \mathbf{b}(\theta_P)]$ is the matrix that contains the P beam vectors $\mathbf{b}(\theta_p) = [b_p(0), ..., b_p((N-1)\theta_0)]^T$. A transformation matrix, $\mathbf{T}$, is used in order to transform the measurement snapshot, $\mathbf{b}$, into an aperture snapshot, $\mathbf{x}$. This is defined as

$$\mathbf{x} = \mathbf{T}\mathbf{b} \tag{4.54}$$

where $\mathbf{T}$ is defined by [14]

$$\mathbf{T} = \left(\mathbf{J}\mathbf{G}_0\mathbf{J}^T\right)^{-1}\mathbf{J}\mathbf{F} \tag{4.55}$$

Here $\mathbf{F}$ is the $N \times N$ DFT matrix and $\mathbf{J}$ is a $L \times N$ selection matrix which chooses only the useful part of $g_0(l/2\pi)$ and is defined as

$$\mathbf{J} = \begin{bmatrix} 0 & 1 & 0 & \cdots & 0 \\ \vdots & \ddots & \ddots & \ddots & \vdots \\ 0 & \cdots & 0 & 1 & 0 \end{bmatrix}^{L \times N} \tag{4.56}$$

The transformation matrix defined in equation (4.55) is a theoretical model and in practice this matrix must be estimated based on array measurements made in an anechoic chamber. Every antenna array is characterised by non-uniform beam patterns, unknown phase factors, inter-element coupling, etc. It is for this reason that array calibration is achieved through the use of $\mathbf{T}$, which transforms the array data. The CUBA calibration method is described in [14, 19]. The array error matrix may be formed by a calibration procedure described in [20]. However, for CUBA ESPRIT the explicit knowledge of the array error matrix is not necessary. The CUBA calibration procedure is not discussed further in this thesis.

With the measures described, the modified virtual aperture space, $\mathbf{x}$, shows the required rotational invariance structure. For both CUBA ESPRIT and CUBA

Unitary-ESPRIT (which can also be applied), the signal subspace can be derived from $\mathbf{x}$ in the same way as described earlier for the standard techniques. Let $\mathbf{x}_k$ denote the part of $\mathbf{x}$ beginning with element k and a length S, given by

$$\mathbf{x}_k = [x_k, x_{k+1}, \ldots, x_{k+(s-1)}]^T \tag{4.57}$$

Then, by using forward smoothing [1], the data matrix $\mathbf{X}_S^f$ can be defined as

$$\mathbf{X}_S^f = [\mathbf{x}_1, \mathbf{x}_2, \ldots, \mathbf{x}_M]^T \tag{4.58}$$

where $M = L - S + 1$. With the reflection matrix (or exchange matrix) $\mathbf{\Pi}$, the data matrix, $\mathbf{X}_S^b = \mathbf{\Pi}\mathbf{X}_S^{f*}$, is defined using backward smoothing. Combining both matrices gives the full data matrix $\mathbf{X}_S$, which can be defined as

$$\mathbf{X}_S = \begin{bmatrix} \mathbf{X}_S^f & \mathbf{X}_S^b \end{bmatrix} = \begin{bmatrix} \mathbf{X}_S^f & \mathbf{\Pi}\mathbf{X}_S^{f*} \end{bmatrix} \tag{4.59}$$

Subsequently, the signal subspace, $\mathbf{E}_S$, can be estimated by taking the SVD of the data matrix, $\mathbf{X}_S$, corresponding to the P left singular vectors of $\mathbf{X}_S$ that belong to the P largest eigenvalues. This is expressed as

$$\mathbf{X}_s = \begin{bmatrix} \mathbf{E}_s & \mathbf{E}_n \end{bmatrix} \begin{bmatrix} \mathbf{\Sigma}_s & 0 \\ 0 & \mathbf{\Sigma}_n \end{bmatrix} \begin{bmatrix} \mathbf{K}_s^H \\ \mathbf{K}_n^H \end{bmatrix} \tag{4.60}$$

Using the selection matrices $\mathbf{J}_1$ and $\mathbf{J}_2$ (corresponding to maximum overlap), the invariance equation is defined as

$$\mathbf{J}_1\mathbf{E}_s\mathbf{\Psi} = \mathbf{J}_2\mathbf{E}_s \Rightarrow \mathbf{E}_{s1}\mathbf{\Psi} = \mathbf{E}_{s2} \tag{4.61}$$

Obviously, this is the same as the invariance equation for standard ESPRIT, defined in equation (4.33). Thus, solving for the eigenvalues of Ψ, gives the DOA estimates. The CUBA ESPRIT algorithm is summarised as follows:

1. Estimate the transformation matrix, $\hat{\mathbf{T}}$, using antenna measurement data and the CUBA calibration method [14, 19].

2. Transform the received array snapshot, **b**, using $\mathbf{x}=\hat{\mathbf{T}}\mathbf{b}$.
3. Form the full data matrix, $\mathbf{X}_S$, from the aperture snapshot **x**. Estimate the signal subspace, $\mathbf{E}_S$, via the SVD of $\mathbf{X}_S$.
4. Solve $(\mathbf{J}_1\mathbf{E}_s)\mathbf{\Psi}=(\mathbf{J}_2\mathbf{E}_s)$ by either a LS or a TLS method.
5. Obtain the DOA estimates by computing the eigenvalues of $\mathbf{\Psi}$ (same as standard ESPRIT).

Since **A** is conjugate centro-symmetric, Unitary-ESPRIT is preferable for a computationally effective implementation. For CUBA Unitary-ESPRIT, the data matrix used is not FB averaged, since Unitary-ESPRIT inherently does this. Thus, only the forward matrix is used, so that

$$T(\mathbf{X}_S^f)=\mathbf{Q}_S^H\left[\mathbf{X}_S^f \quad \mathbf{\Pi}_S\mathbf{X}_S^{f*}\mathbf{\Pi}_M\right]\mathbf{Q}_{2M} \tag{4.62}$$

Similar to the standard Unitary-ESPRIT method, the CUBA Unitary-ESPRIT algorithm can be summarised as follows:

1. Estimate the transformation matrix, $\hat{\mathbf{T}}$, using antenna measurement data and the CUBA calibration method.
2. Transform the received array snapshot, **b**, using $\mathbf{x}=\hat{\mathbf{T}}\mathbf{b}$.
3. Form the data matrix, $T(\mathbf{X}_S^f)$, from the aperture snapshot **x**. Estimate the signal subspace, $\mathbf{E}_S$, via the SVD of $T(\mathbf{X}_S^f)$.
4. Solve $\mathbf{K}_1\mathbf{E}_s\mathbf{Y}=\mathbf{K}_2\mathbf{E}_s$ by either a LS or a TLS method.
5. Obtain the DOA estimates by computing the eigenvalues of **Y**. If some of the eigenvalues appear in complex conjugate pairs, then the algorithm must be restarted.
6. The DOA estimates are then obtained by computing the eigenvalues of **Y** (through linear transformation).

It is important to note that the number of resolvable paths for both algorithms is restricted to the aperture dimension, L, and not the number of antenna elements, N. For a given L, the maximum number of resolvable coherent sources is $2L/3$, and the number of resolvable incoherent signal sources is $L-1$. Also it must be noted that if the antenna array does not have a zero phase centre, the beam pattern for every element must be projected to a zero centre through the use of antenna measurements.

A preliminary ESPRIT and Unitary-ESPRIT algorithm have been developed in MATLAB based on the original CUBA ESPRIT method described in [14] (see accompanying CD-ROM). A full validation program for the CUBA ESPRIT method is documented in [19], with a calibration program and other test programs. Although the ESPRIT techniques are useful, for reasons given in the next section, the SAGE or SAGE-type algorithms are preferred.

4.5 Joint-Parametric Techniques

The knowledge of DOA does reveal key spatial channel characteristics, however other properties such as time of arrival (TOA or path delay) and Doppler frequency are also important. It is extremely valuable for channel characterisation, if both spatial and temporal parameters could be simultaneously deduced without the application of different algorithms. So far, there have been various multi-parameter estimation techniques presented in the literature. Here, only two approaches are presented. The first is an algorithm based on the ML approach and the second is an algorithm which could be used in conjunction with ML, MUSIC, or ESPRIT.

4.5.1 SAGE

The SAGE algorithm [21] is in essence based on the maximisation of the ML function for scenarios of unknown parameters DOA and TOA, using the expectation-maximisation principle. The method presented here includes joint delay, Doppler and azimuth DOA estimation. In order to discuss the SAGE technique, an appropriate multi-parameter signal model must first be defined. This can be formulated as

$$\mathbf{x}(t) = \sum_{k=1}^{P} \mathbf{s}(t;\boldsymbol{\theta}_k) + \mathbf{n}(t) \tag{4.63}$$

where

$$\mathbf{s}(t;\boldsymbol{\theta}_k) = \rho_k \mathbf{a}(\theta_k) e^{j2\pi\nu_k t} u(t-\tau_k) \tag{4.64}$$

Here, $\mathbf{x}(t)$ is the received signal vector at the output of the array and $\mathbf{s}(t;\theta_k)$ denotes the received signal from the k^{th} wave when the signal $u(t)$ is transmitted. Each wave is defined by its complex amplitude, ρ_k, time delay, τ_k, azimuth DOA, θ_k, and Doppler frequency, ν_k. The transmitted signal $u(t)$ is often represented as a train of pulses modulated by a Pseudo Noise (PN) sequence [22]. The measured voltages, $\mathbf{x}(t)$, the steering vector, $\mathbf{a}(\theta)$, and the noise vector, $\mathbf{n}(t)$, are defined as before. The unknowns associated with each path are now $\boldsymbol{\theta}_k = [\tau_k, \theta_k, \nu_k, \rho_k]$, thus the unknowns associated with all paths may be organised in a matrix formulated as $\boldsymbol{\theta} = [\boldsymbol{\theta}_1, \boldsymbol{\theta}_2, ..., \boldsymbol{\theta}_p]$. Thus, the parameters of interest are defined by maximisation of the log likelihood function, $l_{\text{SAGE}}(\theta)$, given by

$$\hat{\boldsymbol{\theta}} = \arg\max_{\boldsymbol{\theta}} l_{SAGE}(\boldsymbol{\theta}) \tag{4.65}$$

It turns out that the maximisation problem stated in equation (4.65) becomes very computationally expensive because there is no closed form solution and the parameter matrix θ is typically of high dimension [6]. By applying the SAGE algorithm, this multi parameter optimisation procedure can be reduced to a one-dimensional problem. The SAGE method solves the maximisation problem iteratively by solving for each path separately and iterating to get the optimal solution. In essence, the idea behind the SAGE method is to first estimate the contribution of each path $\mathbf{x}_k(t)$ to the measured signal $\mathbf{x}(t)$, and then perform the maximisation for each path individually to obtain estimates of the parameters $\hat{\boldsymbol{\theta}}_k$. Subsequently, these parameter estimates are updated, based on which the maximisation is performed again [6]. The iterative procedure is continued until a suitable convergence condition is satisfied. This procedure yields very accurate results and the SAGE technique itself does not rely on a particular array or system configuration. The SAGE algorithm can be described by using the model in equation (4.63), therefore

Expectation step:

$$\hat{\mathbf{x}}_k(t;\hat{\boldsymbol{\theta}}) = \mathbf{x}(t) - \sum_{k'=1,k'\neq k}^{P} \mathbf{s}(t;\hat{\boldsymbol{\theta}}_{k'}) \tag{4.66}$$

Maximisation steps:

$$\hat{\tau}_k' = \arg\max_{\tau_k} \left| Z_k\left(\tau_k, \hat{\theta}_k, \hat{\nu}_k\right) \right| \tag{4.67a}$$

$$\downarrow$$

$$\hat{\theta}_k' = \arg\max_{\theta_k} \left| Z_k\left(\hat{\tau}_k', \hat{\theta}_k, \hat{\nu}_k\right) \right| \tag{4.67b}$$

$$\downarrow$$

$$\hat{\nu}_k' = \arg\max_{\nu_k} \left| Z_k\left(\hat{\tau}_k', \hat{\theta}_k', \nu_k\right) \right| \tag{4.67c}$$

$$\downarrow$$

$$\hat{\rho}_k' = \frac{Z_k\left(\hat{\tau}_k', \hat{\theta}_k', \hat{\nu}_k'\right)}{\left\| \mathbf{a}\left(\hat{\theta}_k'\right) \right\|^2 \cdot E} \tag{4.67d}$$

where

$$Z_k\left(\tau_k, \theta_k, \nu_k\right) = \sum_t u^*(t-\tau_k) e^{-j2\pi\nu_k t} \mathbf{a}^H(\theta_k) \hat{\mathbf{x}}_k(t; \hat{\mathbf{\theta}}) \tag{4.68}$$

In equation (4.67d), E is the energy of the transmitted signal $u(t)$. The delay estimate of path k is found by obtaining the time correlation peak between the transmitted signal, $u(t)$, and the delayed (for each path) signal, $\mathbf{x}_k(t)$. The Doppler is obtained by the Doppler correlation, and the azimuth DOA is determined by a beamforming technique. It must be noted, however, that the iterative steps of the SAGE algorithm require an initial data 'pool' θ and the number of impinging signals p. In [22], the successful implementation of the SAGE method is described in detail. A version of the SAGE method was developed in MATLAB (see accompanying CD-ROM). Where, a peak-search program was used before running the first iterations. Further explanation of these methods and their innate limits are given in chapter 7.

4.5.2 JADE

Another important joint estimation technique is the JADE (Joint Angle-Delay Estimation) algorithm [23]. This method is based on fitting a parametric model of the channel to an unstructured estimate of the channel. If the signal is known at the transmitter, then this estimate can be obtained via an LS approach. However, if the transmitted signal is unknown, a blind channel estimation technique could be applied to obtain an estimate of the channel matrix **H**. The structured channel model is given by

$$\mathbf{H}=\sum_{k=1}^{p}\mathbf{a}(\theta_k)\rho_k\mathbf{g}^T(\tau_k) \tag{4.69}$$

where as before, $\mathbf{a}(\theta_k)$ denotes the steering vector and ρ_k is the path gain. The vector $\mathbf{g}(\tau_k)$ represents the $L \times 1$ sampled transmitted waveform delayed by τ_k [24], and L represents the length of the channel. If the response for a single wave arriving at angle, θ_k, and delay, τ_k, is given by

$$\mathbf{u}(\theta_k,\tau_k)=\mathbf{g}(\tau_k)\otimes\mathbf{a}(\theta_k) \tag{4.70}$$

then the channel relation can be defined as

$$\mathbf{x}(t)=\mathbf{U}(\theta,\tau)\rho(t) \tag{4.71}$$

where $\mathbf{x}(t)$ is the vectorised channel matrix, $\mathbf{\rho}=[\rho_1,\ldots,\rho_p]^T$, and $\mathbf{U}(\theta,\tau)=[\mathbf{u}(\theta_1,\tau_1),\ldots,\mathbf{u}(\theta_p,\tau_p)]$ is the full space-time matrix. By sampling at N_0 instants, the model for the unstructured estimate of the channel matrix could be given by

$$\hat{\mathbf{X}}=\mathbf{U}(\theta,\tau)\mathbf{P}+\mathbf{N} \tag{4.72}$$

where $\hat{\mathbf{X}}$ is $NL \times N_0$ (N denotes the number of antenna elements), $\mathbf{P}=[\rho(1),\ldots,\rho(N_0)]^T$ is $p \times N_0$ and **N**, which is of dimension $NL \times N_0$, represents the error in the channel estimate, $\hat{\mathbf{X}}$. Because of the structure of equation (4.72), many classical array processing techniques can be applied to find the aforementioned parameters. If the noise is AWGN, the ML estimate reduces to a non-linear LS type fit, given by [23]

$$\left\{\hat{\theta},\hat{\tau}\right\}=\arg\min_{\boldsymbol{\theta},\boldsymbol{\tau},\mathbf{P}}\left\|\hat{\mathbf{X}}-\mathbf{U}(\boldsymbol{\theta},\boldsymbol{\tau})\mathbf{P}\right\|_F^2 \tag{4.73}$$

This minimisation is carried out in a similar way as the DML method [6]. There are other versions of JADE based on MUSIC and ESPRIT solutions [23].

4.6 Summary and Conclusions

This chapter presented a basic introduction to DOA estimation techniques for mobile radio environments. First, a classic array data model was presented with a description of spectral-based methods for DOA estimation. The poor performance capability (accuracy and efficiency) of spectral based techniques were discussed with the motivation behind parametric techniques. In particular, ESPRIT-type algorithms were described for both ULAs and UCAs (e.g. CUBA ESPRIT). It was noted that most of these techniques were applicable only to azimuth DOA estimation, even though multidimensional extended versions of these algorithms were presented in the literature. Finally joint parameter estimation techniques were presented, focusing in particular on the SAGE technique, which is primarily used as a DOA estimator in chapter 7 due to its flexibility in a wide range of system configurations.

It should be noted that due to the sheer volume of publications in array signal processing, only a few major DOA estimation techniques were presented in this chapter. A thorough description of antenna array signal processing is given in the definitive texts, including [1, 2, 4-6].

4.7 References

1. H. L. Van Trees, *Detection, Estimation, and Modulation Theory: Detection and Estimation Theory: Optimum Array Processing*: John Wiley & Sons Ltd, 2002.
2. H. Krim, M. Viberg, "Two Decades of Array Signal Processing Research: The Parametric Approach," *IEEE Signal Processing Magazine*, vol. 13, pp. 67-94, 1996.
3. W. H. Kummer, "Basic Array Theory," *Proceedings of The IEEE*, vol. 80, pp. 127-139, 1992.
4. P. S. Naidu, *Sensor Array Signal Processing*: CRC Press, 2000.
5. S. Haykin, Ed., *Array Signal Processing*: Prentice Hall Inc, 1985.
6. L. C. Godara, Ed., *Handbook of Antennas in Wireless Communications*: CRC Press, 2002.
7. G. Strang, *Linear Algebra and Its Applications*, 3 ed: Thomson Learning Inc, 1988.

8. B. D. Van Veen, K. M. Buckley, "Beamforming: A Versatile Approach to Spatial Filtering," *IEEE Signal Processing Magazine*, pp. 4-24, Apr. 1988.
9. M. I. Skolnik, *Introduction to Radar Systems*, 3 ed: McGraw Hill, 2000.
10. J. C. Liberti, T. S. Rappaport, *Smart Antennas For Wireless Communications: IS-95 and Third Generation CDMA Applications*: Prentice Hall PTR, 1999.
11. M. Haardt, J. A. Nossek, "Unitary ESPRIT: How to Obtain Increased Estimation Accuracy with a Reduced Computational Burden," *IEEE Transactions on Signal Processing*, vol. 43, pp. 1232-1242, 1995.
12. H. Minghao, Y. Yixin, Z. Xianda, "UCA-ESPRIT Algorithm for 2-D Angle Estimation," 5th International Conference on Signal Processing, Beijing, China, 2000.
13. P. Satayarak, P. Rawiwan, P. Supanakoon, M. Chamchoy, S. Promwong, P. Tangtisanon, "The Achievable Performance of Unitary-ESPRIT Algorithm for DOA Estimation," International Technical Conference On Circuits/Systems, Computers and Communications, Phuket, Thailand, 2002.
14. A. Richter, R. S. Thomä, "CUBA-ESPRIT for Angle Estimation with Circular Uniform Beam Arrays," Millennium Conference on Antennas & Propagation, Davos, Switzerland, 2000.
15. R. J. Mailloux, *Phased Array Antenna Handbook*: Artech House Inc, 1994.
16. A. W. Rudge, K. Milne, A. D. Olver, P. Knight, *The Handbook of Antenna Design (IEE Electromagnetic Waves Series)*, vols. 1-2, 2 ed. London: Peter Peregrinus Ltd., 1986.
17. C. A. Balanis, *Antenna Theory: Analysis and Design*, 3 ed. Chichester: John Wiley & Sons Ltd., 2005.
18. J. D. Kraus, R. J. Marhefka, *Antennas*, 3 ed: McGraw-Hill Publishing, 2001.
19. K. Stavros, "Direction of Arrival Estimation for Radio Multipath Propagation Channel Characterisation," M.Sc. Dissertation, Dept. of Electrical Engineering and Electronics, UMIST, Manchester, UK, 2002.
20. K. Pensel, J. A. Nossek, "Uplink and Downlink Calibration of an Antenna Array in a Mobile Communication System," COST 259, 3rd Meeting, TD-58, Lisbon, Portugal, 1997.
21. J. A. Fessler, A. O. Hero, "Space-Alternating Generalised Expectation-Maximisation Algorithm," *IEEE Transactions on Signal Processing*, vol. 42, pp. 2664-2677, 1994.

22. B. H. Fleury, M. Tschudin, R. Heddergott, D. Dahlhaus, K. I. Pederson, "Channel Parameter Estimation in Mobile Radio Environments Using the Sage Algorithm," *IEEE Journal on Selected Areas in Communications*, vol. 17, pp. 434-450, 1999.
23. M. C. Vanderveen, C. B. Papadias, A. J. Paulraj, "Joint Angle and Delay Estimation (JADE) for Multipath Signals at an Antenna Array," *IEEE Communications Letters*, vol. 1, pp. 12-14, 1997.
24. A. J. Paulraj, C. B. Papadias, "Space-Time Processing For Wireless Communications," *IEEE Signal Processing Magazine*, vol. 14, pp. 49-83, 1997.

Chapter 5

Wideband Channel Sounding Techniques

5.1 Introduction

In general, propagation studies can be considered to be the basis for the design of any radio system and for this reason a number of channel sounders have been developed over the years. Numerous propagation studies have been carried out with narrowband sounders [1], and are well documented. Therefore in this chapter only wideband channel sounding techniques are described and these can be classified into two major categories, namely time-domain methods which include periodic pulse sounding and spread spectrum sounding and frequency-domain methods which include the chirp technique. In general, time-domain sounding results in measurements which give the channel impulse response. However, if frequency-domain techniques are employed, the measurements result in some representation of the channel transfer function.

All of these sounding methods are briefly described in this chapter. Particular emphasis is placed on chirp sounders, since the system developed to carry out the measurements is based on this technique. With reference to the chirp method, a description is given for how to extract parameters such as the power delay profile (PDP) and Doppler shift from the measured channel data. Finally, a brief description is given for how to extend the chirp concept to MIMO sounding, and the limitations that are inherently imposed by such architectures.

5.2 Wideband Channel Sounding

Due to the requirements for higher data rates and multiple access techniques, most radio communication systems are wideband. While it is possible to characterise the radio channel using a number of narrowband single tone measurements (either in parallel or sequentially), this technique has inherent limitations [1-3]. Thus, it is often preferable to employ a real wideband sounding system.

The word 'sounder' infers that a signal is used at the transmitter to sound or excite the radio channel. The signal observed at the receiver is then stored and analysed for further information. Through data analysis, the time-variant channel impulse response or one of the other system functions described in chapter 2 can be obtained. Figure 5.1 shows the block diagram of a 'generic' sounding system which is conceptually very simple.

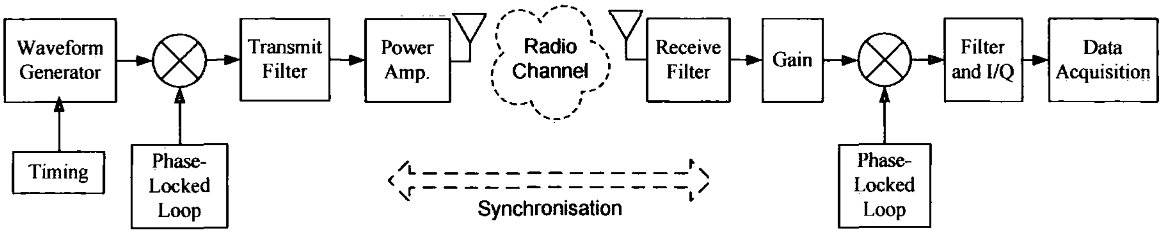

Figure 5.1: Principle of a radio channel sounder, where synchronisation is a fundamental requirement.

For this system, the choice of the transmitted signal and the system properties depend entirely on the sounding technique employed [4]. However, any sounder can be categorised by a set of basic system properties. These are briefly noted in the following:

- System Bandwidth, *B*: The bandwidth of the sounder is inversely proportional to the time-delay resolution of the system. Clearly, a larger bandwidth will correspond to a finer temporal channel resolution. For indoor channels, it is important to have a finer delay resolution and this will be made clear in later sections.
- Waveform Duration, *T*: The duration of the signal, which is inversely related to the sounder repetition frequency should not be longer than the coherent time of the channel. The Doppler range of the sounder is limited by this parameter.
- Time Bandwidth Product, *BT*: The time bandwidth product relates directly to the transmission energy within the sounding signal. Therefore, increasing this product will result in a higher SNR at the receiver (better dynamic range).

- Crest Factor (CF): The crest factor relates to the transmit power efficiency and is simply defined as the ratio between peak signal amplitude and rms signal amplitude. A low crest factor permits efficient use of the power radiated at the transmitter.
- Power Spectral Density (PSD): To reduce interference to other systems, it is important for the PSD of the sounding signal to be uniform across the band of interest, with very little energy being transmitted outside this band. It is also important to reduce interference from other systems. One of the major advantages of the chirp technique is that it offers excellent interference reduction capabilities.

5.3 Time-Domain Sounding

Most radio channel sounders are implemented in the time-domain and therefore often measure directly the channel impulse response. In this section a number of important time-domain methods are described.

5.3.1 Periodic Pulse Sounding

In order to observe the time-variant behaviour of the channel periodic pulse sounding can be employed, as shown in figure 5.2.

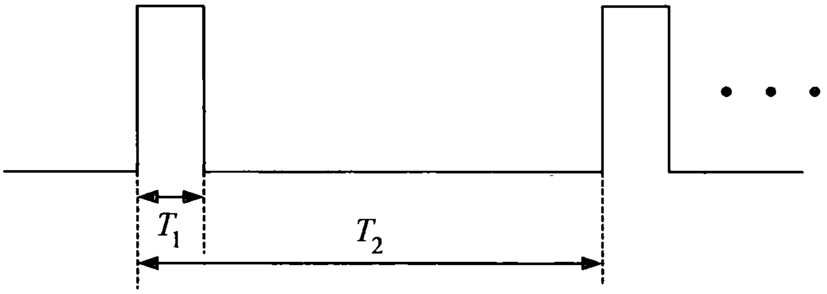

Figure 5.2: Periodic pulse sounding signal, where T_1 represents the minimum echo resolution and T_2 represents the maximum unambiguous echo path delay.

This technique is similar to a wideband pulsed bistatic radar system, which transmits a repetitive pulse of width T_1 and uses a receiver with a wide bandpass filter (with bandwidth $2/T_1$). The signal is then amplified, detected with an envelope detector, displayed and finally stored [5]. This technique provides an immediate measurement snapshot of the square of the channel impulse response convolved with the probing pulse. By averaging these snapshots, the power delay profile can be obtained.

Although this technique is fairly simple to apply and requires only off the shelf components, it has numerous disadvantages that make it unsuitable for efficient high-resolution measurements. One disadvantage is the use of the envelope detector at the receiver, which means that the phase information for the individual multipath components is lost. However, this can be overcome by employing coherent detection. Another significant drawback with such systems is that they have virtually no resistance to channel interference; therefore any signal arriving at the receiver is interpreted as part of the channel impulse response.

The major limitation of the periodic pulse sounding technique is the requirement for a high peak-to-mean power ratio (high CF) to provide adequate detection of weak echoes [3]. Since pulsed transmitters are limited in their peak power, a possible way of overcoming this is pulse compression techniques, which are examined in the following sections.

5.3.2 Spread Spectrum Sounding

Based on the theory of linear systems [6], the system impulse response can be determined by applying white noise $n(t)$ to the input of the system, and cross-correlating the output $w(t)$ with a delayed replica of the input noise $n(t-\tau)$. This can be shown as follows:

$$R_n(t) = E\{n(t)n^*(t-\tau)\} = N_0\delta(\tau) \tag{5.1}$$

Where $R_n(t)$ is the autocorrelation function of noise, N_0 is the one-sided noise power spectral density, and $\delta(\tau)$ is Dirac delta function . The system output is given by the convolution relationship, which is defined as

$$w(t) = \int h(\tau')n(t-\tau')d\tau' \tag{5.2}$$

Hence the cross-correlation of the output and the delayed input is given by

$$\begin{aligned} E\left\{w(t)n^*(t-\tau)\right\} &= E\left\{\int h(\tau')\cdot n(t-\tau')n^*(t-\tau)d\tau'\right\} \\ &= \int h(\tau')R_n(\tau-\tau')d\tau' \\ &= N_0 h(\tau) \end{aligned} \tag{5.3}$$

The channel impulse response is thus determined by using white noise at the input and some method of correlation processing [1]. However, since it is unrealistic to generate white noise, a noise-like deterministic waveform has to be employed to stimulate the channel.

The commonly used pulse compression waveform is the maximal length pseudo-random binary sequence (m-sequence), which is also known as Pseudo-Noise (PN) sequence. An m-sequence is generated using an n-bit shift register with a maximum length of $m = 2^n - 1$. Each bit in the sequence is referred to as a *chip*, with duration T_C and a so-called *chip rate* of R_C ($R_C = 1/T_C$) [3]. PN sequences have excellent periodic autocorrelation properties, as illustrated in figure 5.2. In addition to offering high delay resolution, correlative sounders provide a low CF.

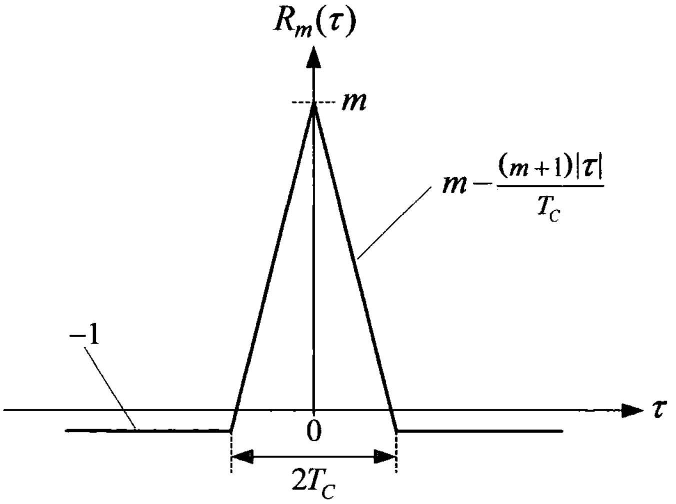

Figure 5.2: Autocorrelation function of a maximal length pseudo-random binary sequence, with chip rate T_C.

In a spread spectrum sounder, a carrier signal is spread over a large bandwidth by mixing it with a binary PN sequence [7]. The power spectrum envelope of the transmitted spread spectrum signal is given by

$$S(f)=\left[\frac{\sin\pi(f-f_c)T_C}{\pi(f-f_c)T_C}\right]^2=\mathrm{Sa}^2(\pi(f-f_c)T_C) \tag{5.4}$$

where the null-to-null RF bandwidth is $2T_C$. There are essentially two techniques for compressing the received spread spectrum signal. One method relies on a convolution matched filter, and the other is based on a sliding cross-correlator technique. Both of these methods are described in the following sections.

5.3.2.1 Convolution Matched Filter

An alternative to correlation processing is the matched filter technique, whereby pulse compression is achieved through the use of a filter which is matched to the sounding waveform. This method is referred to as the convolution matched filter technique and is equivalent to correlation compression. Bajwa and Parsons used this method for investigating the mobile radio channel at 436 MHz [8]. The implementation of this was accomplished by using a Surface Acoustic Wave (SAW) device to realise the matched filter. This is illustrated in figure 5.3.

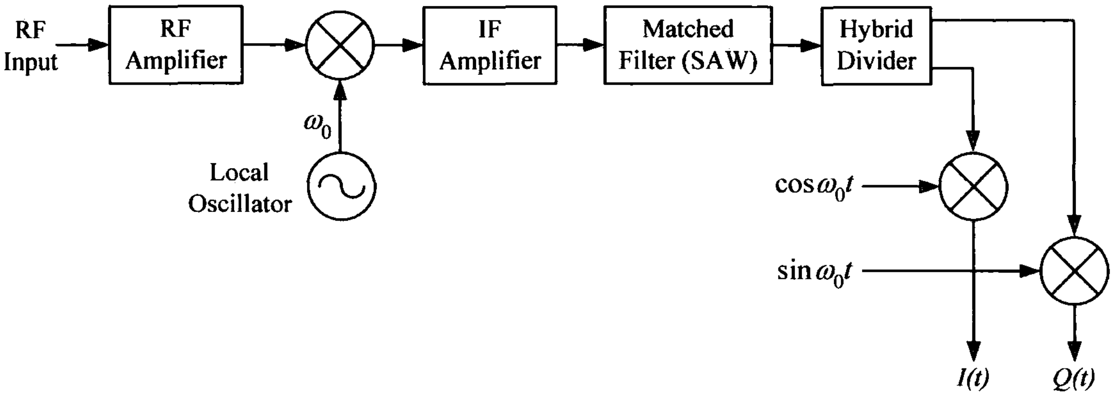

Figure 5.3: Pulse Compression by means of a matched filter.

Because the SAW filter is matched to the specific *m*-sequence used in the transmitter, it is no longer necessary to locally generate this *m*-sequence at the receiver. As a result, this method is often termed asynchronous sounding and has many advantages in terms of cost and complexity [1]. The output of the matched filter sounder consists of both in-phase and quadrature information. Also the system operates in real time because the output of the matched filter is a series of snapshots of the channel response, which amounts to a one-to-one mapping of the time delays in the time domain.

There are, however, several disadvantages in sounding the channel by this technique. One disadvantage is that real time information cannot be recorded by the matched filter sounder unless additional circuitry is built for changing the bandwidth. In general, there are a number of limitations in fabricating SAW devices, which result in the devices having reduced sensitivity to weak echoes. Also the various deficiencies in the device, give an overall restriction to the measurement accuracy and performance of the system [1].

5.3.2.2 Swept Time-Delay Cross-Correlation (STDCC)

As an alternative to the convolution matched filter, it is possible to use correlation processing at the receiver. The STDCC method is a modification of the correlative sounder, which attempts to reduce the sampling rate at the receiver. Standard correlative methods require sampling at the Nyquist rate, however the STDCC sounder requires a sample for each m-sequence at the maximum of the autocorrelation function [4]. Using this technique, the spread spectrum signal is received, filtered, and *despread* using a local PN sequence generator, which is identical to that used at the transmitter. Although the two PN sequences are identical, the transmitter chip clock is run at a slightly faster rate than the receiver chip clock. The reason for having slightly different chip rates is so that the PN code of the faster chip clock slides past that of the slower chip clock. When the two chip sequences are virtually aligned, this gives maximum correlation. Mixing the chip sequences in this fashion implements a *sliding correlator*. When the two sequences are not maximally aligned, mixing the incoming signal with the unsynchronised receiver chip sequence will *spread* this signal into a bandwidth at least as large as the PN sequence at the receiver [3]. Thus, in this case the filter that follows the correlator can reject almost all of the incoming signal power. In an equivalent implementation, instead of clocking the receiver m-sequence at a slightly slower rate, it is possible to use the same clock but to reset the sequence after $m + 1$ bits. By this technique, the two sequences at the transmitter and receiver pass each other in a step-by-step basis, rather than sliding past continuously.

Cox [9] was the first to use a Swept Time-Delay Cross-Correlation (STDCC) sounder and this was followed by others some years later [10-12]. By using coherent detection at the receiver (as reported by Cox), it is possible to acquire the phase information necessary for the extraction of the Doppler shifts associated with each time-delayed echo. In many of the studies only envelope detection was employed. In general, the sliding correlator method can be achieved through a number of architectures, all of which are well documented [1, 3-5, 9-13].

The time resolution of multipath components using a STDCC sounder is T_C (= $1/2R_C$). The sliding correlation process gives equivalent time measurements that are updated according to every time the two sequences are maximally correlated. The time between maximal correlations, ΔT, is given by

$$\Delta T = \beta m T_C \tag{5.5}$$

where β denotes the sliding factor given by

$$\beta = \frac{f_{Tx}}{f_{Tx} - f_{Rx}} \tag{5.6}$$

where f_{Tx} and f_{Rx} denote the transmitter and receiver chip clock rates, respectively. It is important to note that equation (5.5) is an observed measurement time and not the actual propagation time. The PN sequence period is given by mT_C, which gives an estimate of the maximum unambiguous range of incoming multipath signal components [1]. Some of the parameters of a typical STDCC sounder are given in table 5.1.

Time resolution	T_C
Maximum unambiguous echo-path time-delay	mT_C
Scaling factor (β)	$f_{Tx}/(f_{Tx} - f_{Rx})$
Sequence length (m)	$2^n - 1$ bits
Dynamic range	$20 \log_{10} m$
Maximum Doppler shift	$f_D = 1/(2\beta m T_C) = 1/2\Delta T$

Table 5.1: Measurement parameters of the STDCC sounder. The speed resolution is defined by $v_D = c \cdot f_D / f_c$, where f_c is the carrier frequency and c is the speed of light.

There are several advantages to using spread spectrum sounding systems over direct pulse systems. One key advantage is the ability to deal with passband noise, thus improving the coverage range for a given transmitter power. Another important advantage is the considerable reduction in the transmitter power due to the inherent processing gain of spread spectrum systems.

The main disadvantage of the sliding correlator is that the overall impulse response is compiled as the PN codes slide past one another. Depending on the system and the measurement requirements, excessive time may be required for taking power delay profile measurements [3]. Another disadvantage is that even with coherent detection, the sweep time of a spread spectrum signal induces a delay such that the phases of the individual multipath components (with different delays) are measured at distinctly different times, during which the channel might have changed.

5.4 Frequency-Domain Sounding

Because of the fundamental duality between time-domain and frequency-domain, it is possible to measure the channel response in the frequency domain, and extract from this the impulse response in the time domain by an inverse FFT (IFFT) process.

5.4.1 Vector Network Analyser Measurements

Frequency-domain channel sounding is often achieved by employing a vector network analyser (VNA) that sweeps across a frequency band by stepping through discrete frequencies, and an S-parameter test set, which monitors the frequency response of the channel [14, 15]. Figure 5.4 shows a possible implementation of such a sounder.

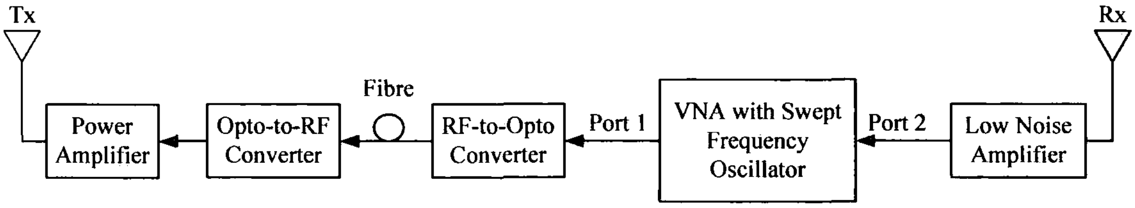

Figure 5.4: Frequency-domain channel sounding using a VNA.

The number and spacings of the frequency steps affect the time resolution of the impulse response measurements. For each frequency step, the S-parameter test set transmits a known signal level at port 1 and monitors the received signal level at port 2. These signal levels allow the VNA to determine the complex response (i.e., the transmissivity, $S_{21}(\omega)$) of the channel over a measured frequency band. The resulting transmissivity response is the frequency domain representation of the channel impulse response and is characterised as the transfer function. This is then converted to the time domain by using IFFT processing and results in a band-limited version of the channel impulse response [3]. This technique can indirectly provide both amplitude and phase information in the time domain. However, careful calibration and hardwired synchronisation of the system is required, limiting the distance over which measurements can be performed. The number and spacings of the frequency steps do affect the time resolution of the impulse response measurements. In general, the time varying nature of the channel cannot be observed accurately using this technique unless a fast enough sweep time is used. A faster sweep time is typically achieved by reducing the number of frequency steps, thus diminishing the temporal resolution of the system.

5.4.2 Frequency-Domain Correlation Sounding

It is possible to implement the correlation process in the frequency-domain and such an example is given in [16], which describes the system (RUSK X) later enhanced and commercialised by MEDAV into the RUSK sounder. The block diagrams of this system are shown in figure 5.5.

For this system, the baseband signal is composed of an interpolated, band-limited and pre-equalised signal based upon a PN sequence or a suitable sounding waveform which is periodically read out of a memory bank (ROM or RAM) [16]. After digital-to-analogue conversion (DAC), low pass filtering, modulation (double side-band), and amplification, the signal is fed to the transmit antenna(s). This transmitted waveform has a line spectrum which has almost constant amplitude across the band of interest (periodic multi-frequency excitation).

At the receiver, a high precision analogue-to-digital converter (ADC) is used at an Intermediate Frequency (IF) range. This is followed by digital quadrature demodulation into the baseband, after which the signal is low pass filtered and down-sampled by a factor of two. For fast computation, the convolution is done in the frequency domain. The multiplication vector C(u) includes the correlation, the equalisation of both magnitude and phase response of the device itself plus the additional windowing. The complex impulse responses are stored for later post-processing.

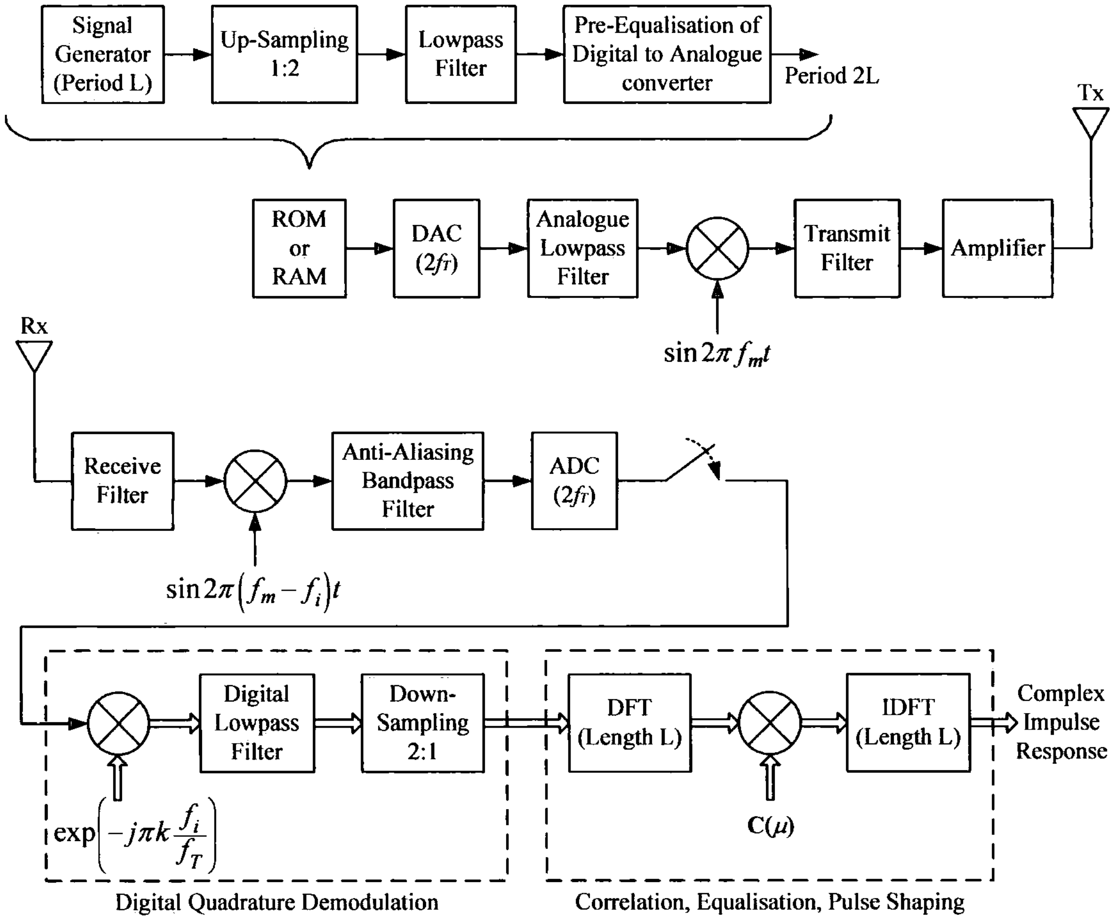

Figure 5.5: Transmitter and receiver block diagrams of the RUSK system [16].

5.5 FMCW (Chirp) Sounding

Another method of frequency-domain analysis is one that employs a frequency swept (chirp) signal to sound the channel [17]. Frequency modulated continuous wave (FMCW), or chirp signals have long been used in HF radar and ionospheric research [18-20]. Pulse compression using the chirp technique has proven to be a powerful method for efficiently measuring the channel response [20-26], since it avoids transmitter peak power limitations and offers excellent interference suppression capabilities. In general, the application of chirp signals for mobile radio channel characterisation has always been limited by the capabilities of modern digital technology. Recent advances in fast sweeping synthesisers and powerful FPGAs have made it possible to implement the chirp sounder [27-29]. In this chapter, the basic chirp sounder theory and parameters are discussed, and the implementation of this system is described in chapter 6.

A conventional chirp sounder transmits a frequency modulated signal which is characterised by a linear frequency increase or decrease over a bandwidth range of *B* Hz in a period of *T* s. Since the chirp signal is defined by a linear frequency-time dependence, its instantaneous frequency is denoted by a linear relationship (i.e, $a \pm bt$). This is given by

$$f_i(t) = \frac{1}{2\pi}\frac{d\phi(t)}{dt} = f_c \pm \frac{B}{T}t \tag{5.7}$$

where f_c is the carrier frequency. The transmitted chirp waveform can be expressed as

$$v_T(t) = A_T \cos\left[\phi_T(t)\right] = A_T \cos\left(2\pi f_c t \pm \pi \frac{B}{T} t^2\right) \tag{5.8}$$

where A_T is the amplitude of the transmitted chirp signal. Figure 5.6 illustrates the frequency-time dependence for a chirp signal that sweeps upwards from f_0 across the measurement band. Here $1/T$ represents the sweep repetition frequency (SRF), also known as the waveform repetition frequency (WRF).

For large time-bandwidth products ($BT >> 1$), the spectrum of the chirp signal is almost constant across the swept bandwidth, and for *BT* values greater than 100, more than 95% of the spectral energy is confined to the bandwidth, *B*. In practice *BT* is often much greater than 100. An approximate spectrum for a chirp signal is given by [30]

$$V_T(f) = \mathbb{F}\left\{v_T(t)\right\} \approx \sqrt{\frac{T}{4B}} \cdot e^{-j\pi\frac{(f_c-f)^2 T}{B}}, \qquad \text{for } BT >> 1 \tag{5.9}$$

where $\mathbb{F}\{\cdot\}$ denotes the Fourier transform (the negative frequency spectrum is the complex conjugate).

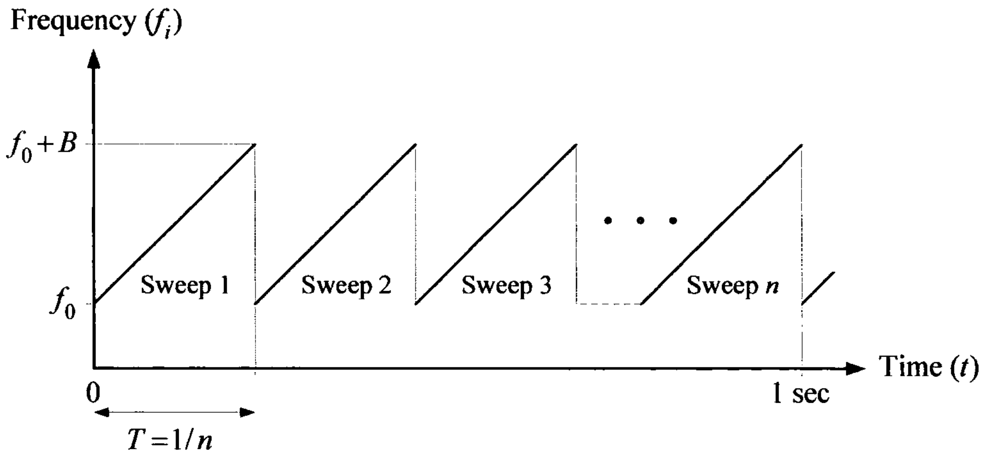

Figure 5.6: Illustration of the frequency-time dependence of a linear chirp waveform.

At the receiver, the chirp signal is compressed to

$$v_d = \sqrt{BT}\left(\frac{\sin(\pi Bt)}{\pi Bt}\right) \tag{5.10}$$

The compression of the chirp signal results in a sin(x)/x function which has amplitude √(BT) and a 4 dB width equal to $1/B$ (where BT defines the processing gain). Therefore, the chirp sounder has a compression gain of 10 log (BT) and the capability of resolving multipath components separated by $1/B$ s. The unambiguous Doppler coverage of the sounder is equal to ± SRF/2 = ± $1/2T$, where SRF denotes the sweep repetition frequency. The Doppler resolution is a function of the channel sampling duration or the coherent integration time and to increase the capability of the system to measure larger Doppler shifts, a higher sweep rate is required.

In order to coherently detect the chirp signal at the receiver, either cross-correlation, or matched filter detection can be employed. With the matched filter technique, the output is not compressed in frequency.

An alternative is to mix the incoming signal with a locally generated chirp signal at the receiver, which has the same signal characteristics (i.e., bandwidth, centre frequency and SRF) as the chirp signal at the transmitter and is synchronised in time to the transmitted signal. Mixing the received signal with this replica then produces sum and difference frequency components. By means of a lowpass filter, the sum frequencies are filtered leaving only the difference components also referred to as beatnotes. These beatnotes are then used to examine the delay and Doppler channel characteristics. This compresses the signal in frequency but not in time, with the beat frequencies being on the order of a few tens of kHz. The beat frequencies, f_{bi}, are related to the multipath delays, τ_i, by the relationship

$$f_{b_i} = \frac{B}{T}\tau_i \tag{5.11}$$

Therefore, the required bandwidth at the output of the detector is determined by the product of the sweep rate (B/T) and the maximum expected time delay (corresponding to the furthest echo). Since the frequency of the beatnotes is on the order of kHz, low speed ADCs could be employed for data acquisition. This is a benefit that is not realisable with the matched filter technique.

It should be noted that by using this method, bandwidth compression is achieved without a significant reduction in the effective repetition rate of the sounder. However, this is not the case with STDCC sounders employing a single cross-correlator, since here bandwidth compression is achieved at the expense of Doppler range [31, 32]. Since the chirp signal linearly maps time into frequency, the output of the detector can be analysed with different time and frequency resolutions in order to obtain various channel parameters. Table 5.2 gives a summary of the basic chirp sounder parameters.

Sweep duration and maximum unambigous delay range	T
Time domain resolution	$\approx 1/B$
Channel sampling rate and the resolution of beat notes	$1/T$
Sweep rate	$B/T = B\cdot\mathrm{SRF}$
Beat notes frequencies	$f_b = B/T\cdot\tau$
Compression gain	10 log (BT)
Unambigous Doppler range	± SRF/2

Table 5.2: Chirp sounder parameters.

5.5.1 Heterodyne Detection

The mathematical expression for the transmitted chirp signal was defined in equation (5.8). Due to the multiple paths in the channel, the received signal will be composed of multiple attenuated, delayed and Doppler shifted versions of the transmitted signal. By assuming that there are L independent multiple paths in the channel, the received signal can be defined as

$$\begin{aligned} v_R(t) &= \sum_{i=1}^{L} A_{R,i}\cos\left[\phi_T(t-\tau_i)\right] \\ &= \sum_{i=1}^{L} A_{R,i}\cos\left(2\pi f_0(t-\tau_i)+\pi\frac{B}{T}(t-\tau_i)^2\right) \end{aligned} \tag{5.12}$$

where $A_{R,i}$ denotes the amplitude of the i^{th} received multipath component [17]. At the receiver, the signal is mixed with a locally generated replica of the transmitted signal Therefore, their product gives

$$\begin{aligned} v(t) = v_R(t)v_T(t) &= \sum_{i=1}^{L} A_{R,i}\cos\left[\phi_T(t-\tau_i)\right]\cdot A_T\cos\left[\phi_T(t)\right] \\ &= \sum_{i=1}^{L} A_T A_{R,i}\cos\left(2\pi f_0(t-\tau_i)+\pi\frac{B}{T}(t-\tau_i)^2\right)\cos\left(2\pi f_0 t+\pi\frac{B}{T}t^2\right) \end{aligned} \tag{5.13}$$

Using the trigonometric relationship: $\cos a\cdot\cos b = 0.5(\cos(a-b)+\cos(a+b))$, equation (5.13) can be defined as

$$\begin{aligned} v(t) &= \sum_{i=1}^{L} A_i\left\{\cos\left[\phi_T(t-\tau_i)-\phi_T(t)\right]+\cos\left[\phi_T(t-\tau_i)+\phi_T(t)\right]\right\} \\ &= \sum_{i=1}^{L} A_i\cos\left(2\pi f_0(t-\tau_i)-2\pi f_0 t+\pi\frac{B}{T}(t-\tau_i)^2-\pi\frac{B}{T}t^2\right) \\ &\quad+\sum_{i=1}^{L} A_i\cos\left(2\pi f_0(t-\tau_i)+2\pi f_0 t+\pi\frac{B}{T}(t-\tau_i)^2+\pi\frac{B}{T}t^2\right) \end{aligned} \tag{5.14}$$

where $A_i = A = 0.5(A_T A_{R,i})$. The second term in equation (5.14) denotes the sum signal which will be filtered out. The first term in equation (5.14) denotes the difference term and contains the time-delay information corresponding to the multipath components. There are essentially two difference frequencies associated with each multipath signal that mixes with the locally generated chirp replica. For the i^{th} signal, these two frequencies are given by [17]

$$f_{1,i} = \frac{1}{2\pi}\frac{d}{dt}\left[\phi_T(t-\tau_i) - \phi_T(t)\right] \tag{5.15}$$

$$f_{2,i} = \frac{1}{2\pi}\frac{d}{dt}\left[\phi_T(t-\tau_i) - \phi_T(t-T)\right] \tag{5.16}$$

It is possible to make a simplification of the above equations by considering a single received signal with delay τ. Thus, equation (5.14) can reduce to

$$v_1(t) = A\cos\left(2\pi f_0(t-\tau) - 2\pi f_0 t + \pi\frac{B}{T}(t-\tau)^2 - \pi\frac{B}{T}t^2\right) \tag{5.17}$$

for which, f_1 and f_2 are given by equations (5.15) and (5.16).

Figure 5.7 illustrates the swept frequency versus time for a single received signal and the corresponding IF frequencies versus time at the output of the detector [33]. Here, the resulting IF signal is represented as a sum of two pulse trains. One with a frequency of f_1 and a pulse width of $T_1 = T - T_0 - \tau$ (note: $T >> \tau$) and the other with a frequency of f_2 and a pulse width of $T_2 = T_0 + \tau$, where T_0 is the initial sounder delay. Since τ and T_0 are considered to be small (i.e., τ, $T_0 << T$), $T_1 \approx T - T_0 \approx T$ and $T_2 \approx T_0$. Furthermore, if the swept bandwidth is considered to be large enough so that $f_2 >> f_1$, the higher frequency component can be removed by lowpass filtering, as will be the case here [17].

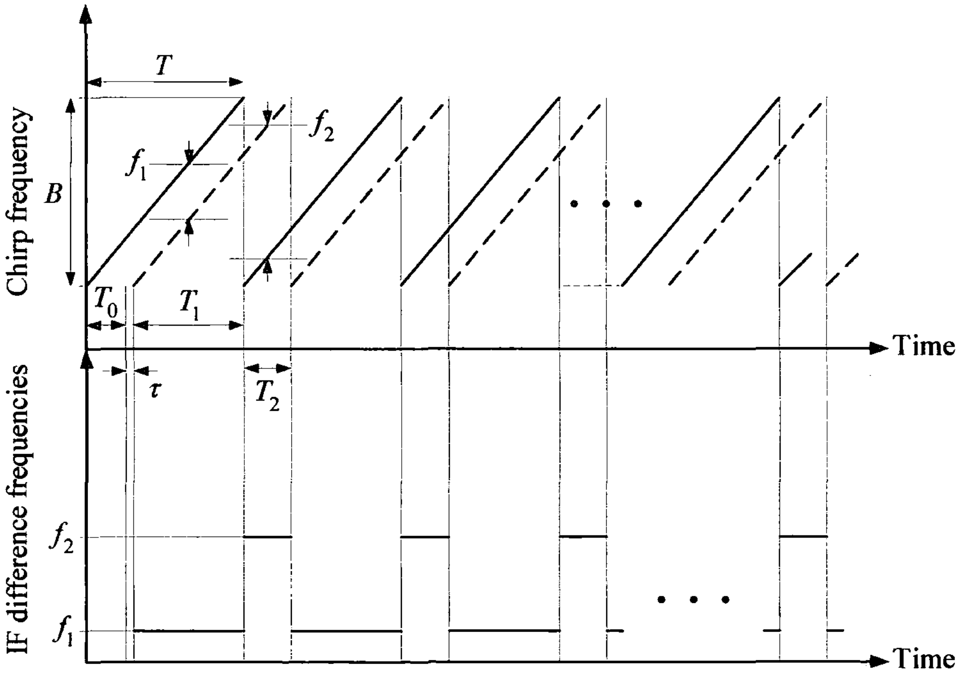

Figure 5.7: Swept frequency vs time and frequency of beatnotes at the detector output.

If the receiver is assumed to be moving at a constant velocity, v, then the change in the path length will cause a change in the time delay of the multipath component. This time delay is given by

$$\because d = d_0 + vt, \tag{5.18}$$

$$\tau = \frac{d}{c} = t_0 + \frac{v}{c}t \tag{5.19}$$

where d is the range as a function of time, d_0 is the initial distance between the transmitter and receiver, and t_0 is the initial delay due to d_0. By redefining the time origin of the signal such that it falls in the centre of the first sweep, i.e. $-T/2 < t < T/2$ the phase $\phi_T(t) + \phi_T(t-\tau)$ from the first term in equation (5.14) can be simplified to

$$\begin{aligned}\phi_1(t) &= \phi_T(t-\tau) - \phi_T(t) \\ &= -2\pi f_0 \tau + \pi\frac{B}{T}(t-\tau)^2 - \pi\frac{B}{T}t^2 \\ &= -\left(2\pi f_0 + 2\pi\frac{B}{T}t\right)\tau + \left(\pi\frac{B}{T}\right)\tau^2 \end{aligned} \tag{5.20}$$

substituting τ from equation (5.19) into the above relationship, yields

$$\phi_1(t) = -\left(2\pi f_0 + 2\pi\frac{B}{T}t\right)\left(t_0 + \frac{v}{c}t\right) + \left(\pi\frac{B}{T}\right)\left(t_0 + \frac{v}{c}t\right)^2 \qquad -T/2 < t < T/2 \tag{5.21}$$

Since $v/c \ll 1$, equation (5.21) simplifies to

$$\phi_1(t) \approx -2\pi f_0 t_0 + \pi\frac{B}{T}t_0^2 - \left(2\pi f_0\frac{v}{c} + 2\pi\frac{B}{T}t_0\right)t \tag{5.22}$$

and by bringing all t_0 terms together:

$$\phi_1(t) \approx \phi_0 - \left(2\pi f_0\frac{v}{c} + 2\pi\frac{B}{T}t_0\right)t \tag{5.23}$$

Hence, the instantaneous frequency, f_1, is defined as

$$f_1 = \frac{1}{2\pi}\frac{d}{dt}\left[\phi_1(t)\right] = f_0\frac{v}{c} + \frac{B}{T}t_0 \qquad (5.24)$$

If t can denote the time within the n^{th} sweep, the interval of interest can be defined as $-(2n-1)T/2 < t < (2n+1)T/2$, and the time to the centre of the n^{th} sweep can be given by nT. Equation (5.19) can therefore be redefined as

$$\tau_{(n)} = \frac{d}{c} = t_0 + \frac{v}{c}(nT + t) = t_0' + \frac{v}{c}t \qquad (5.25)$$

substituting $t_0' = t_0 + (v/c)nT$, which is the initial time-delay within the n^{th} sweep, for t_0 in equation (5.23) gives the phase in the n^{th} sweep, so that

$$\begin{aligned}\phi_{1,n}(t) &\approx \phi_0 - \left(2\pi f_0\frac{v}{c} + 2\pi\frac{B}{T}t_0'\right)t \\ &= \phi_0 - \left(2\pi f_0\frac{v}{c} + 2\pi\frac{B}{T}t_0 + 2\pi B\frac{v}{c}n\right)t \end{aligned} \qquad (5.26)$$

Therefore, the frequency in the n^{th} sweep can be defined as [17]

$$f_{1,n} = \frac{1}{2\pi}\frac{d}{dt}\left[\phi_{1,n}(t)\right] = f_0\frac{v}{c} + \frac{B}{T}t_0 + B\frac{v}{c}n \qquad (5.27)$$

By comparing the frequency in the first sweep, f_1, and that in the n^{th} sweep, $f_{1,n}$, it is possible to observe that there is an additional term for $f_{1,n}$, $Bn(v/c)$, which is introduced because of the movement of the mobile. For large values of n and high velocity observed by the mobile, this additional term cannot be neglected. It should be noted that a change in the path length results in a phase variation from one sweep to another. The phase variations of the incoming signal are used to calculate the velocity of the target in radar applications (Doppler processing). In propagation measurements, the phase variations can be used to resolve the multipath components that fall into the same time delay bin because their propagation paths are similar but they arrive at different impinging angles. All the above derivations assume that the transmitted signal is phase coherent from sweep to sweep [17].

5.5.2 Double FFT Digital Processing

There are essentially two methods for extracting time delay (range) and Doppler shift (velocity) channel information. The first technique employs double FFT processing; where an initial FFT is carried out over a sweep (defined by *T*) in order to extract time delay information, and another FFT is carried out over *N* sweeps (defined by *NT*) for each single time delay bin in order to determine Doppler shift information. The second technique employs a long FFT process over *N* sweeps in order to provide simultaneous delay/Doppler channel information. Both techniques are identical and have the same number of computational steps [17]. However, in this case the chirp sounder parameters are obtained through the former technique (double FFT), which is described in this section.

For a single transmission path, the Fourier transform over a single sweep *n* is given by

$$V_{1,n}(f)=\int_{-T/2}^{T/2}\left\{A\cos\left[\phi_{1,n}(t)\right]\right\}e^{-j2\pi ft}dt \tag{5.28}$$

using Euler's definitions: $\cos x=(e^{jx}+e^{-jx})/2$, $\sin x=(e^{jx}-e^{-jx})/2j$, and $\int e^{ax}dx$ $=e^{ax}/a$, equation (5.28) becomes

$$\begin{aligned}V_{1,n}(f)=&\frac{AT}{2}\left\{\frac{\sin\left(2\pi\left(f-f_{1,n}\right)T/2\right)}{\left(2\pi\left(f-f_{1,n}\right)T/2\right)}e^{-j\phi_0+j2\pi f_0\frac{v}{c}nT}\right\}\\&+\frac{AT}{2}\left\{\frac{\sin\left(2\pi\left(f+f_{1,n}\right)T/2\right)}{\left(2\pi\left(f+f_{1,n}\right)T/2\right)}e^{+j\phi_0-j2\pi f_0\frac{v}{c}nT}\right\}\end{aligned} \tag{5.29}$$

Thus, the detected signal spectrum is a sin(*x*)/*x* pulse whose frequencies are related to the delay experienced by the multipath components in the channel. The number of such pulses is determined by the multipath structure of the channel and also the time delay resolution of the sounder, which is $1/B$.

For any practical system, the measured data is defined as samples of the received signal (obtained by employing an analogue to digital converter), therefore, the FFT is required to obtain the discrete spectrum of the sin(x)/x pulses. If M denotes the number of points used in the FFT, then the output of the FFT performed on M samples over a sweep will result in M discrete frequency points whose values range from $-F_S/2$ to $F_S/2$, where F_S denotes the sampling rate. By symmetry the negative frequency components can be ignored, leaving $M/2$ beat frequency bins.

By adhering to the Nyquist sampling theorem, F_S must be at least twice the maximum expected beat frequency, denoted by f_{lmax}. Therefore, the required number of samples per sweep, M, can be calculated by $M \geq (2\, f_{lmax})/\text{SRF}$. This infers that the maximum time delay that can be measured is given by [27]

$$\frac{f_{l\max}}{\text{Sweep Rate}} = \frac{f_s/2}{B \cdot SRF} = \frac{f_s}{2B \cdot SRF} \tag{5.30}$$

Performing the first FFT process on M samples within a sweep gives $M/2$ time delay bins per sweep. Performing the FFT process over N sweeps and digitally storing the values for each sweep in a row of a data matrix gives an $M/2 \times N$ matrix containing both delay and Doppler information. This is illustrated in figure 5.8.

$$\begin{array}{cc}
 & \xleftrightarrow{\text{Time delay (range) bins}} \\
\text{Sweeps (Doppler bins)}\ \updownarrow &
\begin{bmatrix}
S_{11} & S_{12} & \cdots & S_{1m} & \cdots & S_{1M/2} \\
S_{21} & S_{22} & \cdots & S_{2m} & \cdots & S_{2M/2} \\
\vdots & \vdots & \ddots & \vdots & \ddots & \vdots \\
S_{n1} & S_{n2} & \cdots & S_{nm} & \cdots & S_{nM/2} \\
\vdots & \vdots & \ddots & \vdots & \ddots & \vdots \\
S_{N1} & S_{N2} & \cdots & S_{Nm} & \cdots & S_{NM/2}
\end{bmatrix}
\end{array}$$

Figure 5.8: Matrix containing samples of complex impulse responses for successive sweeps. There are N sweeps, each containing $M/2$ samples.

The columns of the matrix represent the time delay bins (after the first FFT), and the rows of the matrix hold the channel impulse responses for successive sweeps. The elements of each column represent the digital samples of a beat frequency component obtained every T seconds. For each successive sweep the elements of the matrix columns will change because the beat frequency corresponding to a multipath component after the mixer and filter, $f_{l,n}$, and the phase term, $2\pi f_c(v/c)nT$, are changing from sweep to sweep due to the relative motion between the transmitter and receiver. The amplitude of a multipath component also changes from sweep to sweep due to the minor shift in the position of the beatnote. However this change is small enough to be neglected [17]. Every sweep takes T seconds, therefore NT seconds is required to fill the matrix shown in figure 5.8.

It can be concluded from the above that the main variations within a column are due to the phase factor, thus

$$S_{nm} = K(f)e^{j2\pi f_0 \frac{v}{c} nT} = K(f)e^{j2\pi f_0 \frac{v}{c} t_n} \tag{5.31}$$

where $t_n = NT$ represents the discrete time flow from sweep to sweep and $K(f)$ is the amplitude variation defined by

$$K(f) = \frac{\sin\left(2\pi\left(f - f_{1N/2}\right)T/2\right)}{\left(2\pi\left(f - f_{1N/2}\right)T/2\right)} \tag{5.32}$$

The Fourier transform of equation (5.31) over t_n from 0 to NT is given by

$$S_m = K(f)NT\frac{\sin\left(2\pi\left(f - \frac{v}{c}f_0\right)NT/2\right)}{\left(2\pi\left(f - \frac{v}{c}f_0\right)NT/2\right)} \tag{5.33}$$

The above equation shows that the movement of the mobile results in a displacement of the $\sin(x)/x$ pulse. This is known as the Doppler shift $f_D = (v/c)f_0 = v/\lambda$. Equation (5.33) also suggests that if a number of paths fall into the same time delay resolution bin, then they can be further resolved if the rate of change in their path lengths is different due to the movement of the mobile. This is observed from the output of the second FFT (over N sweeps), which gives separate peaks as a result of this.

The output of the second FFT is N discrete Doppler frequency points, with the Doppler frequency window defined between the interval $-\mathrm{SRF}/2 \leq f_D \leq \mathrm{SRF}/2$. Since N is the number successive sweeps included in the second FFT, the resolution of the Doppler frequencies is determined by NT. The SRF (= $1/T$) denotes the channel sampling rate and therefore according to the Nyquist sampling theorem, it must be at least twice the maximum expected Doppler shift, v_{max}, so that

$$SRF \geq \frac{2v_{\max}}{\lambda} \tag{5.34}$$

One inherent disadvantage with the $\sin(x)/x$ pulse, is that it has high sidelobes. In order to alleviate this, an appropriate windowing function must be applied to each sweep data before FFT processing. Hanning, Hamming and Kaiser (dynamic) windows can considerably reduce sidelobes and have been used for previous studies [33]. A number of very important windowing functions are described and compared by Harris [34]. Several MATLAB programs are listed on the accompanying CD-ROM for extracting delay/Doppler information (also see appendix A1.1).

In practice, both the number of samples per sweep, M, and the number of sweeps, N, are limited by the sampling at the digital to analogue converter and the storage memory for the acquired data. For a desired time delay window, τ_w, and a given time delay resolution, $\Delta\tau$, the number of samples per sweep is given by

$$M = 2\frac{\tau_w}{\Delta\tau} = 2B\tau_w \tag{5.35}$$

where the time delay window, τ_w, is defined as

$$\tau_w = \frac{B_{Filter}}{B \cdot SRF} \tag{5.36}$$

here B_{Filter} is the given bandwidth of the low pass filter prior to the analogue to digital conversion stage.

The range resolution of the sounder must be larger than the displacement of the receiver, i.e. $vNT < \Delta d$. If the speed of the mobile receiver cannot be constant during the data collection time, then the velocity resolution, Δv, must be larger than the product of the coherent integration time and the rate of change of the velocity at the receiver (acceleration). This is expressed as

$$\Delta v > NT\frac{dv(t)}{dt} \tag{5.39}$$

A summary of some of the chirp parameters and related processing parameters are shown in table 5.3.

Number of Sweeps	N
Number of samples per sweep	$M = F_s/\text{SRF}$
FFT over M samples	M/2 range (time delay) bins
Sampling rate	$F_s \geq 2f_{\text{beat(max)}}$, thus $f_{max} \leq (M\cdot\text{SRF})/2$
Time resolution	$\Delta\tau = \tau_w/(M/2) = 1/B$
Range resolution	$\Delta d = c\cdot\Delta\tau$
Doppler window	$-\text{SRF}/2 \leq f_D \leq \text{SRF}/2$
Doppler frequency resolution	$1/NT$

Table 5.3 Chirp parameters related to the digital signal processing. The speed resolution is given by $v_D = c\cdot f_D / f_c$.

5.6 Extension to MIMO Channel Sounding

So far the concepts behind various channel sounding systems have been reviewed primarily for single antenna radio links (SISO). In order to extend these concepts to multiple transmit, multiple receive systems, some basic sounder limitations and requirements must be adhered to.

By and large, the main channel sounding requirements are determined by the time delay resolution, which defines the transmitted bandwidth, and the maximum expected Doppler shift, which defines the SRF. The SRF also determines the maximum unambiguous time delay window. These fundamental requirements are not altered for multi-antenna channel sounding.

For SIMO/MIMO radio channel sounding, there are a number of architectures that can be implemented. The simplest approach is to use a virtual array system. Such a sounder employs an x-y positioning system to physically move the sensor to a different location for each measurement snapshot. This approach captures virtually no time variable channel data due to the time required for moving the antenna. A more popular approach is based on the idea of sequential sounding (TDM mode) and uses a single channel sounder with multiple sequentially switched antenna arrays at both ends of the radio link. Although this is only an extension of the SISO sounder, it does provide a valuable method for measuring the MIMO channel. The main restriction with such architecture is that the switching must be done within the coherent time of the channel to enable sufficient Doppler coverage. Hence, for outdoor use this can be very restrictive. For a sequential 8 × 8 MIMO sounder, the required SRF is 64 times that of the SISO sounder and in addition, this number may be doubled to allow switching transients to die out [36].

As apposed to a sequential architecture, a parallel architecture can transmit different (separate) signals on each antenna in the transmit array and receive on parallel channels [37]. Other techniques include systems based on frequency division multiplexing (FDM) and code division multiplexing (CDM) [38].

An alternative is to switch at one end of the link while keeping parallel operation at the other, i.e. to employ a semi-sequential approach. This effectively reduces the loss of temporal information as compared to a fully sequential system. The MIMO chirp sounder developed for this study is based on this principle, where an RF switch is used at the transmitter and up to 8 parallel channels can be used at the receiver. It has 300 MHz bandwidth, and a sweep repetition frequency (SRF) of 100-300 Hz for indoor use. By employing a 5-way RF switch at the transmitter, a maximum Doppler range of ± 25 Hz can be realised. In [35], several indoor campaigns were carried out, where the measurement data implied a maximum effective Doppler of ± 5 Hz. Therefore using this sounder with 4 transmit and 4 receive antennas, will permit more than the required indoor Doppler coverage. In chapter 6, the architecture of this MIMO sounder (based on the chirp principle), will be described in more detail.

5.7 Summary and Conclusions

This chapter provided a basic overview of channel sounding techniques for wideband applications. Two main categories of sounders were discussed, namely time-domain and frequency-domain methods. These included direct pulse techniques, spread spectrum techniques and frequency domain techniques. Emphasis was placed on the chirp sounding technique, since this was the method implemented for the measurement system described in chapter 6. The extraction of time delay and Doppler shift information from chirp sounder channel measurements was examined through the use of double FFT processing. Finally, some of the basic measurement restrictions were described in order to extend the chirp concept to MIMO sounding.

5.8 References

1. J. D. Parsons, *The Mobile Radio Propagation Channel*, 2 ed: John Wiley & Sons Ltd, 2000.
2. R. Vauhgan, J. B. Anderson, *Channels, Propagation and Antennas for Mobile Communications*: IEE Press, 2003.
3. T. S. Rappaport, *Wireless Communications: Principles and Practice*, 2 ed: Prentice Hall PTR, 2002.
4. A. F. Molisch, *Wireless Communications*, John Wiley and Sons Ltd., 2005.
5. T. S. Rappaport, S. Y. Seidel, R. Singh, "900 MHz Multipath Propagation Measurements for U.S. Digital Cellular Radiotelephone," *IEEE Transactions on Vehicular Technology*, vol. 39, pp. 132-139, 1990.
6. A. Papoulis, S. U. Pillai, *Probability, Random Variables and Stochastic Processes*, 4 ed: McGraw Hill, 2002.
7. R. C. Dixon, *Spread Spectrum Systems with Commercial Application*, 3 ed: John Wiley & Sons Ltd, 1994.
8. A. S. Bajwa, J. D. Parsons, "Small-Area Characterisation of UHF Urban and Suburban Mobile Radio Propagation," *Proceedings of IEE, Part F*, vol. 129, pp. 102-109, 1982.
9. D. C. Cox, "Delay Doppler Characteristics of Multipath Delay Spread and Average Excess Delay for 910 MHz Urban Mobile Radio Paths," *IEEE Transactions on Antennas and Propagation*, vol. 20, pp. 625-635, 1972.
10. D. M. J. Devasirvatham, "Time Delay Spread and Signal Level Measurements of 850 MHz Radio Waves in Building Environments," *IEEE Transactions on Antennas and Propagation*, vol. 34, pp. 1300-1305, 1986.
11. R. J. C. Bultitude, G. K. Bedal, "Propagation Characteristics of Microcellular Urban Mobile Radio Channels at 910 MHz," *IEEE Journal on Selected Areas in Communications*, vol. 7, pp. 31-39, 1989.
12. O. Landron, M. J. Feuerstein, T. S. Rappaport, "A Comparison of Theoretical and Empirical Reflection Coefficients for Typical Exterior Wall Surfaces in a Mobile Radio Environment," *IEEE Transactions on Antennas and Propagation*, vol. 44, pp. 341-351, 1996.
13. K. Pahlavan, A. H. Levesque, *Wireless Information Networks*: John Wiley & Sons Ltd, 1995.

14. J. Medbo, J. Berg, H. Asplund, M. Riback, "MIMO Channel Characteristics in a Small Macrocell Measured at 5.25 GHz and 200 MHz Bandwidth," IEEE VTC-Fall, Dallas, USA, 2005.
15. K. Haneda, J. Takada, "High-Resolution Estimation of NLOS Indoor MIMO Channel with Network analyzer Based System," 14th IEEE International Personal, Indoor and Mobile Radio Communications (PIMRC 2003), Beijing, China, 2003.
16. K. Schwarz, U. Martin, H. W. Schüßler, "Devices for Propagation Measurement in Mobile Radio Channels," 4th IEEE International Personal, Indoor and Mobile Radio Communications (PIMRC 1993), Yokohama, Japan, 1993.
17. D. E. Barrick, "FM/CW Radar Signals and Digital Processing," *U.S. Department of Commerce, National Oceanic and Atmospheric Administration (NOAA) Technical Report ERL 283-WPL 26*, 1973.
18. B. R. Mahafza, *Radar Systems Analysis and Design Using MATLAB*, 2 ed: Chapman & Hall/CRC, 2005.
19. M. I. Skolnik (ed.), *Radar Handbook*: McGraw Hill, 1990.
20. S. Salous, "FMCW Channel Sounder with Digital Processing for Measuring the Coherence of Wideband HF Radio Links," *IEE Proceedings on Communications*, vol. 133, pp. 456-462, 1986.
21. S. Salous, N. Bajj, N. Nikandrou, "Wideband Channel Characterisation with a Chirp Sounder," IEE Colloquium on Radio Communications at Microwave and Millimetre Wave Frequencies (Digest No. 1996/239), pp. 2/1-2/5, London, 1996.
22. S. Salous, N. Bajj, "Urban Wideband Measurements at 1.8 GHz With Different Chirp Bandwidths," IEEE VTC'98, Ottawa, Ontario, Canada, pp. 697-701, 1998.
23. S. Salous, P. Fillipides, I. Hawkins, "A Multi Channel Sounder Architecture for Spatial and MIMO characterisation of the Mobile Radio Channel," IEE Seminar: MIMO Communication Systems from Concept to Implementation, London, 2001.
24. S. Salous, H. Gokalp, "Dual-Frequency Sounder for UMTS Frequency-Division Duplex Channels," *IEE Proceedings on Communications*, vol. 149, pp. 117-122, 2002.
25. S. Salous, V. Hinostroza, "High Resolution Indoor and Indoor to Indoor Measurements," Euro-COST 273 TD(02) 064, Espoo, Finland, 2002.

26. S. Salous, V. Hinostroza, "Bi-Dynamic indoor measurements with high resolution channel sounder," 5th Symposium on Wireless Personal Multimedia Communications, Sheraton Waikiki, Honolulu, Hawaii, pp. 262-266, 2002.
27. S. Salous, P. Pantzaris, P. Green, "An ASIC Solution for Programming Digital Synthesizers for the Generation of Spread Spectrum Signals," 5th Bangor Communications Symposium, Wales, pp. 191-194, 1993.
28. S. Salous, P. Green, "A Novel Digital Chirp Generator Using a Dual Clock Field Programmable Gate Array Architecture," 6th International Conference on HF Radio Systems and Techniques, London, pp. 391-395, 1994.
29. S. Salous, N. Nikandrou, N. Bajj, "Digital Techniques for Mobile Radio Chirp Sounders," *IEE Proceedings on Communications*, vol. 145, pp. 191-196, 1998.
30. G. F. Gott, *Class Reader for Digital Communications (M.Sc/M.Eng) - Part 2*. UMIST, Manchester, U.K., 2002.
31. S. Salous, P. Pantzaris, P. Green, "FMCW Waveforms for UHF/SHF Wideband Channel Sounders," IEE Colloquium on High Bit Rate UHF/SHF Channel Sounders - Technology and Measurement, pp. 2/1-2/5, 1993.
32. S. Salous, L. Bertel, T. Dupaquier, "VHF Diversity Measurements using PRBS and Chirp Sounders," IEE National Conference on Antennas and Propagation, London, pp. 81-84, 1999.
33. H. Gokalp, "Characterisation of UMTS FDD Channels," Ph.D. Thesis, Dept. of Electrical Engineering and Electronics, UMIST, Manchester, UK, 2001.
34. F. J. Harris, "On the Use of Windows for Harmonic Analysis with the Discrete Fourier Transform," *Proceedings of IEEE*, vol. 66, pp. 51-83, 1978.
35. V. Hinostroza, "Indoor Wideband Mobile Radio Channel Characterisation System," Ph.D. Thesis, Dept. of Electrical Engineering and Electronics, UMIST, Manchester, UK, 2002.
36. S. Salous, "Chirp Waveforms for Multiple Antenna Channel Sounders," 27th URSI General Assembly, Maastricht, Netherlands, 2002.
37. P. Filippidis, "Multi-Channel Sounder for Directional Measurements," Ph.D. Thesis, Dept. of Electrical Engineering and Electronics, UMIST, Manchester, UK, 2002.
38. K. Kuroda, K. Sakaguchi, J. C. Takada, K. Araki, "FDM Based MIMO Spatio-Temporal Channel Sounder," 5th International Symposium on Wireless Personal Multimedia Communications, Honolulu, Hawaii, 2002.

Chapter 6

Semi-Sequential MIMO Chirp Sounder Architecture

6.1 Introduction

The system developed for wideband MIMO channel measurements is based on the sounder described in [1]. Various RF and digital printed circuit boards (PCBs) were implemented in order to construct the semi-sequential MIMO sounder. In addition to this, a number of inter-digital (mechanical) band-pass filters and PLL synthesisers were designed and developed. In the following, a systems level description of the chirp sounder is given with some basic system tests to evaluate its measurement capability.

6.2 Semi-Sequential Sounder Requirements

The measurement system is required for characterisation of the MIMO channel for both UMTS and Wi-Fi/WiMAX systems. In particular the 2.4 GHz ISM band (ad-hoc) and the UMTS-FDD uplink (Cellular) frequencies are of interest. Since indoor MIMO channels are of primary interest, a number of sounder system requirements must first be examined.

6.2.1 Delay and Doppler Resolution

The time delay resolution which is defined as the inverse of the system bandwidth, *B*, is essentially a measure of how closely two distinct paths can be resolved in time delay. For the sounder, the chirp waveform is generated by a state-of-the-art DDFS (Direct Digital Frequency Synthesiser) which has a baseband bandwidth of up to 400 MHz. In the subsequent chapters, data will be presented for bandwidths of 60, 96, and 240 MHz, where the latter provides more resolution for characterising indoor channels.

Doppler shift resolution is a measure of how closely paths can be resolved in velocity and is fundamentally set by the inverse of the channel sampling duration. Therefore, a longer sampling duration will correspond to a finer Doppler resolution. Since the entire channel measurements are performed for a duration of 1 second a Doppler shift resolution of 1 Hz is expected.

6.2.2 Measurement Range

The sweep repetition frequency (SRF), also known as $1/T$, where T is the duration of the chirp sweep, limits the unambiguous Doppler range to $\pm 1/2T$ Hz. In the case of MIMO sounding where the transmitter is sequentially switched, this Doppler range will be reduced in accordance to the total number of switched array positions. Hence, a 5 position switching system at the transmitter for 4 antennas (plus 1 gap period) will result in a Doppler range of $\pm\ 1/10T$ Hz.

In general, the choice of SRF is a compromise between time delay window and Doppler range. For a given LPF (within the heterodyne chain), a longer sweep duration would result in a greater time delay window. Thus, the duration of the chirp sweep must be chosen to allow the maximum expected time delay to be acquired unambiguously, while being short enough to observe the time variant nature of the channel from sweep to sweep. Here, the time delay window is defined as $B_{LPF} \times (T/B)$ seconds, where B_{LPF} is the bandwidth of the filter.

6.2.3 Spatial MIMO Sounder Resolution

For MIMO (and double-directional) channel measurements, there are some antenna array conditions which must first be met in order to allow sufficient spatial resolution. In general, there are more stringent constraints for spatial array measurements, where the object of the data processing is to identify directional or double directional multipath components for a given channel. Since most of the spatial channel measurements are done using circular arrays, a number of simple array parameters need to be identified. When employing circular array configurations for direction finding, the radius of the array is often the most critical parameter and is reviewed in [2, 3]. Reducing the radius of the antenna array will result in smaller side-lobe levels on the antenna correlation function. Here, the maximum array radius is given by

$$r_{max} = \frac{N\lambda}{4\pi} \tag{6.1}$$

where λ is the wavelength and N is the number of antenna elements. In [2] it was shown through extensive numerical simulations that the optimum radius required to enhance the performance of SAGE-type algorithms was

$$r_{opt} \approx \frac{N\lambda}{16} \le r_{max} \tag{6.2}$$

In most cases, the largest circumferential spacing between the adjacent array elements is $\lambda/2$, thus adhering to the spatial Nyquist sampling theorem [1]. Increasing the number of antenna elements in the array will often result in more accurate channel estimates. For general MIMO scenarios, where the main performance characteristic is channel capacity, the antenna array requirements are not so inflexible. Here, a $\lambda/2$ inter-element spacing would imply uncorrelated signals, however there is no reason why this spacing should not be greater. A larger inter-element spacing would generally result in less correlation between the antenna elements.

6.2.4 System Dynamic Range and Sensitivity

The instantaneous dynamic range is given as the ratio between the strongest and the weakest signal levels present at the same time for a given channel impulse response. A higher dynamic range would imply better detection of weak echoes as well as strong ones. Although a better SNR is generally desirable, it should be noted that signals which exceed a certain level could result in many undesirable characteristics. This includes amplifier saturation, and harmonic distortion introduced by the mixers. Therefore, the dynamic range is a compromise between SNR and distortion generated by sounder equipment itself. For real channel measurements, in-band interference can cause the overall noise floor to increase therefore decreasing the instantaneous dynamic range.

Ultimately the dynamic range is determined by the inherent characteristics of the sounder components. These include: phase noise of the phase-locked loops

(PLLs), harmonic distortion from the DDFS, number of bits used in the ADC (for data acquisition), distortion effects caused by high signal levels at the receiver, and the minimum detectable signal level at the receiver (i.e. the sensitivity).

Harmonic distortion caused by the high signal levels at the receiver front-end and the sensitivity of the sounder determine the upper and lower limits of the measurement range, respectively. High sensitivity at the receiver is critical for a reasonable dynamic range. This can be achieved by having a lower noise level at the IF output as well as having minimum noise contributions from the antennas and the receiver front-end components. Minimising the noise contribution from the receiver front-end can often be achieved by employing low noise amplifiers (LNA). For MIMO semi-sequential sounding, a number of other limitations are caused by the switching performed at the transmitter.

6.2.5 Frequency Standards

For most sounders, low drift frequency standards are required at both the transmitter and the receiver. The reliability of the sounder in unambiguously resolving the absolute time-delay and the smallest Doppler shift component is determined by the drift between the frequency standards. The relative drift between these units causes a shift in the time delay domain and is therefore required to be negligible compared to the channel sampling.

Rubidium frequency oscillators (PRS10 from Stanford Research Systems) have been employed as high standard 10 MHz reference clocks at the transmitter and the receiver [1]. Prior to any channel measurements these rubidium reference clocks have been adjusted by projecting them one against the other on the oscilloscope. The adjustment is in the order of ~0.9 ns/min. This gives a range error of less than 16.2 m within an hour, which corresponds to 3.24 range bins for a 60 MHz bandwidth signal [1].

6.3 Semi-Sequential MIMO Sounder Architecture

The basic principle of the semi-sequential chirp sounder is illustrated in figure 6.1. Here, the system sequentially transmits a wideband chirp sweep on each of the antennas. At the receiver, a replica of this transmitted chirp signal is mixed with the received signal, the output of which is then filtered leaving a beatnote for every propagation path (heterodyning principle). The sounder receiver employs multiple channels all the way from the RF front-end to the data acquisition board. Each RF channel is connected to a separate antenna in the receiver array. The use of parallel receive channels allows high resolution spatio-temporal measurements of the radio environment without further reducing the effective channel sampling rate. After the beatnotes are acquired, the information is digitised and stored on a computer for offline analysis. The frequency of the beatnote (or beat frequency) is linearly proportional to the delay experienced in the channel for each resolvable multipath component.

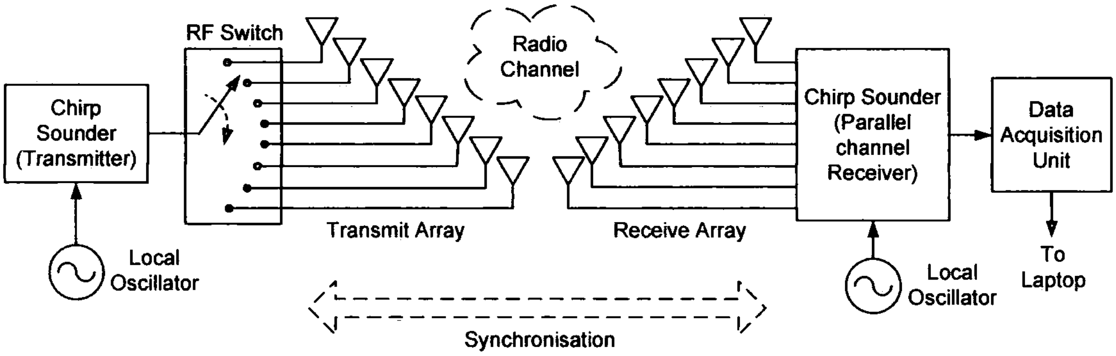

Figure 6.1: The concept of semi-sequential MIMO chirp sounding.

Synchronisation of the sounder units is critical for practical channel measurements. This is to ensure that the chirp waveforms generated at both ends of the channel are aligned such that any discernible time delay difference can be analysed. Synchronisation can be achieved through different means [4, 5]. A wire link between the transmitter and the receiver can be used to achieve synchronisation, however this is not very practical for channel sounding due to the inherent flexibility issues. Another method is synchronisation via the GPS (Global Positioning Satellite), however this is also impractical for indoor channel measurements. The technique employed here was to introduce a programmable start-of-sweep delay in the generation of the chirps, such that synchronisation is achieved at both ends of the radio link. Due to the low drift between system clocks, this delay needs to be introduced only once at the start of the measurement process.

6.3.1 Generation of the Chirp Signal

The MIMO chirp sounder developed here has a programmable bandwidth up to 300 MHz and a SRF up to 300 Hz. The sounder employs a programmable DDFS, which is clocked at 1.6 GHz to produce a swept output signal at up to 400 MHz. This is preferred, since it avoids flyback transients of phase-locked loop (PLL) generation techniques and gives programmability of bandwidth and repetition rate, which cannot be achieved with passive surface acoustic devices [6]. A block diagram of the chirp generator is illustrated in figure 6.2. This consists of a DDFS, two PLL synthesisers, a mixer, an inter-digital band-pass filter (BPF) and a high stability Rubidium clock.

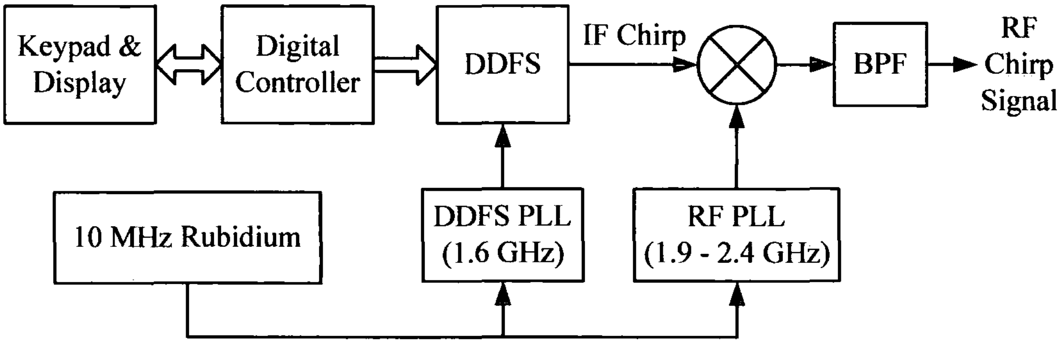

Figure 6.2: RF Chirp generator block diagram.

The chirp signal bandwidth, B, centre frequency, f_c, and SRF are entered into the keypad in order to program the digital controller board. The digital controller via an on board accumulator then continuously programs the DDFS with 24 binary bits at an update rate of 1.25 MHz between the initial frequency f_1, and the final frequency f_2 with Δf frequency step. The chirp signal is then up-converted after mixing with a RF carrier. The frequency of this carrier is programmable according to the measurement specifications, however, a 2.36 GHz carrier is assumed here. A band-pass filter is employed to suppress the unwanted frequency band produced after the mixing process. This process is illustrated in figure 6.3 for suppression of the upper frequency band.

The major advantage of the aforementioned approach is the flexibility in changing the band that the sounder operates in, which is achieved by programming the RF PLL to operate at a different frequency, and adjusting the band-pass filter settings.

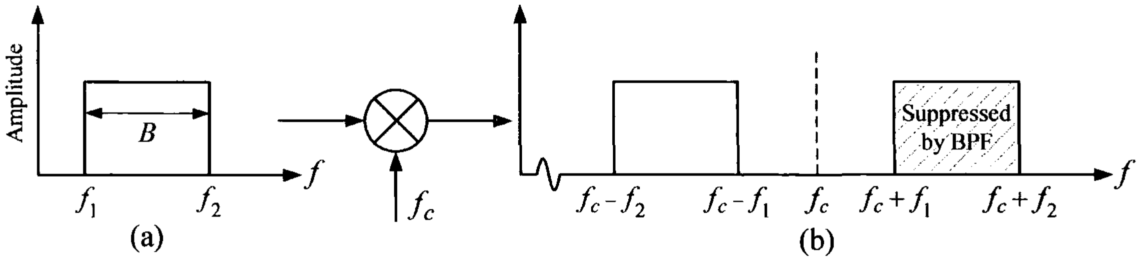

Figure 6.3: (a) Spectrum of the IF chirp signal generated at the output of the DDFS, and (b) up-converted and filtered RF chirp signal.

The chirp generator employs a staircase type approximation to the ideal chirp spectrum, meaning that the DDFS has to sweep from frequency f_1 to f_2 in steps of Δf. In essence, this infers switching between frequency components that are Δf_i Hz apart every Δt_i seconds, as shown in figure 6.4. Consequently, this introduces unwanted sidebands, whose levels are related to the frequency step size, Δf_i, and the switching time interval, Δt_i.

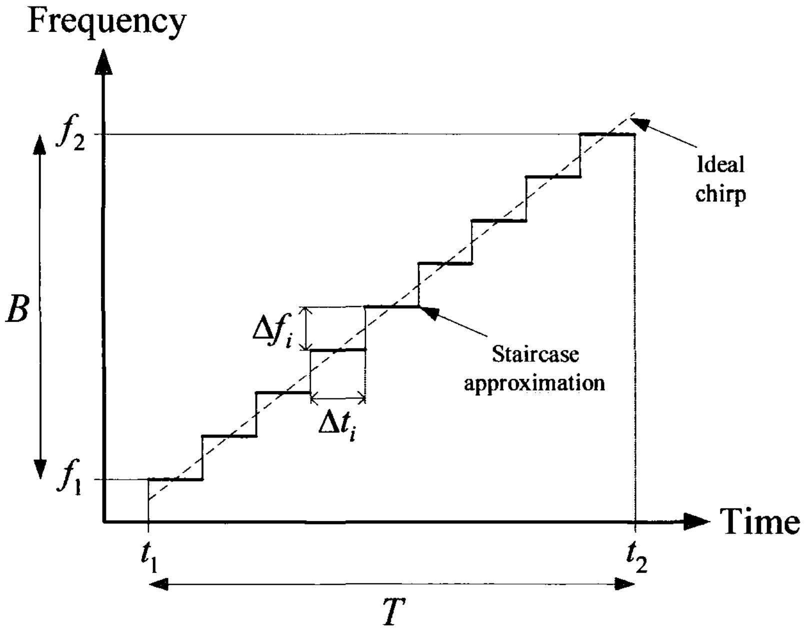

Figure 6.4: Staircase approximation of the chirp signal.

In the above, Δf_i is the frequency step and Δt_i is the time duration with respect to the DDFS output. The DDFS update rate, F_U, in this case is 1.25 MHz, which corresponds to $\Delta t_i = 800$ ns.

There are other chirp generation techniques including passive generation and quadrature analogue generation. The passive generation technique utilises SAW

(Surface Acoustic Wave) devices in order to generate the chirp signal. However, the major limitation with this technique is the low time-bandwidth product, which leads to low processing gain and short chirp durations. In quadrature analogue generation, the output of the DDFS is taken in both in-phase and quadrature, and is then combined using an analogue SSB (Single Sideband) modulator.

6.3.1.1 Digital Controller Board

The DDFS is programmed to produce the chirp signal at IF, but also provides the synchronisation for the system by allowing a programmable delay at the start of the sweep [7-11]. A block diagram of the digital controller board is shown in figure 6.5.

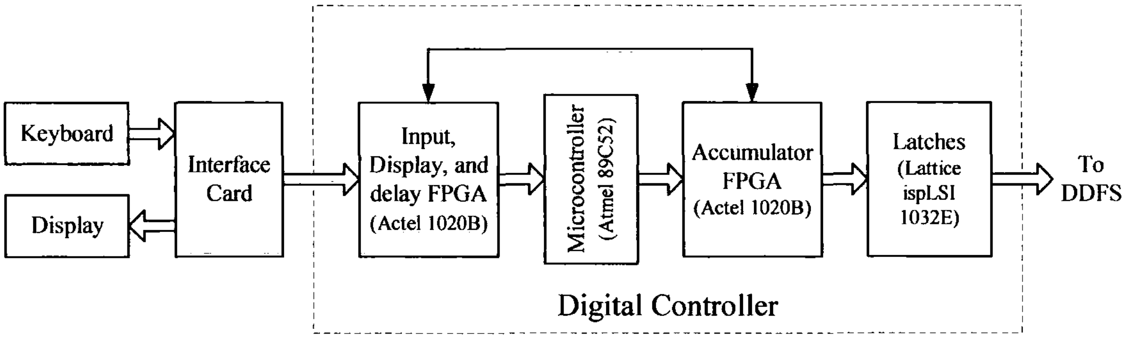

Figure 6.5: Digital controller block diagram.

The first section shown in figure 6.5 is the front panel interface, which consists of a hex keypad used to enter the chirp parameters (B, f_c, and SRF), an alphanumeric (LED) display for displaying the entered parameters and a card which acts as the logic interface between the entered chirp parameters (via the keyboard) and the digital controller board [12]. Once all the parameters are entered, they are transferred to the first FPGA (Field Programmable Gate Arrays) by a push button. This input, delay, and display FPGA acts as the initial buffer on the board by storing the entered parameters. It provides the interface between the keypad and the display and also the control logic corresponding to the keys on the front panel, such as enter, clear, reset and start. This input FPGA also contains a delay counter (BCD down-counter), which makes it possible to introduce a variable delay in the generation of the chirp signal. This is so that the synchronisation of the chirps can be achieved in the transmitter and the receiver units.

The next stage of the digital controller is the microcontroller. This has the main task of performing the calculations required to transform the entered parameters into binary values f_1, Δf, and f_2, and sending these binary values to the accumulator FPGA. The microcontroller also allows programmability via an RS232 serial interface, which makes it possible to enter all parameters via the PC. The parameter conversion in the microcontroller is described in appendix A2. This includes part of the PLM file used to program the microcontroller.

The accumulator FPGA actually holds the binary values of f_1, Δf, and f_2. It then performs the accumulation process from the initial chirp frequency, f_1, to the final chirp frequency, f_2, in incremental frequency steps of Δf. Each increment value is latched and sent to the DDFS, in order to generate N sine waves with frequencies f_1, $f_1 + \Delta f, f_1 + 2\Delta f, \ldots, f_2$. As shown in appendix A3, the digital controller was built with on-board latches and a timing circuit. Two controller boards were made using Protel Software. The FPGA logic designs (Actel) are given in [11].

6.3.1.2 Direct Digital Frequency Synthesiser (DDFS)

In direct digital synthesis (or digital lookup synthesis), a digital-to-analogue converter (DAC) uses the output from a digital sine and/or cosine lookup table to generate a sinusoidal waveform. In general, a direct digital synthesiser consists of a phase accumulator (an adder), a sine lookup table (read-only memory), a DAC and a low-pass filter (LPF), as shown in figure 6.6 [13].

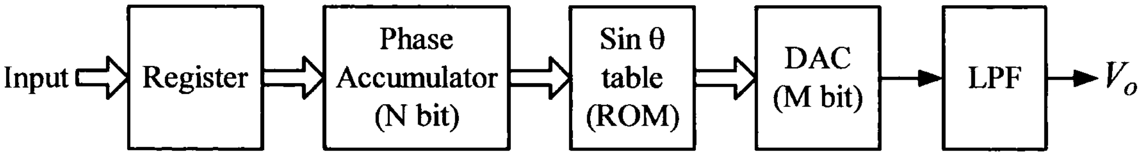

Figure 6.6: block diagram of the direct digital synthesis technique.

For the DDFS used in the sounder (Sciteq ADS-431-403A), there are two memories (sine and cosine), two DACs, and two low-pass filters, which are used to produce a quadrature output (I and Q). The system clock used in this case is 1.6 GHz at ~10 dBm, allowing a maximum frequency output of 400 MHz (1.6 GHz / 4). For the Sciteq model, a frequency strobe is used to control the latching of the programmable bits into the DDFS register (figure 6.6). The register stores these bits until the next time the frequency strobe signal goes high (level triggered). It should be noted that the phase accumulator can be reset at any point in the synthesiser's operation by a reset button on the front panel. For the sounder, a phase reset (i.e., the SRF) is used to reset the accumulator at the end of every chirp sweep. The sounder described here utilises only one sinusoidal output to produce the chirp waveform at IF.

The sine lookup table stores 2^N uniformly spaced values of the sine function, and provides a digital output that is equal to the sine of the linearly increasing phase data from the accumulator. The DAC converts the digital values into a discretised sine waveform, which is low-pass filtered to provide an analogue sine wave output. The output waveform can be expressed as

$$V_o = A\sin\left(\frac{2\pi f_c W t}{2^N}\right) \tag{6.3}$$

where f_c is the clock frequency, and W is the input frequency control word. For the DDFS, f_c is equal to 1.6 GHz and W is a control word which determines the output frequency. For 30 bits and 1.6 GHz, this is 0.745 Hz. For the present IF chirp generator, a 24-bit (24 most significant bits) parallel control line was adequate giving a frequency resolution of 23.84 Hz.

6.3.2 MIMO Sounder Transmitter

The following describes the operation of the semi-sequential transmitter unit, which was developed as modular sub-systems. A photo of the MIMO sounder transmitter accompanied by a detailed block diagram is shown in figure 6.7 and figure 6.8, respectively. From these figures, it is possible to identify the various transmitter sub-systems. These are: (1) the 10 MHz Rubidium clock with a number of TTL (and sinusoidal 50 ohm) outputs, (2) the IF chirp generator, including keypad and display, (3) the programmable 1.6 GHz PLL synthesiser for the DDFS, (4) the programmable RF PLL synthesiser, (5) the up-converting unit, consisting of a mixer, band-pass filter and amplifier, (6) the 8-way RF switch, and (7) the high-power amplification stage used only for certain long-range outdoor measurements.

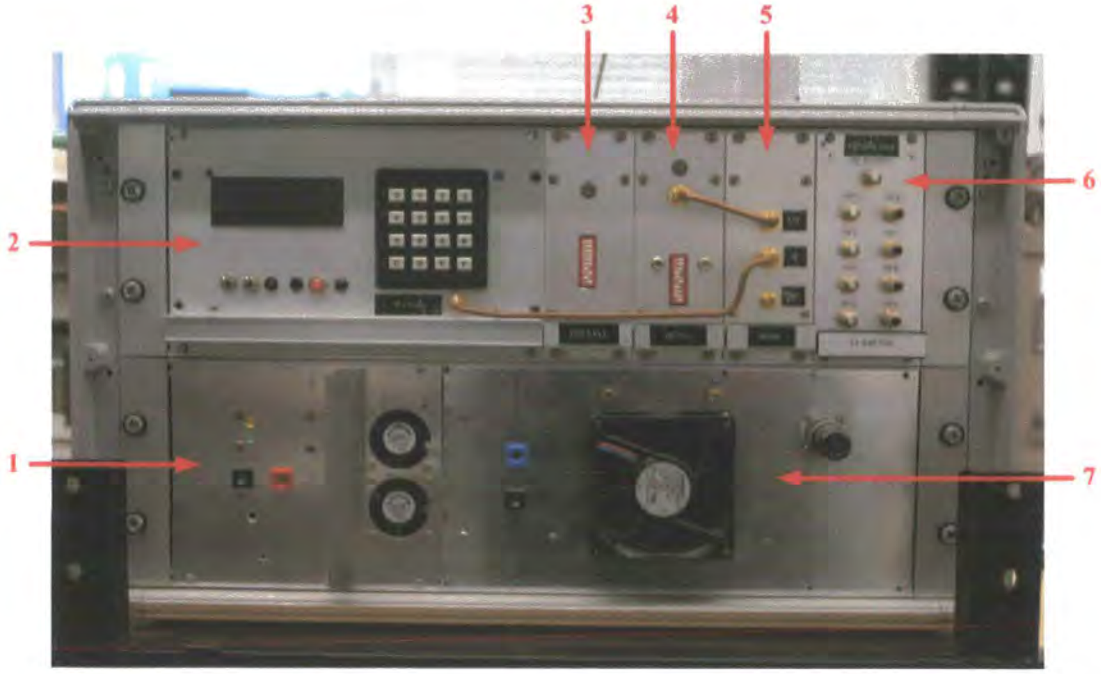

Figure 6.7: Photo of MIMO chirp sounder transmitter.

The transmitter rack consists mainly of an AC-DC converter (mains 240 V_{AC} to 24 V_{DC}) and a number of DC-DC converters for 5V, 12V, and 15V supplies. The RF section of the transmitter consists of two amplifiers, generating a 1 W output. However, most of the measurements presented in this thesis use transmit power levels below 20 dBm (sub 100 mW). It should be noted that the output of the DDFS (IF chirp) in figure 6.8 is at -4 dBm, while the output of the RF PLL is at ~ 7 dBm (level-7 mixer). Attenuators are used for 50 Ω matching into the mixer ports. Once the IF Chirp signal is up-converted and filtered (leaving a single measurement band), a multiplexer is employed to switch between the antennas in the transmit array. The switching of the antennas in this case is achieved by a programmable control FPGA.

Figure 6.9 shows a typical RF chirp sweep which is transmitted sequentially on each antenna. Here, the bandwidth is 240 MHz and the SRF is 250 Hz. The band of interest in this case is from 2.26 GHz to 2.5 GHz.

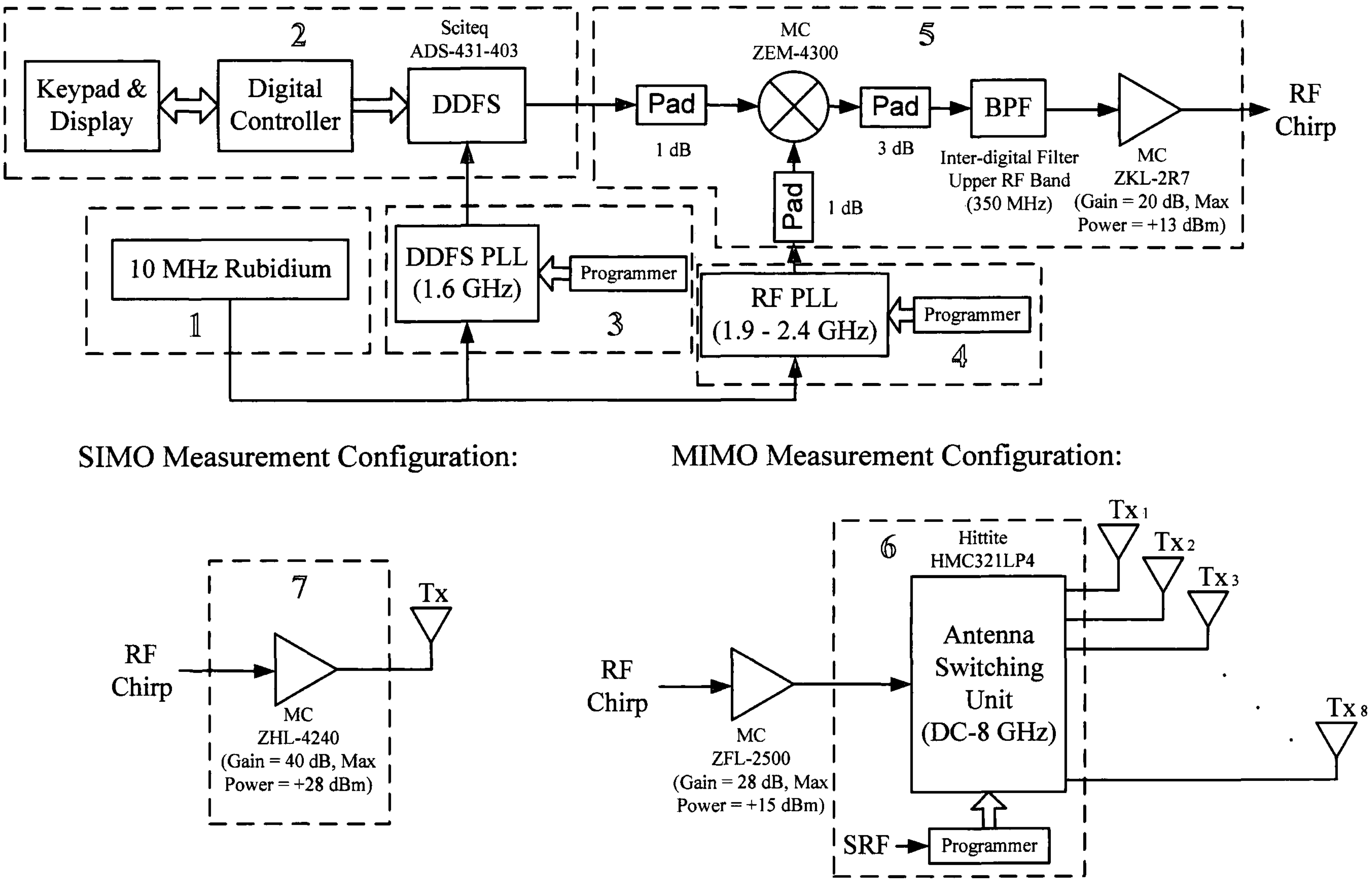

Figure 6.8: Detailed block diagram of transmitter.

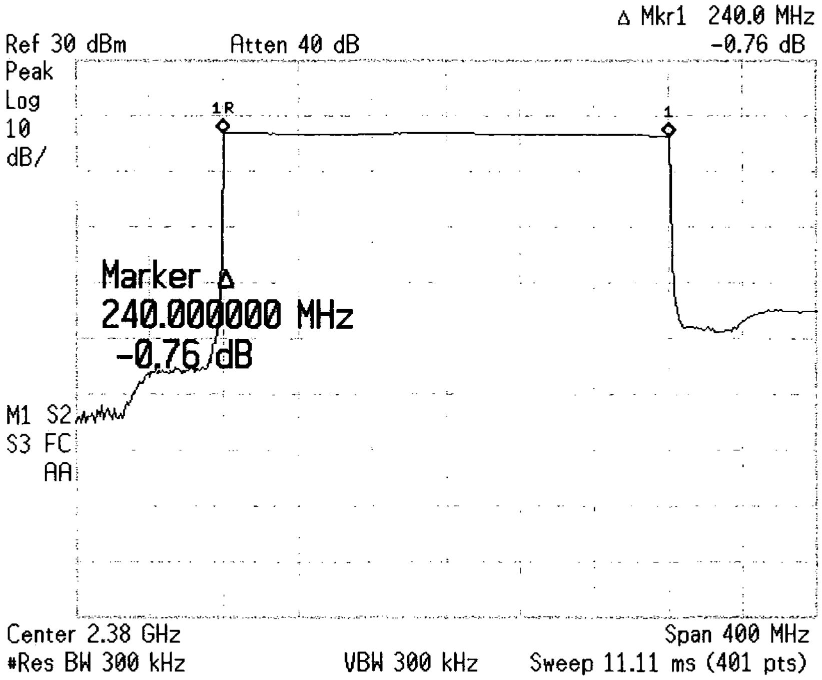

Figure 6.9: Spectrum of the RF chirp signal with 240 MHz bandwidth.

6.3.3 MIMO Sounder Receiver

The 8-channel receiver architecture is shown in figure 6.10 and figure 6.11. This receiver contains: (1) the 10 MHz Rubidium clock with multiple TTL and sinusoidal outputs, (2) the IF chirp generator, (3) the programmable 1.6 GHz PLL synthesiser for the DDFS, (4) the programmable RF PLL synthesiser, (5) the up-converting unit required to produce the replica chirp waveform at RF, (6) the 8-way local oscillator distributor required to produce 8 replicas of the RF chirp signal with gain, one for each channel, (7) the 8-channel receiver RF front-end (each section containing 2 channels) consisting of several amplifiers and a filter per input, (8) the synchronisation unit, and (9) the 8-channel signal conditioning unit which uses a set of small signal amplifiers and low-pass filters. Units (1) – (5) are common in both the transmitter and the receiver systems. Details of the DAU interface software and units (7) – (9) are provided in [1].

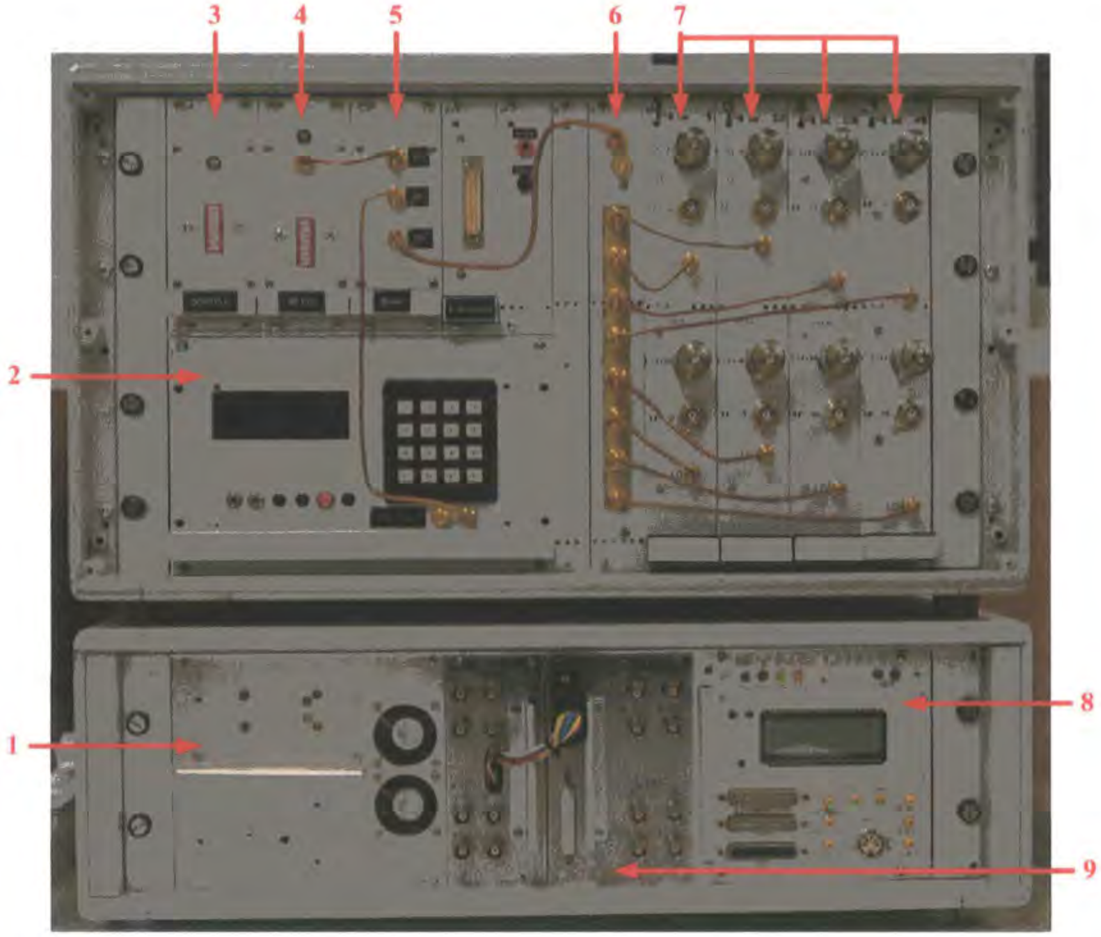

Figure 6.10: Photo of MIMO chirp sounder receiver.

The power supplies in the receiver racks are similar to those used in the transmitter. An additional 12V 2.5A supply was required to provide an adequate DC supply. The generation of RF chirp signal in the receiver rack is identical to that used in the transmitter. This signal is amplified and split 8-ways to provide a local oscillator (LO) signal to each channel. Here, the RF chirp replica is at ~ 10 dBm for a level-10 mixer (MC145). In the receiver front-end a ZEL1724LN low noise amplifier (LNA) is used to amplify the received signal, while minimising the noise power, and this is then followed by a band-pass filter. The received signal is further amplified to provide an adequate signal level before the mixer (up to ~ 60 dB of gain prior to the mixer). In addition to this gain, a 5-bit Hittite HMC235QS16G digital attenuator is employed to provide up to 31 dB of attenuation. These attenuators are controlled by an 8 line logic bus which would normally connect to the synchronisation unit and is visible on the front rack. These attenuators are important for close range measurements were it is possible to overload the mixers.

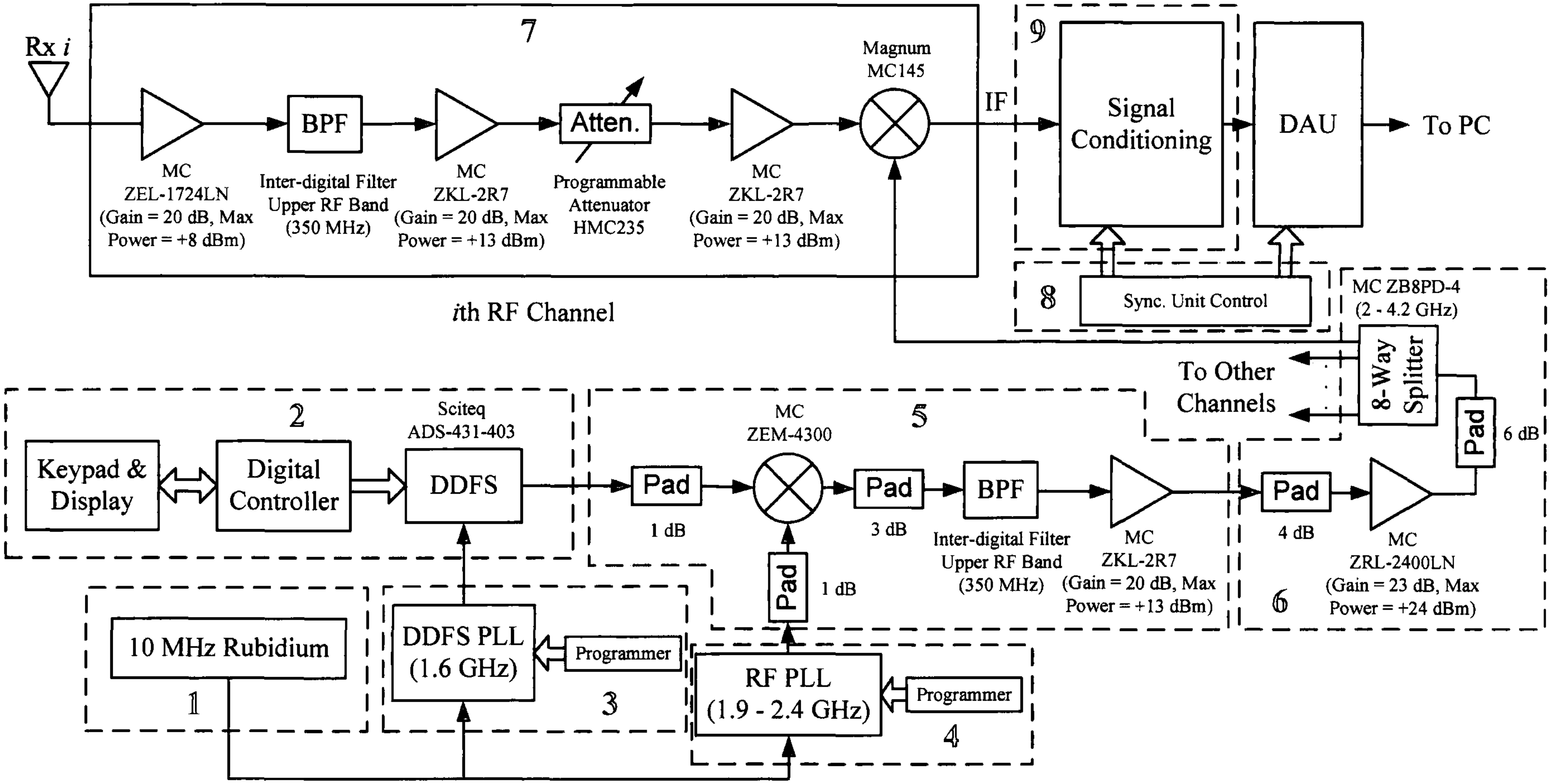

Figure 6.11: Detailed block diagram of receiver (only showing a single RF channel).

As noted previously, compression is achieved by mixing the amplified receive signal with a locally generated chirp replica. The IF output is then fed into the signal conditioning unit which consist mainly of variable gain amplifiers and low-pass filters (LPFs) [1]. The IF signals are typically filtered to remove the sum components, therefore leaving just the beatnotes, which are then digitised and stored using the data acquisition unit (DAU). The other purpose of the LPFs is to provide the different time delay windows which are required and to act as an anti-aliasing filter. Since most time-series data (beatnote signals) are acquired at a sampling rate of 1 MSamples/s, a suitable cut-off frequency for the filters is 250 kHz.

The role of the synchronisation unit within the receiver system is critical [1]. This unit is actually responsible for all the command-controls of the system. It controls the flow of the data between the PC (which contains the DAU) and the sounder, the signal conditioning unit, the programmable attenuators within each RF channel, and a host of other sub-systems [1]. In addition to these, it creates all the necessary synchronised clocks for the DAU.

After the pre-conditioning of the IF signals via the signal conditioning unit, the beatnotes are band-limited and within the range of the DAU in the PC, which is -1.25V to +1.25V (2.5V peak-to-peak). The DAU was constructed at UMIST (Manchester) by Dr. Ian Hawkins. This eight single-ended channel data acquisition card contains 128 MB on board RAM with programmable sampling rate up to 1 MSamples/s. The ADCs used in the board are serial 8-bit converters, giving a dynamic range of 48.16 dB ($20\times\log_{10}(2^8)$). The card has an ISA interface bus and programmable circuitry to enable the choice of the sampling rate, the number of sweeps to be sampled, and the number of simultaneous channels to be digitised. The card also counts the number of samples per sweep and communicates this to the host PC. The interface software displays the digitised signal either in the time domain or in the frequency domain for online monitoring of the impulse response [1]. The data is then stored and transferred to another PC for offline analysis. For the measurement results presented in the forthcoming chapters, the number of sweeps collected was typically 250 at a rate of 1 MSamples/s, corresponding to 4000 samples per sweep.

6.3.4 Antenna Switching

The RF switch used for sequentially selecting the antennas in the transmit array is the HMC321LP4 model from Hittite Microwave Corporation. The HMC321LP4 is a broadband (DC – 8 GHz) non-reflective GaAs SP8T switch, which can permit the switching of up to 8 antenna elements. This switch has an integrated positive supply 3:8 TTL decoder, meaning that only 3 control lines (A, B, C) are required to select any of the antennas at any one time. The setup required for the switching of 4 transmit antennas is shown in figure 6.12, where a lattice FPGA (model ispLSI 1032E) is used as a re-programmable control unit with the SRF as the input and control lines A, B, and C, as the outputs. The RF switch typically provides 35-40 dB of isolation, which is adequate for MIMO channel measurements. Better isolation could be provided by relay switches, however the switching time required is far too long for the applications mentioned here.

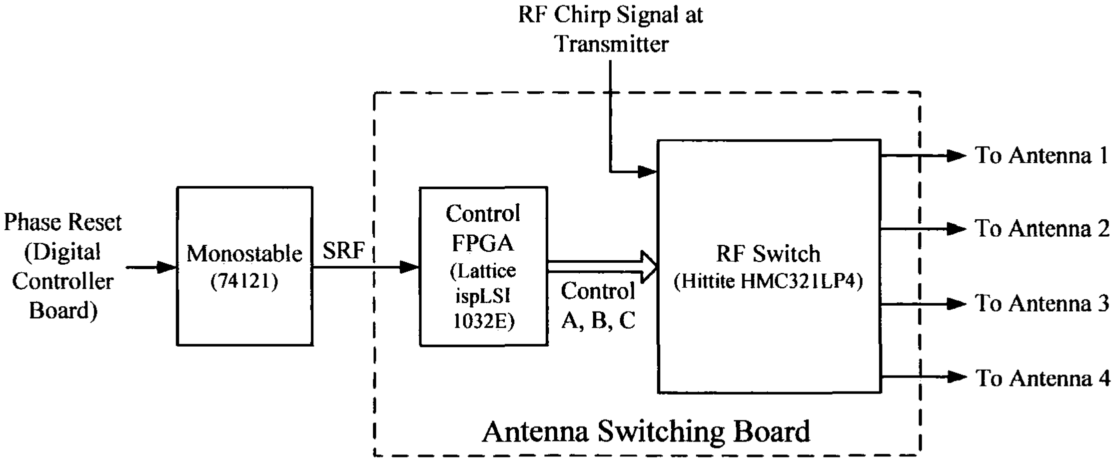

Figure 6.12: Block diagram of the antenna switching board (for 4 transmit antennas).

The low frequency SRF input into the FPGA is derived from the phase reset on the digital controller board. This is achieved by widening the narrow phase reset pulse used to control the reset of the DDFS after every chirp sweep. A photo of the RF switching unit (inside enclosure) is shown in figure 6.13. Originally two of these units were developed (for the transmitter and the receiver) to allow the use of a single channel, fully sequential sounder, if required.

Figure 6.13: Photo of 8-way RF switch.

6.3.4.1 Switching Control

The antenna switching at the transmitter can be achieved by a simple synchronous counter, which is required so that there is no accumulated drift in the switching time. If the RF switch is to transmit sequentially on 4 antennas without any gap period, a very simple two-stage synchronous counter could be used. In such a case, the MSB (most significant bit) control line on the switch can be held high, or low. Using D-type flip-flops, the general rule for an n-stage synchronous counter is

$$D_n = Q_n \oplus Q_{n-1} \cdot Q_{n-2} \cdots Q_2 \cdot Q_1 \tag{6.4}$$

where D_n is the D input of n^{th} flip-flop, and Q_n is the Q output of the n^{th} flip-flop. In the above, the symbol ⊕ denotes an exclusive OR operation. For a two-stage counter:

$$D_1 = Q_1 \oplus 1 = \bar{Q}_1 \tag{6.5}$$

$$D_2 = Q_2 \oplus Q_1 \tag{6.6}$$

However, this simple two-stage counter is not the best choice. For MIMO channel sounding, it is practical to have at least a single gap period in the transmit sequence, such that the MIMO data matrix at the receiver could be easily constructed by knowing the sequence of transmit antennas. For example, this infers that for a 4 × 4 channel matrix, an additional gap should be used at the transmitter such that the multiplexing occurs across 5 switch ports instead of 4 (figure 6.14). Here the synchronous counter is slightly more complicated, since it does not have a full range of 2^n states. With this in mind, the counter's present and corresponding next states are listed and then the count is prematurely terminated on the 5th state. The undefined states are then labelled as 'don't care' terms and all of the states are transferred to Karnaugh maps where the corresponding canonical logic expressions are extracted and simplified [14]. These functions are then used to define the synchronous counter. Further information about the logic used in the FPGAs is provided in appendix A4.1. The programming of the Lattice ispLSI 1032E chips was done via ispDesignExpert v8.0 (mature software product). A PC parallel port interface can be used to reprogram the chirps for different switching configurations.

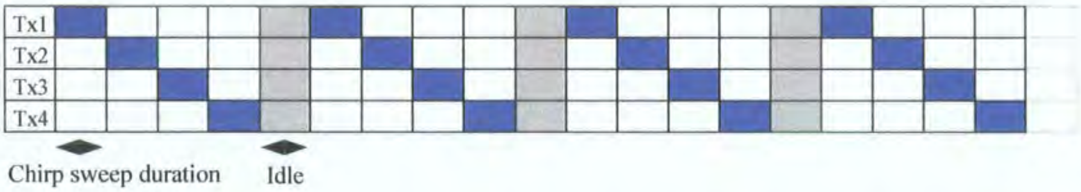

Figure 6.14: Antenna switching scheme when 4 transmit antennas are employed.

6.3.5 Inter-digital Filters

Band-pass filters are necessary to reject unwanted frequencies. In the case of the RF front-end, 8 filters (per channel) are required for out-of-band interference, while the filters employed in the chirp generators have the purpose of passing only a single frequency band after the mixer. Because of interference from the UMTS-FDD downlink band (2.11 – 2.17 GHz), band-pass filters were designed to reject these unwanted frequencies and to give a pass-band of at least 300 MHz for the chirp signal. The design process for these filters is based on [15-19] and is described in great detail in appendix A5. In total, 11 filters were cut by the machine shop, within the School of Engineering. Figure 6.15 shows a photo of one filter, where brass screws were used for tuning the frequency response.

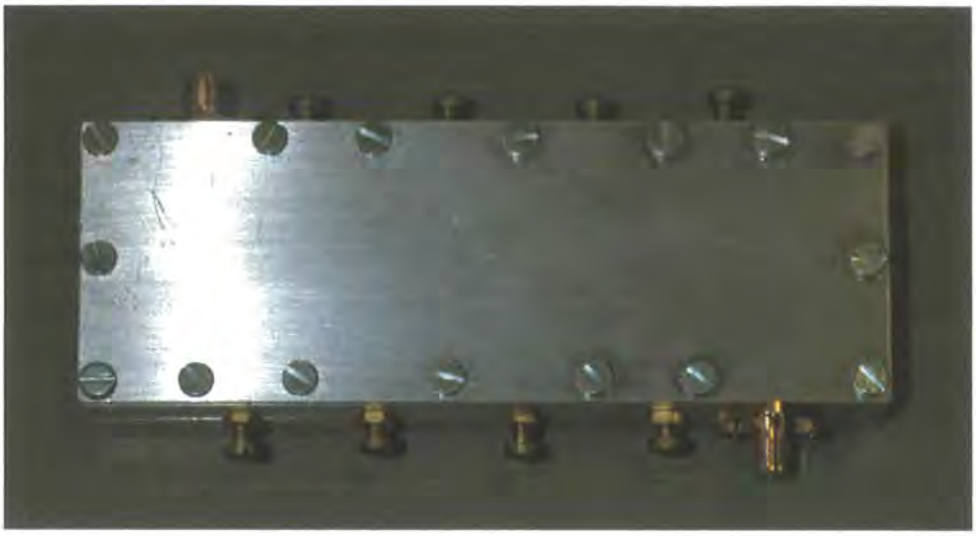

Figure 6.15: Photo of inter-digital band-pass filter.

6.3.6 PLL Synthesisers

Phase-locked loop (PLL) synthesisers are the building blocks of many communication systems. In the sounder described so far, these oscillators are locked to the 10 MHz rubidium standard and provide the source signal for the DDFS and the RF up-converter/down-converter units. The requirement here was to develop four synthesisers, two working at 1.6 GHz for the DDFS in both the transmitter and the receiver, and another two working between 1.9 – 2.4 GHz (optimally at 2.36 GHz but adequate performance down to 2.1 GHz) for the RF up-converter (transmitter) and the down-converter (receiver).

The design for these PLLs are based on the Zarlink (originally by Plessey) parallel load 2.8 GHz synthesiser (part# SP8855E) and the Micronetics (originally by Qualcomm) voltage controlled oscillator (VCO part# M3500C-1324T or M3500C-2032T). The choice of synthesiser is mainly due to the programmability of the oscillator frequency. This is particularly useful for the RF PLLs described in the system block diagrams.

The suggested design approach and analysis for these PLLs are provided in the SP8855E data sheet. Information about the design parameters of the PLL synthesisers is given in [20-24]. A detailed description of the PLL designs and performance tests is provided in appendix A6. Figure 6.16 shows a photo of the PLL synthesisers used in the transmitter rack.

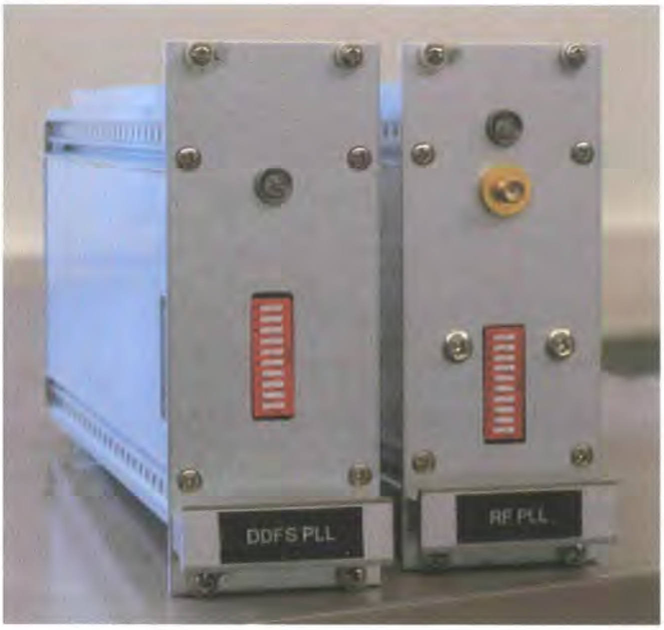

Figure 6.16: Photo of the PLLs used in the sounder.

6.4 Wideband Multi-Channel Sounder Performance

This section describes a number of calibration tests used to asses the performance of the wideband multi-channel chirp sounder. These tests are namely, the single-tone test including the ambiguity function of the system (delay vs. Doppler), and the two-tone test.

6.4.1 Single-Tone Test

The single-tone test is the most basic method of examining the performance of the sounder. This test provides the back-to-back impulse response and ambiguity function (delay vs. Doppler) of the sounder in the presence of a single arriving wave, which is achieved through the use of an RF cable between the transmitter and the receiver, with the necessary attenuators to reduce the signal power. Figure 6.17 shows the basic configuration required to test the system response for 8 channels simultaneously. For a sensible power level, there is typically ~ 70 dB of attenuation before the receiver due to the 60 dB of gain in each of the RF front-end channels. This depends entirely on the transmit power level and in case the power amplifier is used as shown in figure 6.8, ~ 100 dB of attenuation is required. Therefore, a typical power level at the receiver RF input is between -80 to -90 dBm.

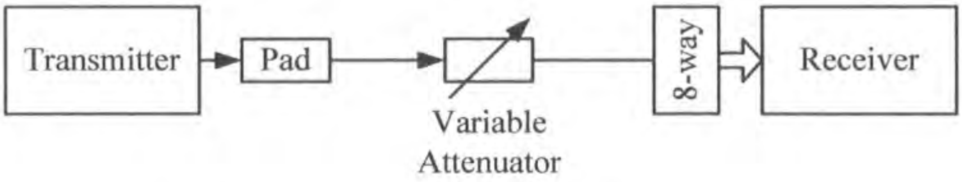

Figure 6.17: Configuration for single-tone test.

Figures 6.18 and 6.19 show the sounder back-to-back response which was averaged over 250 sweeps (in 1 second) for all 8 receive channels. These figures show the beatnote power against time delay normalised to the overall maximum power. From this it can be deduced that a dynamic range of at least 30 dB is attainable for a broadband 240 MHz sweep centred on 2.38 GHz. At closer inspection (figure 6.19), the 6 dB width of the impulse response from the peak is typically less than 8 ns (~ 2 range bins). The maximum delay range (τ_{max}) for the 240 MHz sweep in this case is 4.17 us.

The FFT of the channel impulse response gives the time-variant transfer functions per sweep. By averaging this over all the sweeps in 1 second, a similar result could be achieved in the frequency domain. Figure 6.20 shows the average channel transfer function for all 8 receive channels.

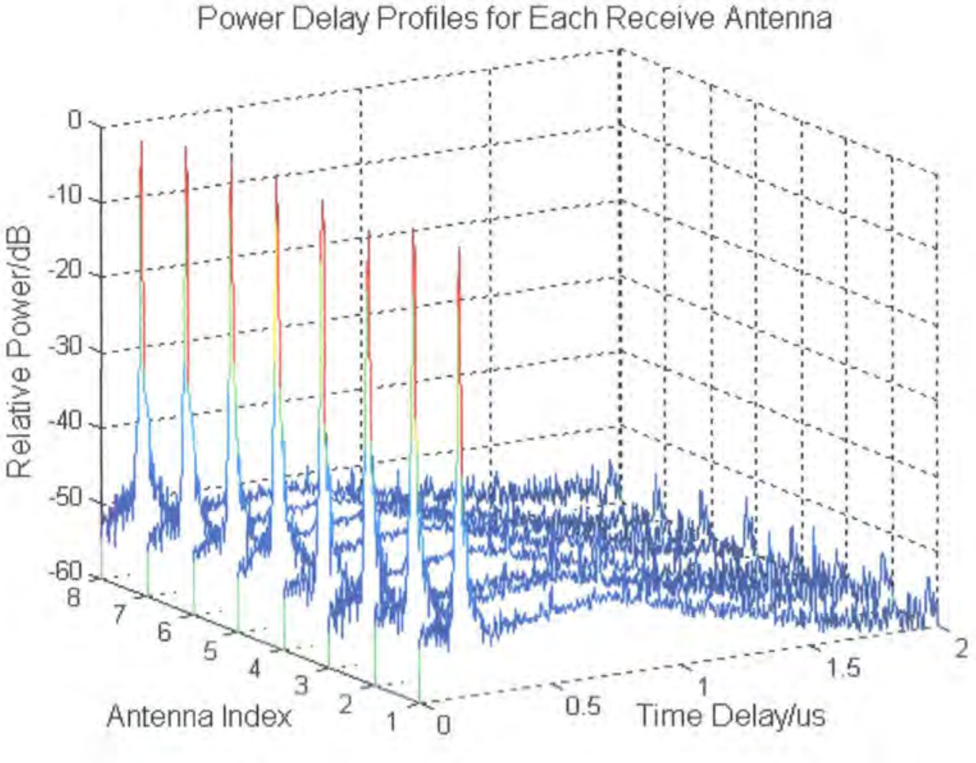

Figure 6.18: Single-tone impulse response.

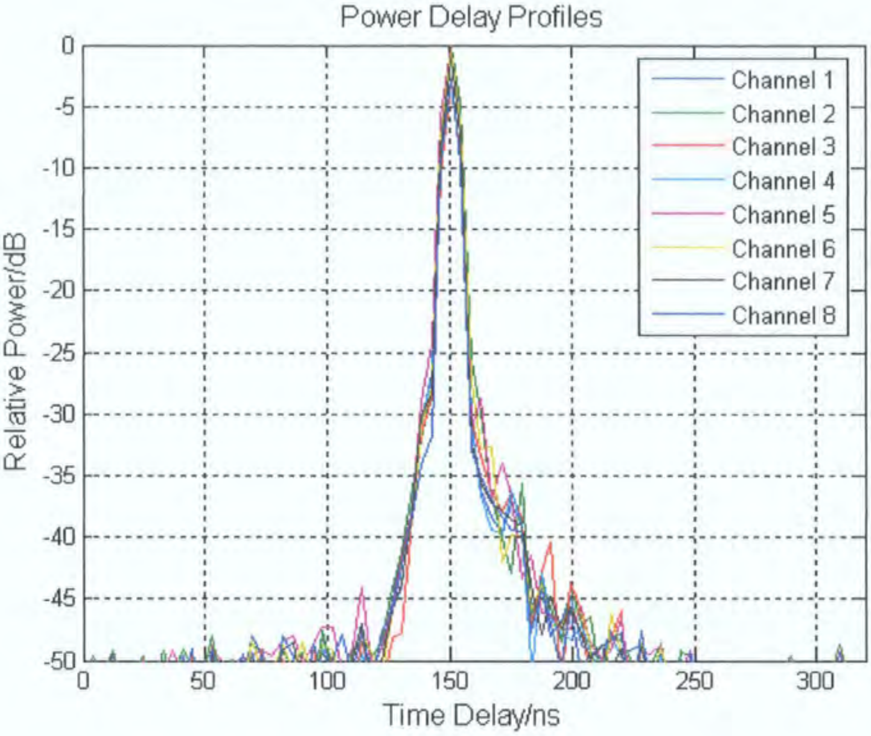

Figure 6.19: Single-tone impulse response (zoom).

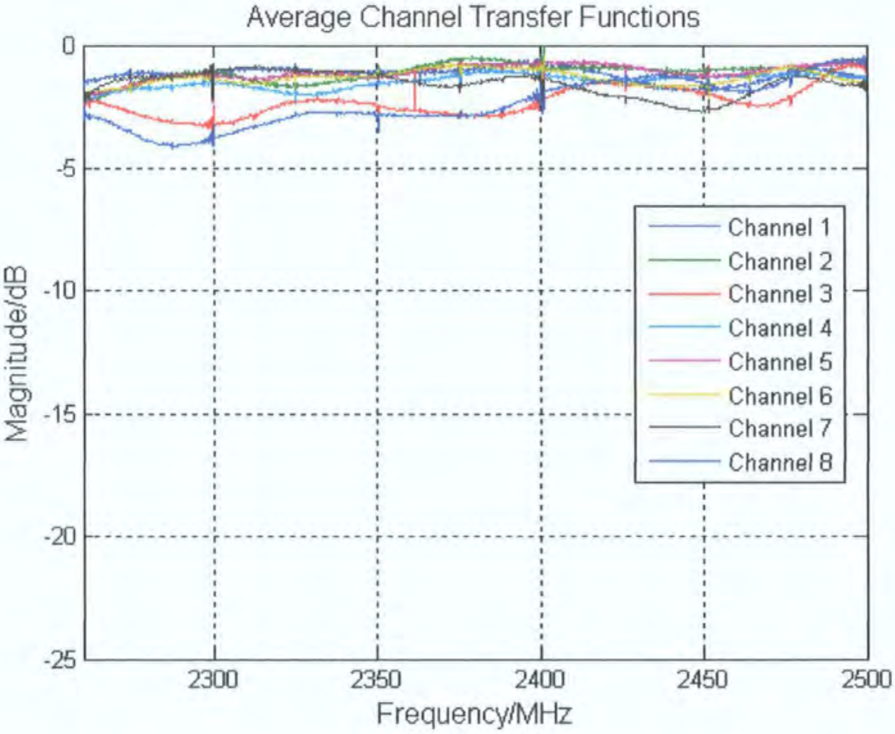

Figure 6.20: Back-to-back average transfer function.

6.4.1.1 Ambiguity Function

The ambiguity function is necessary to evaluate the Doppler shift resolution of the sounder. Figure 6.21 shows 8 plots, which represent the received single-tone response as a function of both time delay and Doppler shift information per channel. These plots correspond to a dynamic range of 35 dB (baseline). For 250 sweeps acquired in 1 second, the Doppler range for this system is ± 125 Hz for a SIMO configuration and typically ± 25 Hz for a 4 × 4 MIMO configuration.

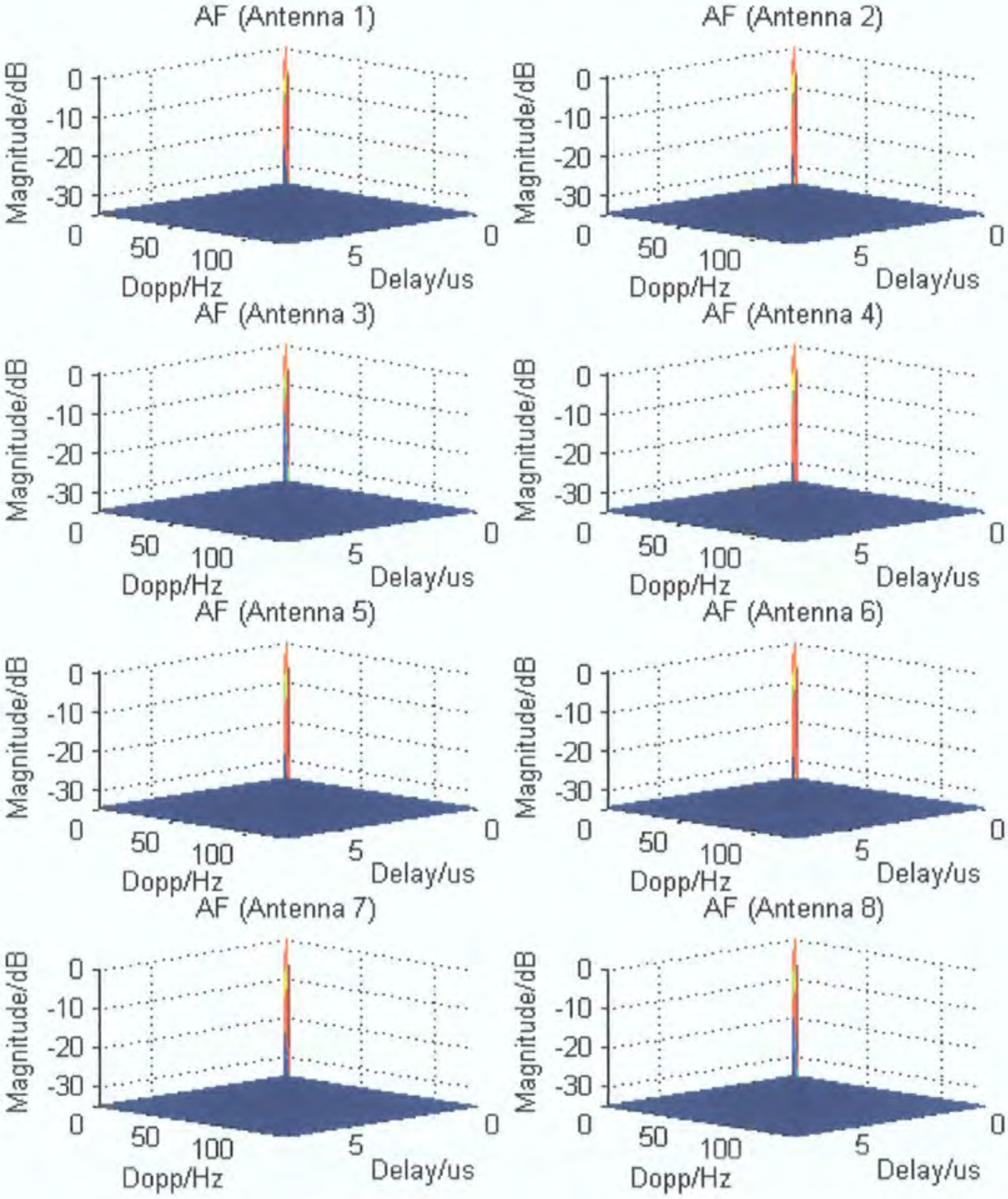

AF (Antenna 1)

AF (Antenna 2)

AF (Antenna 3)

AF (Antenna 4)

AF (Antenna 5)

AF (Antenna 6)

AF (Antenna 7)

AF (Antenna 8)

Figure 6.21: Ambiguity function for each channel.

In general, single-tone tests present a first order assessment of the system performance and are often performed prior to any measurement campaigns. Apart from showing the innate measurement range of the sounder, these results are also used to compensate for the channel gains of the sounder.

6.4.2 Two-Tone Test

A two-tone test is commonly used in order to assess whether there are any inter-modulation products introduced by the system when the received signal contains one echo. For this test, the transmitter signal is connected to a two-way power splitter, where one of the outputs is connected to an attenuator with a short cable (typically ~ 1m), and the other is connected to a longer length or reel of cable. These outputs are then combined and connected to the receiver via more attenuators, thus producing two distinct tones at the receiver. The delay of the second tone is dependent on the cable length. For this case, a 1 meter cable was used for the principle beatnote and a 4 meter length of cable was used to produce the echo path. Since the speed through a coaxial cable is approximately 0.7 times that of free space, it could be estimated that the relative delay between the two paths is 14.3 ns (3m/0.7×c). As previously noted, an appropriate level of attenuation was required before the receiver, and here the overall attenuation was 80 dB. The basic configuration for a two-tone test is shown in figure 6.22, followed by the delay response shown in figures 6.23 and 6.24. The results demonstrate that for this input level, there are no observable inter-modulation products introduced by the system and that the performance of the sounder across all 8 channels is similar.

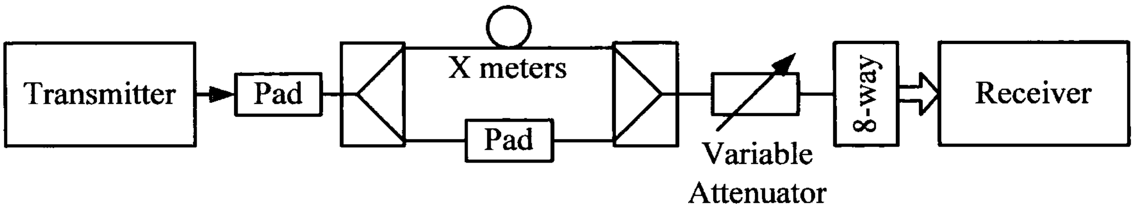

Figure 6.22: Configuration for two-tone test.

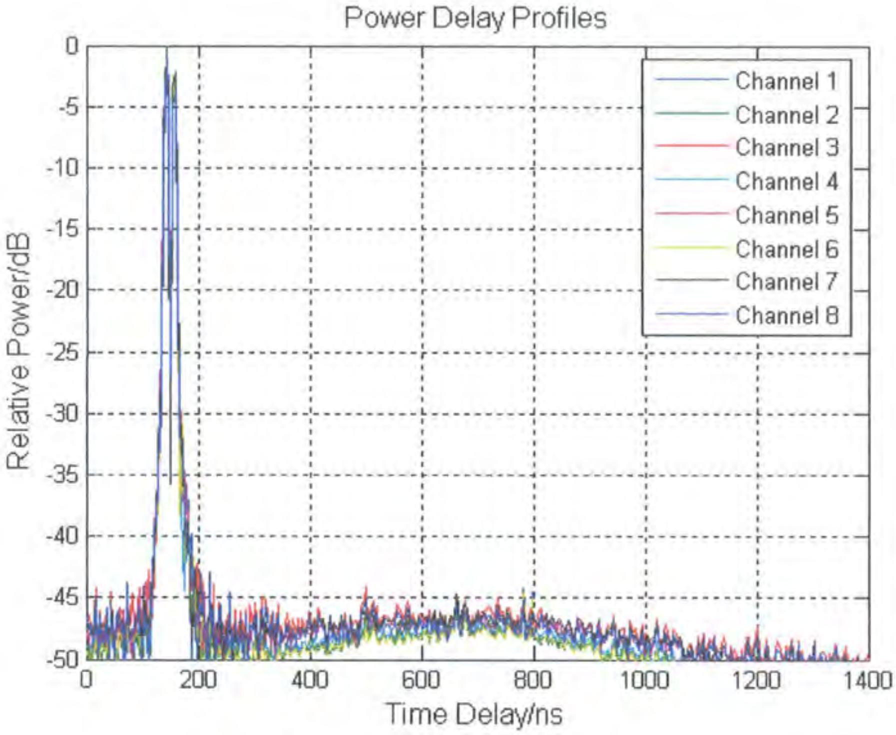

Figure 6.23: Two-tone channel delay response.

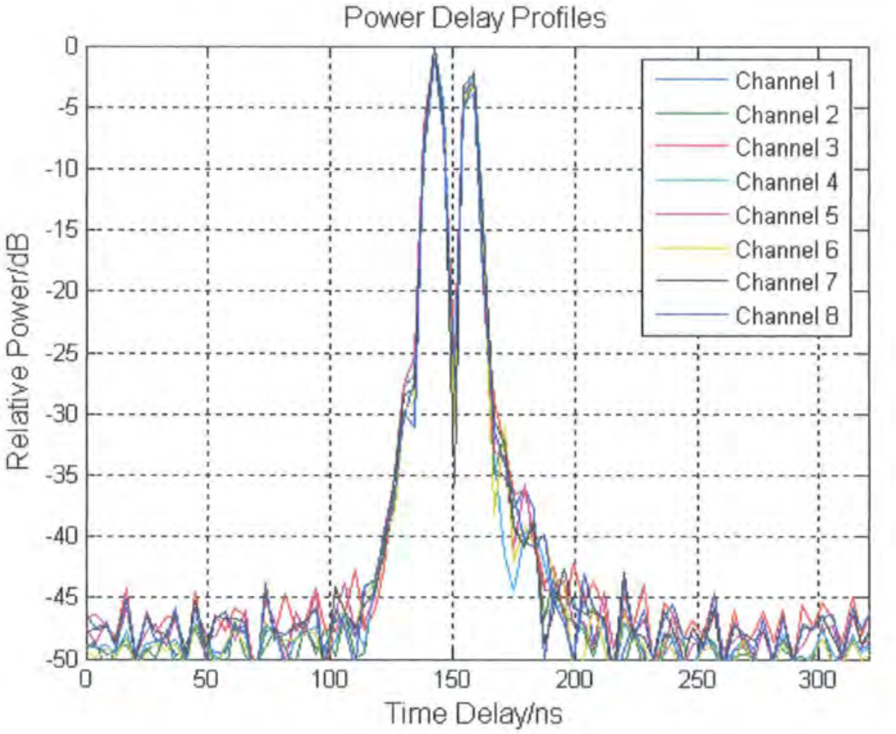

Figure 6.24: Two-tone channel delay response (zoom).

6.4.3 Receiver Gain Calibration

Although all the channels have similar responses, they differ slightly because of the inherent hardware imperfections. For this reason, it is important to perform calibration tests for each receive channel. Such tests are often performed in order to determine the gain response of each RF channel for varying amplitude levels, the purpose of which is to compensate the measurement data.

The sounder receiver unit includes various gain blocks all the way from the RF front-end down to the signal conditioning (SC) unit which has automatic gain control. The SC unit is essential for amplifying and filtering the IF signal and therefore needs to be calibrated [1]. An important calibration measurement, is to record the back-to-back response of the system for varying SC gain levels. By knowing the level of the signal into the receiver front-end, and evaluating the peak-to-peak voltage of the recorded beatnote, it is possible to calculate the overall gain per receive channel. Such a result is presented in figure 6.25 for all 8 receive channels. These measurements were done with a 240 MHz chirp centred on 2.38 GHz.

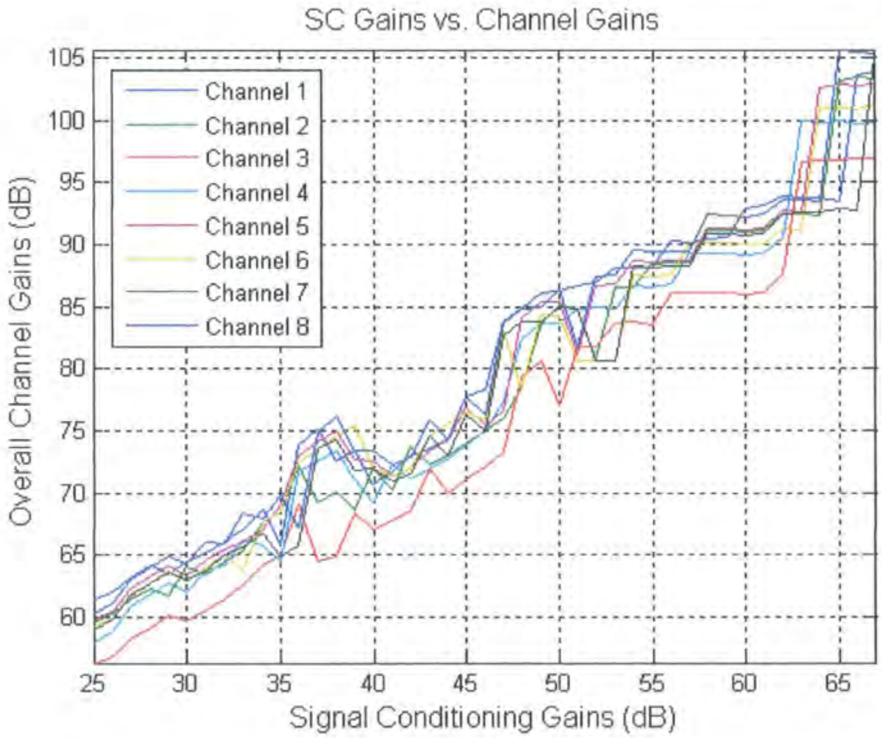

Figure 6.25: Overall gain of each receive channel with respect to SC gains.

Because of the digital nature of the SC unit [1], a pre-determined gain value is used for each channel measurement. This gain does not correspond exactly to the gain set via the data acquisition software. Instead the digital potentiometers in the SC unit give a staircase response as shown in figure 6.25.

6.5 Antenna Array Calibration

It was noted in earlier chapters that some of the analysis in this thesis will focus on array signal processing where the primary objective is to determine direction of arrival as well as direction of departure information (for double directional measurements). Therefore, this section briefly describes the antennas which will be used to assess such spatial data and the corresponding calibration measurements used to determine the spatial resolution of the antenna arrays.

6.5.1 Array Calibration System

The actual calibration rig used for the array antennas is described in [1, 25]. Additional modifications were performed in [26] in order to acquire complex IQ data for each channel. The antenna calibration rig consists mainly of a turntable, on which the test array is mounted and a test transmitter which is used to illuminate this array. The turntable is rotated by a stepper motor via a gearbox. The stepper motor is controlled by a PC which has a data acquisition card fitted. The outputs from the elements of the test array are amplified and detected by an eight channel logarithmic receiver or an IQ demodulator. These outputs are then digitised by the data acquisition card in the PC and recorded onto disc for further analysis. Currently the rig operates in the 1.9 GHz to 2.4 GHz band, however modifications could be made to extend this frequency range.

6.5.2 Array Antennas

A few of the array antennas used in this study were developed in [27]. These arrays consist mainly of directional patch antennas which were used to construct circular arrays as well as some linear ones. Additional arrays, which were used primarily for MIMO capacity studies included wideband discone antenna arrays covering 2 – 6 GHz and simple omni-directional (dipole) arrays. The photos of the various arrays used for channel measurements are shown in figures 6.26 - 6.28.

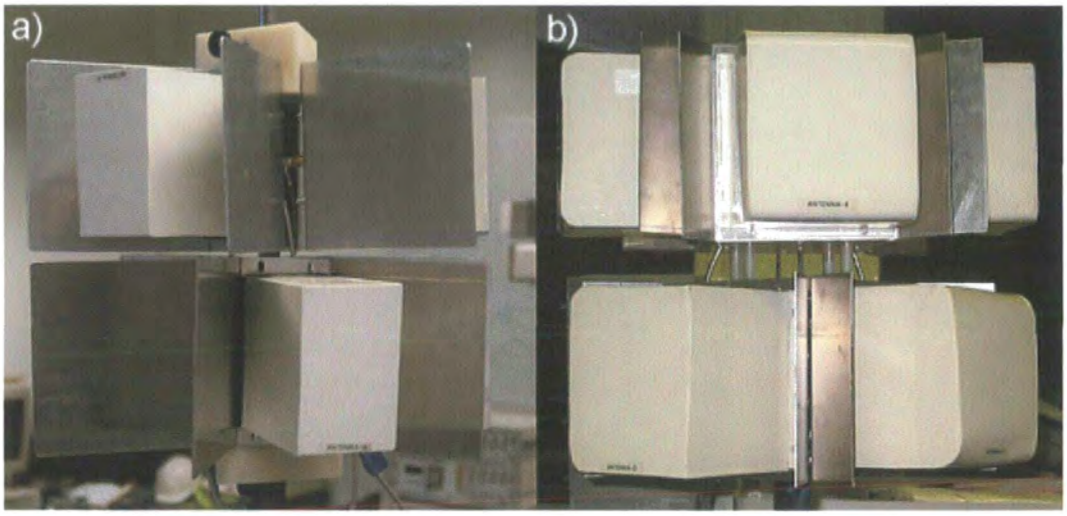

Figure 6.26: Vertically polarised directional circular patch array (VPDCPA) with a) 6 elements, and b) 8 elements. The array bandwidth is typically 1.7 – 2.6 GHz.

Figure 6.27: Wideband (2-6 GHz) Discone circular array (showing 4 elements) [28].

Figure 6.28: Omni-directional dipole linear array (showing 8 elements). This array is nominally working at UMTS frequencies.

6.5.3 Calibration for Spatial Array Processing

The antenna arrays shown in figure 6.26 are used primarily for directional and double directional channel measurements. The calibration data for such arrays is used to compute spatial channel information. Therefore some basic analysis of this data will be provided here to evaluate the suitability of these antennas for direction finding. Firstly, the beam patterns of the two arrays are shown in figure 6.29 and 6.30.

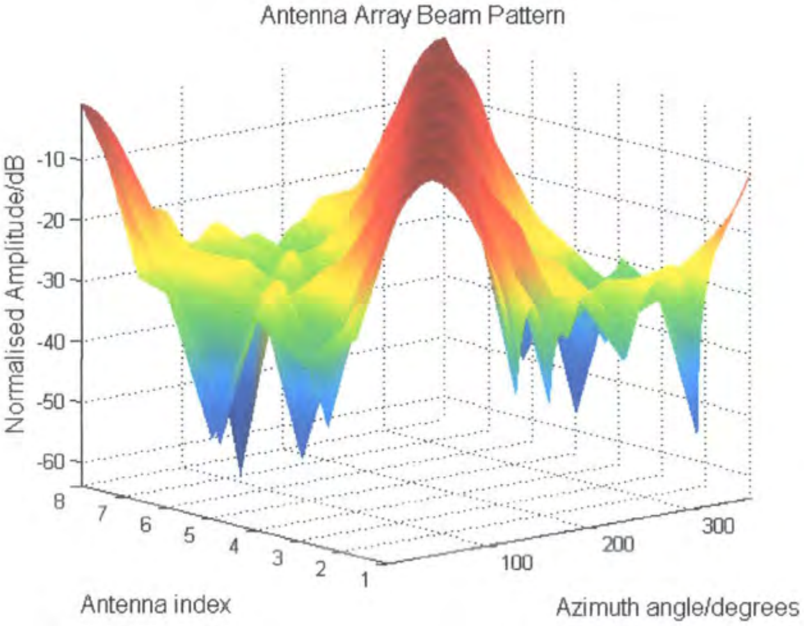

Figure 6.29: Normalised beam patterns for the 8 element directional patch array.

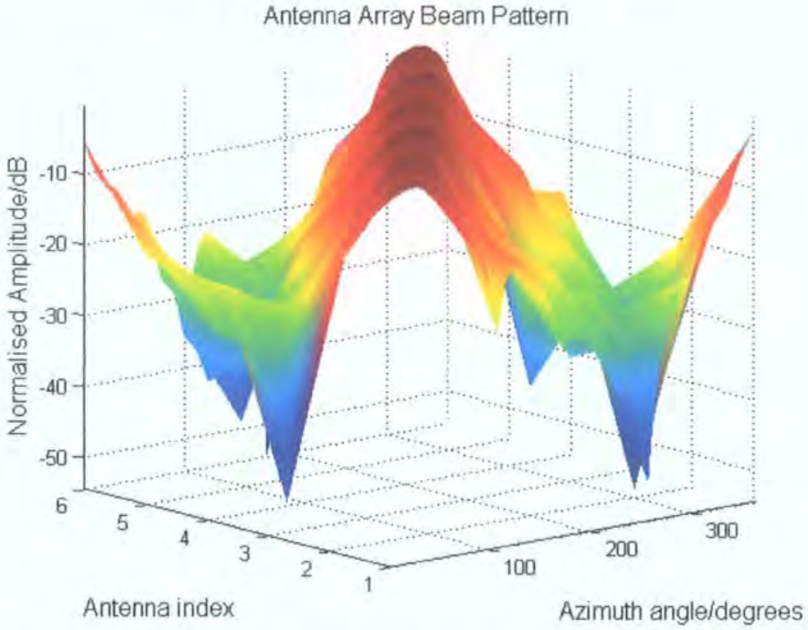

Figure 6.30: Normalised beam patterns for the 6 element directional patch array.

Figure 6.29 and 6.30 represent the calibration data which is used to estimate directional channel information for sounder measurements. This is given in terms of azimuth angle in degrees and antenna element index. The directional (or sectorised) nature of the antenna elements is apparent in these plots.

One of the primary tests used to assess the performance of the antennas for direction finding is the array correlation function (orthogonality function) [2, 3]. The correlation function for both arrays is shown in figures 6.31 and 6.32. The purpose of such a result is to see the cross-correlation coefficient of the array (i.e. the side-lobes on the correlation function). High cross-correlation coefficients severely affect the resolution capability of the array for super-resolution algorithms (see chapter 4). The worst case scenario is when these coefficients are as high as the main lobe.

Figure 6.31 shows the orthogonality of the array response between different angles for the 8 element patch array. It can be observed from this figure that the antenna cross-correlation coefficients between the array responses with an angular seperation of approximately 60° are roughly 5dB below the main peak. Therefore such an array would be suitable for high resolution direction-of-arrival estimation [2, 3].

Figure 6.32 shows a similar plot to figure 6.31 but for the 6 element patch array. Here, it should be observed that the antenna cross-correlation coefficients are larger, however this array is still adequate for direction finding. The resolution of the array reduces considerably as the number of elements in the array decreases. Additional information about these arrays is provided in [27].

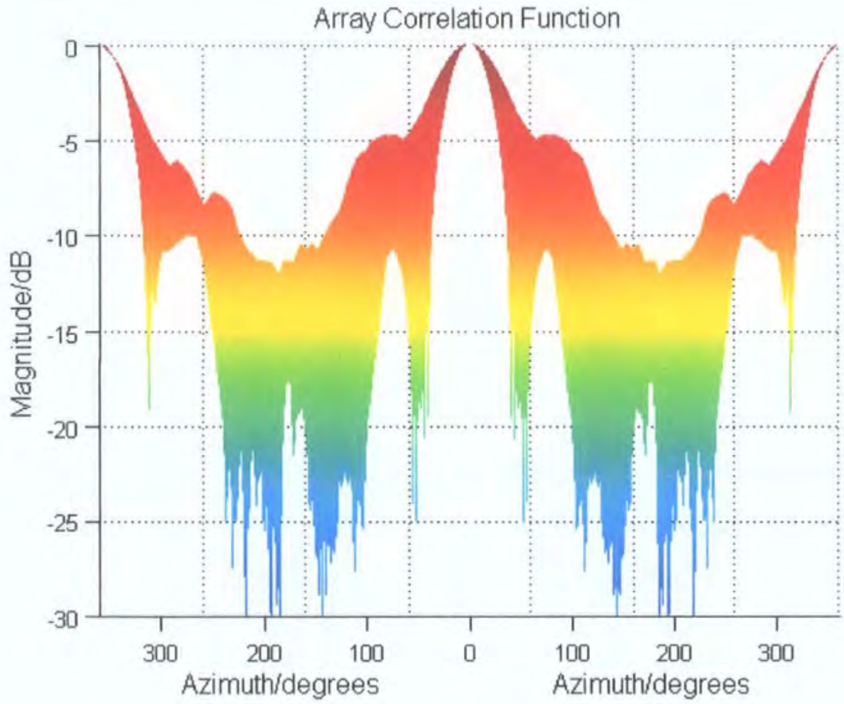

Figure 6.31: Correlation function for 8 element directional patch array (cross view).

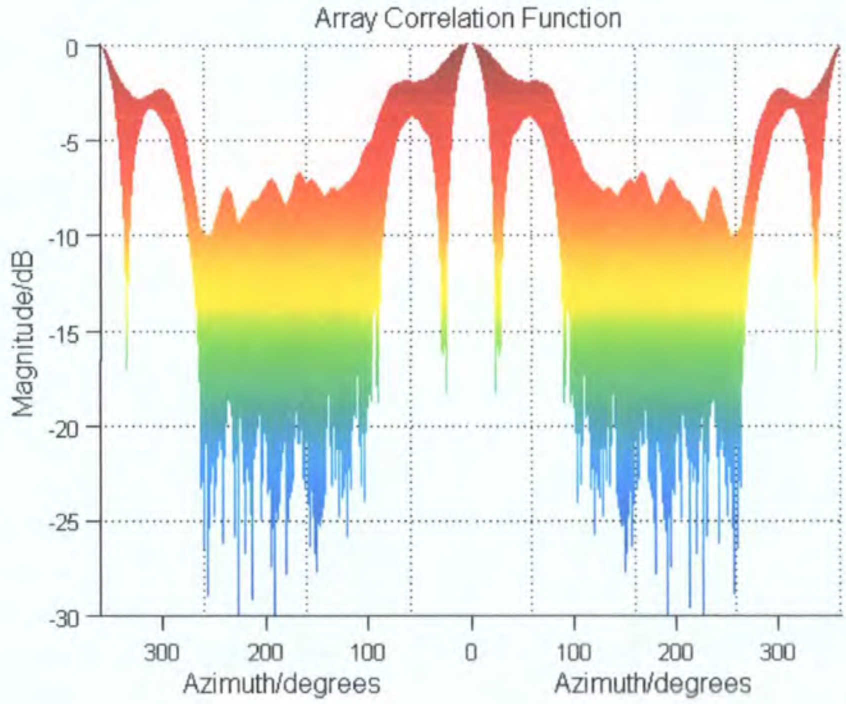

Figure 6.32: Correlation function for 6 element directional patch array (cross view).

6.6 Summary and Conclusions

In this chapter, the semi-sequential MIMO chirp sounder architecture was presented in some detail, including descriptions of the measurement range and resolution of the system. Various aspects of the system building blocks were discussed including the chirp generator and the RF switch. Some basic performance tests used to assess the capability of the sounder were discussed. Finally, a brief description of the array calibration system was given along with some of the calibration data.

6.7 References

1. P. Filippidis, "Multi-Channel Sounder for Directional Measurements," Ph.D. Thesis, Dept. of Electrical Engineering and Electronics, UMIST, Manchester, UK, 2002.
2. C. M. Tan, P. Fletcher, M. A. Beach, A. R. Nix, N. Landmann, R. S. Thomä, "On The Application of Circular Arrays in Direction Finding, Part I: Investigation Into The Estimation Algorithms," 1st Annual COST 273 Workshop, Espoo, Finland, 2002.
3. C. M. Tan, M. Landmann, A. Richter, L. Pesik, M. A. Beach, Ch. Schneider, R. S. Thomä, A. R. Nix, "On The Application of Circular Arrays in Direction Finding, Part II: Experimental Evaluation on SAGE with Different Circular Arrays," 1st Annual COST 273 Workshop, Espoo, Finland, 2002.
4. P. H. Lehne, M. Pattersen, R. Eckhoff, O. Trandem, "A Method for Synchronising Transmitter and Receiver Antenna Switching When Performing Dual Array Measurements," 27th URSI General Assembly, Maastricht, Netherlands, 2002.
5. M. Kihara, S. Ono, P. Eskelinen, *Digital Clocks for Synchronization and Communications*. Norwood: Artech House (Telecommunications Library), 2003.
6. S. Salous, V. Hinostroza, "Indoor and Between Building Measurements with High Resolution Channel Sounder," 12th International Conference on Antennas and Propagation, Exeter, UK, 2003.
7. N. F. Bajj, "Chirp for Mobile Radio Channel Characterisation," M.Sc. Thesis, Dept. of Electrical Engineering and Electronics, UMIST, Manchester, UK, 1996.

8. N. C. Nikandrou, "Digital Generation of Wideband Chirp Signals for Channel Characterisation," M.Sc. Thesis, Dept. of Electrical Engineering and Electronics, UMIST, Manchester, UK, 1997.
9. S. Salous, and N. Nikandrou, “Architecture for advanced FMCW sounding,” *International Journal of Electronics*, vol. 84, 1998, pp 429-436.
10. S. Salous, N. Nikandrou, N. Bajj, "Digital Techniques for Mobile Radio Chirp Sounders," *IEE Proceedings on Communications*, vol. 145, pp. 191-196, 1998.
11. Z. M. Ng, "Gate Array Integration for Chirp Synthesiser," B.Eng Report, Dept. of Electrical Engineering and Electronics, UMIST, Manchester, UK, 1999.
12. V. Hinostroza, "Indoor Wideband Mobile Radio Channel Characterisation System," Ph.D. Thesis, Dept. of Electrical Engineering and Electronics, UMIST, Manchester, UK, 2002.
13. D. M. Pozar, *Microwave and RF Design of Wireless Systems*: John Wiley & Sons Ltd, 2001.
14. D. H. Green, *Modern Logic Design (Electronic Systems Engineering Series)*: Addison-Wesley, 1986.
15. G. Matthaei, L. Young, E.M.T. Jones, *Microwave Filters, Impendence-matching Networks, and Coupling Structures*. Norwood: Artech House, 1980.
16. G. L. Matthaei, "Interdigital Band-Pass Filters," *IEEE Transactions on Microwave Theory and Techniques*, vol. 10, pp. 479-491, 1962.
17. A. B. Williams, F. J. Taylor, *Electronic Filter Design Handbook*, 3 ed: McGraw-Hill, 1995.
18. A. I. Zverev, *Handbook of Filter Synthesis*: John Wiley & Sons, 1967.
19. W. J. Getsinger, "Coupled Rectangular Bars Between Parallel Plates," *IEEE Transactions on Microwave Theory and Techniques*, vol. 10, pp. 65 - 72, 1962.
20. H. Gokalp, "Characterisation of UMTS FDD Channels," Ph.D. Thesis, Dept. of Electrical Engineering and Electronics, UMIST, Manchester, UK, 2001.
21. A. B. Przedpelski, "Analyze, Don't Estimate, Phase-Lock-Loop Performance of Type-2, Third-Order Systems," *Electronic Design*, vol. 26, 1978.
22. R. E. Best, *Phase-Locked Loops: Design, Simulation, and Applications*, 5 ed: McGraw-Hill, 2003.
23. J. A. Crawford, *Frequency Synthesizer Design Handbook*: Artech House, 1994.
24. W. P. Robins, *Phase Noise in Signal Sources: Theory and Applications (IEE Telecommunications Series)*: Peter Peregrinus, 1984.

25. R. Lewenz, P. Fillipidis, S. Salous, "Antenna Array Calibration for a Multi-Channel Direction of Arrival Sounder," High Frequency Postgraduate Conference, Cardiff, UK, 2001.
26. M. Abdalla, S. M. Feeney, S. Salous, "Antenna Array and Quadrature Calibration for Angle of Arrival Estimation," World Multi-Conference on Systemics, Cybernetics and Informatics, SCI2003, Florida, USA, 2003.
27. M. Abdalla, "Directional Antenna Array for Channel Measurement System," Ph.D. Thesis, School of Electrical and Electronic Engineering, The University of Manchester, Manchester, UK, 2005.
28. S. Salous, S. Feeney, N. Razavi-Ghods and R. Lewenz, "Measurements in the 2 – 6 GHz Band," XXVIIIth General Assembly of International Union of Radio Science (URSI GA 2005), New Delhi, India, October 2005.

Chapter 7

Spatio-Temporal Channel Measurements

7.1 Introduction

This chapter describes the wideband multi-antenna measurements collected in and around the University of Durham. The measurements presented here are separated into two main groups. The first group comprises of measurements made with 60 MHz bandwidth for directional (SIMO) outdoor UMTS-FDD uplink channels. The second group of measurements are for double-directional indoor links in the 2.4 GHz ISM band using 240 MHz bandwidth and 6 × 8 antenna arrays.

The primary objective of this chapter is to process the measurement data and present results such as power delay profiles, scattering (Doppler-delay) function, and time-variant transfer function. This chapter also presents directional and double-directional spatial channel results using both simple beamforming and the more sophisticated SAGE-type estimation technique.

7.2 Measurement Campaigns

The outdoor measurement campaigns were performed for a number of different SIMO environments including line-of-site (LOS), two path, and non-LOS environments. These measurements were all carried out in the UMTS-FDD uplink frequencies, i.e. 60 MHz centred on 1.95 GHz. For the non-LOS environment, the setup was achieved by placing the transmit antenna (directional patch antenna) on the roof of the old School of Engineering (SoE) building and then moving the receiver unit around on a trolley. The locations of the non-LOS measurements are shown in figure 7.1. Over 80 files were collected along the measurement routes shown in blue and green.

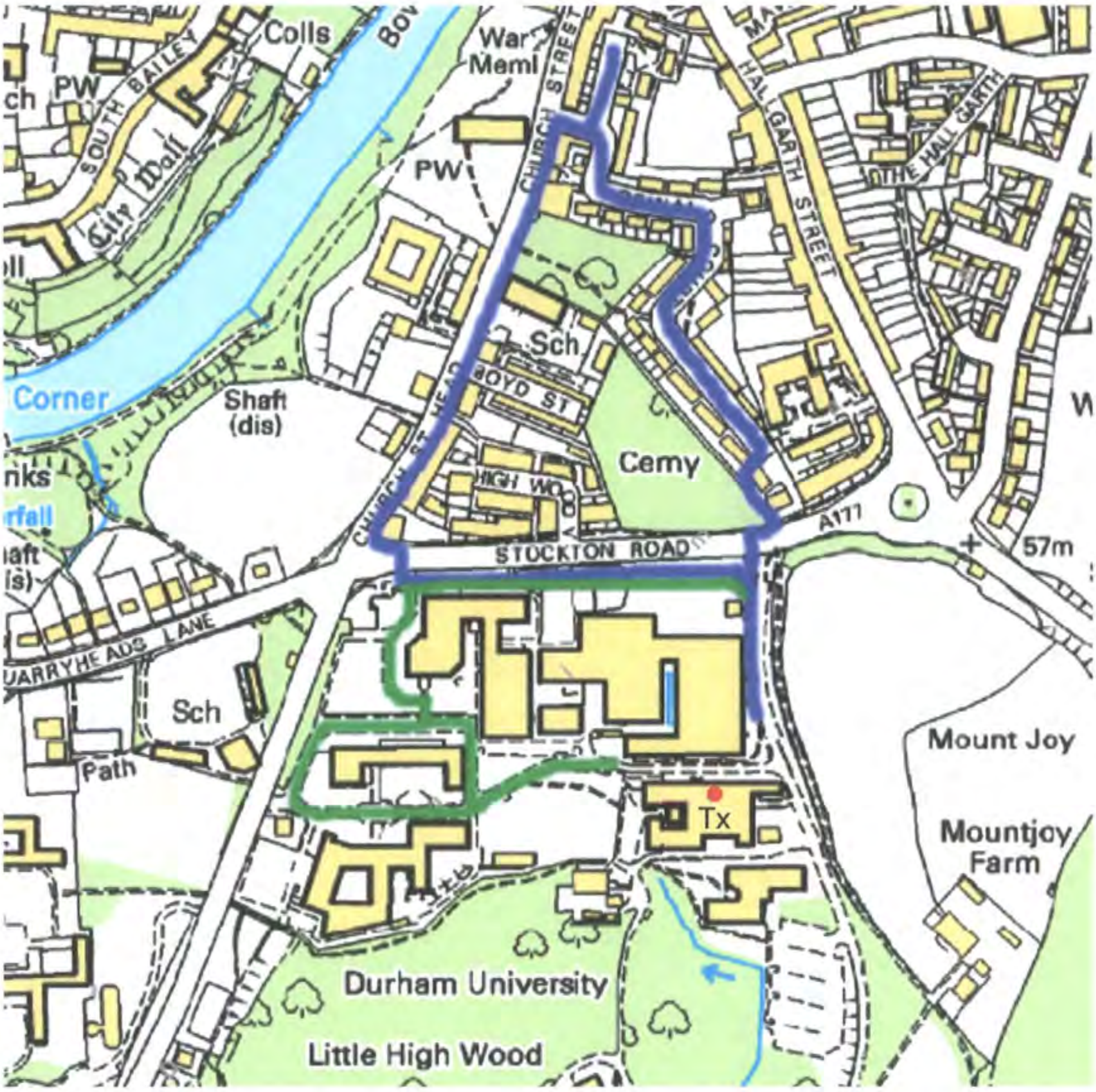

Figure 7.1: Measurements collected around Durham University (from Edina Digimap, Scale 1:5000). The blue and green lines represent the routes taken by the receiver.

For the LOS Measurements, the transmitter was placed on the 3rd level of the old Engineering building with the antenna pointing directly towards the multi-channel receiver placed on the roof. Measurement files were collected by rotating the receiver array [1].

The final set of outdoor results was collected using two separated transmitters, referred to from hereon in as the two path measurements. Results were collected by placing both the transmitter and receiver units on the flat Engineering car park. The sounding signal was then transmitted on two directional patch antennas which were separated as shown in figure 7.2.

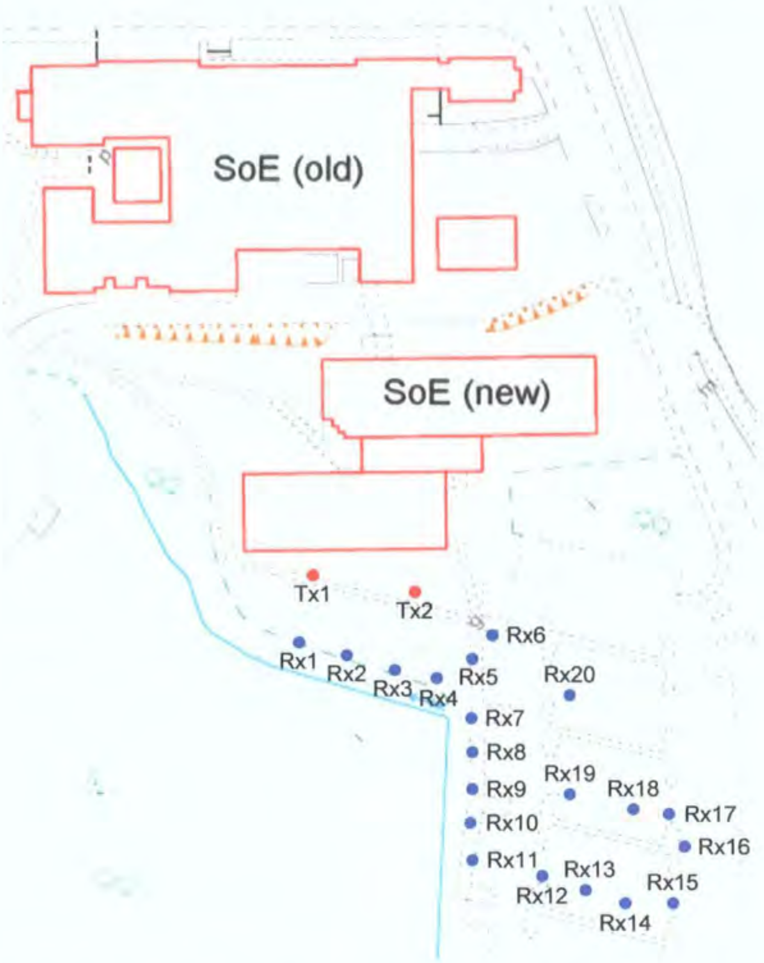

Figure 7.2: Measurements collected in the SoE car park using two transmitters. Map from Edina Digimap, Scale 1:1250.

The measurement parameters for these campaigns are shown in table 7.1. Here, an 8 element vertically polarised directional circular patch array (VPDCPA) was used at the receiver.

Centre frequency	1950 MHz
Swept bandwidth	60 MHz
Sweep repetition frequency	250
DAU sampling rate	1 MSample/s
Sweeps collected per second	250
Samples per sweep	4000
Time delay resolution	16.67 ns
Range resolution	5 m
Time delay window	33.33 us
Doppler range	± 125 Hz

Table 7.1: Measurement parameters for SIMO environments.

The double-directional measurements were performed mainly for indoor channels using 240 MHz bandwidth. These measurements were carried out in the 2.4 GHz ISM band for WLAN applications which are proposed primarily for indoor office and home environments. Here, both LOS and non-LOS 6 × 8 measurements were made in the School of Engineering building, floor 2b. As shown in figure 7.3, the receiver was placed in the Electronics lab and the transmitter was moved around the SoE. At each location shown in figure 7.3, measurements were made in addition to noting the position of the transmitter array since the receiver location was fixed.

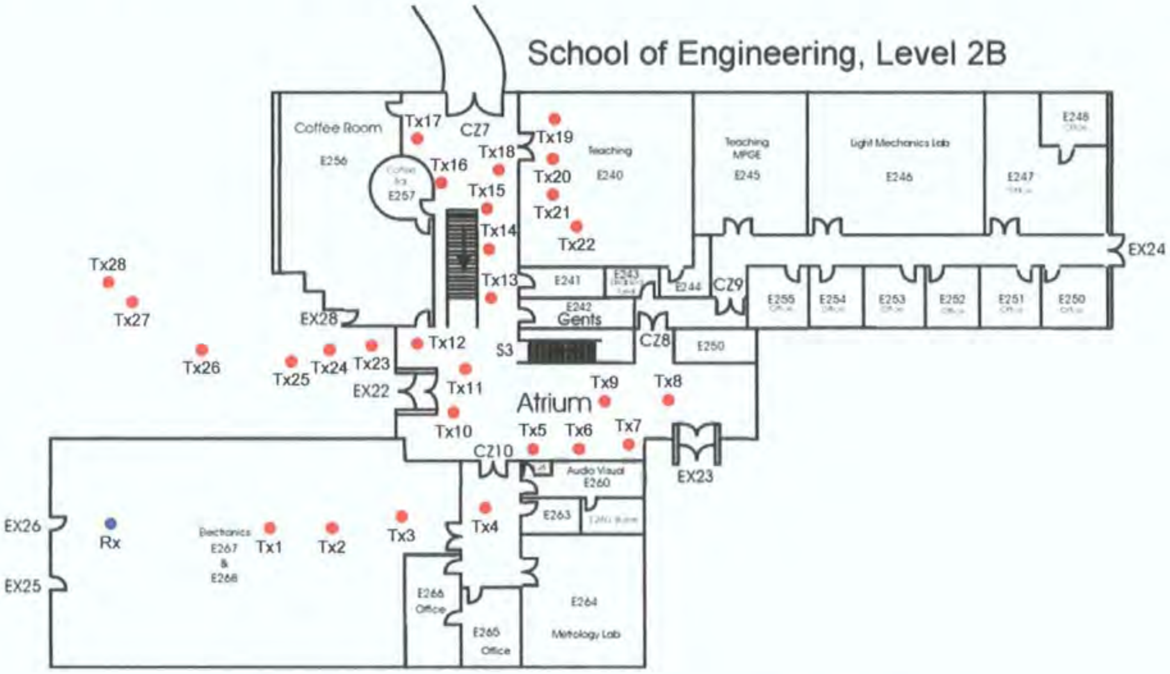

Figure 7.3: MIMO Measurements collected in the SoE.

The measurement parameters for these campaigns are shown in table 7.2. Here, a 6 element VPDCPA was used at the transmitter and an 8 element VPDCPA was employed at the receiver. Because most of the measurements were relatively short range (< 1 km), the transmit power for both indoor and outdoor measurements was typically no more than 500 mW.

Centre frequency	2380 MHz
Swept bandwidth	240 MHz
Sweep repetition frequency	250
DAU sampling rate	1 MSample/s
Sweeps collected per second	250
Samples per sweep	4000
Time delay resolution	4.17 ns
Range resolution	1.25 m
Time delay window	8.33 us
Doppler range	± 15.6 Hz

Table 7.2: Measurement parameters for 6 × 8 MIMO environments.

7.2.1 Measurement Procedures

For any of the measurement campaigns, the initial step is to wait at least 15 minutes after start-up so that the Rubidium sources are locked. After sufficient warm up time, the sounder is programmed via the keypad to produce the chirp signal. The next stage of the procedure is to synchronise the sweeps at both ends of the system using the manual delay of the sweep at the receiver. The aim of this procedure is to get the beatnote (IF signal) down to a few tens of kHz. It is practically not possible to bring the beat signal all the way down to DC, however the optimum is often achieved by placing this signal within 40 – 90 kHz. Once the system is synchronised at the beginning of any measurement campaign, this process does not need to be repeated, since the drift between the rubidium clocks is negligible in practical terms.

The data are subsequently acquired using the acquisition unit (DAU) described in [2]. The DAU software checks the relevant clocks and confirms the SRF, the number of sweeps to be collected per second, and the samples per sweep. Before using the DAU software to acquire any data, it is important to run the automatic gain control (AGC) routine which makes certain that the beat signal is within the amplitude range of the DAU by controlling the gain level (digi-pots) in the signal conditioning unit as well as the RF attenuation level for each of the front-end cards [2]. At this point, it is standard practice to collect a reference file, which is simply a back-to-back test. This ensures that the sounder is operating in the correct mode. There should be sufficient dynamic range when observing the power delay profile (time averaged impulse response). The SNR for the measurement files should typically be greater than 25 dB. The measurement procedure is shown in figure 7.4

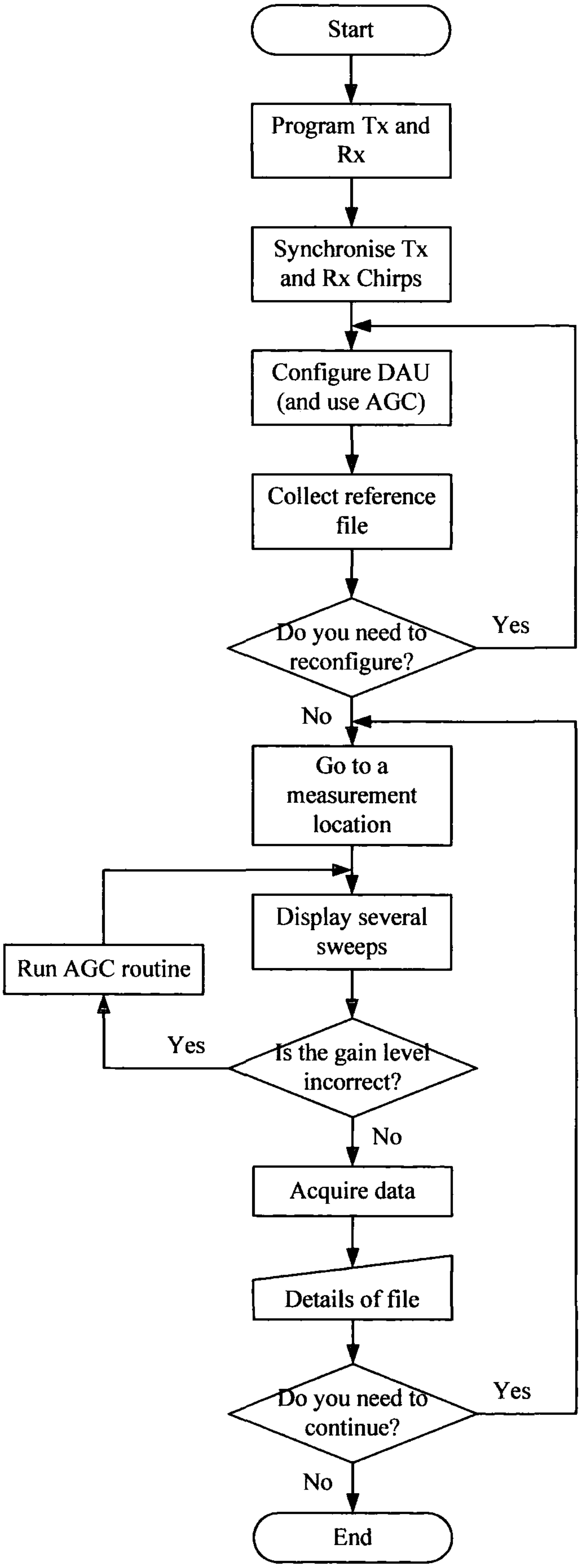

Figure 7.4: Flow chart of channel measurement procedure.

Channel measurements are made at each location by firstly displaying several data sweeps on the PC screen, configuring the DAU (if required) and then saving the measurement file onto the PC hard disk. For MIMO measurements, displaying consecutive sweeps is very helpful, since it shows the antenna switching at the transmit array.

It should be noted that for each measurement location, full notes are made about the system settings, the surrounding environment, and the position of antenna 1 in the receive array. In the case of double-directional measurements, it is important to know the position of both the transmit array and the receive array.

7.3 Data Processing

By employing the sounder as described in figure 7.4, it is possible to carry out a variety of radio channel measurements. The acquired raw data files are essentially the sampled time-series of the beat notes in the channel. In order to perform any type of data analysis, it is necessary to further process these channel snapshots. This can be achieved using any high-level programming language, such as C++ or MATLAB. Because of the enormous library of subroutines and powerful processing capability, MATLAB was employed in this case. The processing requirements in this chapter rely mainly on the FFT routine and the more advanced super-resolution algorithms, such as SAGE (described in chapter 4). This is reviewed in the following.

7.3.1 Delay-Doppler Processing

To obtain the channel functions (figure 7.5), FFT processing was performed on the time-series data (see appendix A1.1). As described in chapter 6, the data were initially compensated using the sounder calibration files. This was proceeded by filtering and windowing. The windowing function used here was the Hamming window [3, 4], however for computing the complex time-variant transfer functions, it was necessary to avoid any windowing prior to the FFT, since this would mask the shape of the transfer function.

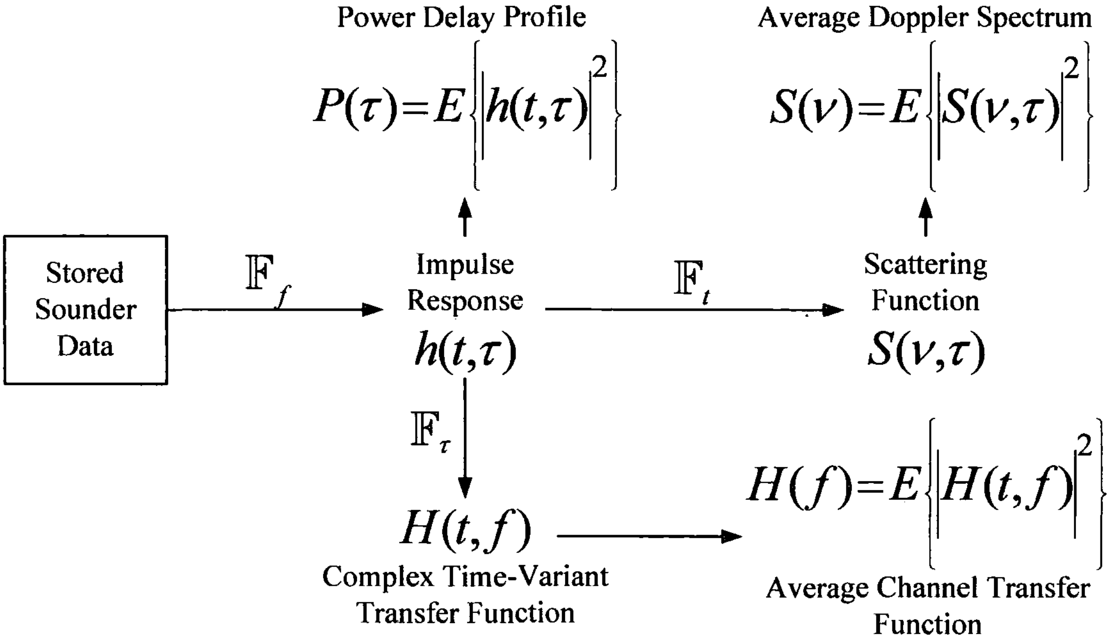

Figure 7.5: Data processing tree, where $\mathbb{F}$ represents the FFT with respect to a particular variable.

7.3.2 Spatial Parameter Estimation

The theory behind many parameter estimation techniques were described in chapter 4, with emphasis placed on ESPRIT and SAGE. Although algorithms were developed for both techniques, the inherent flexibility of the SAGE method and its joint estimation capability made it far superior [5]. Therefore, the estimation of angular information at the receiver (and at the transmitter) were performed using SAGE-type methods, which are described here.

The practical implementation of this algorithm simply follows on from the previous section. The SAGE algorithm is in many ways an ML-type approach where the main aim is to fit the predicted (modelled) signal to the measured one in a one-dimensional optimisation procedure. The measured signal in this case is the channel impulse responses and the optimisation is performed over both the expectation (E) and the maximisation (M) steps. The effectiveness of this technique to resolve channel parameters relies heavily on the system model. Although most of the literature on this subject refers to models which are constructed as Dirac-delta functions, it is important to note that in real systems, the basic measurement capability is defined as a finite width pulse given by the back-to-back test.

The basic version of the SAGE technique described here is based on three main parameters, namely, α, τ, and ϕ, where α is the amplitude, τ is the delay, and ϕ is the angle of arrival (in azimuth). The algorithm relies on the one-dimensional iteration procedure which is done over all parameters until the EM process converges to a solution. Convergence is achieved much quicker if there are initial estimates of these parameters. This initial parameter matrix can be defined by performing a parameter (peak) search on the calculated channel impulse responses. Figure 7.6 shows a simple flow chart which describes the SAGE technique implemented here.

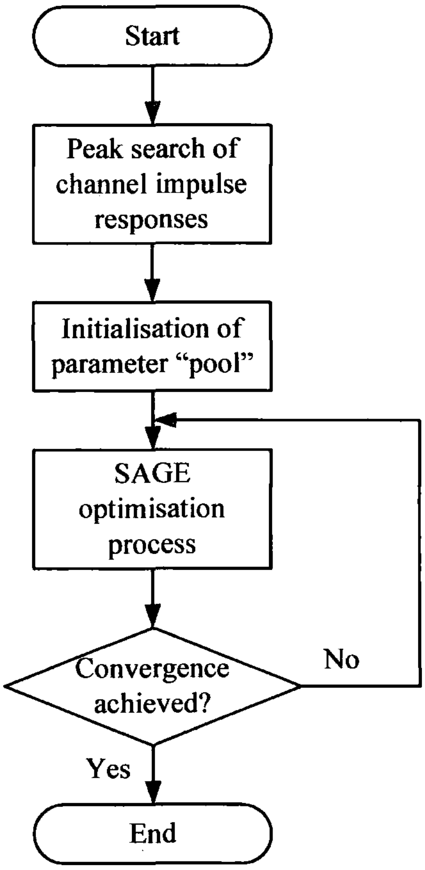

Figure 7.6: Basic SAGE estimation of channel parameters.

The process shown in figure 7.6 relies on an iteration procedure which is done with respect to each multipath component. The initial parameter matrix (or pool) is limited primarily by the dynamic range of the system. It should be noted that the SAGE iterations are performed mainly for determining (with higher resolution) the angular information in the channel, since the FFT process performed on the measurement data gives adequate temporal channel information. As noted in previous chapters, the primary factor in defining the system time-delay resolution is the swept bandwidth.

The implementation of these super-resolution techniques for parameter estimation is often complicated because of the practical limitations of measurement data, such as range, resolution, channel samples, etc. It is possible to develop more efficient algorithms which are directly suited not only to the sounding method but also to the array type and geometry. This is a subject which requires further work.

The peak search and SAGE iteration algorithms for estimating channel parameters were written in MATLAB (see appendix A1.3). These programs were written for better understanding of the estimation problem as opposed to computational efficiency.

7.4 Spatio-Temporal Results for 60 MHz Bandwidth (SIMO)

In this section, various results are presented for the UMTS measurements carried out with 60 MHz system bandwidth.

7.4.1 Power Delay Profiles

The impulse response of the channel can be obtained by performing an FFT on the time-series data as shown in figure 7.5. For the sounder configuration described so far, the time-series data are represented as a 4000 × 250 size array per sampled channel. Here, the 4000 frequency points represent the samples per sweep, for 250 sweeps (acquired in 1s). Each sweep is then filtered to remove close to DC transients and is multiplied by the Hamming window to reduce the level of the sidelobes. The result of the Hamming window is that each range bin is widened by the effective noise bandwidth (ENBW) [4]. For a two term Hamming given in [4], this is defined as 1.36. Figure 7.7 shows a typical single sweep of the raw data.

The sweeps shown in figure 7.7 correspond to a data set collected using the 8-element sectorised array (VPDCPA) in a non-LOS environment (file: NOV30F on Oswald Court), as shown in figure 7.1. Performing an FFT on each of the measured sweeps (time-series shown in figure 7.7), results in a complex channel impulse response. These impulse responses are shown in figure 7.8. This FFT process results in 4000 time-delay bins, half of which are redundant. The algorithms available on the

CD-ROM use zero padding, which gives a 2048 (2^{11}) bin length impulse response per sweep. By averaging these impulse responses over all 250 sweeps, the channel power delay profile (PDP) can be determined. This is shown in figure 7.9. These plots show the relative (normalised) multipath power against excess time delay.

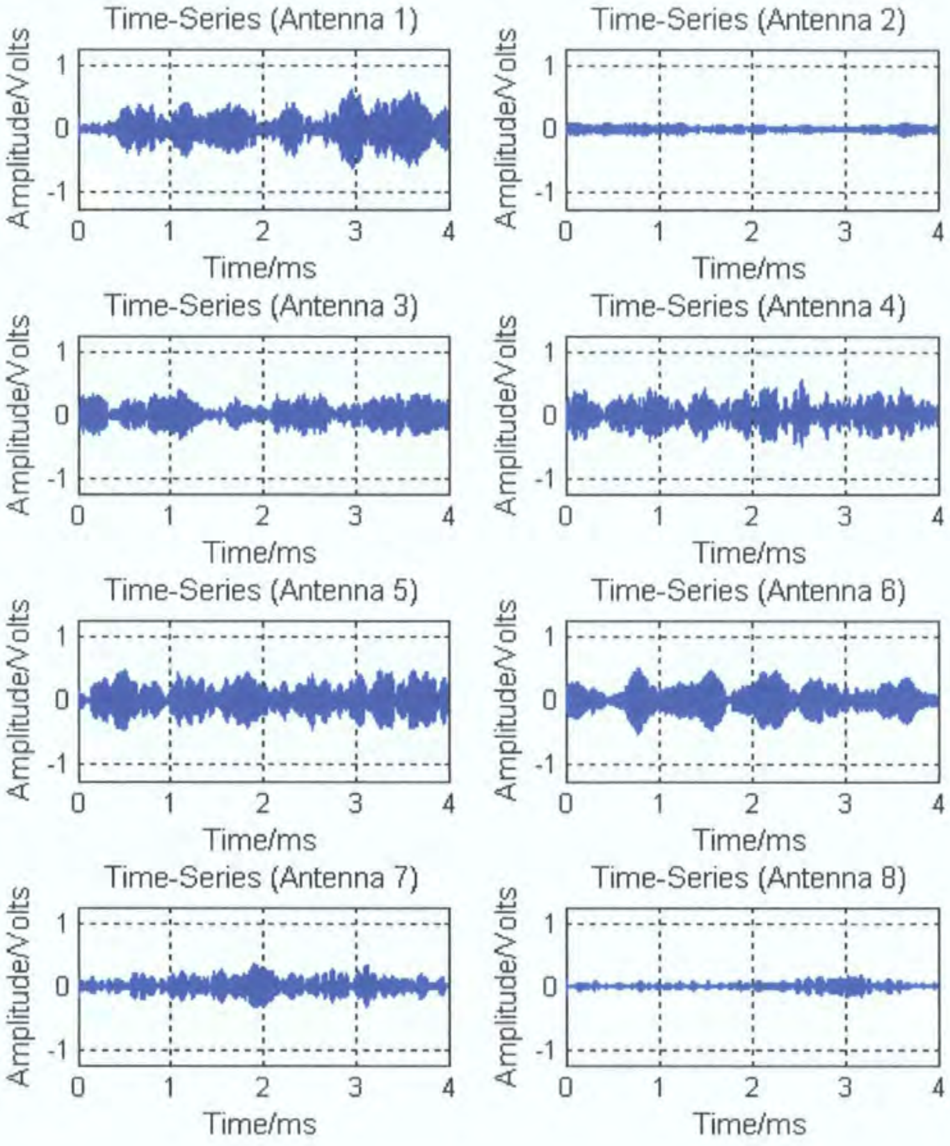

Figure 7.7: Non-LOS time-series data for 8 channels (single sweep of period 4 ms).

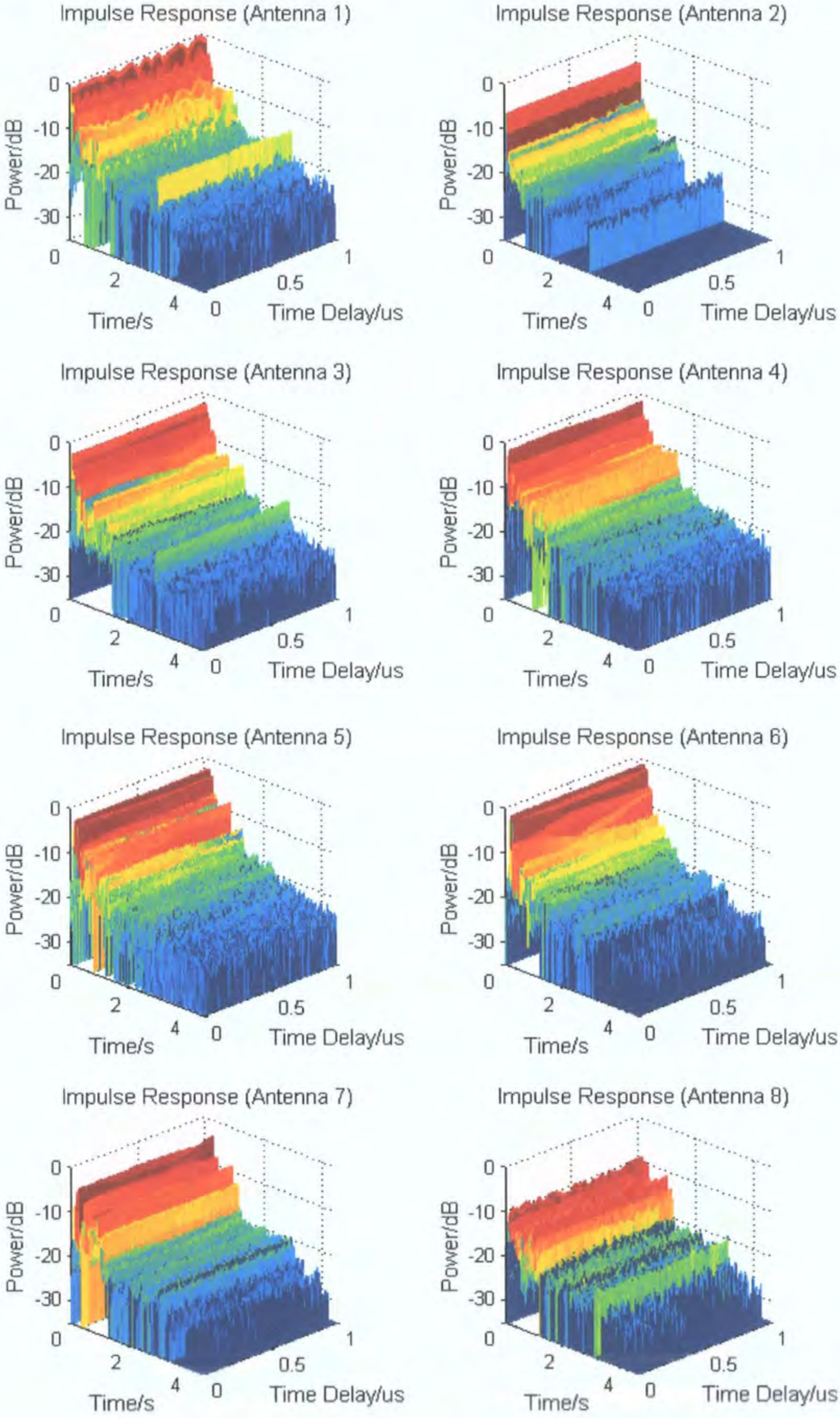
Impulse Response (Antenna 1)
Impulse Response (Antenna 2)
Impulse Response (Antenna 3)
Impulse Response (Antenna 4)
Impulse Response (Antenna 5)
Impulse Response (Antenna 6)
Impulse Response (Antenna 7)
Impulse Response (Antenna 8)

Figure 7.8: Non-LOS time-variant impulse responses for each receive channel.

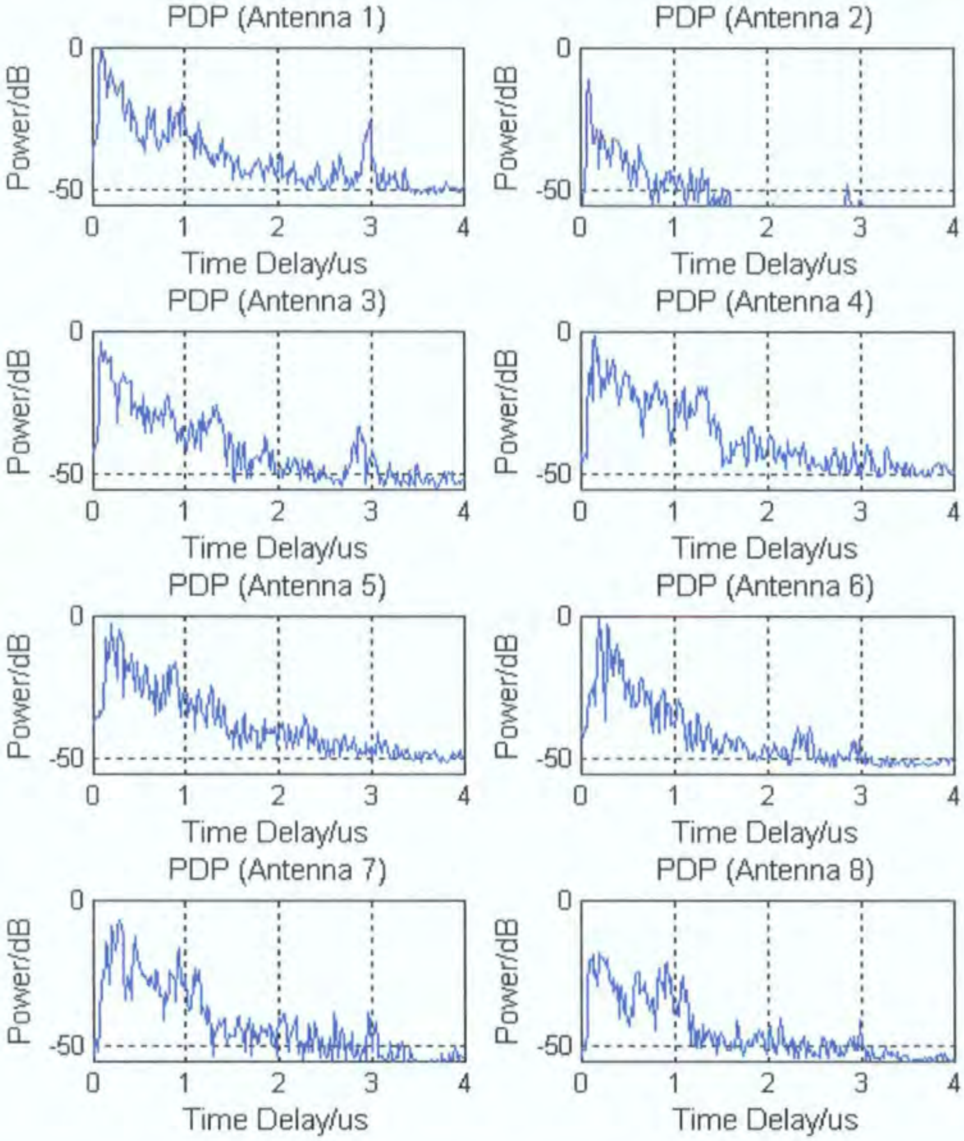

Figure 7.9: Non-LOS power delay profile for each receive channel. The plots are normalised with respect to the maximum channel path.

The above PDPs show significantly different profiles since each antenna in the array has a different look angle with 45 degree beamwidth (at the 3 dB point). Figure 7.10 shows the PDPs for a LOS environment, measured with the receiver array located on the roof of the engineering building. Here, the transmit antenna is pointing directly towards receiver antenna 7.

Figure 7.11 shows a similar figure but here there are two distinct paths measured on the School of Engineering car park (figure 7.2, Rx2). The setup here was such that the most direct signal was being received on antenna 5 and the delayed copy on antenna 4. The spatial characteristics of the channel shown in figure 7.11 are quite apparent, since each antenna in the array is covering a 45 degree sector.

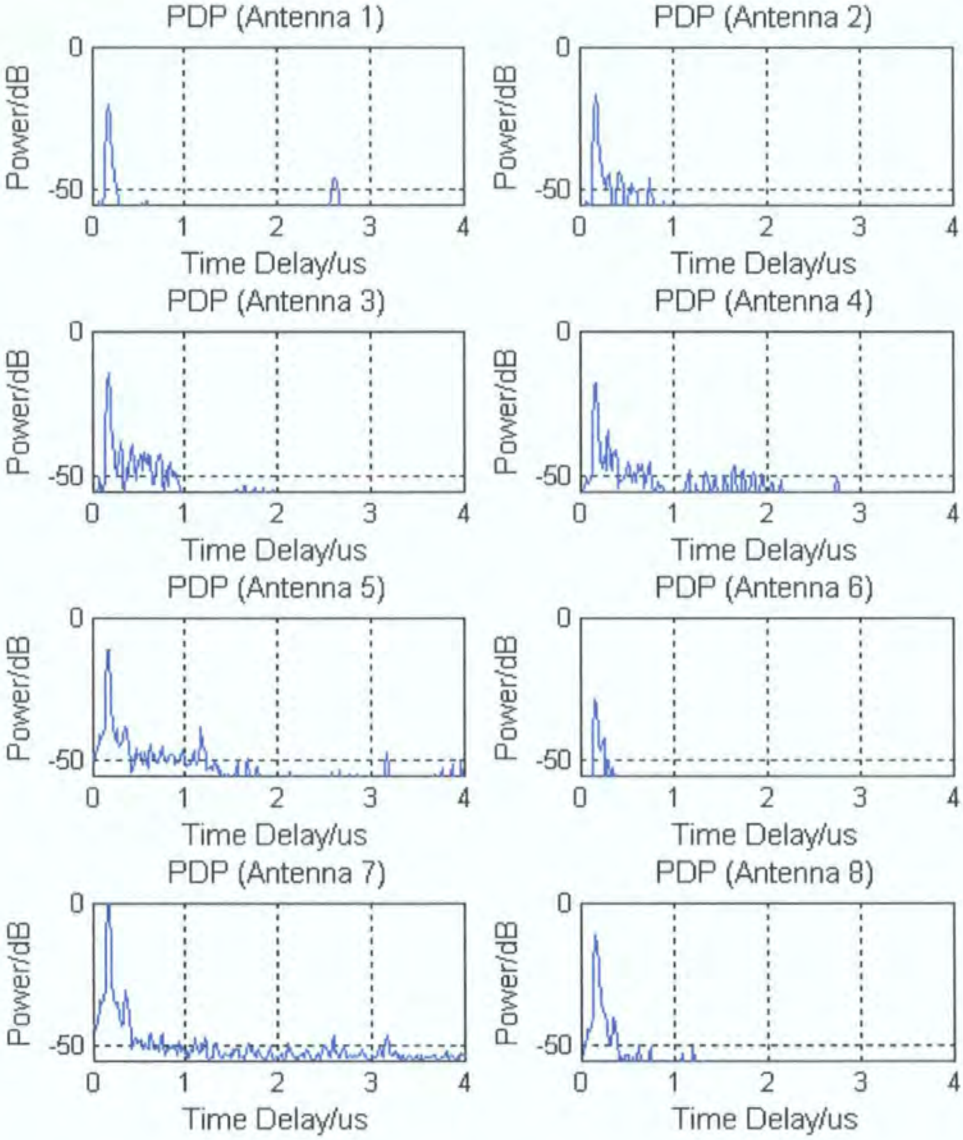

Figure 7.10: LOS (antenna 7) power delay profile for each receive channel.

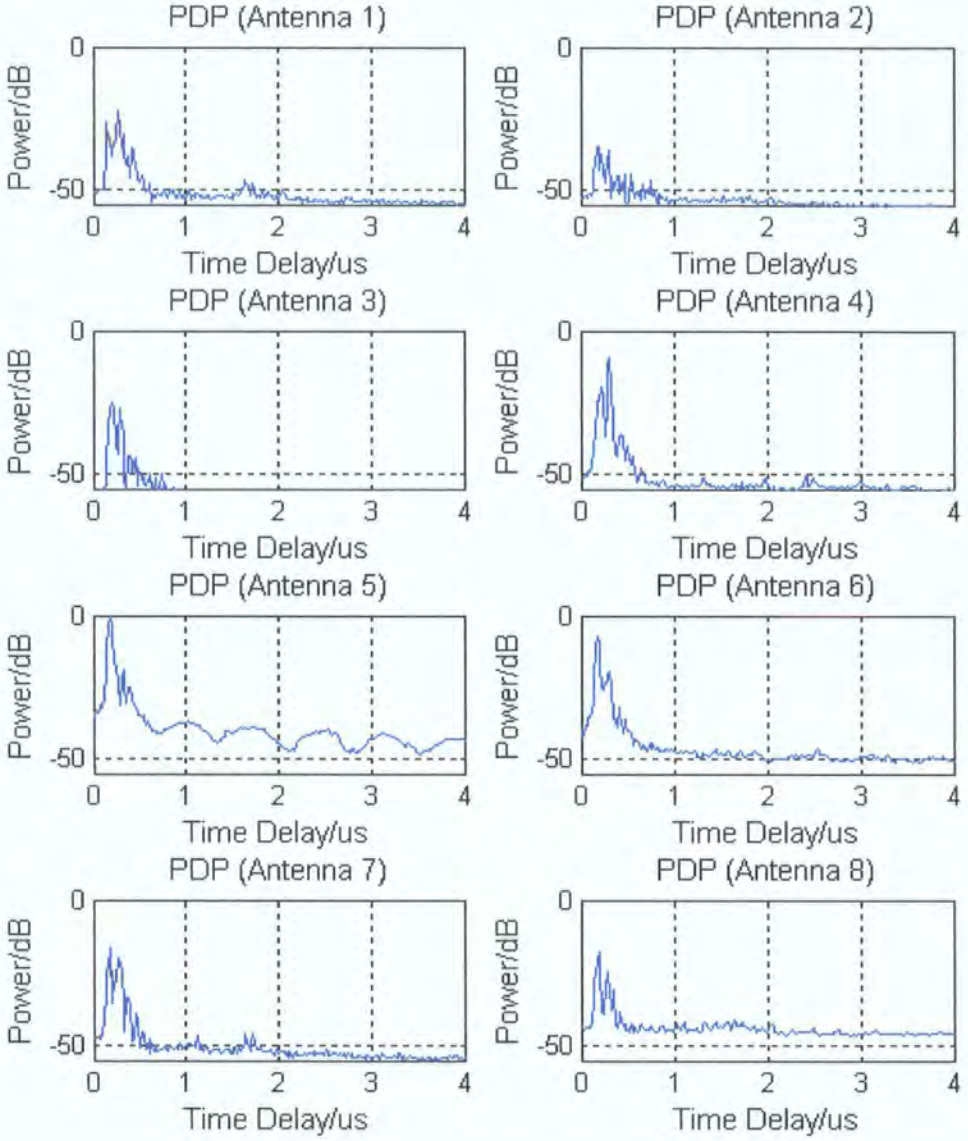

Figure 7.11: Two-path power delay profile for each receive channel. Direct signal received on antenna 5 and indirect (delay) signal received on antenna 4.

In general, some care must be taken when averaging the channel impulse responses, especially in circumstances where there is considerable Doppler in the channel either due to movement of the sounder units and/or the time-variation in the environment under test. For 60 MHz bandwidth, the range bin is defined as 5 meters and it is important that the averaging of sweeps be done within the local area. To avoid erroneous results, it is preferable not to move longer than half a range bin within the data acquisition time. Issues with averaging occur only when a multipath component falls into adjacent bins causing a broadening of the signal peak. In the majority of the measurements presented in this chapter and the next, averaging is performed over one second.

7.4.2 Scattering Function

The scattering function is obtained by performing a second FFT on the complex time-variant impulse responses after another Hamming window. Here, the FFT is carried out over successive sweeps (i.e. the time variable) for each range bin as shown in figure 7.5. Figure 7.12 shows the channel scattering functions for the same data as shown in figure 7.9.

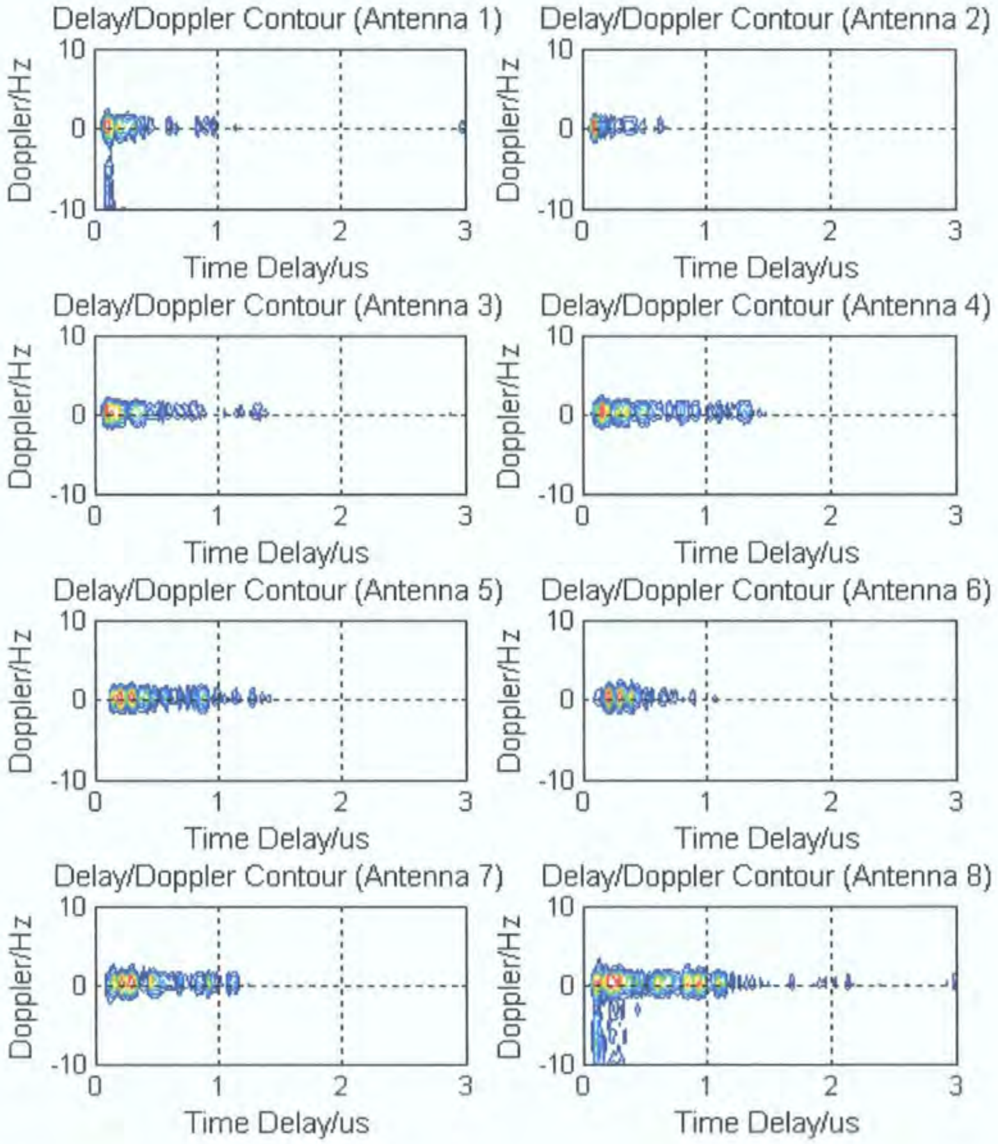

Figure 7.12: Non-LOS delay-Doppler contour plot for each receive channel.

The plots in figure 7.12 represent the delay-Doppler matrix [9] which has 2048 delay bins and 250 Doppler bins. All plots are normalised with respect to their own maxima and show the multipath components down to a threshold of -35 dB. The scattering function for channel 8 is shown in more detail in figure 7.13, since it is clear that this channel has more Doppler variation.

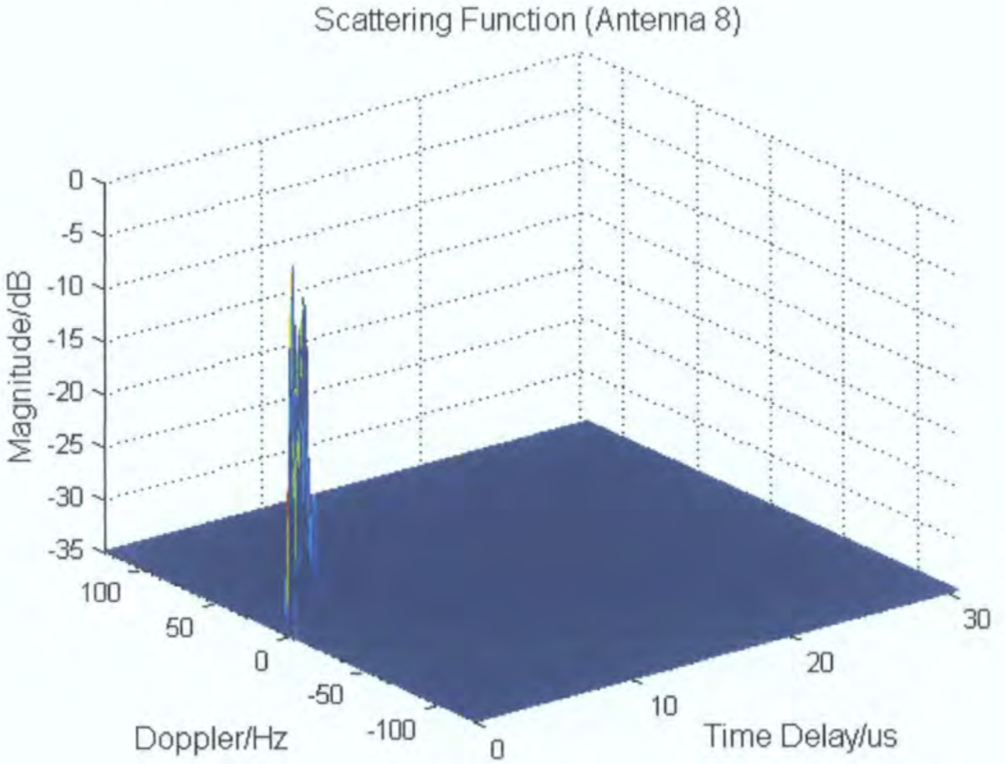

Figure 7.13: Scattering function for receive channel 8.

The maximum Doppler shift in the channel is defined by a simple relationship to the speed of the mobile ($f_{D,max} = v_{max} / \lambda$). In the SIMO case, the Doppler range of the sounder is given by ± $1 / 2T$, where T is the duration of the sweep defined as 4 ms [10]. This corresponds to a maximum observable speed of 69 km/h. From visual inspections of the scattering function, it was observed that for most of the measurements (where both the transmitter and the receiver were stationary), the maximum Doppler shift was typically less than 15 Hz. Plots of the average Doppler spectra can also be attained by averaging over the time delay variable. This can be particularly useful in high Doppler scenarios.

7.4.3 Time-Variant Transfer Function

There are essentially two techniques for obtaining the channel transfer function (TF). As shown in figure 7.5, the time-variant transfer function can be obtained by performing an FFT on the time variant impulse response over the time-delay variable [11]. This function shows the variability of the mobile channel in time and frequency. Here, no windowing is applied prior to any FFT processing, since it will mask the shape of the frequency transfer function.

The alternative technique for computing the transfer function is to apply an envelope detector to the sounder data (raw). The easiest method for doing this is to detect the positive signal peaks and to apply interpolation between the points. The major disadvantage of using this method is that it produces a rather coarse approximation of the transfer function, particularly when there is a strong multipath component with very low beat frequency. This is simply because with a low frequency sinusoidal waveform there are not many peaks to follow the envelope. Therefore, all the transfer function data presented in this thesis will be computed using FFT processing.

Figure 7.14 shows the frequency time transfer function for two antennas which have directly opposite look angles. The data are for measurements carried out on Oswald Court, Durham (channel 1 and channel 5 from NOV30F). Figure 7.15 shows the time-variant transfer functions for all 8 receive channels.

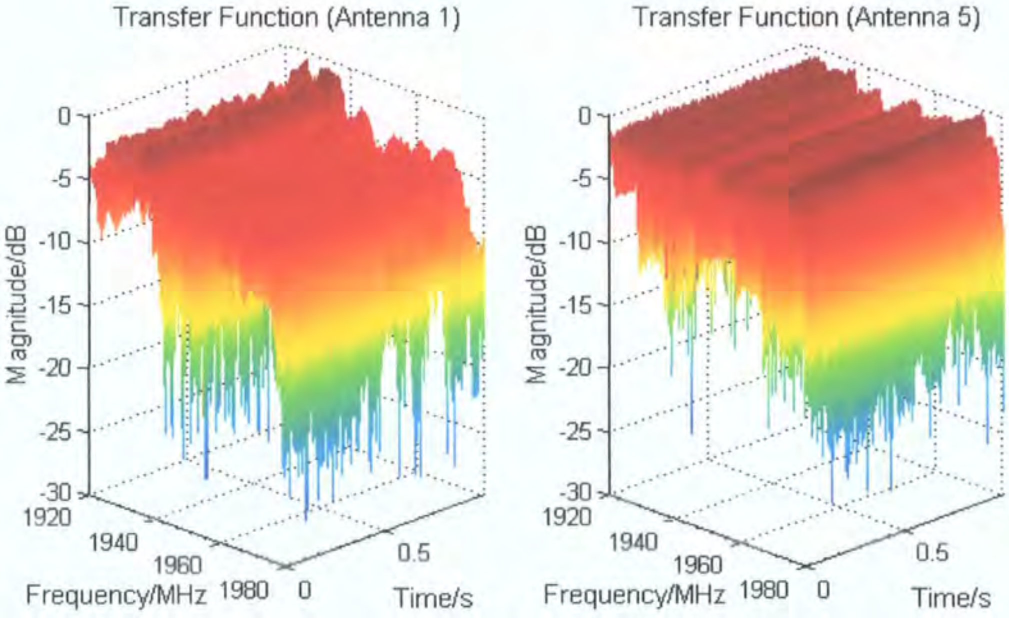

Figure 7.14: Non-LOS time-variant transfer function for 2 antennas.

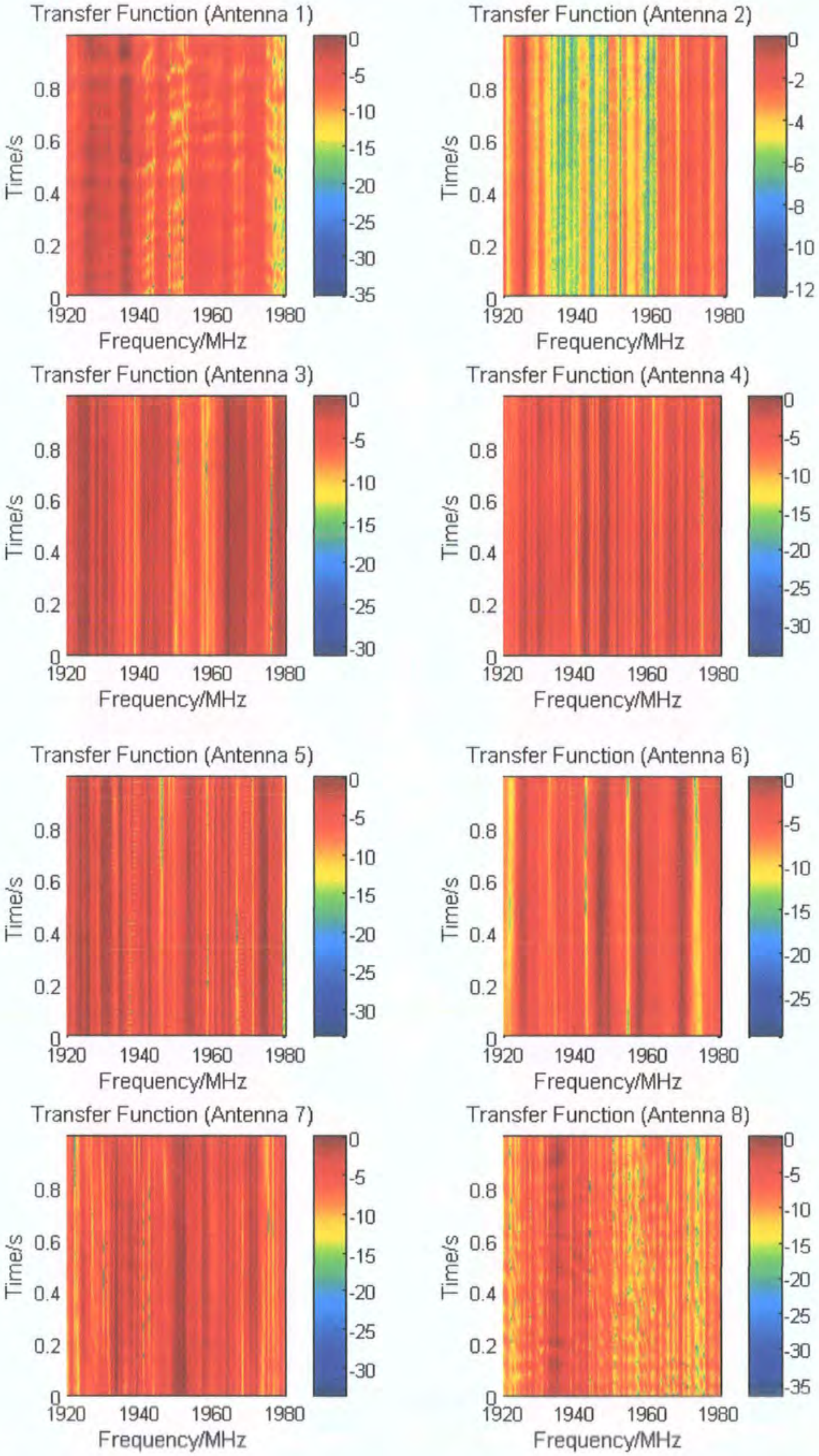

Figure 7.15: Non-LOS time-variant transfer functions. Each transfer function is normalised to its own maxima.

The plots in figure 7.15 show distinctly different frequency time characteristics as expected. In most of the environments measured around Durham, there was low temporal variation. This can be observed from the aforementioned plots, which show relatively small changes across the time variable with the exception of channels 1 and 8.

The transfer functions can be averaged across the time variable to provide the average channel transfer function in the same way that the PDP can be obtained. Here the same limitations apply, namely that the channel under test must be slow time-varying. Figure 7.16 shows such a plot for the non-LOS environment.

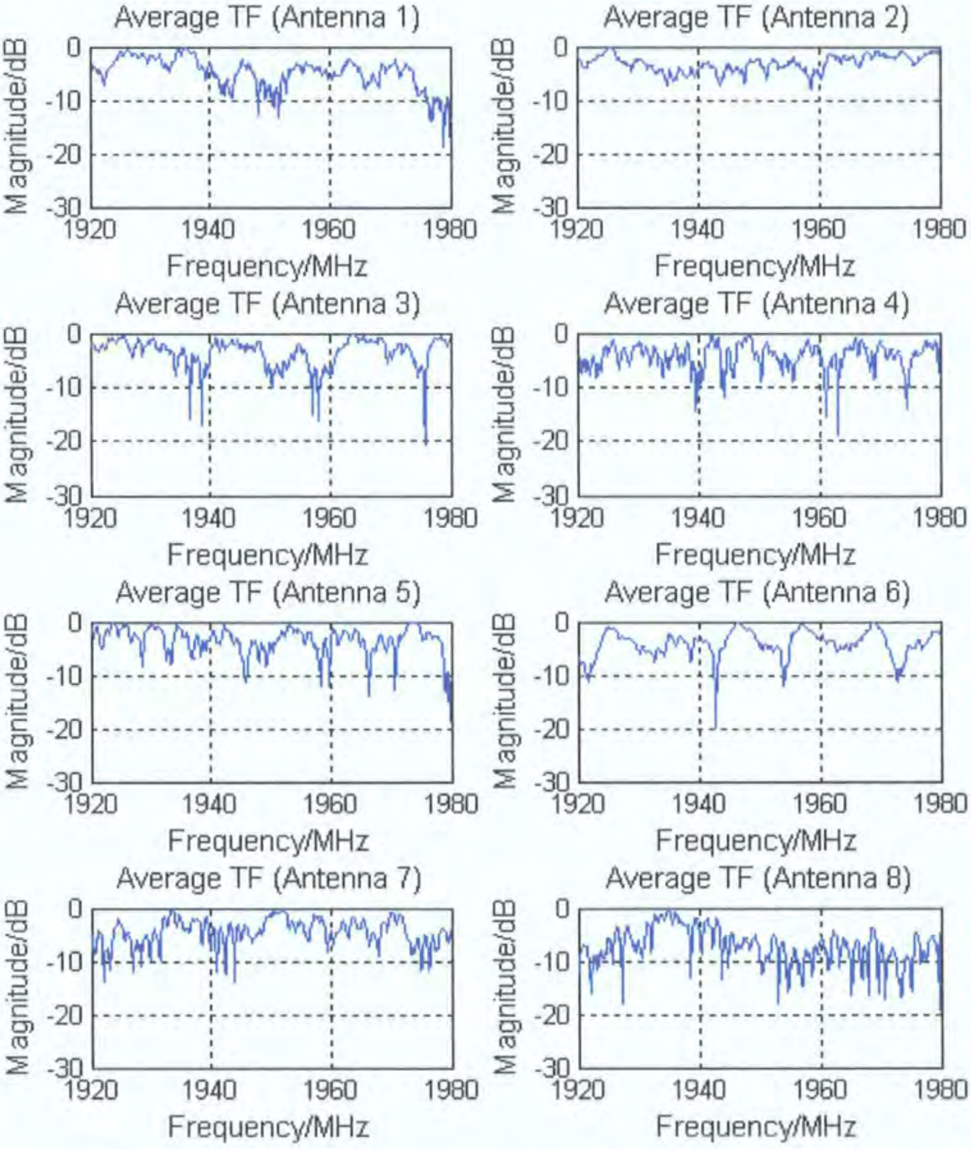

Figure 7.16: Typical non-LOS average channel transfer functions.

Figure 7.17 shows the transfer function plots for a LOS environment. Here, the transmit antenna is pointing directly towards receiver antenna 1. As expected, this results in a frequency-flat transfer function for antenna 1, as well as for antenna 8 which is next to it on the circular array.

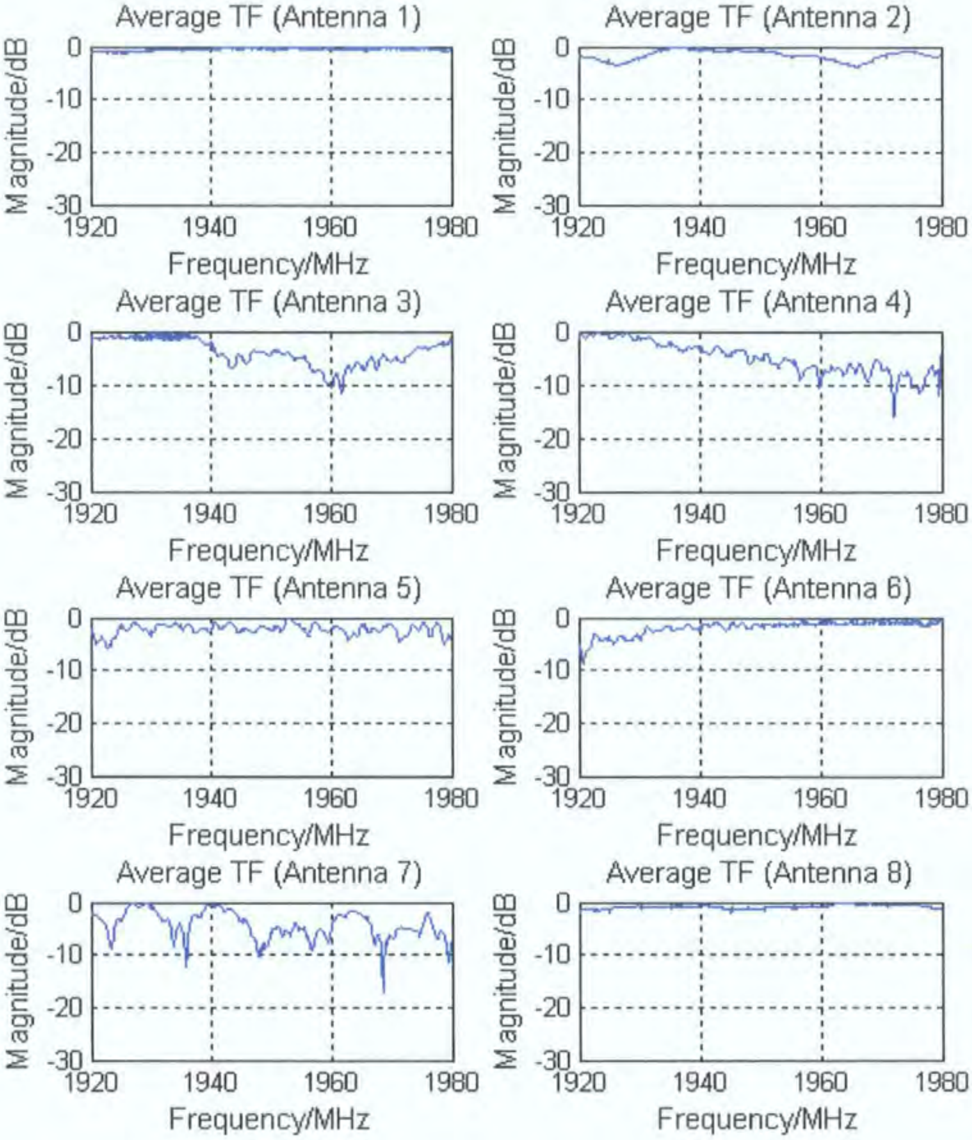

Figure 7.17: Typical LOS average channel transfer functions.

7.4.4 Spatial (DOA) Analysis

Analysis of DOA information is vital in characterising the spatial radio propagation channel. Most of the tools used for analysing such channel information were introduced in chapter 4. This section describes the processed DOA data using simple beamforming and the more sophisticated SAGE technique.

7.4.4.1 Beamforming

The beamforming algorithm is perhaps the simplest approach in analysing spatial channel data. By using the array calibration data (steering matrix) and the measurement data, it is possible to form a beam which represents the DOA spectrum (see chapter 4). The array beampatterns for the 8-element VPDCPA were provided in chapter 6. Figure 7.18 shows beamforming applied to LOS data where the transmitter is pointing towards receiver antenna 1 (reference at 50 degrees). In general, beamforming often provides a first estimate of the spatial spectrum, where the dominant (principle) DOA can be given by

$$\phi_{main} = \arg\max_{\phi}\left\{\sum\left|\mathbf{a}^{H}(\phi)h(t,\tau)\right|^{2}\right\} \tag{7.2}$$

here, as in chapter 4, $\mathbf{a}(\phi)$ represents the steering vector and $h(t,\tau)$ is the time-variant impulse response.

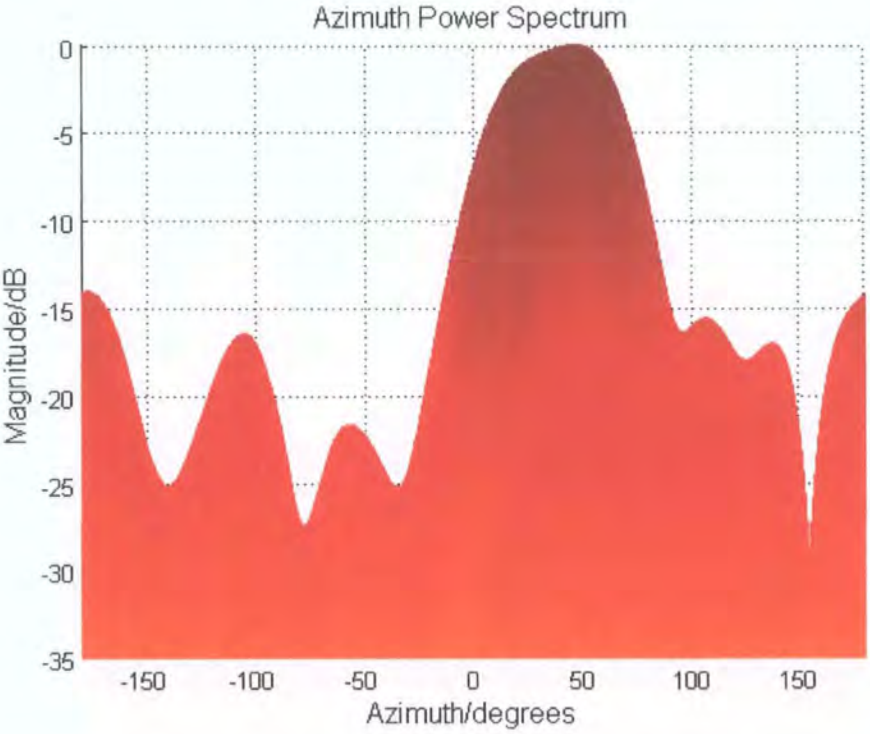

Figure 7.18: DOA power spectrum for LOS data.

Figures 7.19 and 7.20 show beamforming applied to two-path and non-LOS scenarios, respectively. In figure 7.19, the two directional transmitters are separated by ~ 90 degrees (Rx2 in figure 7.2). Clearly the beamformer can distinguish between the two paths and provides a crude DOA approximation of the impinging signals. In the non-LOS scenarios, beamforming can be quite limited in resolving the DOAs.

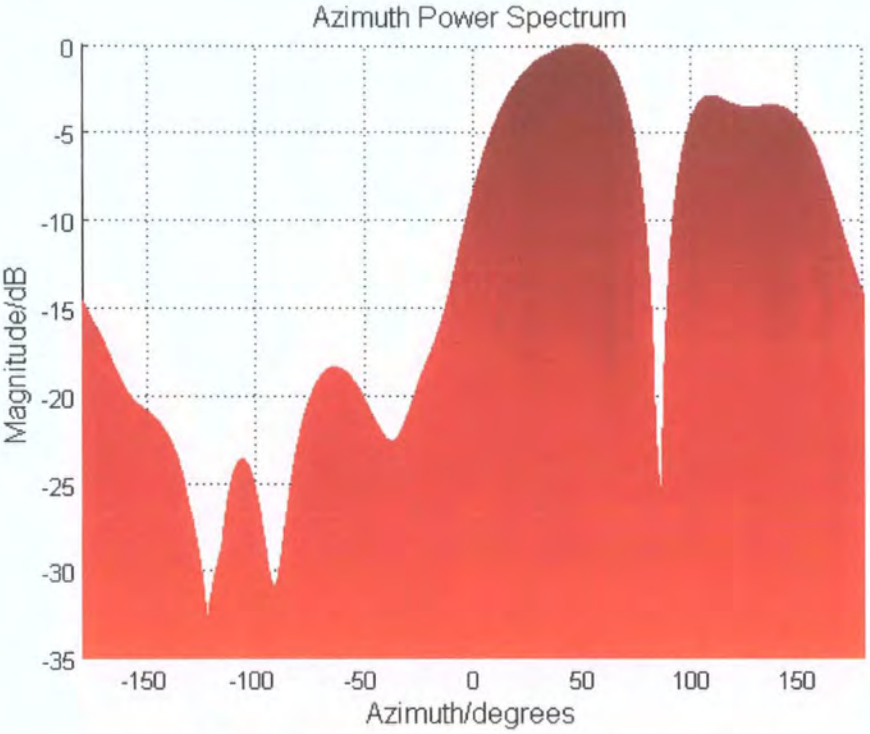

Figure 7.19: DOA power spectrum for two-path data.

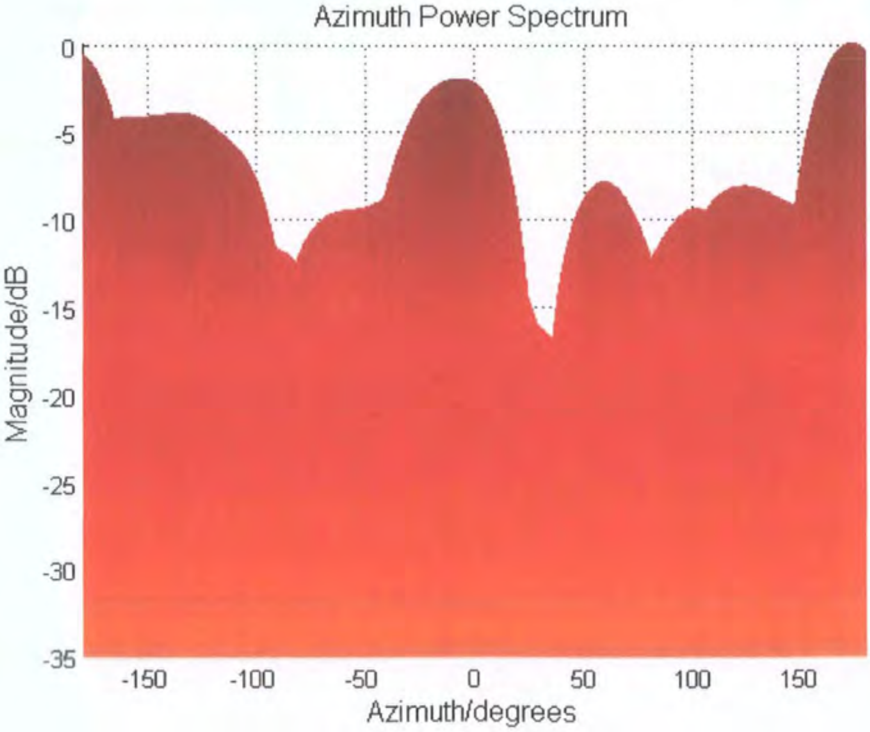

Figure 7.20: DOA power spectrum for non-LOS data.

As noted in chapter 4, beamformers often have limited spatial resolution. However, all of these figures were used to provide basic validation of the DOA using the SAGE technique implemented in the next section.

7.4.4.2 DOA Estimation Using the SAGE Technique

The SAGE algorithm implemented in this case relied on initial estimates via a path search procedure, the purpose of which was to find multipath component delays and amplitudes. This is shown in figure 7.21 for non-LOS data collected in Durham using a threshold of 20 dB (refer to figure 7.1).

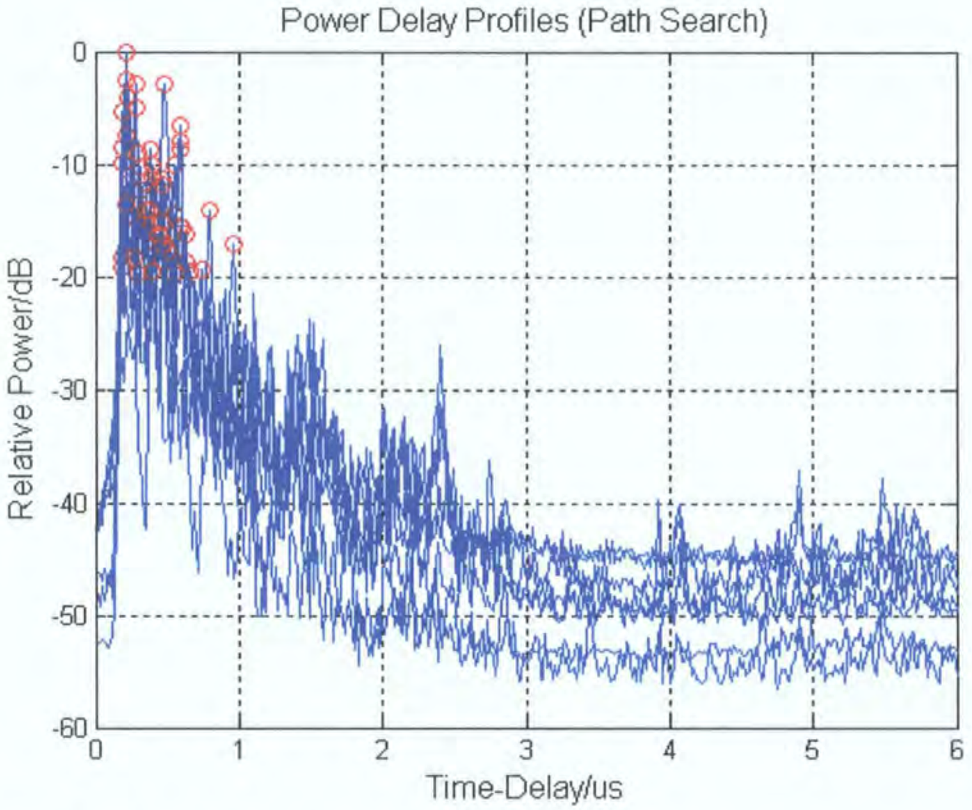

Figure 7.21: Path (peak) search performed on non-LOS data across all 8 channels.

The red dots shown in figure 7.21 represent the components found across the array above a certain threshold, which in this case was -20 dB. Such a threshold is more than adequate for resolving the major multipath components in the measurement environment. These values can then be defined as the SAGE 'data pool' which is used to find the DOAs.

After inputting the parameter into the SAGE (optimisation) program, the iterative procedure yields the component estimates. Figure 7.22 shows SAGE applied to the data in figure 7.21. Here there are 25 distinct components resolved in delay and azimuth angle domains.

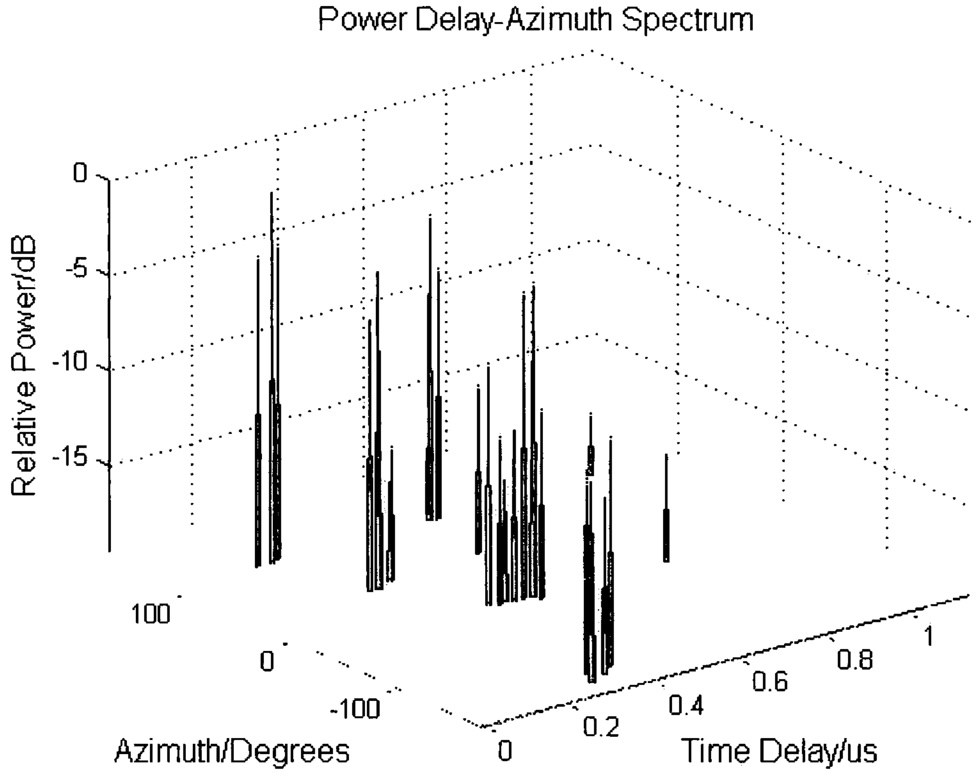

Figure 7.22: Power-delay-azimuth spectrum for non-LOS data.

Further analysis of such measurement data reveals a number of multipath clusters. These clusters can be viewed primarily in the angle domain which infers that the components within a particular cluster have similar DOAs. A more stringent definition of clusters is multipath components which not only have similar DOAs but also similar time-delays. Figure 7.23 shows that in the above data there are 4 DOA clusters, namely at -160, -30, 40 and 110 degrees. For all the measurement files collected in non-LOS environments around Durham, there were on average 4 to 5 DOA clusters for the same threshold level. In figure 7.24, the computed DOAs are shown for three typical outdoor environments using a threshold level of -20 dB.

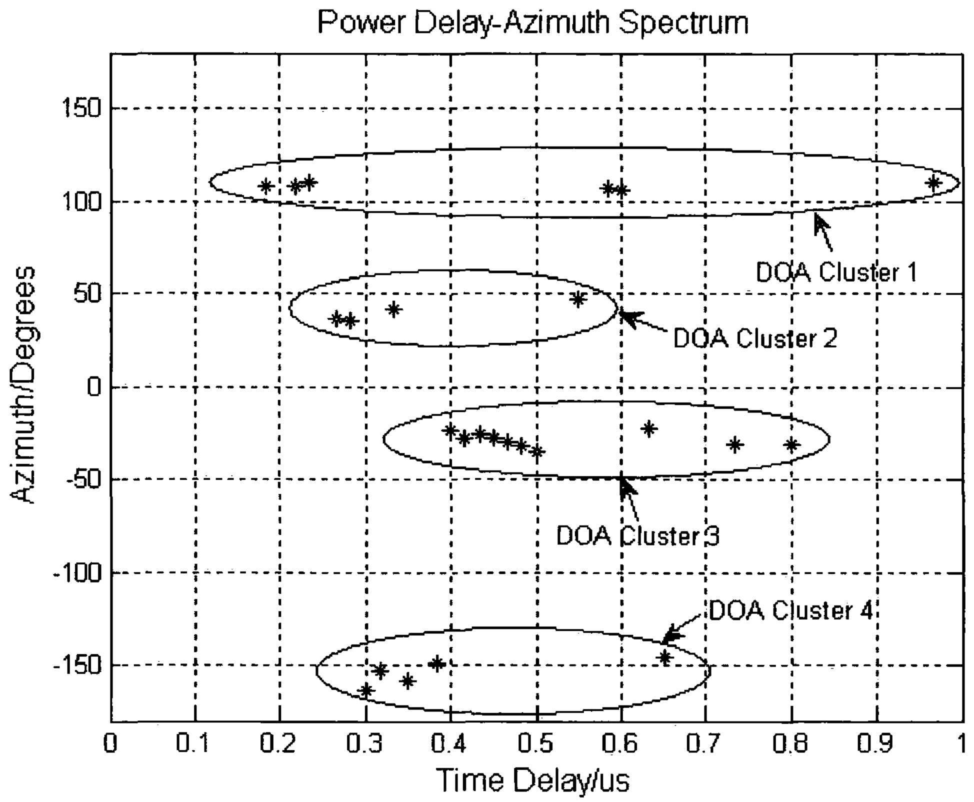

Figure 7.23: Delay-azimuth spectrum for non-LOS data. The data reveals 4 clusters in the angle domain.

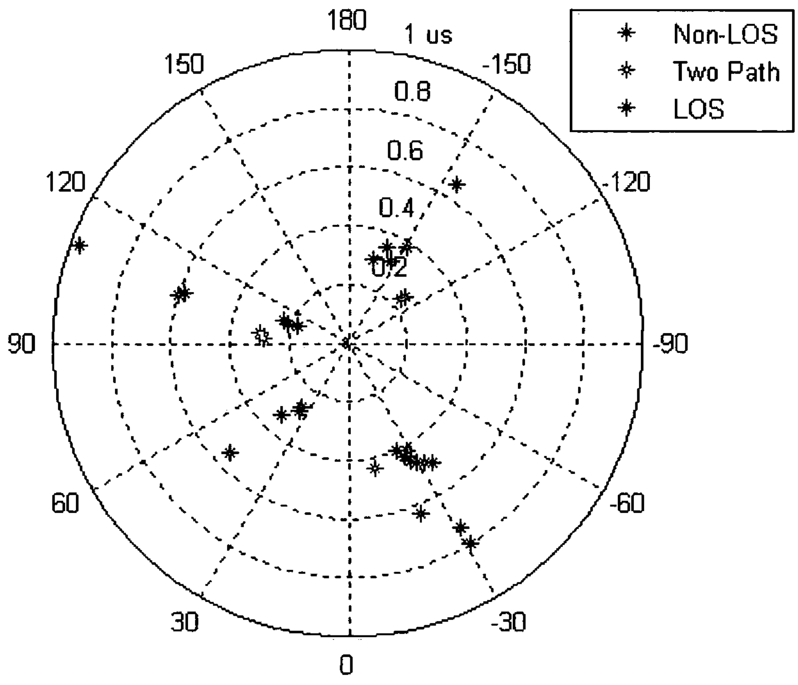

Figure 7.24: Typical DOA components resolved for three different environments.

7.5 Spatio-Temporal Results for 240 MHz Bandwidth (MIMO)

So far various characteristics have been examined for 60 MHz bandwidth outdoor channels in the UMTS FDD band. This section presents double-directional (6 × 8) measurements collected with 240 MHz bandwidth in the 2.4 GHz ISM band. The measurements are collected primarily for indoor WLAN type environments (see figure 7.3). As noted earlier, increasing the swept bandwidth results in a greater time-delay resolution. In this case the time-delay resolution is 4 times greater than in the previous results, which is especially useful for double-directional indoor sounding. These measurements are presented in the following sections.

7.5.1 Power Delay Profiles

The indoor measurements presented here are in the School of Engineering, level 2b. Figure 7.25 shows the MIMO 6 × 8 power delay profiles for an indoor environment where there was no direct LOS signal (Tx21 in figure 7.3).

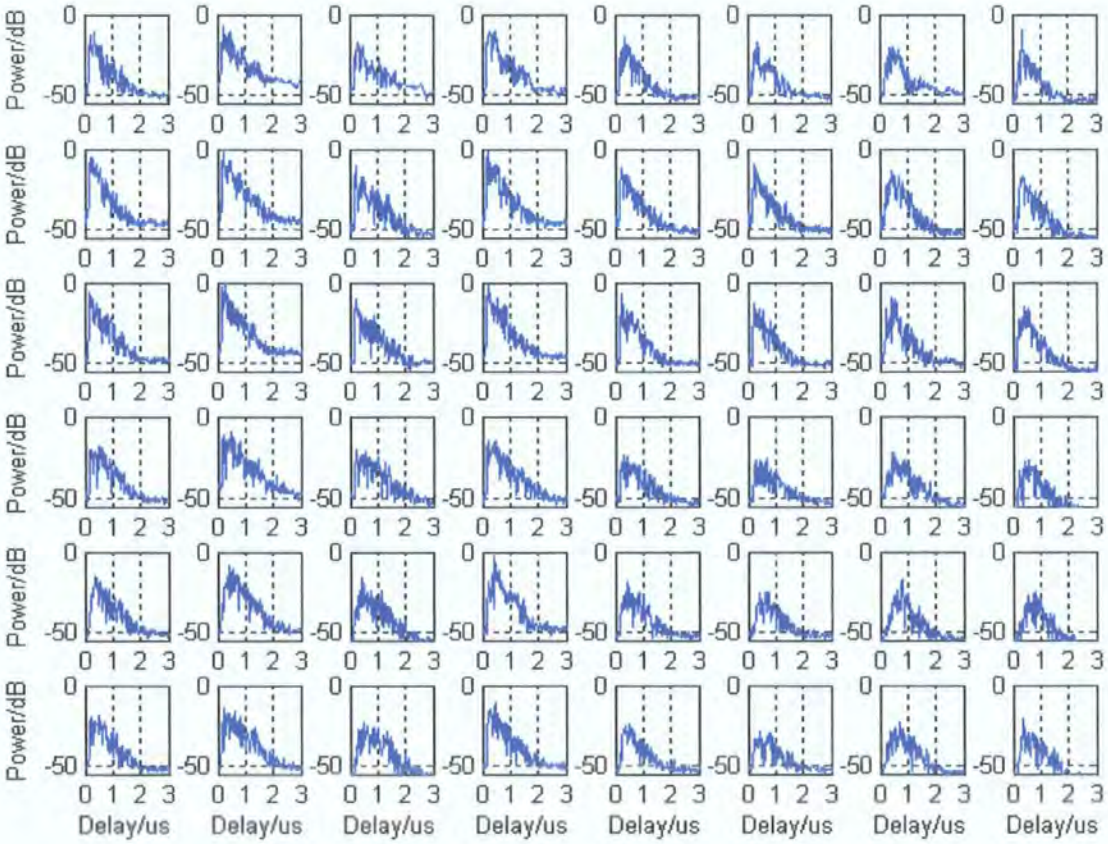

Figure 7.25: Typical indoor non-LOS MIMO power delay profiles.

In figure 7.25, the rows represent the transmitters in sequence, while the columns represent the receive channels in sequence. Thus, row 3 shows receive channels 1 to 8 for transmit antenna 3. This matrix representation will be used throughout the rest of this thesis.

In the PDP results shown above, transmit antenna 2 and receive antenna 2 correspond to the largest signal level, which is consistent with the measurement setup. Figure 7.26 shows PDP results for a LOS location (Tx1 in figure 7.3). In this case, transmit antenna 1 and receive antenna 1 are in direct LOS. As expected, the other channels (MIMO elements) have much lower beatnote power.

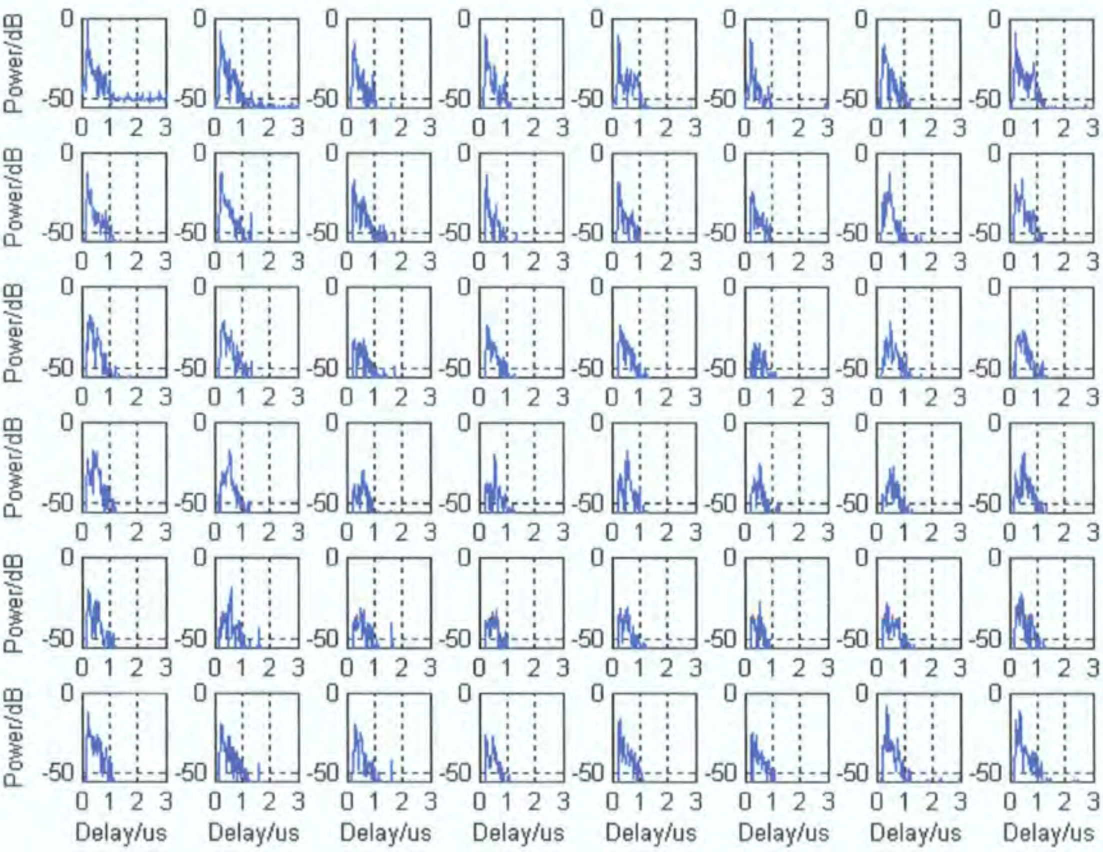

Figure 7.26: Typical indoor LOS (Tx1, Rx1) MIMO power delay profiles.

In general, these PDP results show the multipath structure of each MIMO (element) channel, which is different in its own right. Such results are particularly useful in correlation analysis.

7.5.2 Scattering Function

The scattering functions can also be shown for the MIMO channel matrix. As noted previously, the Doppler range is directly limited by the number of switching ports at the transmitter. Here a Doppler range of ± 15.6 Hz was obtainable. This is more than adequate for the majority of indoor measurement campaigns, where the channel is mostly stationary. Indoor results indicate that the Doppler shift is typically lower than ± 5 Hz, also consistent with SISO results in [13]. Figure 7.27 shows the 6 × 8 scattering functions for a typical non-LOS scenario (File: Tx 21).

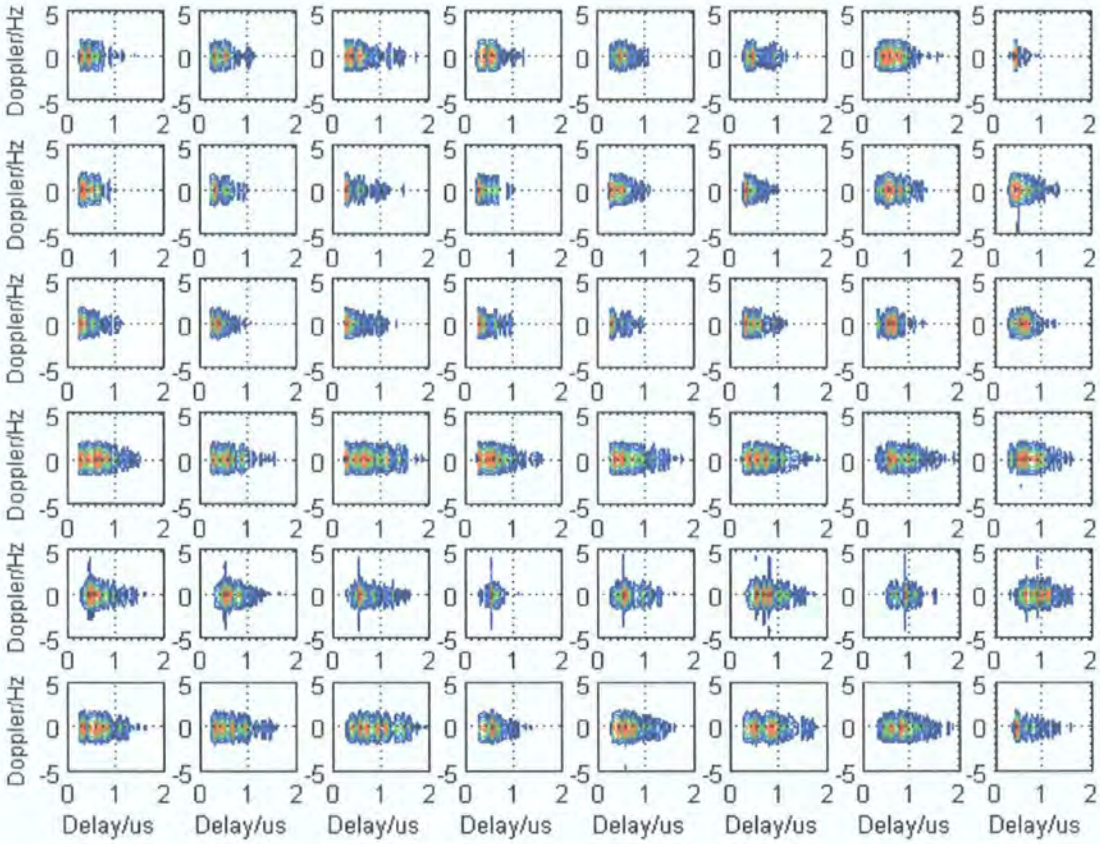

Figure 7.27: Typical indoor non-LOS MIMO scattering functions.

In the above results, more temporal variations are apparent on all receive channels corresponding to transmit antenna 5. For this measurement, transmitters 4 and 5 were pointing towards the windows in the teaching lab (see Tx21 in figure 7.3). Results such as those in figure 7.27 often indicate how static a particular environment is. For these indoor measurements, which were made while both the transmitter and receiver were stationary, the maximum Doppler variation was typically lower than ±

5 Hz, corresponding to a measurement speed of less than 1 m/s. Results with greater Doppler shifts will be presented in the next chapter.

7.5.3 Time-Variant Transfer Function

In general, most of the computations performed on the measurement data are carried out on the MIMO frequency-time transfer function matrix. The transfer function matrix, **H**, is thus represented as a four-dimensional complex array of size $n_R \times n_T \times N_f \times N_t$, where n_T and n_R represent the number of antennas at the transmitter and at the receiver, respectively and the parameters N_t and N_f are used to define the number of samples in time and in frequency, respectively. A wide range of channel calculations and statistics presented in the following chapter are based on these data samples. Figure 7.28 shows the MIMO time-variant transfer functions for the same non-LOS environment.

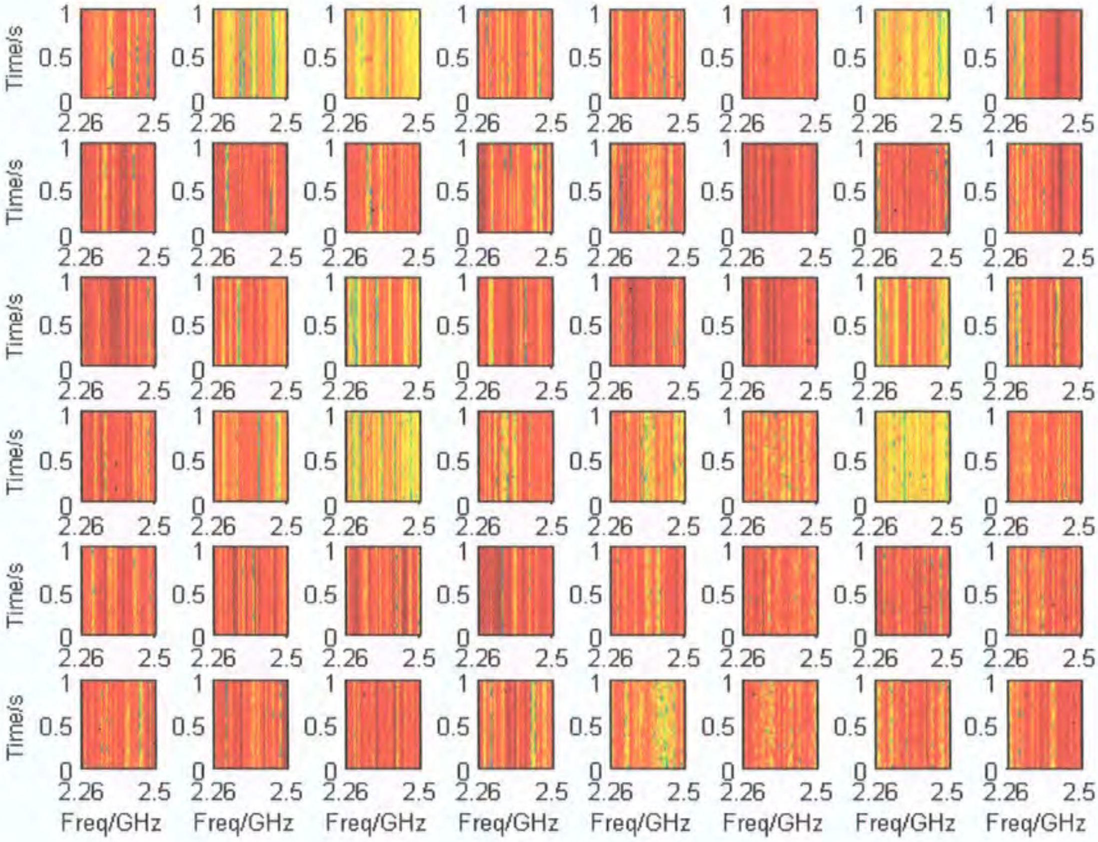

Figure 7.28: Typical indoor non-LOS MIMO transfer functions.

It is important to note that these results are for a system where n_T is not equal to n_R, i.e. there are more receivers than transmitters. The significance of such a system is that it relies on diversity at the receiver end. Antenna diversity can be seen in figure 7.29, which shows all the transfer functions for receiver antenna 1. The line shown at point X indicates a spot where at least 3 transmitters (1, 2, and 5) are in a fade.

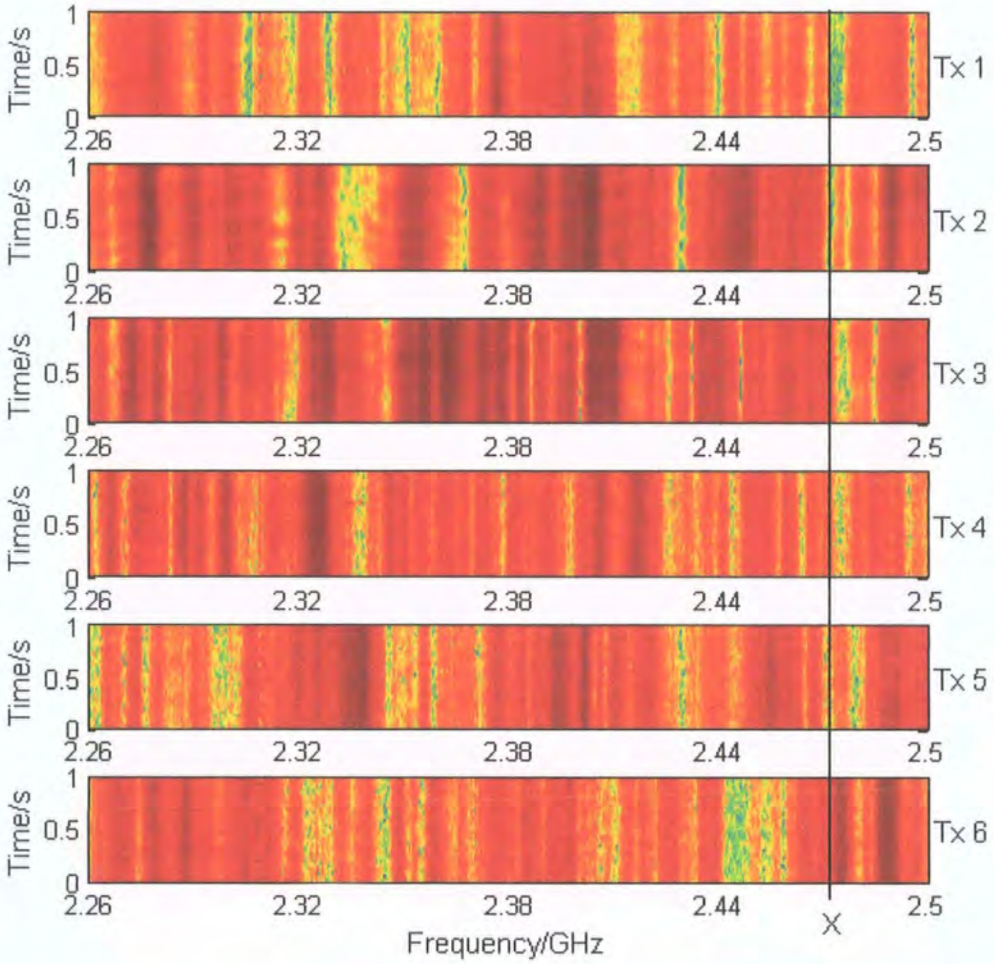

Figure 7.29: Typical indoor non-LOS MIMO transfer functions for receiver 1.

7.5.4 Double-Directional Channel Analysis

The primary purpose of the measurements collected in the School of Engineering as outlined in figure 7.3 was to analyse the double-directional channel data, defined here as azimuth DOA and DOD. In the following, results will be presented for the different double-directional indoor scenarios using both beamforming and the SAGE method.

7.5.4.1 Double-Directional Beamforming

The beamforming concept can easily be applied to double-directional channels, where there is a defined transmit array and receive array. As before an 8-element VPDCPA is employed at the receiver end, however now there is also a 6-element VPDCPA employed at the transmitter. For this setup, the joint steering vector is defined as

$$\mathbf{a}\left(\phi_{Tx},\phi_{Rx}\right)=\mathbf{a}_{Tx}\left(\phi_{Tx}\right)\otimes\mathbf{a}_{Rx}\left(\phi_{Rx}\right) \tag{7.3}$$

where $\mathbf{a}_{Tx}(\phi_{Tx})$ and $\mathbf{a}_{Rx}(\phi_{Rx})$ are the usual array steering vectors at the transmitter and the receiver, respectively and ⊗ represents the Kronecker product [14]. The sample covariance matrix is calculated on the vectorised channel data. This essentially means that the MIMO matrix data is stacked as a vector for all such computations. Figure 7.30 shows beamforming applied to averaged LOS data (Tx 3) where receive antenna 1 and transmit antenna 4 are in direct LOS.

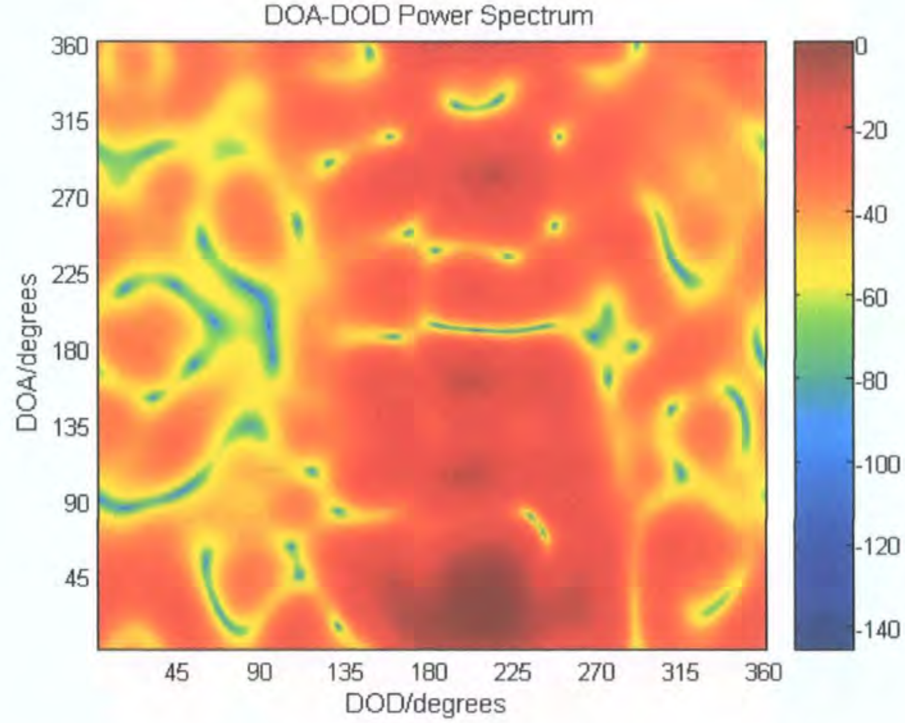

Figure 7.30: DOA-DOD (Azimuth) power spectrum for LOS data.

In figure 7.30, the dominant DOA-DOD component is at 39 and 212 degrees, respectively. Of course the indoor laboratory environment (figure 7.3) presents additional scatterings which can be seen along the DOA axis for a mean DOD of 195 degrees. Typical non-LOS results are shown in figures 7.31 and 7.32.

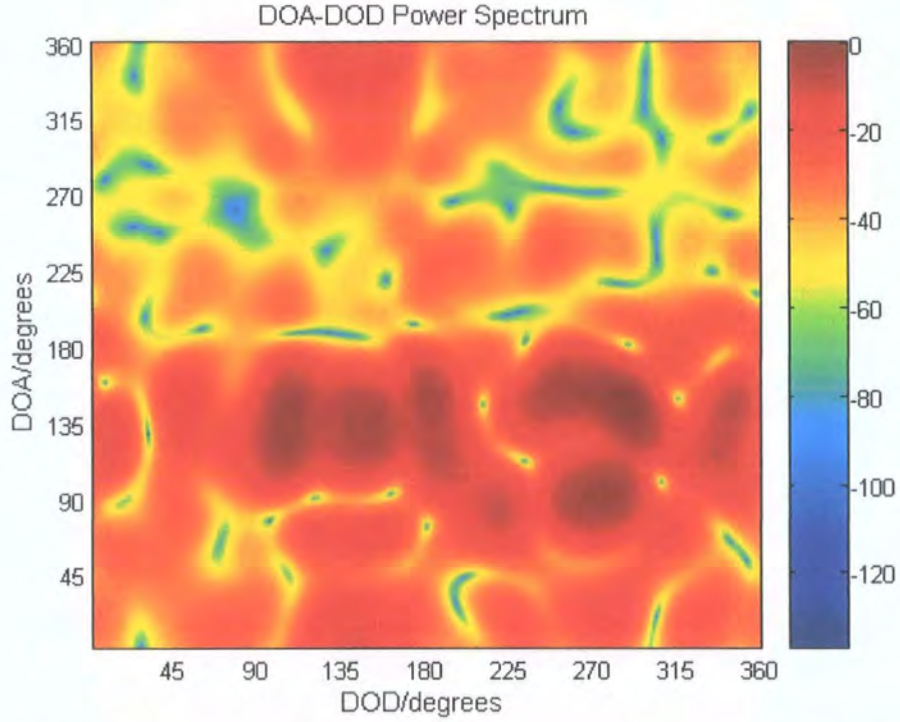

Figure 7.31: DOA-DOD (Azimuth) power spectrum for non-LOS data (Tx 14).

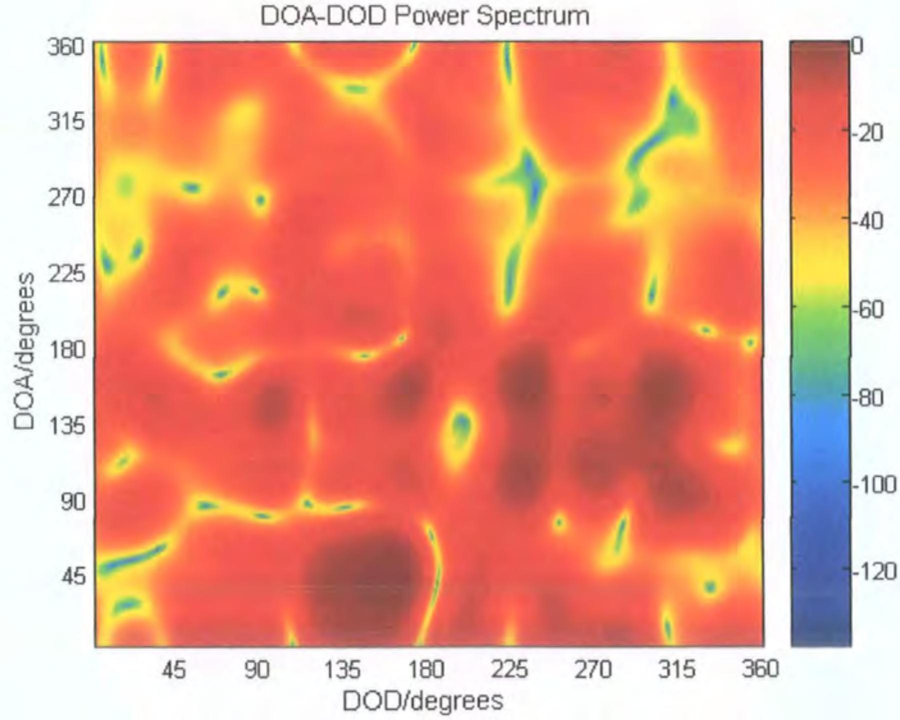

Figure 7.32: DOA-DOD (Azimuth) power spectrum for non-LOS data (Tx 17).

The measurements in the School of Engineering provided a wide range of non-LOS and LOS scenarios, some of which have been shown. Since the beamformers applied here are still somewhat limited in resolution, the following section explores the application of the SAGE method in order to provide more accurate path estimates.

7.5.4.2 DOA-DOD Estimation Using the SAGE Technique

In order to estimate the angles at both ends of the channel, a SAGE-type method was employed for each path (validation using beamforming). This again was applied after performing a path search on the double-directional data. The difference here was that the channel was vectorised as in the previous case and the so-called Cost function [5] had an additional variable corresponding to the DOD. Figure 7.33 shows the various components resolved for LOS data at position Tx3. Here the path search algorithm found 11 components above a -20 dB threshold as before. Clearly, this shows a scattering radio channel, where there are other significant multipath components in addition to the direct (LOS) path. A more severely scattered non-LOS environment is shown in figure 7.34, where 33 multipath components were resolved.

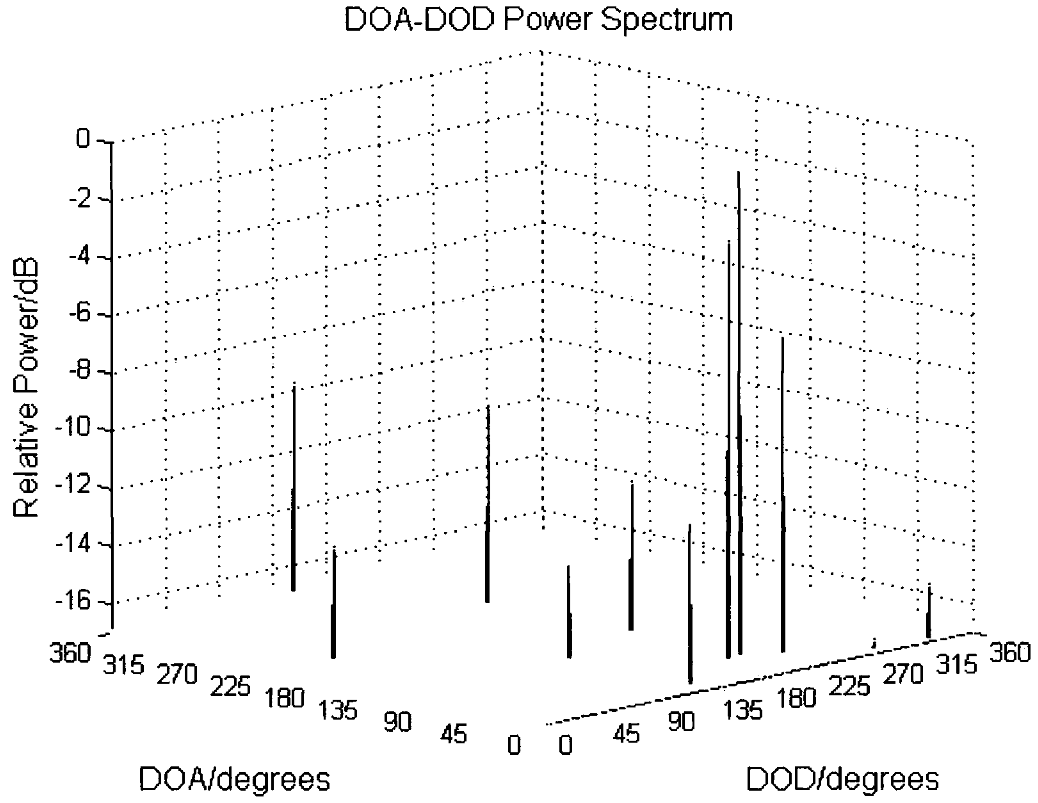

Figure 7.33: DOA-DOD (azimuth) spectrum for LOS data.

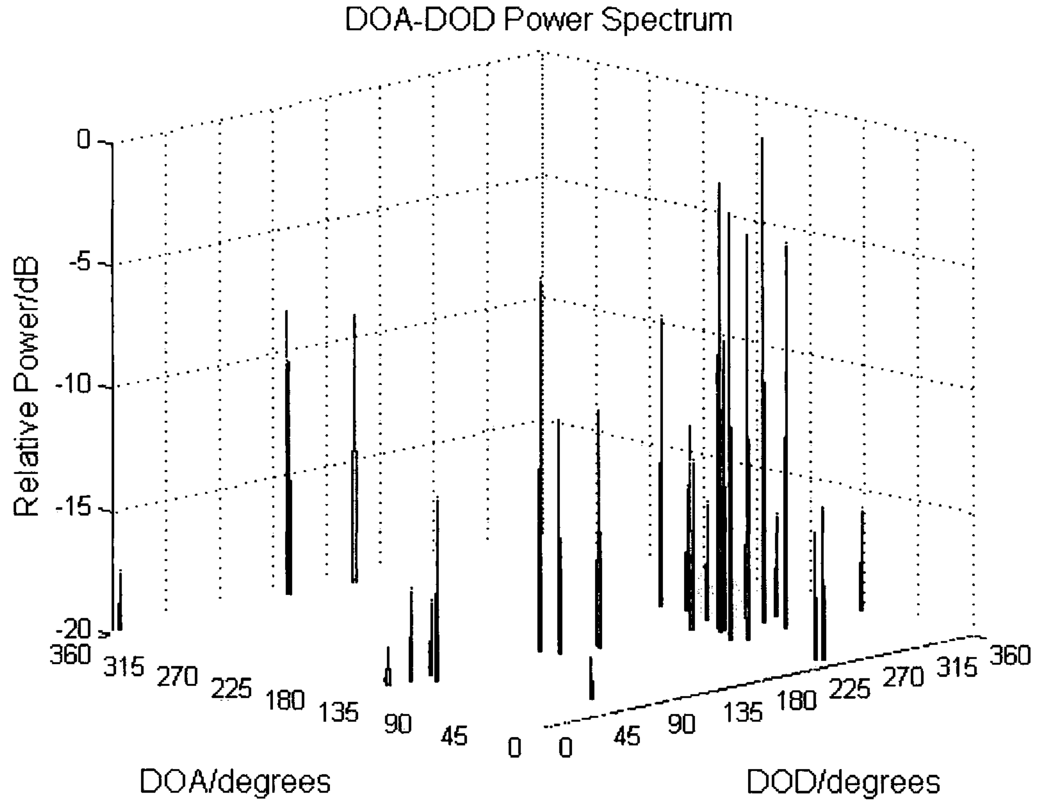

Figure 7.34: DOA-DOD (azimuth) spectrum for non-LOS data (Tx 14).

In general, the non-LOS locations used for these measurements varied considerably. Figure 7.34 shows the spatial channel information for one measurement location. Various other double-directional measurements are shown in figure 7.35 along with the number of multipath components resolved. Similarly to the SIMO results presented earlier in the chapter, the double-directional spatial data here could be placed into clusters. Such clusters could be used to identify multipath components which have DOAs and DODs in close proximity to one another.

It is important to note that the distances between the measurement locations for the data presented here varied appreciably. This meant that statistical analysis of the double-directional angular spread was somewhat limited, therefore such results are not presented here. The average number of components resolved for the non-LOS files collected in the School of Engineering using the SAGE method was ~ 24 (with standard deviation of the number of resolved components equal to ~ 10).

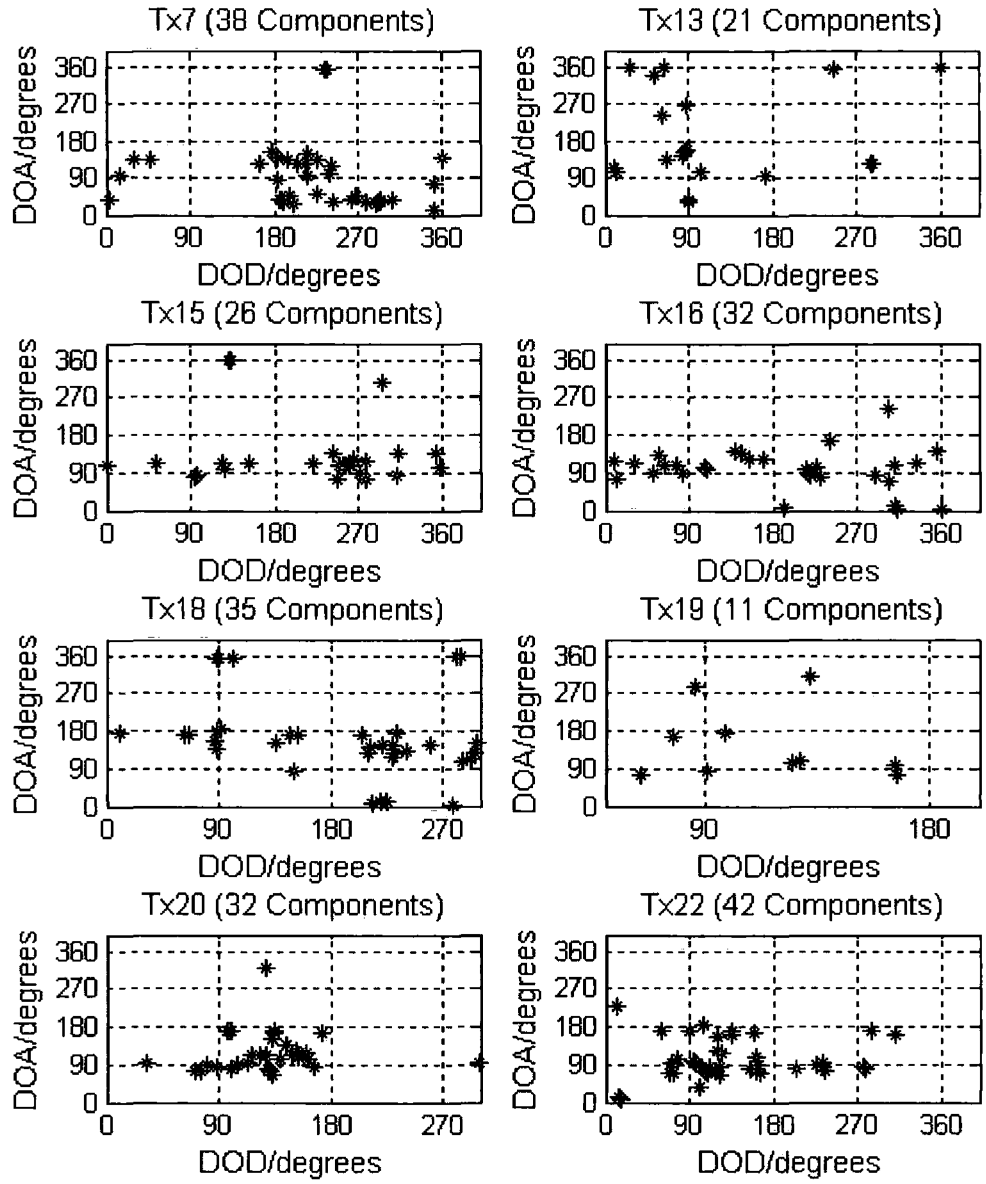

Figure 7.35: DOA-DOD (azimuth) spectrum for various non-LOS data.

7.6 Summary and Conclusions

This chapter presented various spatial and temporal channel measurements for multiple antenna radio links. The focus here has been to show results for two different environments, namely outdoor UMTS links and indoor adhoc (WLAN type) channels. The data processing has been described for obtaining the different types of results. The processed data has included power delay profiles, scattering function, time-variant transfer function, azimuth angle power spectrum, amongst other results. Directional and double-directional channel information has been computed via two different techniques which have shown good agreement.

7.7 References

1. M. Abdalla, N. Razavi-Ghods and S. Salous, "Performance Evaluation of Sector Antenna arrays for Angle of Arrival Estimation," International Symposium on Antenna Technology and Applied Electromagnetics (ANTEM 2005), Saint-Malo, France, June 2005.
2. P. Filippidis, "Multi-Channel Sounder for Directional Measurements," Ph.D. Thesis, Dept. of Electrical Engineering and Electronics, UMIST, Manchester, UK, 2002.
3. D. G. Manolakis, V. K. Ingle, S. M. Kogon, *Statistical and Adaptive Signal Processing: Spectral Estimation, Signal Modeling, Adaptive Filtering and Array Processing*: McGraw Hill International Editions, 2000.
4. F. J. Harris, "On the Use of Windows for Harmonic Analysis with the Discrete Fourier Transform," *Proceedings of IEEE*, vol. 66, pp. 51-83, 1978.
5. B. H. Fleury, M. Tschudin, R. Heddergott, D. Dahlhaus, K. I. Pederson, "Channel Parameter Estimation in Mobile Radio Environments Using the Sage Algorithm," *IEEE Journal on Selected Areas in Communications*, vol. 17, pp. 434-450, 1999.
6. K. Pahlavan, A. H. Levesque, *Wireless Information Networks*: John Wiley & Sons Ltd, 1995.
7. J. D. Parsons, *The Mobile Radio Propagation Channel*, 2 ed: John Wiley & Sons Ltd, 2000.
8. T. S. Rappaport, *Wireless Communications: Principles and Practice*, 2 ed: Prentice Hall PTR, 2002.
9. D. E. Barrick, "FM/CW Radar Signals and Digital Processing," *U.S. Department of Commerce, National Oceanic and Atmospheric Administration (NOAA) Technical Report ERL 283-WPL 26*, 1973.
10. S. Salous, "Chirp Waveforms for Multiple Antenna Channel Sounders," 27th URSI General Assembly, Maastricht, Netherlands, 2002.
11. R. Steel, Hanzo, L., *Mobile Radio Comunications: Second and Third Generation Cellular and WATM Systems*, 2 ed: John Wiley & Sons Ltd, 1999.
12. K. Witrisal, K. Yong-Ho, R. Prasad, "Frequency-Domain Simulation and Analysis of the Frequency-Selective Ricean Fading Radio Channel," IEEE

International Symposium on Personal, Indoor and Mobile Radio Communications, Boston, USA, 1998.

13. V. Hinostroza, "Indoor Wideband Mobile Radio Channel Characterisation System," Ph.D. Thesis, Dept. of Electrical Engineering and Electronics, UMIST, Manchester, UK, 2002.
14. B. Maharaj, J. Wallace, M. Jensen, "Comparison of Double-Directional Channel Response at 2.4 and 5.2 GHz from Indoor Co-located Wideband MIMO Channel Measurements," XXVIIIth URSI GA, New Delhi, India, 2005.

Chapter 8

MIMO Channel Characterisation

8.1 Introduction

The previous chapter outlined the types of measurement results obtained for SIMO and MIMO channels, including delay-Doppler characteristics and azimuth power spectra. The focus in this chapter is to examine the MIMO matrix data, with emphasis on channel throughput analysis. The results presented in this chapter are separated into indoor and outdoor measurements. More emphasis is placed on the indoor campaigns which include 60 MHz bandwidth UMTS-FDD measurements, 96 MHz bandwidth dual band (centre frequency of 2.25 and 5.8 GHz) measurements, and various types of wideband (240 MHz) measurements in the 2.4 GHz ISM band. Outdoor measurements were carried out primarily in the UMTS-FDD uplink band for different array configurations. Comparisons are made between the different MIMO channel environments.

The objective of this chapter is to characterise various types of MIMO radio propagation channels by statistically analysing the MIMO matrix data. Results include CDF plots of channel capacity for different array sizes and geometries. In the previous chapter it was shown that the data processing could be achieved by FFT techniques. In addition to this, matrix manipulations and capacity computations are described in this chapter, including the concept of channel normalisation.

8.2 Measurement Campaigns

8.2.1 Indoor MIMO Campaigns

The indoor measurements can be sub-divided into three sets. The first set of measurements was acquired for the 60 MHz UMTS-FDD uplink band, in the School of Engineering (SoE), floor 2a. Figure 8.1 displays the measurement locations and figure 8.2 shows photos of the environment. At each measurement location multiple files (red dots) were collected by rotating the array at the transmit end in order to change the spatial environment. In total ~ 90 files were collected for different array configurations in non-LOS scenarios.

The sounder parameters for these measurements are shown in table 8.1. The sampling parameters are the same as those described in chapter 7. In this set, various indoor channel measurements were made for square MIMO systems (i.e. $n \times n$ channels) up to a 4 × 4 configuration using omni-ULAs at both ends. In addition to this, 2 × 8 channel measurements were made using the 8-element vertically polarised directional circular patch array (VPDCPA) at the receiver end and a simple 2-element omni array at the transmitter.

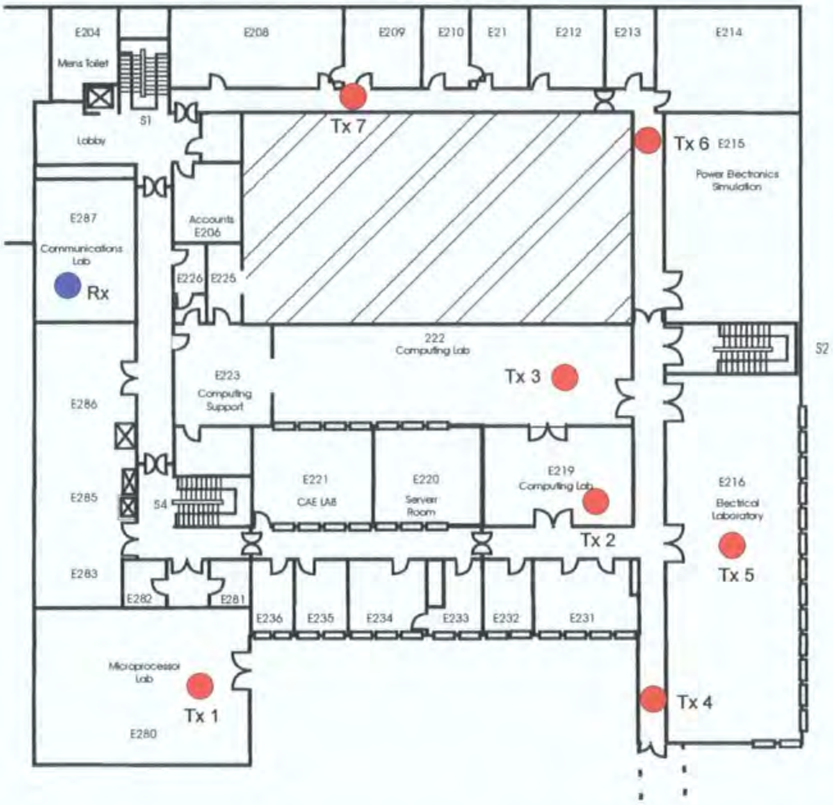

Figure 8.1: Location of MIMO measurements in the SoE for the UMTS-FDD band. The dotted lines show the path between the two SoE buildings.

Figure 8.2: Photos of different measurement environments in the SoE, floor 2a.

Array Size	Up to 4 × 4 (sqr. matrix), 2 × 8
Array geometry	ULA (both sides), UCA at Rx
Centre frequency	1950 MHz
Swept bandwidth	60 MHz
Time delay resolution	16.67 ns
Range resolution	5 m
Time delay window	33.33 us
Doppler range	± 25 Hz (or ± 15.6 Hz)

Table 8.1: Parameters for MIMO measurements (first indoor set).

The second set of MIMO measurements were made in the BBC training studios at Evesham. MIMO 4 x 4 channel measurements were carried out in two simultaneous frequency bands centred on 2.25 GHz and 5.8 GHz with a bandwidth of 96 MHz. The measurements for the 5.8 GHz band (higher ISM band) were made using the 2 - 6 GHz frequency extenders described in [1].

The block diagram of this particular measurement configuration is shown in figure 8.3. The main difference here is that two frequency bands are simultaneously transmitted on 4 discone antennas (4-element UCA with radius of $\lambda/2$ at 2.25 GHz).

This is achieved by generating the upper and lower sidebands at 2 GHz and up-converting the lower band. At the receiver, 4 of the 8 receive channels are used within the usual band (i.e. 2.2 – 2.3 GHz), while the input to the other 4 channels is the down-converted band from 5.8 GHz.

The requirement for such measurements was founded on the proposal to implement wideband MIMO-OFDM video links in studio environments as a real alternative to cable connections. The measurements took place in 3 main locations, where the first Studio (Studio A) was larger in size than the others. Figure 8.4 shows the locations of the measurements in studio A (2 sets). Here, the blue dot represents the receiver position and the red dots represent the transmitter locations.

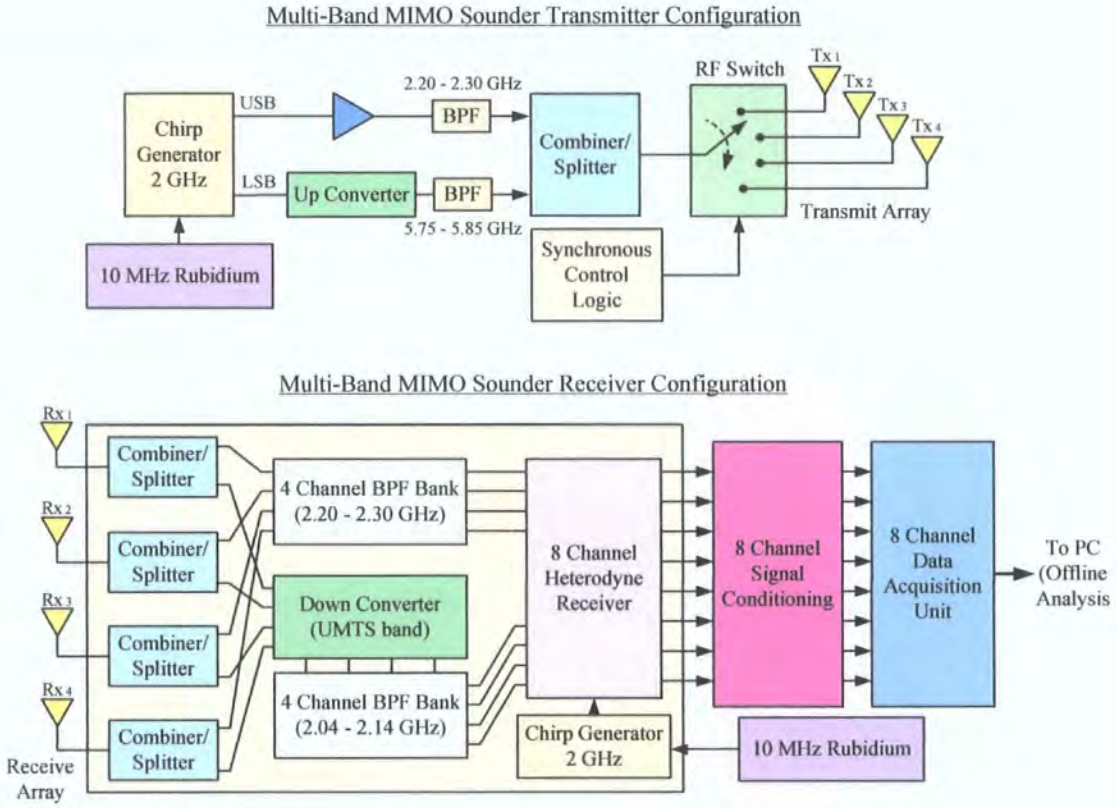

Figure 8.3: MIMO sounder configuration for the BBC (Evesham) measurements.

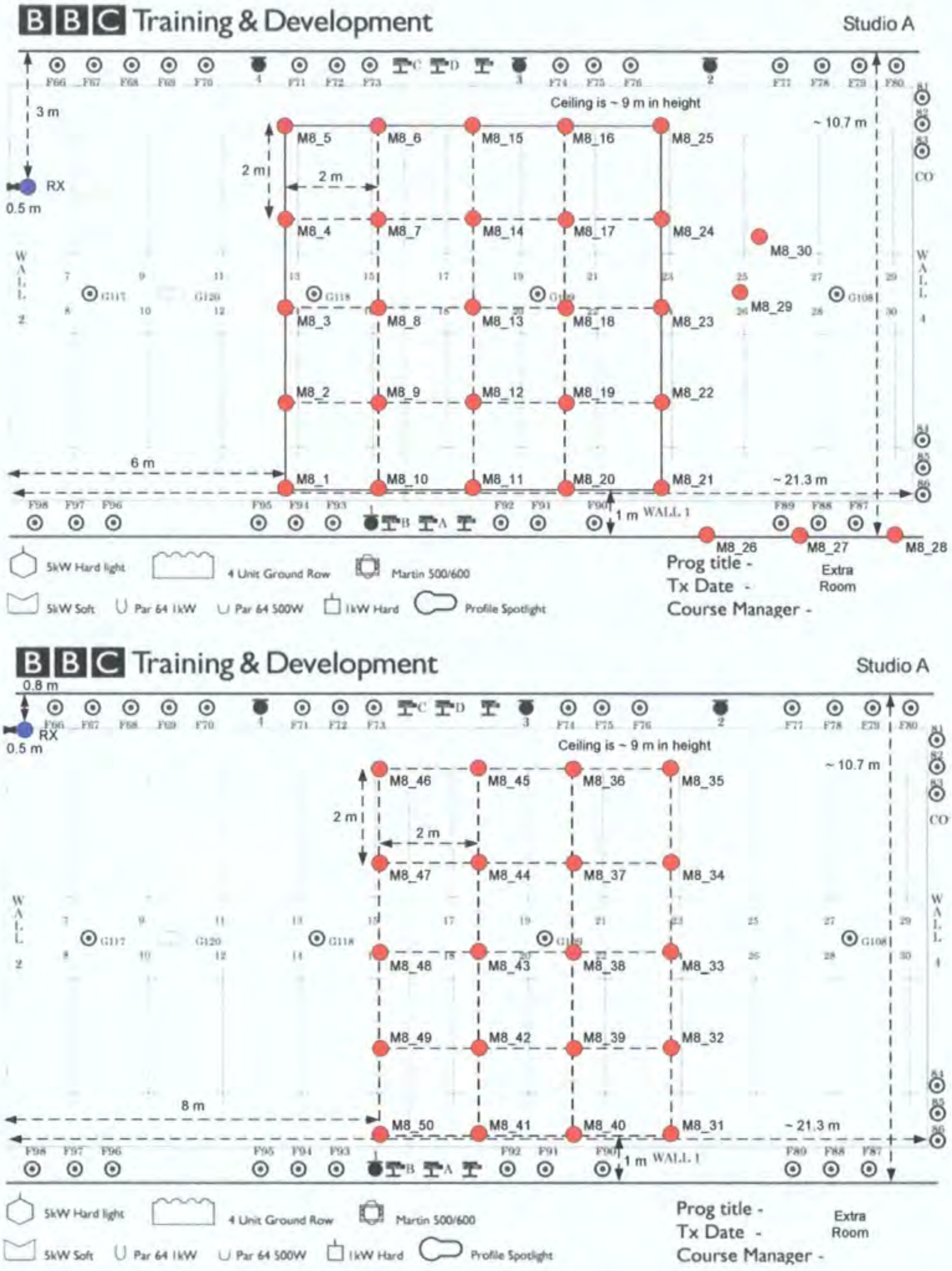

Figure 8.4: Location of MIMO measurements in BBC Studio A (sets 1 & 2).

Similarly, MIMO measurements were made in Studio C (figure 8.5), which was smaller than studio A. Here, measurement sets 1-3 were made using two receiver array configurations, including the standard discone circular array (UCA) and a linear array configuration where the antennas were spaced 0.5 m apart. In set 4, the receiver array was arranged as a cross polar array.

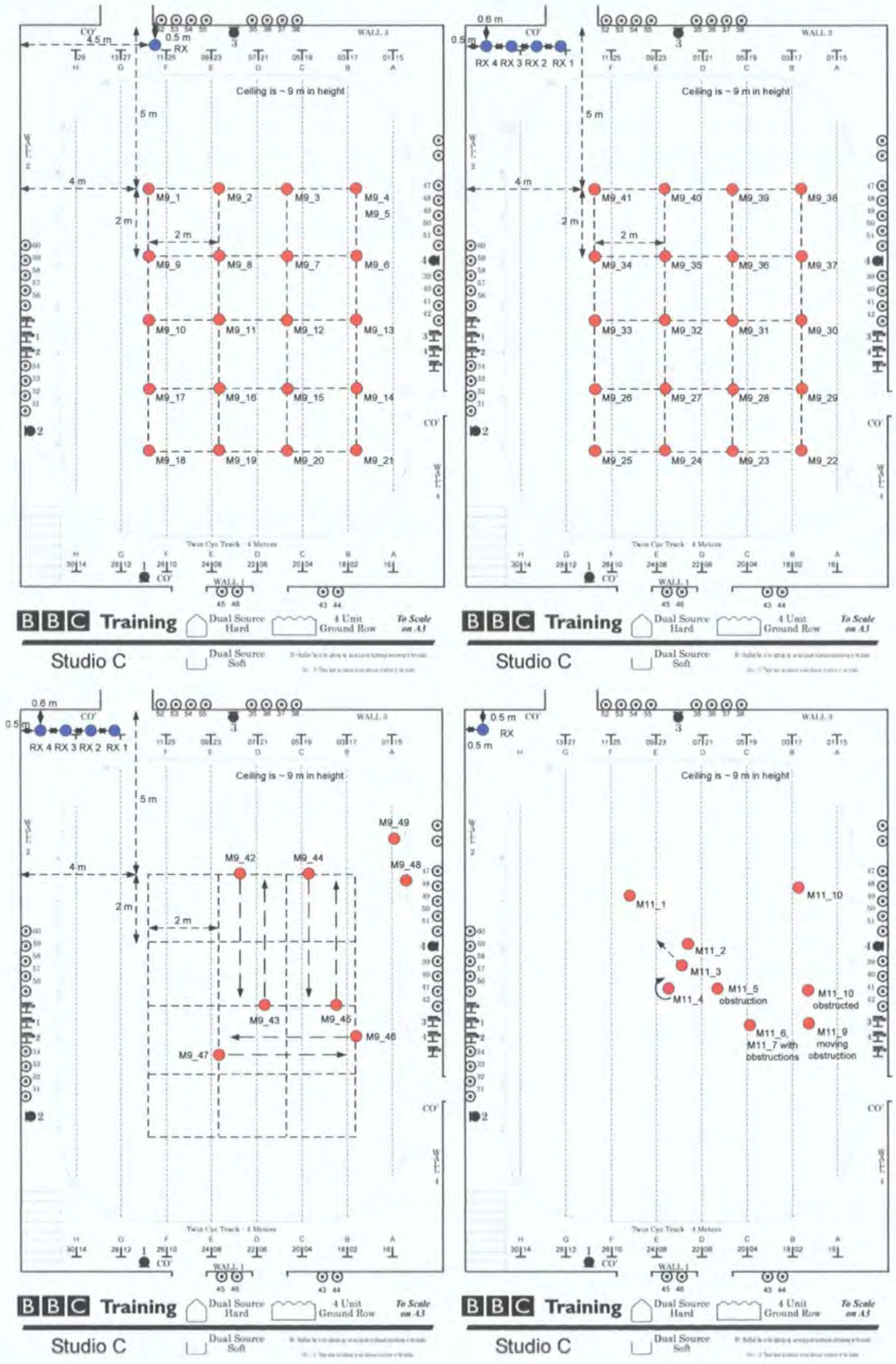

Figure 8.5: Location of MIMO measurements in BBC Studio C (sets 1 - 4).

The measurements in studio C included files which were collected while the transmitter was moving at speeds of ~ 2 m/s (shown by arrows). The purpose of such measurements was to continuously collect data while the structure of the multipath environment was changing. The Doppler information would provide interesting channel throughput results, especially for LOS environments. Channel measurements were also made inside Laboratory V2 (3 sets in figure 8.6).

Figure 8.6a: Location of MIMO measurements in BBC Lab V2 (sets 1 & 2).

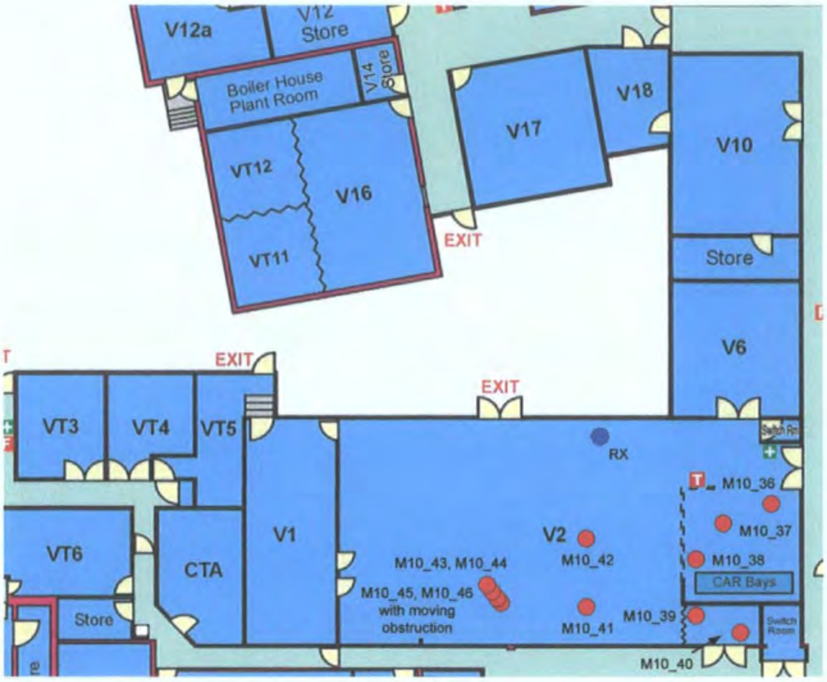

Figure 8.6b: Location of MIMO measurements in BBC Lab V2 (set 3).

The measurements shown in figure 8.6 were all collected using the 4 × 4 UCA discones. Set 1 included outdoor measurements. Figures 8.7 – 8.9 show photos of the 3 main BBC measurement environments.

Figure 8.7: Photo of BBC training studio A.

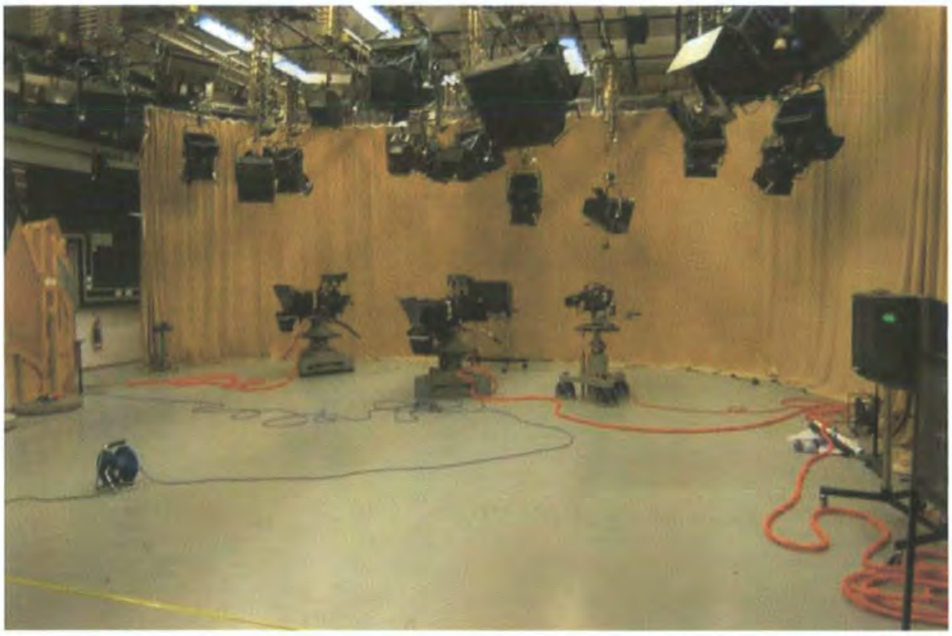

Figure 8.8: Photo of BBC training studio C.

Figure 8.9: Photo of outdoor environment (BBC laboratory V2).

Overall 155 measurement files were collected and many of the environments presented a LOS path. The sounder parameters for these measurements are shown in table 8.2. In addition to this, a summary of the measurement files is made in table 8.3, which includes information about the array type and geometry. The main data analysis is performed on conventional MIMO data for file sets m8, m9, and m10.

Centre frequency	2250 MHz and 5800 MHz
Swept bandwidth	96 MHz
Time delay resolution	10.42 ns
Range resolution	3.13 m
Time delay window	20.08 us
Doppler range	± 25 Hz (at 2.25 GHz)

Table 8.2: Parameters for BBC measurements (second indoor set).

File name	Location	Transmit antenna array	Receive antenna array	Comments
m8_1 to 50	Studio A	4-element discone (UCA)	4-element discone (UCA)	Two receiver locations with 25 files each
m9_1 to 49	Studio C	4-element discone (UCA)	1-21 using 4-element discone (UCA) 22-49 using 4-element spaced discone (ULA)	42-47 moving transmitter (Tx)
m10_1 to 46	Inside and outside laboratory V2	4-element discone (UCA)	1-35 using 4-element discone at height 2m (UCA) 36-46 using 4-element discone at height 1m (UCA)	1-15 outside 16-31 inside 32-35 inside, moving Tx 36-46 inside with 45-46 with moving obstruction
m11_1 to 10	Studio C	BBC antenna array	Cross polar array (4-element)	Single band (2.25 GHz)

Table 8.3: Summary of BBC MIMO measurements.

The final set of indoor measurement data was collected in the School of Engineering, floors 2a, 3a, and 2b. The measurements were done with 240 MHz bandwidth centred on 2.38 GHz (band 2.26 – 2.5 GHz) for various array sizes and configurations. These included channels 2 × 2, 2 × 4, 4 × 2, 3 × 3, 3 × 4, 4 × 4, and 6 × 8. The last set of measurements (6 × 8) was carried out on floor 2b. All the other channel measurements were collected on floors 2a and 2b. Two sets of 4 × 4 measurements were made, one with the usual discone array configuration (UCA) and the other for varying antenna spacings of $\lambda/3$, $\lambda/2$, λ, and $3\lambda/2$. Figures 8.10 and 8.11 show the measurement locations.

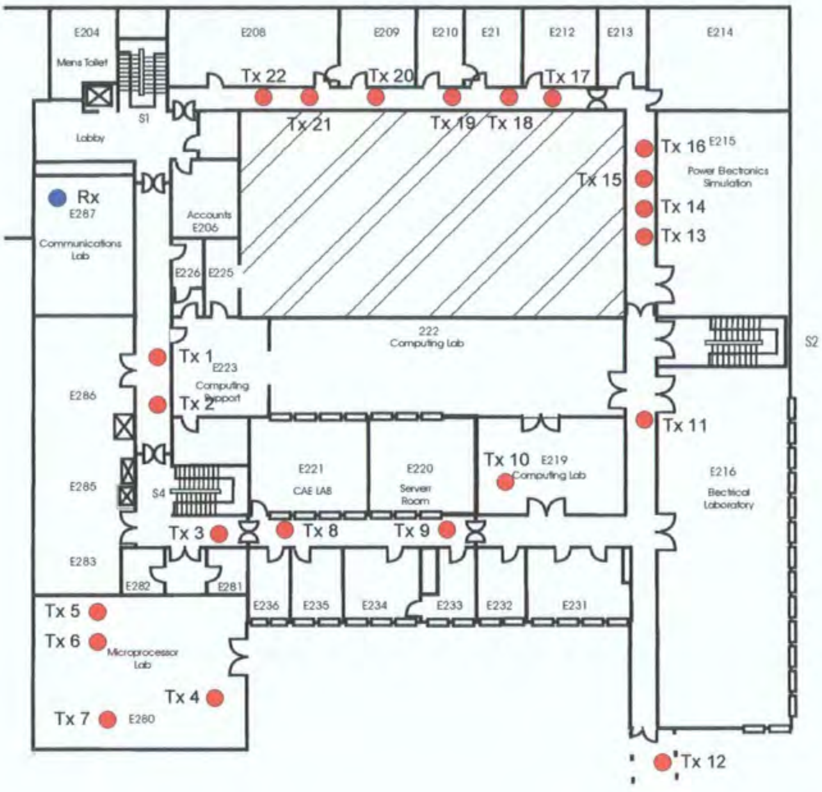

Figure 8.10: Location of MIMO measurements in the SoE, floor 2a.

Figure 8.11: Location of MIMO measurements in the SoE, floor 3a (Rx on floor 2a).

In figures 8.10 and 8.11, there were typically up to 5 additional files collected for LOS environments and higher Doppler scenarios (moving the transmitter). The measurement parameters are shown in table 8.4. Near 300 measurement files were acquired during this particular indoor campaign and the details of this are given in table 8.5.

Centre frequency	2380 MHz
Swept bandwidth	240 MHz
Time delay resolution	4.17 ns
Range resolution	1.25 m
Time delay window	8.33 us
Doppler range	± 25 Hz (± 15.6 Hz for 6 × 8)

Table 8.4: Parameters for MIMO measurements (third indoor set).

Files per set	Location	Array size	Array type & geometry	Comments
41	SoE, floor 2a, 3a	2 × 2	Rx – 2 discone (ULA) Tx – 2 discone (ULA)	Including Doppler and LOS data.
40	SoE, floor 2a, 3a	2 × 4	Rx – 4 discone (UCA) Tx – 2 discone (ULA)	Including Doppler and LOS data.
38	SoE, floor 2a, 3a	3 × 3	Rx – 3 discone (ULA) Tx – 3 discone (ULA)	Including Doppler and LOS data.
22	SoE, floor 2a	3 × 4	Rx – 4 discone (UCA) Tx – 3 discone (ULA)	-
40	SoE, floor 2a, 3a	4 × 2	Rx – 2 discone (ULA) Tx – 4 discone (UCA)	Including Doppler and LOS data.
41	SoE, floor 2a, 3a	4 × 4	Rx – 4 discone (UCA) Tx – 4 discone (UCA)	Including Doppler and LOS data.
44	SoE, floor 2a, 3a	4 × 4	Rx – 4 discone (ULA) Tx – 4 discone (ULA)	Data for different antenna spacing
28	SoE, floor 2b	6 × 8	Rx – 8 (VPDCPA) Tx – 6 (VPDCPA)	Including LOS data.

Table 8.5: Summary of MIMO measurements in the SoE.

8.2.2 Outdoor MIMO Campaigns

In addition to the indoor measurements, three sets of outdoor measurements were carried out around the Science Laboratories, University of Durham as shown in figure 8.12. Around 90 non-LOS MIMO 4 × 8 measurements were acquired for the 60 MHz UMTS-FDD uplink band. The sounder setup was the same as in table 8.1.

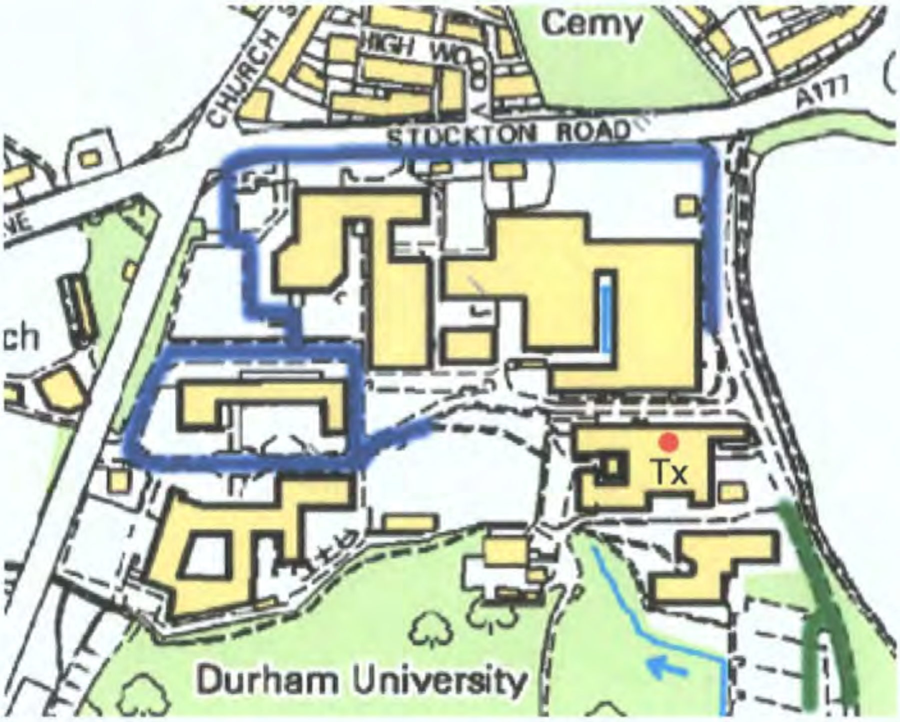

Figure 8.12: Measurements collected around Durham University (from Digimap, Scale 1:5000). The blue line represents the routes taken by the receiver.

The primary purpose of these measurements was to examine the effect of directional antennas, particularly at the transmit end [2]. For this purpose, three data sets were acquired. The first set used a 4-element VPDCPA at the transmitter, similar to those described in chapter 6. The second set used a 4-element vertically polarised directional linear patch array (VPDLPA) with the same patch antennas at the transmitter [3]. The final data set used a 4-element linear array made from simple commercial dipoles. This was referred to as a 4-element vertically polarised uniform linear dipole array (VPULDA).

8.3 MIMO Data Processing

The MIMO channel matrix is generally represented as a four-dimensional complex transfer function matrix, **H**, the size of which is given by $n_R \times n_T \times N_f \times N_t$, where n_T and n_R represent the number of antennas at the transmitter and at the receiver, respectively and the parameters N_t and N_f are used to define the number of samples in time and in frequency, respectively. Most of the computed parameters, including channel capacity are based on these data (see appendix A1.2).

In chapter 3, the MIMO channel matrix was described in some detail with reference to various matrix computations including eigenvalues and the Frobenius norm. This section extends this information to describe the way in which the MIMO data was first normalised and then used to calculate link throughput.

8.3.1 Channel Normalisation

The normalisation of the MIMO channel matrix is of critical importance for assessing channel capacity for a range of environments. However, there is often no clear 'best way' solution to do this. The fundamental problem is that the power/noise levels which are present when measurements are carried out are not necessarily realistic for a true communication system. For example, for channel measurements, it is conceivable that sufficient power can be transmitted to achieve 35 dB or more SNR at the receiver. However, in a practical mobile radio system, it is unlikely to achieve such a level of SNR. Thus, in computing channel capacity, it is assumed that the measured channel (sampled) matrices are exact (i.e. no noise) in order to scale the transmit power/receiver noise in the calculations to achieve a certain assumed receiver (SISO) SNR. This SNR is then used as the SNR of the target communication system whose performance is to be examined. Normalisation just simplifies the process of selecting the appropriate (required) transmit power/receiver noise to achieve a given SNR.

There are different techniques of normalising the MIMO channel data. Perhaps the most accurate technique is to normalise the channel matrices so that the Frobenius norm is equal to $n_R n_T$, which gives an average SISO gain of one [4]. It is, however, unrealistic to force each individual sampled channel matrix to have a SISO gain of one, since this assumes some kind of power control which allows the receiver to always have the same SNR, regardless of path loss [4]. It is far more practical to force the average over all SISO gains to be one, thus assuming an average SNR. This would allow the successive time sample data to be processed correctly and would account for varying path loss since only one constant is used for normalisation.

Since in this thesis, the focus is placed on wideband channels, it is possible to take each frequency bin (out of N_f bins) and perform the computation. It is generally unrealistic to normalise each frequency bin to have the same SISO gain. Therefore each sample is normalised to the same constant (i.e. the average norm for all time and frequency snapshots). If the sampled channel matrix for a particular snapshot is denoted by $\hat{\mathbf{H}}$, then the normalised channel matrix, $\mathbf{H}$, can be defined by the relationship

$$\mathbf{H}^{(f_n)} = \beta \hat{\mathbf{H}}^{(f_n)} \tag{8.1}$$

where β represents the normalisation constant for each time snapshot and f_n represents the frequency sample index. Therefore the specified unity power gain constraint may be expressed as

$$\frac{1}{N_f \cdot n_R n_T} \sum_{f_n=1}^{N_f} \sum_{i=1}^{n_R} \sum_{j=1}^{n_T} \left| \beta \hat{H}_{ij}^{(f_n)} \right|^2 = 1 \tag{8.2}$$

Solving this equation for β gives

$$\beta = 1 \Bigg/ \sqrt{\left(\frac{1}{N_f \cdot n_R n_T} \sum_{f_n=1}^{N_f} \sum_{i=1}^{n_R} \sum_{j=1}^{n_T} \left| \hat{H}_{ij}^{(f_n)} \right|^2 \right)} \tag{8.3}$$

where N_f denotes the total number of MIMO channel snapshots.

There are somewhat varied views on channel normalisation in the international research community. In terms of computing channel capacity using this particular sounder, the calculation was performed for each chirp sweep by using the constant corresponding to the overall Frobenius norm. The spectral capacity would then be given (as an average) in terms of bits/s/Hz. Multiplying this by the system bandwidth would give the overall capacity in bits/s.

8.3.2 Capacity Computation

The evaluation of link capacity can provide a valuable measure of the channel's upper bound limit on achievable data rate. This is particularly useful when assessing the capabilities of MIMO systems for both indoor and outdoor channels. The capacity of a frequency-selective fading MIMO channel can be calculated by dividing the frequency band into N narrower (frequency-flat) sub-channels, which in this case is defined as the frequency bins across the band of interest [5]. Therefore, each of the i^{th} MIMO sub-channels ($i = 1,2,\ldots,N$) can be denoted as

$$\mathbf{H}_i = \begin{bmatrix} h_{11}^{(i)} & h_{12}^{(i)} & \cdots & h_{1n_T}^{(i)} \\ h_{21}^{(i)} & h_{22}^{(i)} & \cdots & h_{2n_T}^{(i)} \\ \vdots & \vdots & \ddots & \vdots \\ h_{n_R1}^{(i)} & h_{n_R2}^{(i)} & \cdots & h_{n_Rn_T}^{(i)} \end{bmatrix} \tag{8.4}$$

The overall input-output relationship of such a system is given by

$$\underbrace{\begin{bmatrix} \mathbf{y}_1 \\ \mathbf{y}_2 \\ \vdots \\ \mathbf{y}_N \end{bmatrix}}_{\mathbf{Y}_{WB}} = \sqrt{\frac{E_s}{n_T}} \underbrace{\begin{bmatrix} \mathbf{H}_1 & 0 & \cdots & 0 \\ 0 & \mathbf{H}_2 & \cdots & 0 \\ \vdots & \vdots & \ddots & \vdots \\ 0 & 0 & \cdots & \mathbf{H}_N \end{bmatrix}}_{\mathbf{H}_{WB}} \underbrace{\begin{bmatrix} \mathbf{x}_1 \\ \mathbf{x}_2 \\ \vdots \\ \mathbf{x}_N \end{bmatrix}}_{\mathbf{X}_{WB}} + \underbrace{\begin{bmatrix} \mathbf{n}_1 \\ \mathbf{n}_2 \\ \vdots \\ \mathbf{n}_N \end{bmatrix}}_{\mathbf{N}_{WB}} \tag{8.5}$$

where E_s is the total average energy available at the transmitter over a symbol period and *WB* denotes a frequency-selective fading channel. The frequency-selective channel capacity can therefore be expressed in terms of the narrowband capacity, given by

$$C_{WB} \approx \frac{1}{N}\sum_{i=1}^{N} C_{NB}^{(i)} \tag{8.6}$$

$$\therefore C_{WB} = \frac{1}{N}\sum_{i=1}^{N} \log_2\left[\det\left(\mathbf{I}_{n_R} + \frac{\rho}{n_T}\mathbf{H}_i\mathbf{H}_i^H\right)\right] \tag{8.7}$$

where ρ denotes the SNR and $\mathbf{H}_i$ is the $n_R \times n_T$ matrix containing the sampled channel transfer functions for each of the sub-channels.

8.3.3 Correlation Analysis

Correlation analysis is an important part of MIMO channel characterisation as there is inherent correlation information contained within MIMO capacity results. Here, the correlation coefficients are defined using $H_{i,j}^{(k)}$, which is the k^{th} channel frequency bin from the j^{th} transmit element to the i^{th} receive element [8, 9]. Therefore the correlation coefficient at the receiver with a particular element spacing is defined as

$$\gamma_{d,RX} = \frac{\sum_{k=1}^{N_f}\sum_{j=1}^{n_T}\sum_{i=1}^{n_R-d} H_{i,j}^{(k)} H_{i+d,j}^{(k)*}}{\sqrt{\left(\sum_{k=1}^{N_f}\sum_{j=1}^{n_T}\sum_{i=1}^{n_R-d}\left|H_{i,j}^{(k)}\right|^2\right)\left(\sum_{k=1}^{N_f}\sum_{j=1}^{n_T}\sum_{i=1}^{n_R-d}\left|H_{i+d,j}^{(k)}\right|^2\right)}} \tag{8.8}$$

where N_f is the total number of samples (frequency bins) and d is the element spacing, typically defined as 1.

The transmit correlation coefficient is calculated by interchanging the roles of the transmitter and receiver [8]. The analysis of these coefficients can be useful when MIMO measurements are performed with different inter-element spacing.

8.4 Indoor MIMO Channel Characterisation

The results of the indoor measurements include temporal characteristics such as delay profiles and time-variant transfer functions, and a range of channel capacity and correlation results, including CDF plots, with more emphasis placed on channel capacity.

8.4.1 UMTS Measurements

This section describes the first set of MIMO measurements collected in the UMTS FDD uplink band with 60 MHz system bandwidth. All of the measurements were acquired in the SoE, floor 2a, while the transmitter and receiver were stationary. Figure 8.13 shows the power delay profiles for a 4 × 4 non-LOS channel (position: Tx4 in figure 8.1). Here, as in previous MIMO figures, the rows represent the transmit elements in sequence, while the columns represent the receive elements in sequence. Figure 8.13 shows at least two dominant multipath components as a result of the receiver location within the School. This was particularly apparent at location Tx4, where the transmitter was placed near the link connecting the two Schools shown in figure 8.1.

Figure 8.14 shows the time-variant transfer function data for the same 4 × 4 MIMO set. It is possible to see from the time axis of these plots that the channel was relatively stationary. These plots are normalised for each MIMO element and the deepest fade for this measurement set was – 36.4 dB at 0.76 s and 1966 MHz (Tx 4, Rx 1).

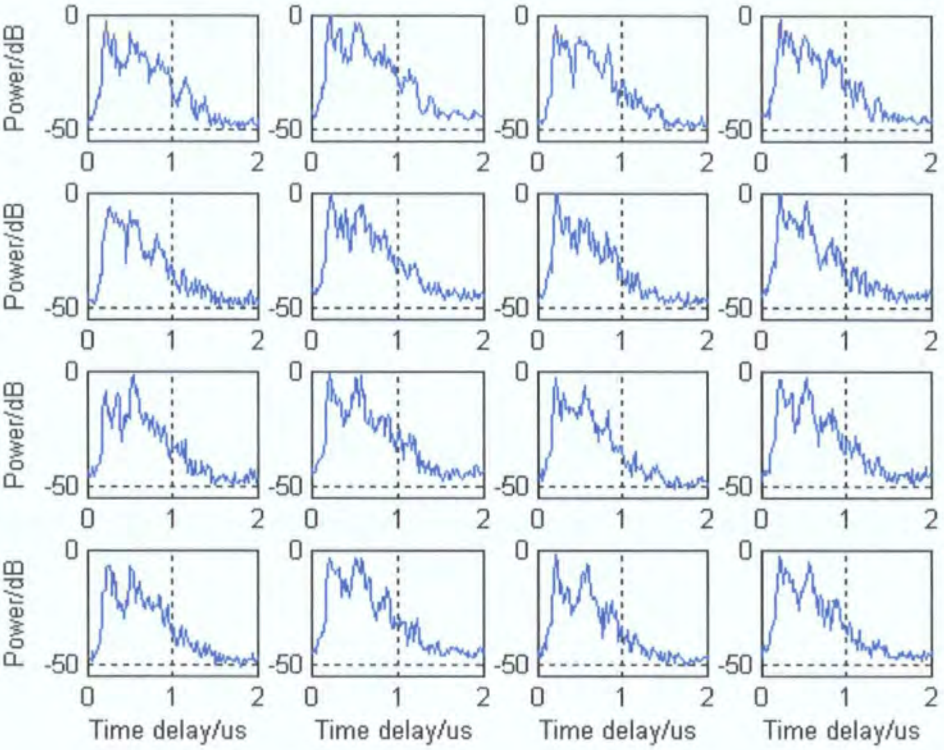

Figure 8.13: MIMO (4 × 4) PDP for non-LOS indoor UMTS channel.

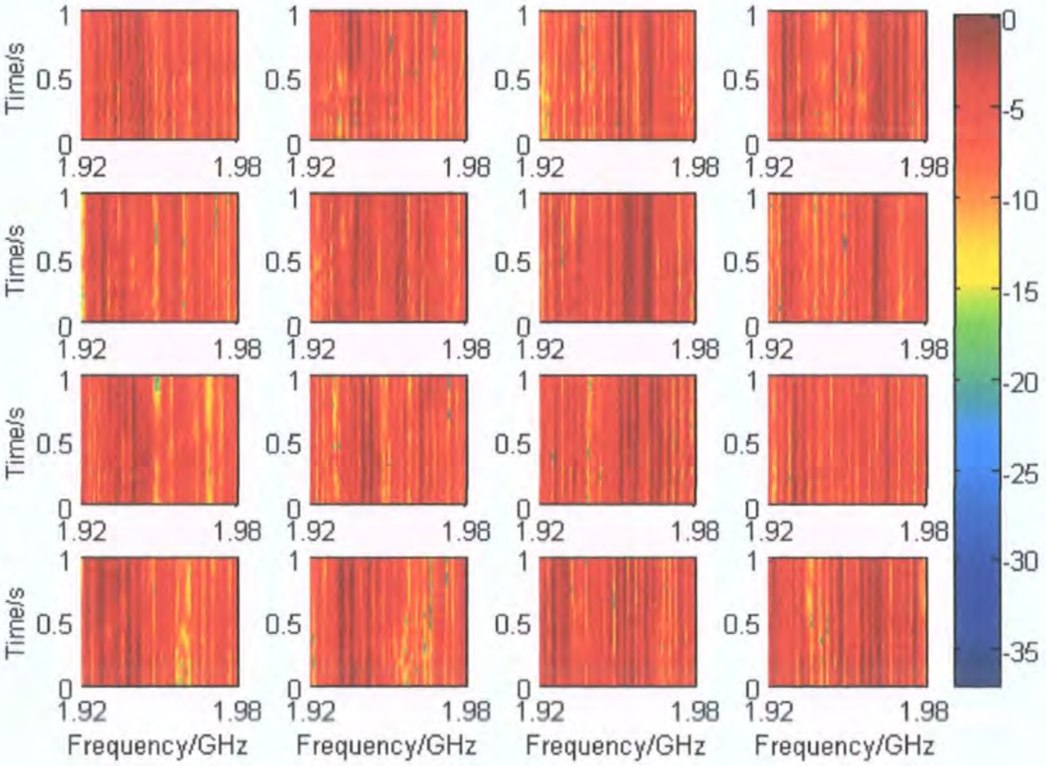

Figure 8.14: MIMO (4 × 4) transfer functions for non-LOS indoor UMTS channel.

Before examining MIMO capacity for a range of channels which include 2 × 2, 3 × 3, 4 × 4, and 2 × 8, it is useful to show the eigenvalues which correspond to the min(n_R, n_T) modes in the channel and are related to capacity. Figure 8.15 shows such a plot for a 4 × 4 non-LOS MIMO link as a function of time. Here, 4 eigenvalues (λ_1, λ_2, λ_3, λ_4,) of $\mathbf{HH}^H$ are plotted for 1 second, corresponding to 30 consecutive data sweeps. Again, this shows that the environment under test is fairly benign in respect to time variability. Figure 8.16, shows the same data as a function of frequency.

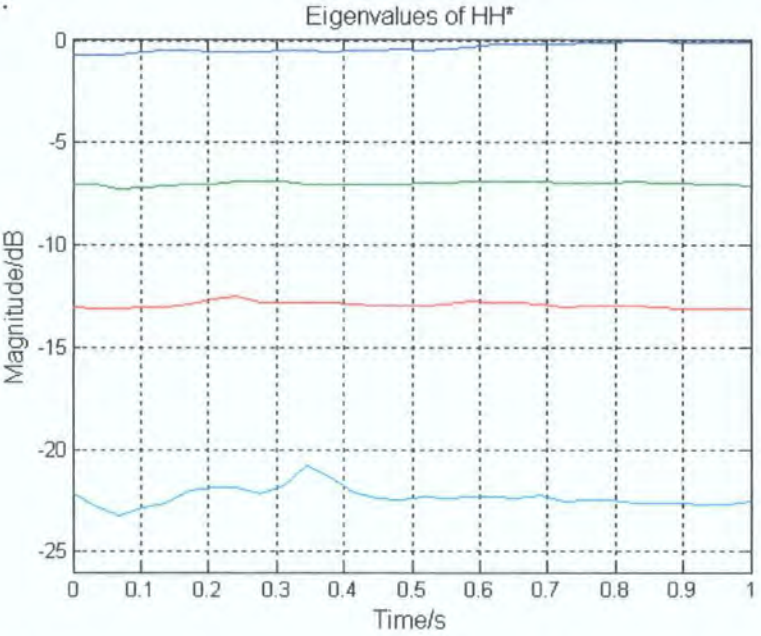

Figure 8.15: MIMO (4 × 4) eigenvalues for non-LOS indoor UMTS channel.

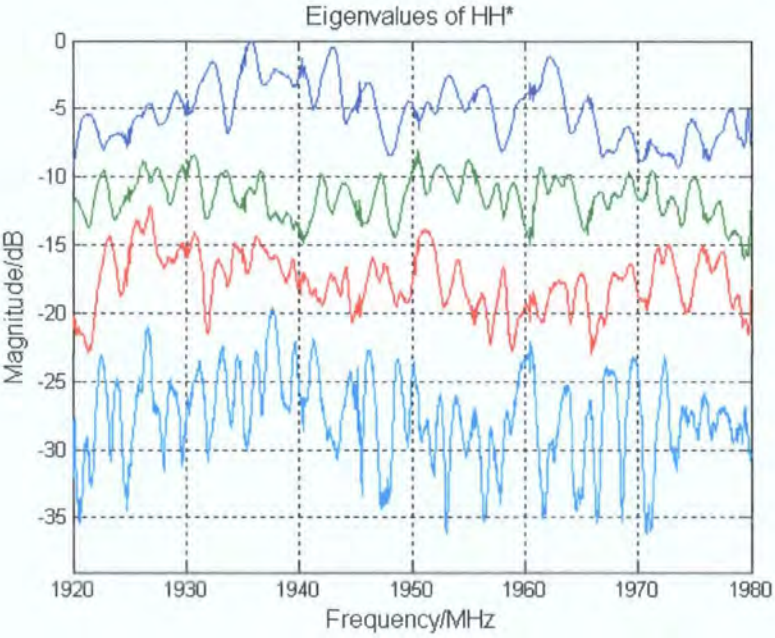

Figure 8.16: MIMO (4 × 4) eigenvalues for non-LOS indoor UMTS channel.

Figure 8.17 shows capacity results for the same link assuming a SNR of 30 dB.

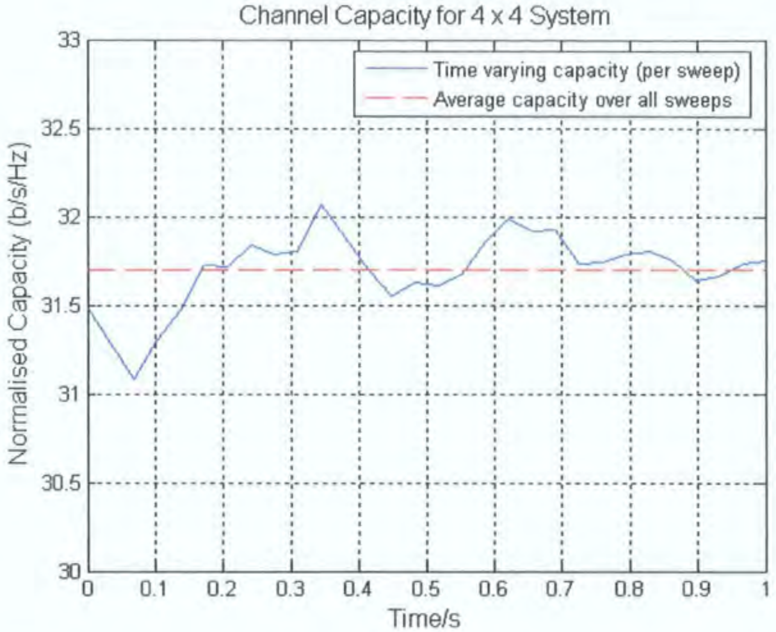

Figure 8.17: MIMO (4 × 4) capacity for non-LOS indoor UMTS channel.

Although these results provide insight into the measurement environment, it is more significant to examine these parameters for the data set. Figure 8.18 shows the mean eigenvalues for various 4 × 4 channels within the SoE (Tx1 – Tx7: same array rotation). Similarly figure 8.19 shows the average (normalised) capacity at each location for 3 array sizes, assuming 30 dB SNR.

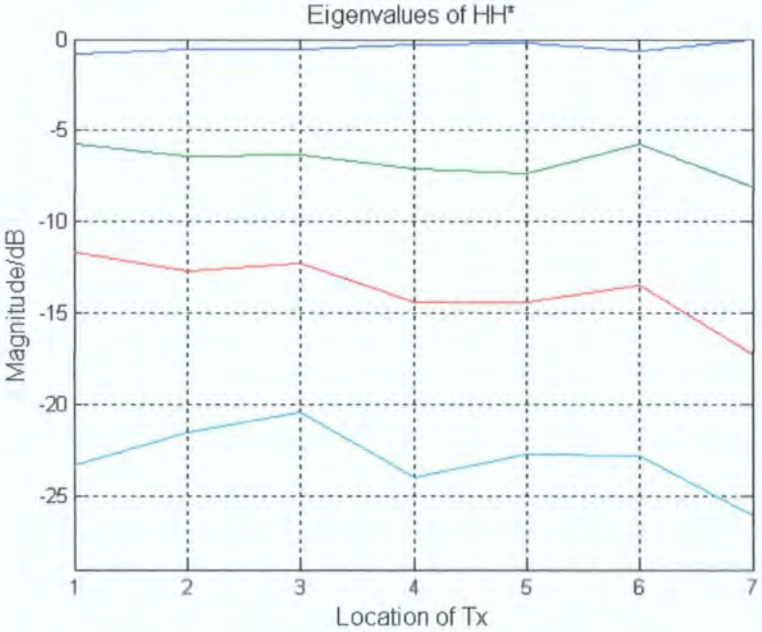

Figure 8.18: MIMO (4 × 4) eigenvalues for non-LOS indoor UMTS channels.

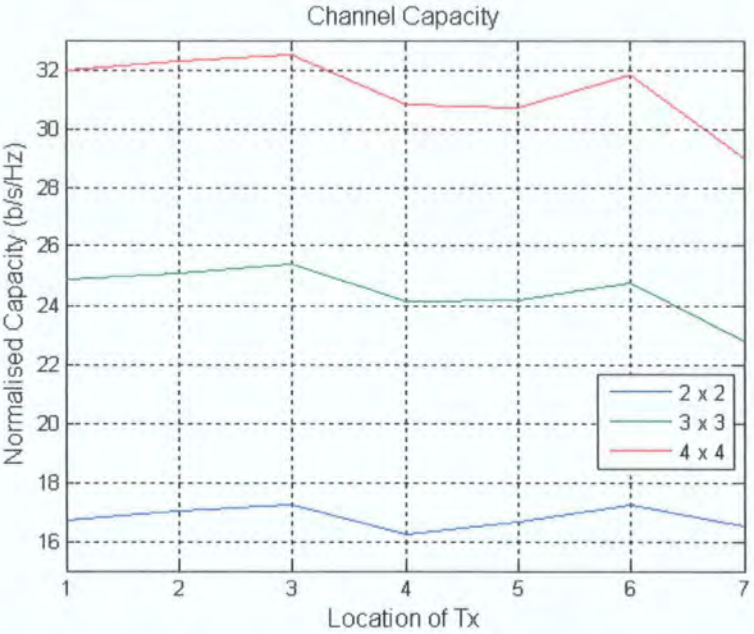

Figure 8.19: MIMO capacity for non-LOS indoor UMTS channels.

The variation of channel capacity is more evident from figure 8.20 which shows the CDF of channel capacity for various arrays. This includes measurements conducted using a simple 2-element omnidirectional array at the transmitter and the 8-element VPDCPA at the receiver. Such a setup explores diversity gain at the receiver array, however, figure 8.20 shows that even with an 8-element array at the receiver, the mean capacity (30 dB SNR) is still below that of a 3 × 3 square system.

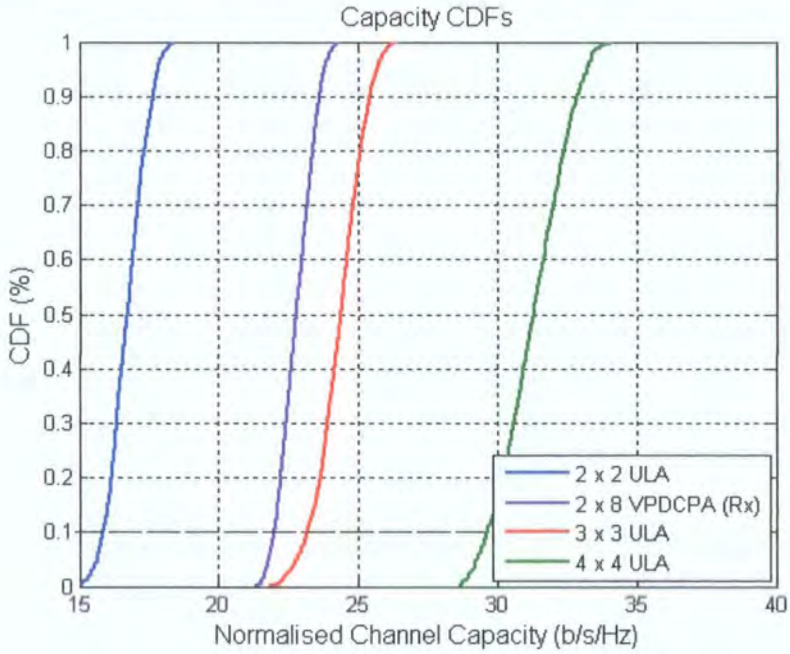

Figure 8.20: MIMO capacity CDFs for non-LOS indoor UMTS channels.

The importance of outage capacity was discussed in chapter 3 and figure 8.20 shows the 10% outage capacity point. This provides a more practical estimation of channel capacity since it gives the information rate that is guaranteed for 90% of channel realisations. Table 8.6 shows the mean and the 10% capacity results from the above CDF plots (30 dB SNR).

Array size	Mean Capacity (b/s/Hz)	10 % Outage Capacity (b/s/Hz)
2×2	16.73	15.85
2×8	22.80	21.99
3×3	24.33	23.18
4×4	31.29	29.63

Table 8.6: Mean and 10% outage capacity results for indoor MIMO measurements.

In the case of the results shown in table 8.6, the mean (calculated) data rate for a SISO link was 9.91 b/s/Hz with 30 dB SNR. This shows that assuming full spatial multiplexing, a 4 × 4 system may provide 3 times the throughput that would be expected from the same spectrum using a conventional SISO system. Theoretically, a capacity of up to 4 times (i.e. $4n$) should be attainable but this is practically improbable. In addition to this, the codes developed to date are still somewhat limited and do not allow full spatial multiplexing, although it is possible to get very close to this limit.

Another important result is capacity plotted against varying SNR. Figure 8.21 shows this result for all the array configurations. In addition to this, the capacity results for the simulated Independent and Identically Distributed (IID) channel model are shown for comparison (see chapter 3). Figure 8.21 shows that for the indoor measurements, the average capacity is typically greater than 85% of the IID case. For a 30 dB SNR, the computed capacity for all channels is above 90% of the IID channel realisations. This suggests that for the indoor measurements described here, the MIMO channel is comparatively uncorrelated. Figure 8.21 also shows that at ~ 24.7 dB SNR, the measured capacity curves for 2 × 8 and 3 × 3 channels intersect. At low SNRs (below 10 dB), more throughput is expected from the 2 × 8 system than the other array setups. This is due to the fact that at low SNRs, diversity gain is more prominent in the channel.

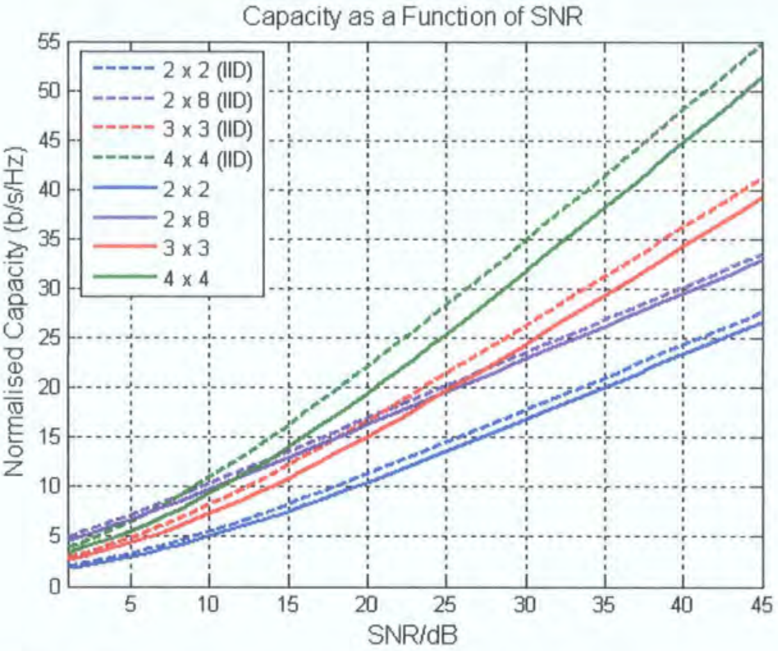

Figure 8.21: MIMO capacity vs. SNR for non-LOS indoor UMTS channels.

8.4.2 TV Studio Measurements

The measurement campaign at the BBC training studios were split into several data sets. The first set of measurements was collected in Studio A (see section 8.2.1), which covered an area of ~ 230 m^2. Although for most of the measurements, a LOS component was present, there were enough obstructions in Studio A (screens, cameras, reflectors, etc) to provide a more scattering environment, which could help a MIMO link. The BBC measurements are hereafter classified as LOS and obstructed LOS (OLOS).

In figures 8.22 and 8.23, typical OLOS capacity results (m8_7) are shown for both the 2.25 GHz and 5.8 GHz frequency bands using 2 × 2 and 4 × 4 array configurations. Here, normalised capacity is shown as a function of time, corresponding to 50 consecutive data sweeps. The computed results show that more capacity is available in the 2.25 GHz band (more than 3 b/s/Hz for the 2 × 2 array and more than 8 b/s/Hz for the 4 × 4 array).

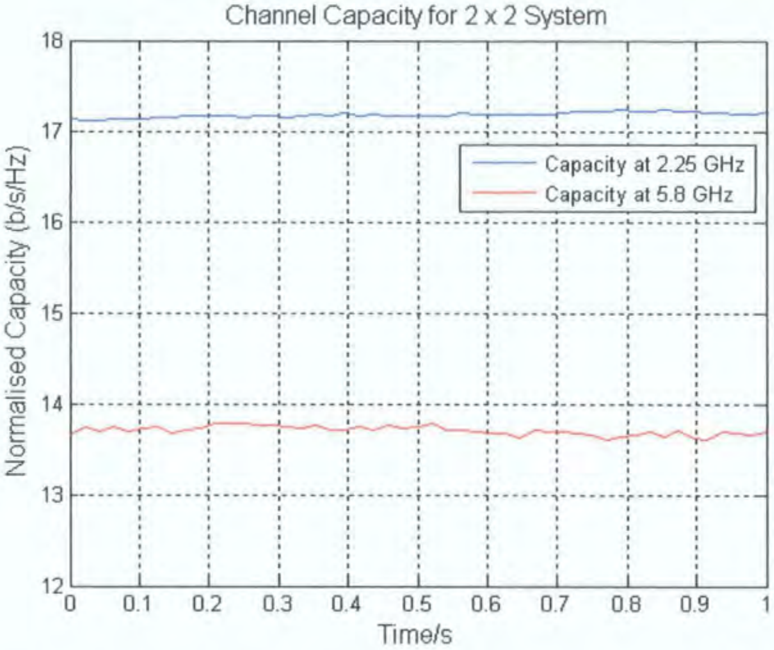

Figure 8.22: MIMO (2 × 2) capacity results for BBC data in OLOS indoor environment (m8_7).

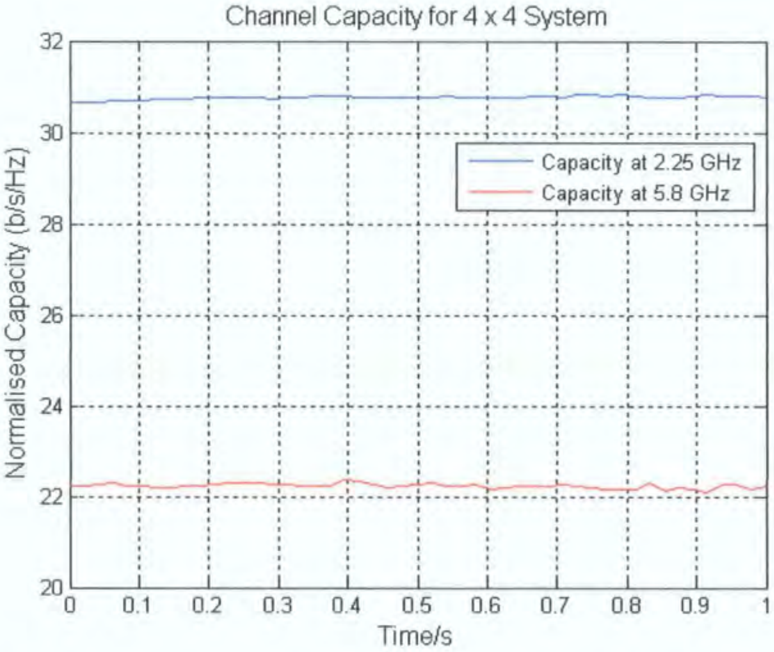

Figure 8.23: MIMO (4 × 4) capacity results for BBC data in OLOS indoor environment (m8_7).

Figures 8.24 – 8.27 show OLOS capacity results as a function of a 25 point grid (in studio A), where each point is separated from the adjacent one by 2m. These figures show the range of results expected for varying locations on the grid.

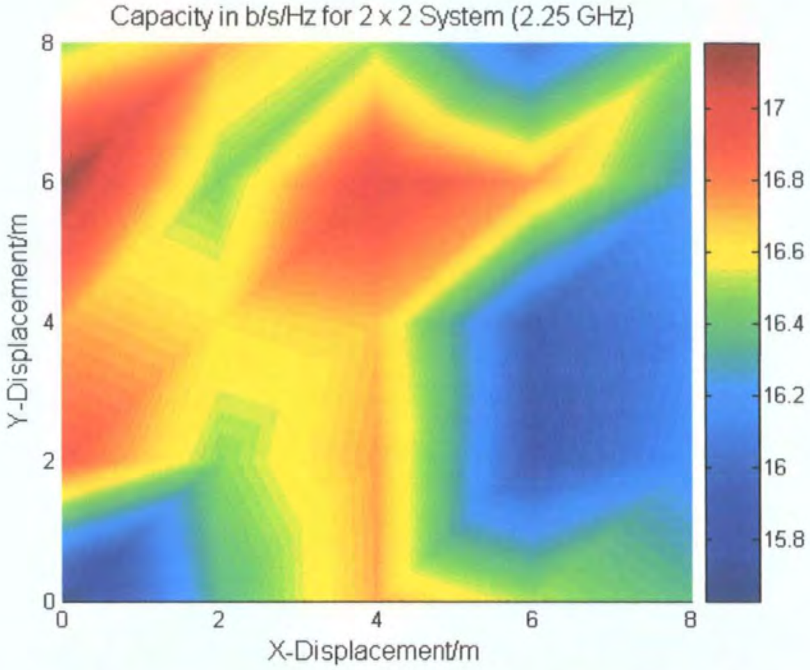

Figure 8.24: MIMO (2 × 2, 2.25 GHz) grid capacity results for BBC data in OLOS indoor environment.

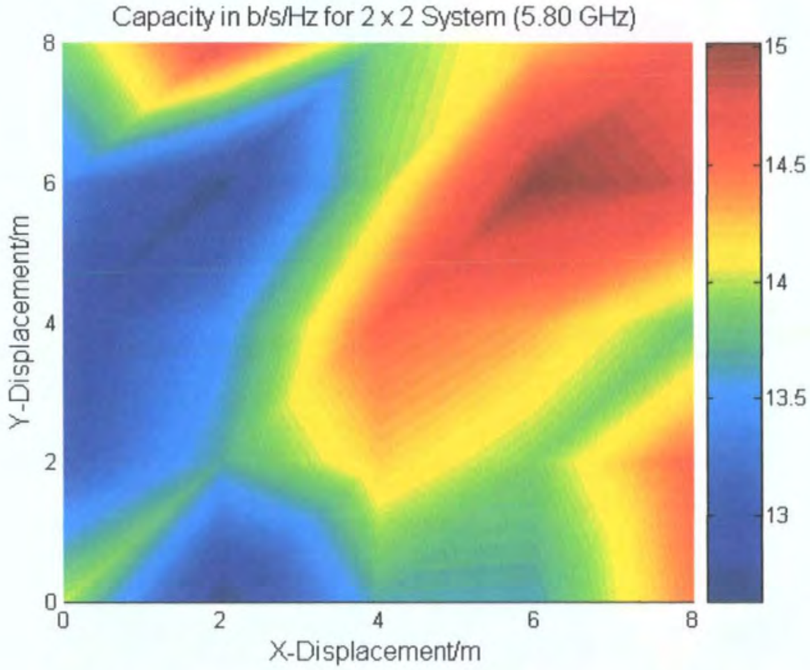

Figure 8.25: MIMO (2 × 2, 5.8 GHz) grid capacity results for BBC data in OLOS indoor environment.

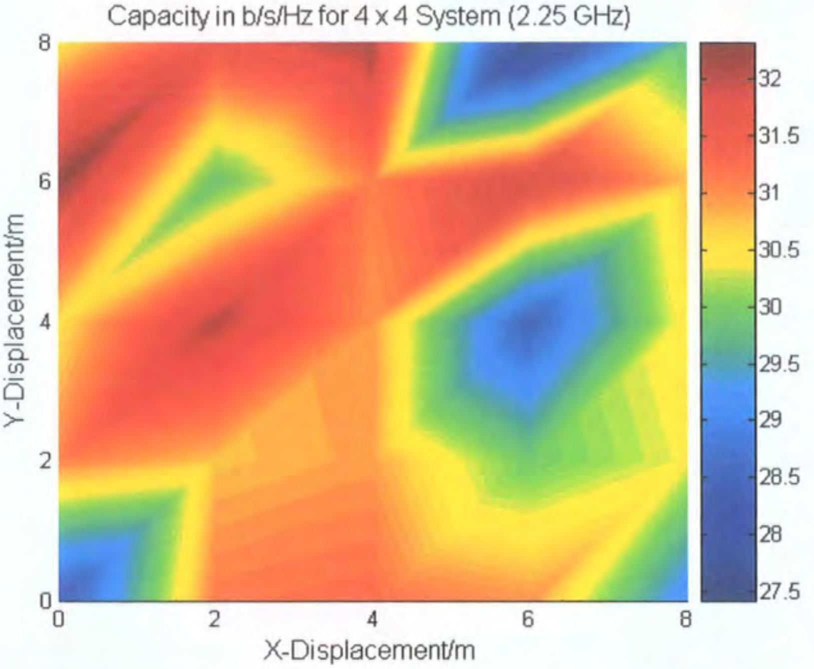

Figure 8.26: MIMO (4 × 4, 2.25 GHz) grid capacity results for BBC data in OLOS indoor environment.

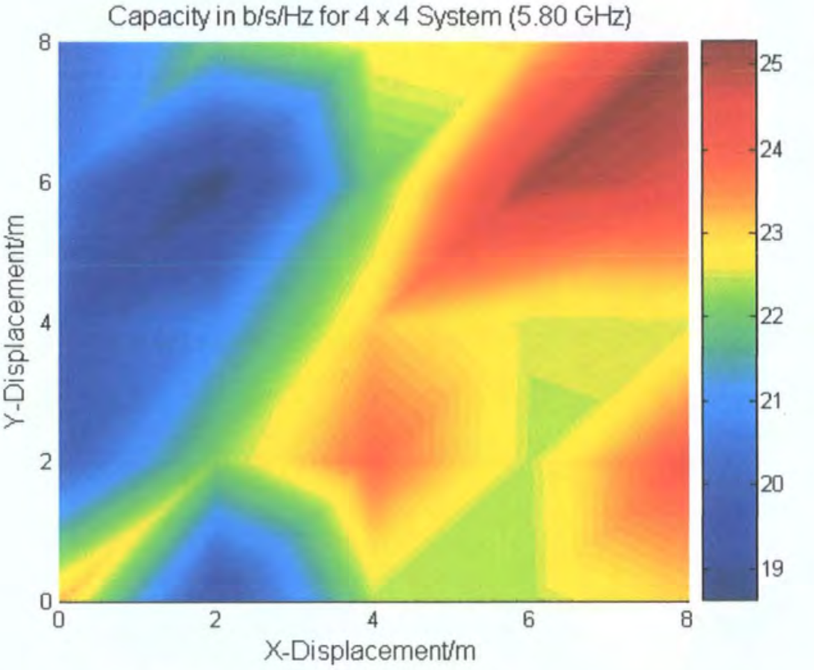

Figure 8.27: MIMO (4 × 4, 5.8 GHz) grid capacity results for BBC data in OLOS indoor environment.

These figures show that in the 5.8 GHz channels, the computed capacity is typically lower and more varied. The results also show that moving several meters can dramatically change the scattering environment and therefore the computed capacity results. This is particularly evident from figures 8.26 and 8.27, which show the 4 × 4 capacity results. The difference here can be attributed to the different frequency selective fading across the frequency band. In [10] it was shown that significant differences could be expected for the two UMTS-FDD bands, which were measured simultaneously. Here, the difference in wavelength which is more than 2.5 times, could explain some of the characteristics between the computed results.

The measurements here were classified as obstructed LOS (OLOS) and LOS, where the latter represents a highly correlated (singular) channel. Figures 8.28 and 8.29 show the capacity CDFs for both the 2.25 GHz band and the 5.8 GHz band, for LOS and OLOS. The mean and 10% outage capacities are shown in tables 8.7 and 8.8, respectively.

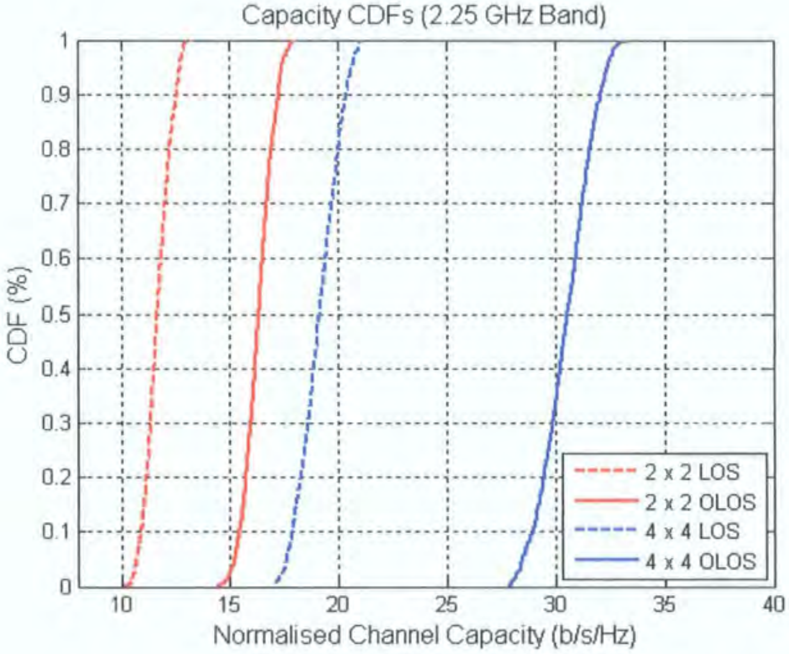

Figure 8.28: MIMO capacity CDFs for BBC data.

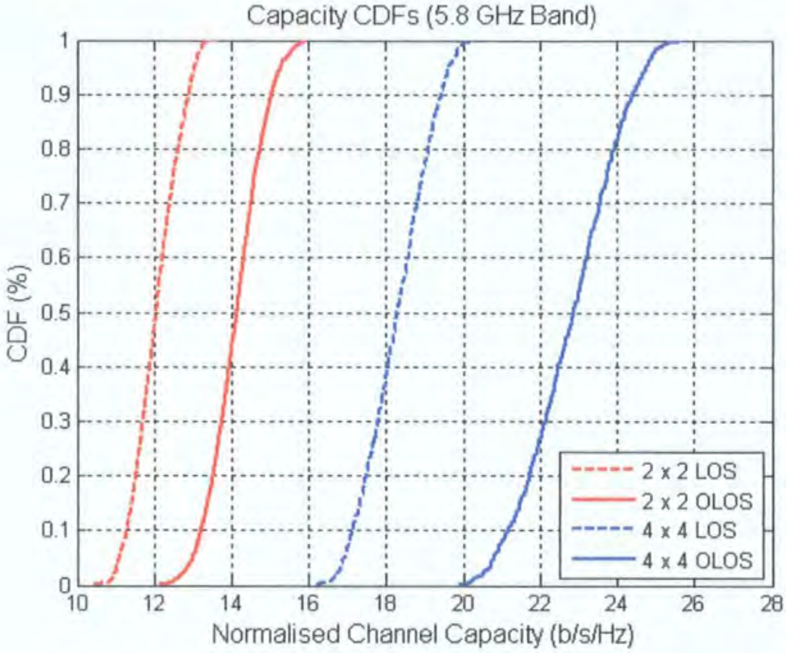

Figure 8.29: MIMO capacity CDFs for BBC data.

Array size	Mean Capacity (b/s/Hz) for 2.25 GHz band	Mean Capacity (b/s/Hz) for 5.8 GHz band
2 × 2 LOS	11.68	12.05
2 × 2 OLOS	16.32	14.14
4 × 4 LOS	19.13	18.29
4 × 4 OLOS	30.54	22.87

Table 8.7: Mean capacity results for indoor studio MIMO measurements.

Array size	10 % Outage Capacity (b/s/Hz) for 2.25 GHz band	10 % Outage Capacity (b/s/Hz) for 5.8 GHz band
2 × 2 LOS	10.92	11.27
2 × 2 OLOS	15.42	13.21
4 × 4 LOS	17.87	17.13
4 × 4 OLOS	28.94	21.14

Table 8.8: 10% outage capacity results for indoor studio MIMO measurements.

It would be expected that for a multimedia service where transmission is available on two bands simultaneously (as was suggested at the BBC), there would be an advantage in the form of frequency diversity. The results here show that far better performance is expected in the lower 2.25 GHz band rather than the higher 5.8 GHz band. Since the radius of the 4-element discone array was λ/2 at the 2.25 GHz band, this would mean a radius greater than 5λ/4 at 5.8 GHz and therefore a greater capacity estimate would be expected for the higher band. On closer examination of the measurement results, higher correlation was apparent at the transmit side in the 5.8 GHz band than the 2.25 GHz band. This was due to 10 dB lower isolation in the GaAs transmit switch at the higher frequency band and would explain the difference in the OLOS results in tables 8.7 and 8.8. The LOS results would be less affected by this since the channel would be highly correlated in both bands. To address this, channel measurements should be done using a switch matrix which provides approximately the same level of isolation or alternatively a switch for each band, which runs from the same control line clock (SRF) and provides similar isolation (more than 30 dB should be obtainable).

The results also show that for a near LOS condition (i.e. highly correlated channels) a reasonable level of capacity could be expected. In fact for the measurements described here, a LOS path does not greatly degrade the channel, providing that there is a scattering environment and that the different MIMO element channels are not correlated. Also, greater antenna spacing and/or different antenna polarisations can improve the link performance. The subject of antenna spacing will be examined in the next section.

In respect to spatial multiplexing systems, it stands that the more varied the individual MIMO channels are, the greater the channel capacity. The CDF plots demonstrate this, since it is shown that highly correlated links can be more limited in throughput performance. Although some measurements were collected in indoor-to-outdoor locations, examination of the data showed that there was no significant difference between the capacity results corresponding to these locations.

In addition to all the stationary measurements, some files were also collected while the transmitter was being moved at walking speeds. Figure 8.30 shows the 4 × 4 scattering function for such a channel (m10_32) at 2.25 GHz, where the Doppler scattering floor is set to -35 dB. The figure shows that certain MIMO elements have more Doppler variation. This can also be translated into the MIMO transfer functions as shown in figure 8.31, where a notable contrast can be seen between the 16 elements of the MIMO channel. In particular, the transfer function plots in figure 8.31 show how the radio channel varies in the dimension of time as the transmitter moves.

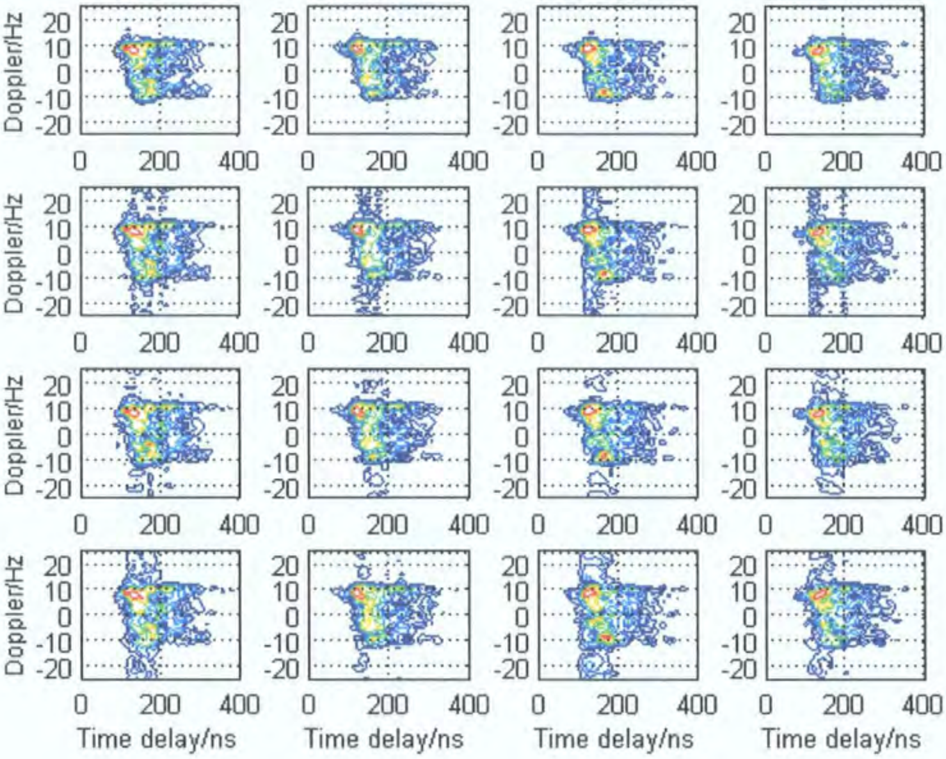

Figure 8.30: MIMO (4 × 4) high Doppler scattering function for BBC data in the 2.25 GHz band.

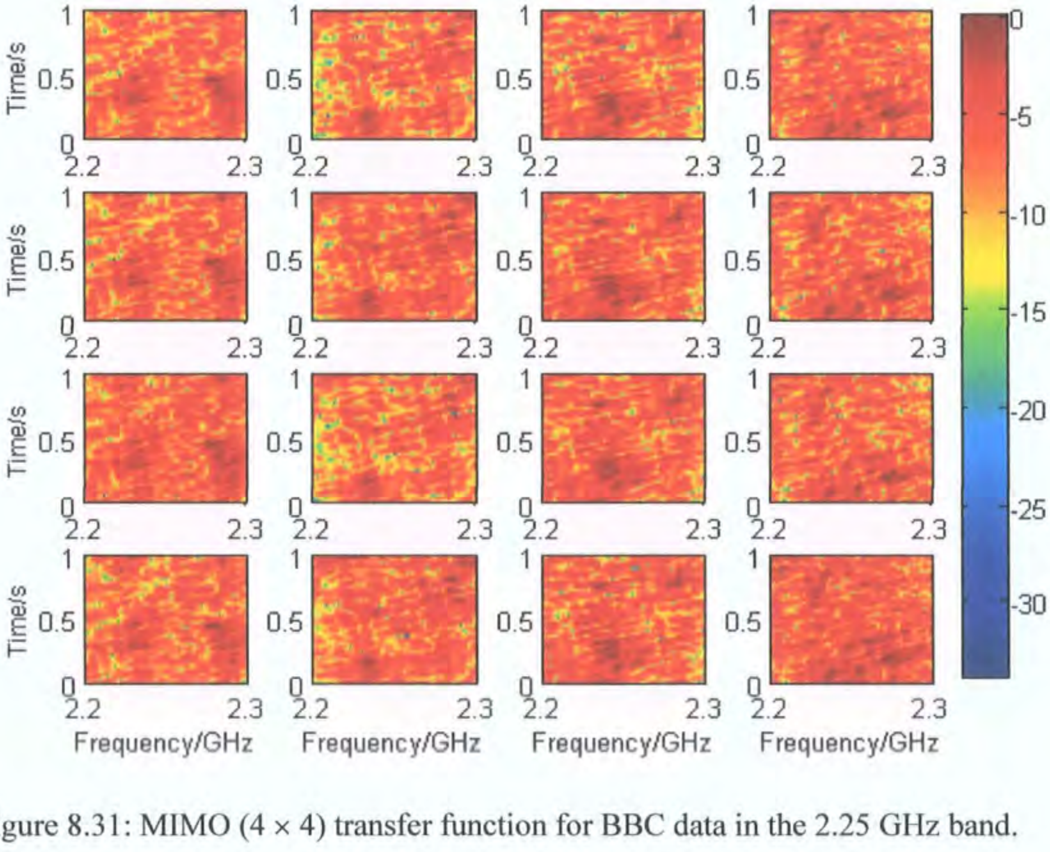

Figure 8.31: MIMO (4 × 4) transfer function for BBC data in the 2.25 GHz band.

Multiple high Doppler measurement files were acquired while there was a direct LOS path between the transmitter and the receiver. Figure 8.32 shows the eigenvalues of the aforementioned channel at 2.25 GHz. Similarly, the time variant channel capacity is shown in figure 8.33 for the same band. Figures 8.34 and 8.35 show the time variant eigenvalues and channel capacity for the 5.8 GHz band, respectively.

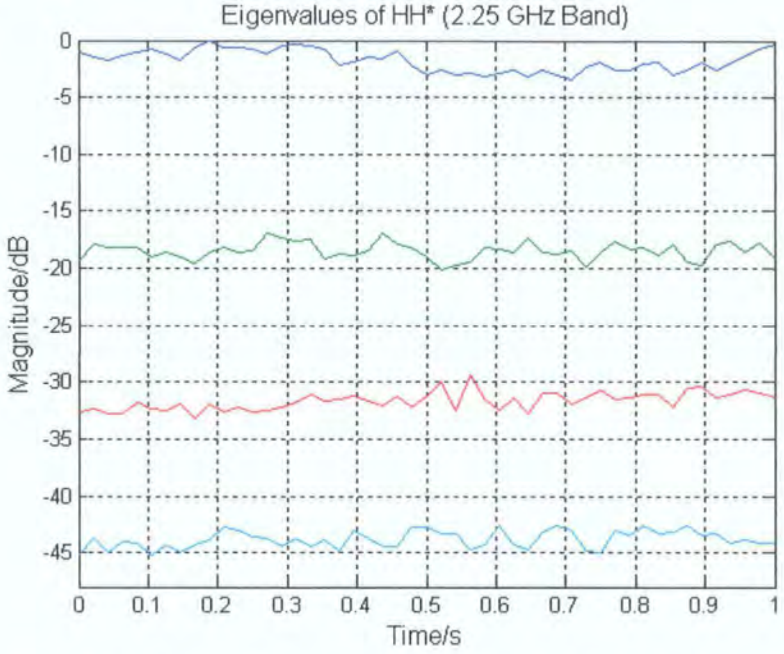

Figure 8.32: MIMO (4 × 4) eigenvalues for BBC data in the 2.25 GHz band.

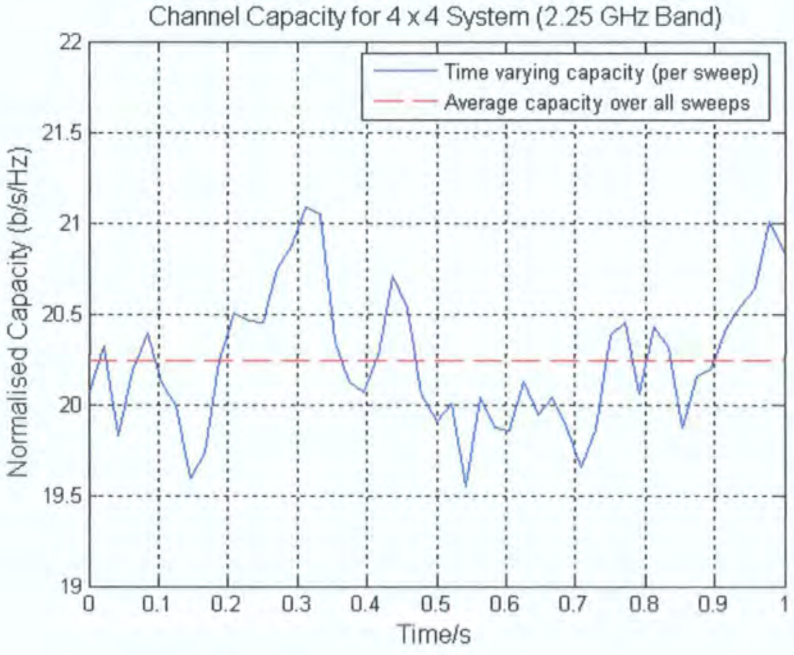

Figure 8.33: MIMO (4 × 4) capacity for BBC data in the 2.25 GHz band.

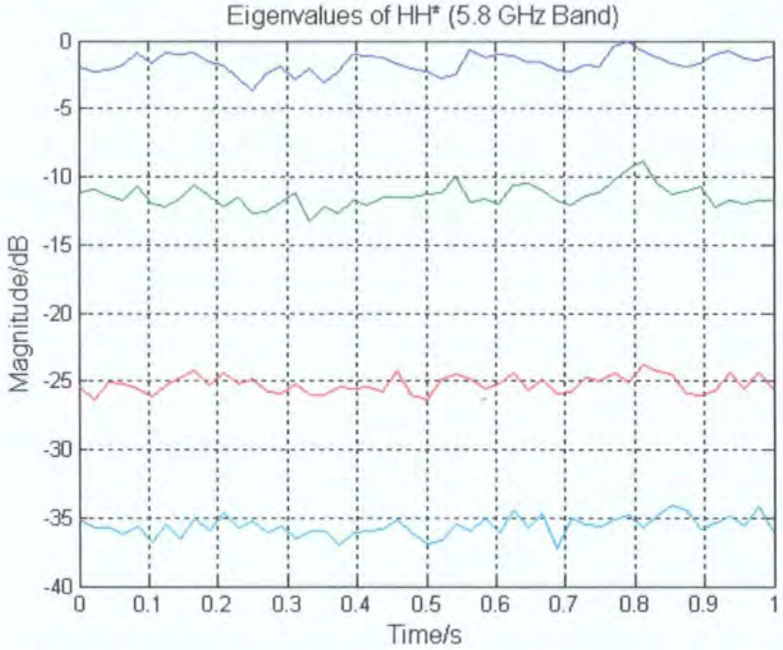

Figure 8.34: MIMO (4 × 4) eigenvalues for BBC data in the 5.8 GHz band.

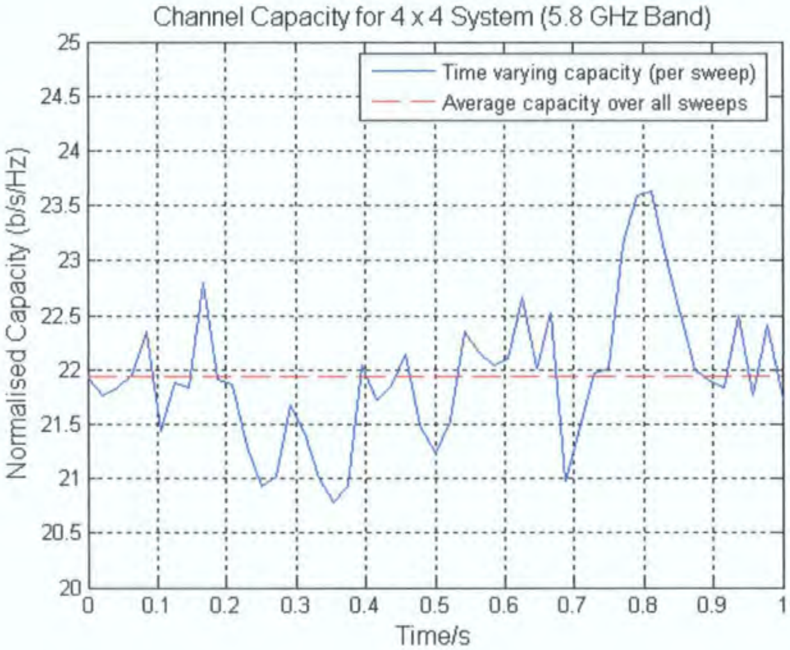

Figure 8.35: MIMO (4 × 4) capacity for BBC data in the 5.8 GHz band.

These figures suggest that not only are the capacity results more varied, as would be expected, but they are also typically higher than those results collected for stationary channels. The figures also show that the Doppler is exacerbated at the 5.8 GHz which is true to theory and this causes a higher capacity result.

In general, higher Doppler channels (Doppler effecting each multipath component independently) would result in more spatial variation and since this would cause the MIMO elements to be less correlated, it is reasonable to assume that from an information theoretic perspective, movement in the channel would increase the rank of the channel and therefore channel capacity. From a MIMO system design and development aspect, very high Doppler channels would present a problem associated with the adaptive channel estimation at the receiver end. Furthermore, in scenarios where CSI information is required at the transmitter via some feedback technique, the study of time variation becomes very critical, where high Doppler could mean that the channel has changed enough for the feedback information to be ineffective.

Not enough measurements were made during the BBC campaign to analyse the effect of Doppler on channel capacity with a high degree of statistical accuracy, however, all of the data files collected showed higher throughput estimates than the average stationery channel.

8.4.3 Wideband ISM (2.4 GHz) Measurements

So far MIMO technology has been envisaged primarily for ad-hoc wireless systems, which are typically employed in the ISM bands. The measurements presented in this section are used to characterise the 2.4 GHz ISM band using a large system bandwidth, which in turn means a finer delay resolution than the other measurements presented in the chapter. This resolution is demonstrated in figure 8.36, which shows a typical 4 × 4 PDP response (Tx9).

The majority of the data were acquired in non-LOS locations, however a number of files were collected while there was a strong LOS component. Figure 8.37 shows a typical PDF (density) plot of the magnitude and phase data of the channel transfer matrix (vectorised channel snapshots) collected in a non-LOS environment. This is followed by figure 8.40, which shows the same channel generated by an IID model, described in previous sections.

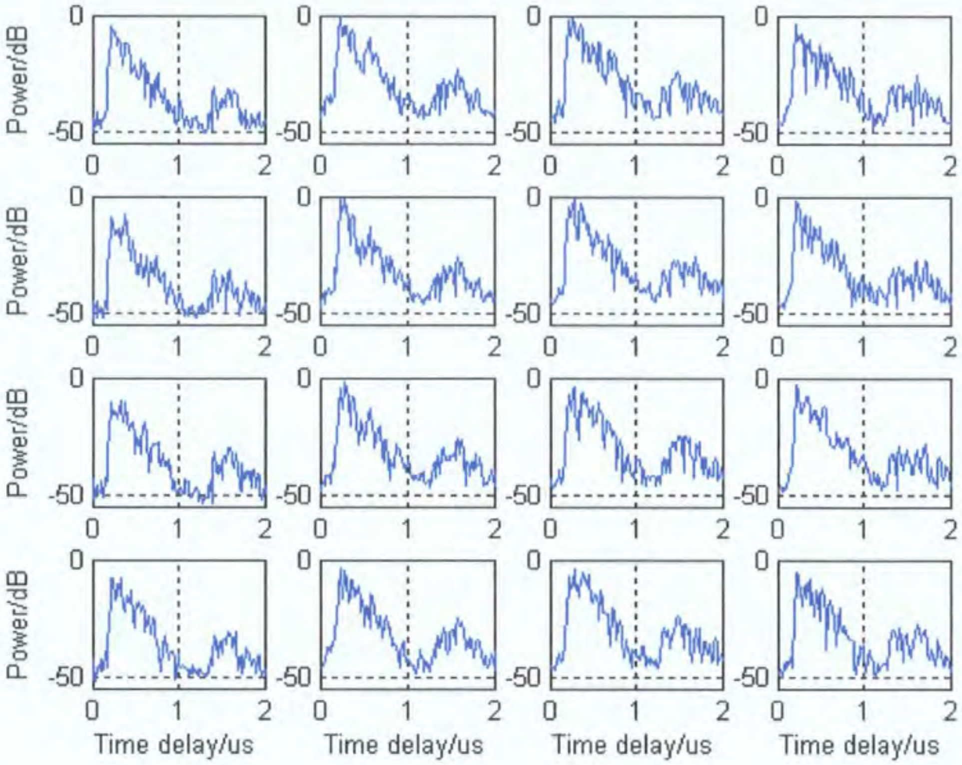

Figure 8.36: MIMO (4 × 4) PDP for non-LOS indoor 2.4 GHz ISM channel.

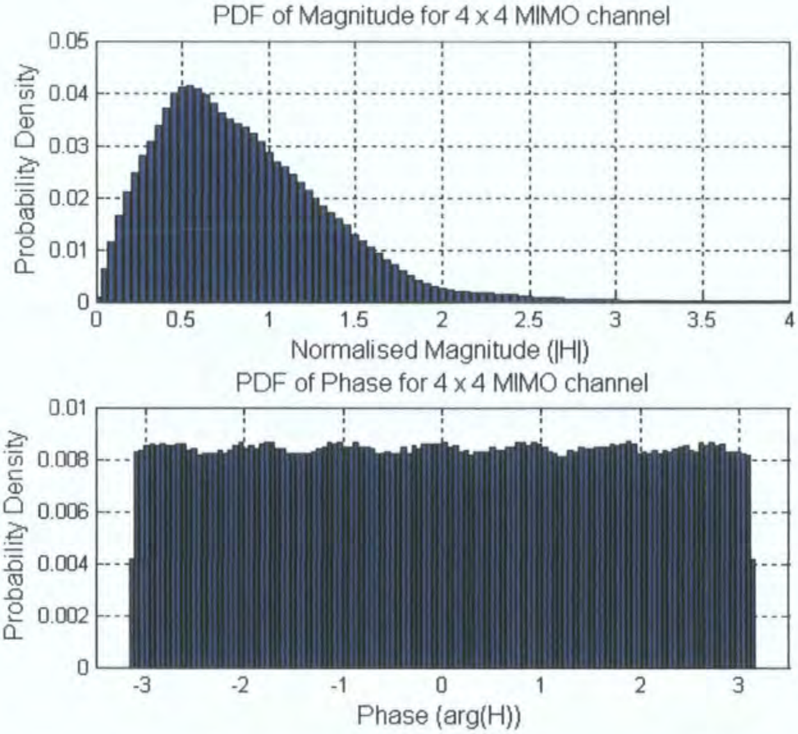

Figure 8.37: MIMO (4 × 4) PDF (density) for non-LOS indoor 2.4 GHz ISM channel.

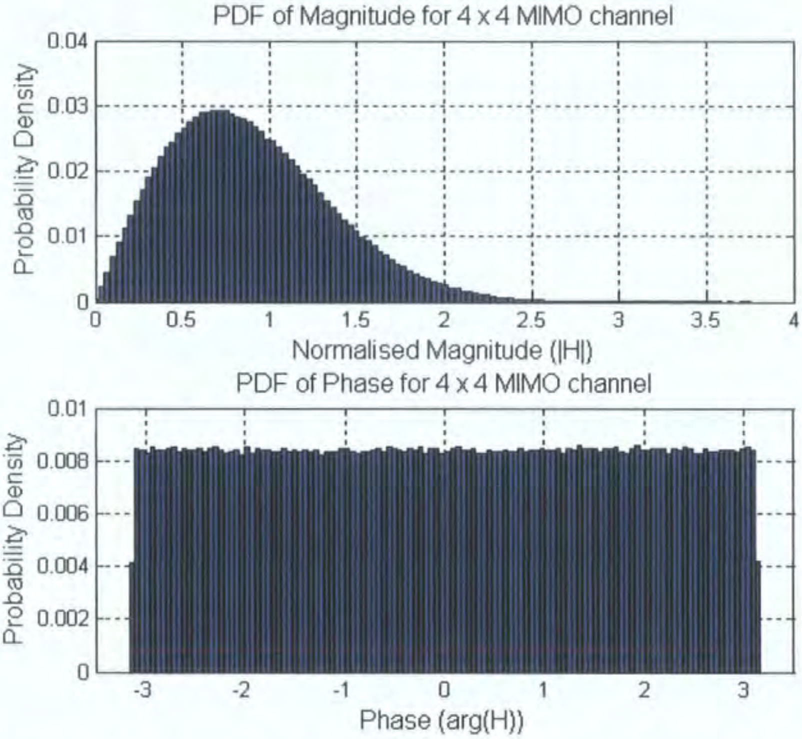

Figure 8.38: MIMO (4 × 4) PDF (density) for IID channel model.

Figure 8.39 shows the channel eigenvalues versus different locations within the SoE for the 4 × 4 array setup. Here, locations 1 and 2 relate to data collected in a LOS link. Similarly, figure 8.40 shows the capacity results for these locations. The figures show that for a basic λ/2 spaced array, an unobstructed path would typically reduce the overall channel throughput.

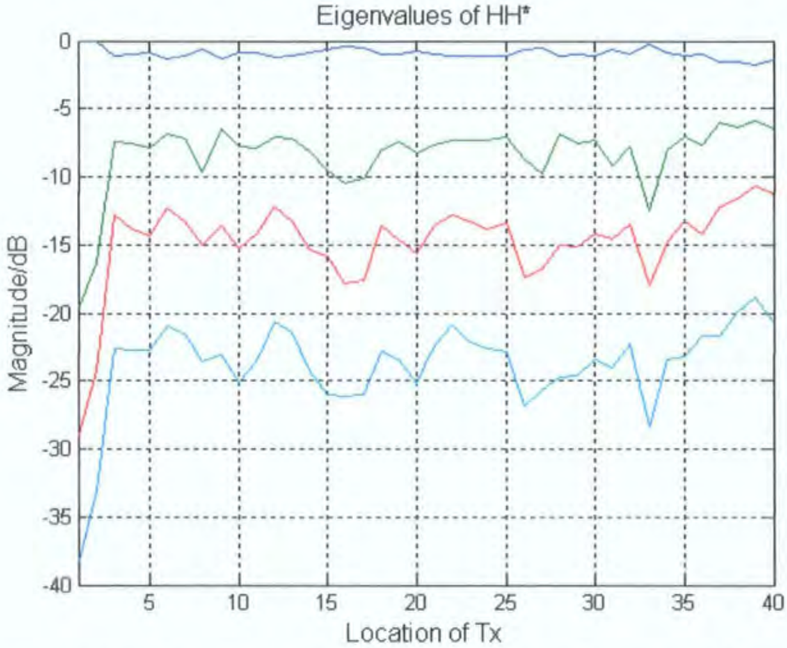

Figure 8.39: MIMO (4 × 4) eigenvalues for indoor 2.4 GHz ISM channels.

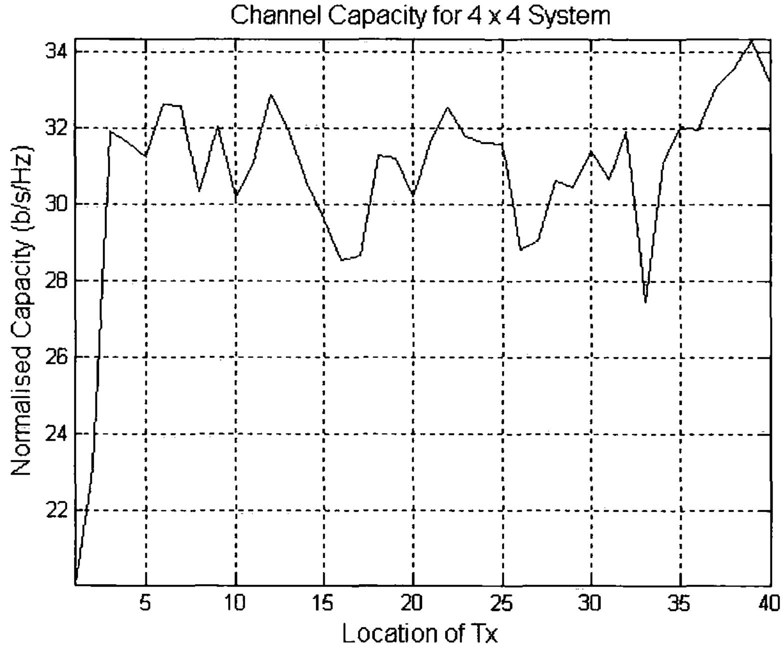

Figure 8.40: MIMO (4 × 4) capacity for indoor 2.4 GHz ISM channels.

Figure 8.39 shows how the channel would become singular if there was only one dominant multipath component. This can be further explained when analysing the number of resolvable (distinct) channel paths. Figure 8.41 shows the number of components resolved above a 20 dB threshold. Locations 1 and 2 show very few resolvable paths, while locations 19 and 22 show the highest number of components. This again reaffirms the principle that multipath is generally beneficial to the operation of a MIMO space-time system.

It is important to conclude from the studies so far that a LOS link does not necessarily infer poor MIMO performance from a channel capacity standpoint. The performance of the system is a function of the multipath environment, operational frequency, and antenna spacing amongst other factors.

Figure 8.42 shows the array correlation coefficients corresponding to the same locations for both the transmitter and the receiver. Locations 1 and 2 show that both correlation coefficients are quite high (above 0.7) and this fits in with the assessment of the channel so far.

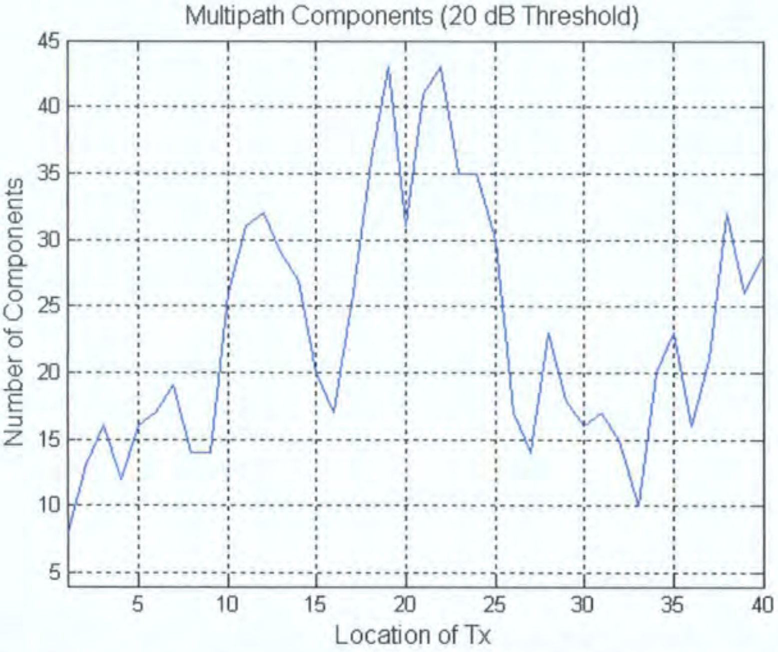

Figure 8.41: Multipath components resolved above a 20 dB threshold for 4 × 4 indoor 2.4 GHz ISM channels.

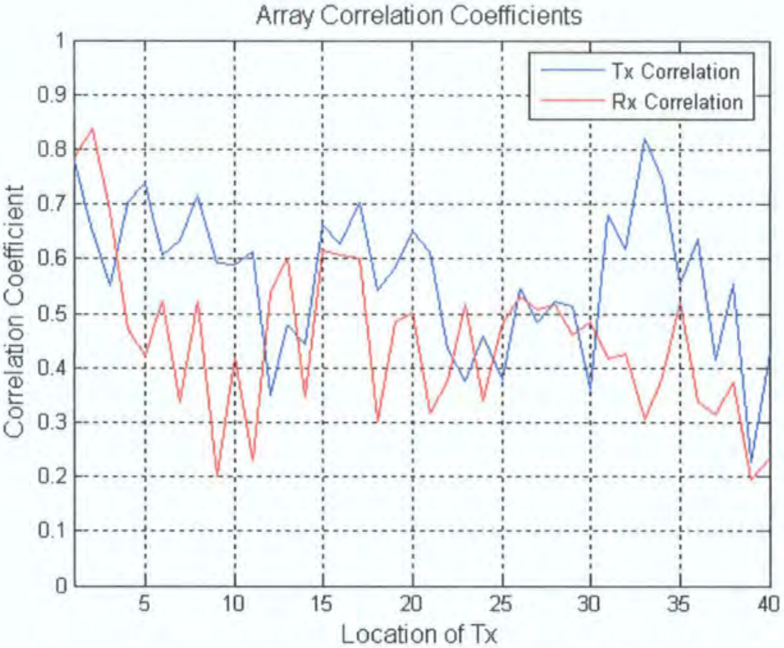

Figure 8.42: Transmit and receive array correlation coefficients for 4 × 4 indoor 2.4 GHz ISM channels.

A basic summary of the parameters described so far is shown in tables 8.9 and 8.10 for all array sizes. The columns show the data set minima, maxima, means and standard deviations. The values relating to the 5 × 5 and 6 × 6 configurations were calculated from a sub-set of the 6 × 8 measurement data.

Array size	Tx. Corr. (mean)	Tx. Corr. (std)	Rx. Corr. (mean)	Rx. Corr. (std)
2 × 2	0.72678	0.15012	0.57877	0.16846
2 × 4	0.65417	0.19695	0.40546	0.13179
3 × 3	0.35119	0.10402	0.541	0.17224
3 × 4	0.35113	0.088504	0.34908	0.1274
4 × 2	0.48675	0.13461	0.80887	0.18692
4 × 4	0.56416	0.13154	0.4517	0.14607
5 × 5 (sub)	0.35907	0.097621	0.42031	0.056721
6 × 6 (sub)	0.30875	0.10622	0.40028	0.080943
6 × 8	0.2996	0.11633	0.41542	0.082419

Table 8.9: Tx and Rx array correlation coefficients for indoor 2.4 GHz channels.

Array size	No. Paths (min)	No. Paths (max)	No. Paths (mean)	No. Paths (std)
2 × 2	6	30	16.606	7.0018
2 × 4	9	45	22	9.4182
3 × 3	12	41	22.952	8.986
3 × 4	13	43	27.474	11.057
4 × 2	12	105	24.722	15.465
4 × 4	8	43	23.2	9.2797
5 × 5 (sub)	7	45	23.341	9.4873
6 × 6 (sub)	8	49	24.318	9.7083
6 × 8	8	47	24.545	10.577

Table 8.10: Number of components (20 dB threshold) for indoor 2.4 GHz channels.

All of the aforementioned parameters depend primarily on the measurement environment as well as other factors. For example examining the number of components depends very much on the sounding bandwidth. As shown in the previous section, the multipath environment is very much a function of the measurement band. In table 8.10, the average number of components is similar for all the non-LOS environments measured. In the case of transmit and receive array correlation, the results are dependent on the array type and geometry. For example, circular directional arrays will result in different correlation coefficients than linear omni-directional arrays. In table 8.9, the mean correlation coefficient shows that as the array size at both ends increases, there is a general downward trend in the correlation. This is due to the averaging being done over a larger array section and therefore causing a lower mean correlation value.

The next stage in the characterisation of these channels is to evaluate link capacity for all array configurations. Figure 8.43 shows capacity CDFs of the 2 × 2, 2 × 4, 3 × 3, 3 × 4, 4 × 2, and 4 × 4 arrays. Similarly, figure 8.44 shows the CDFs of channel capacity for 5 × 5, 6 × 6, and 6 × 8 arrays. For all computations, a SISO SNR of 30 dB was assumed as before. The greatest gain in channel throughput is achieved by increasing the number of both transmitters and receivers. Figure 8.43 shows that a more significant capacity increase is expected from a 3 transmit, 3 receive system than from a 2 × 4, or 4 × 2 setup. It is also interesting to note from figure 8.43 that a 2 × 4 setup results in ~ 2 b/s/Hz increase in channel capacity over a 4 × 2 setup. The results in figure 8.44 are also consistent, with the 6 × 8 array giving the highest capacity estimate at 48.5 b/s/Hz (10% outage capacity).

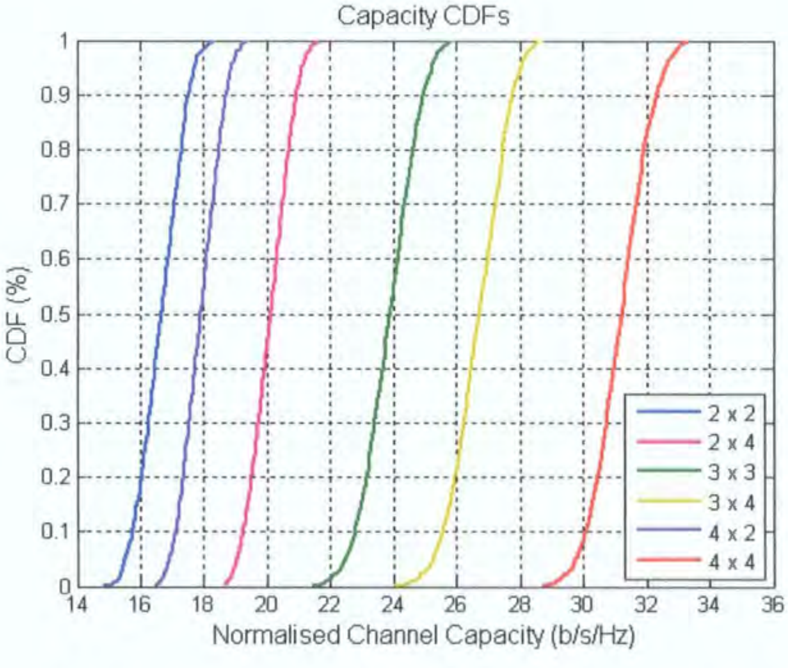

Figure 8.43: MIMO capacity CDFs for indoor 2.4 GHz ISM channels.

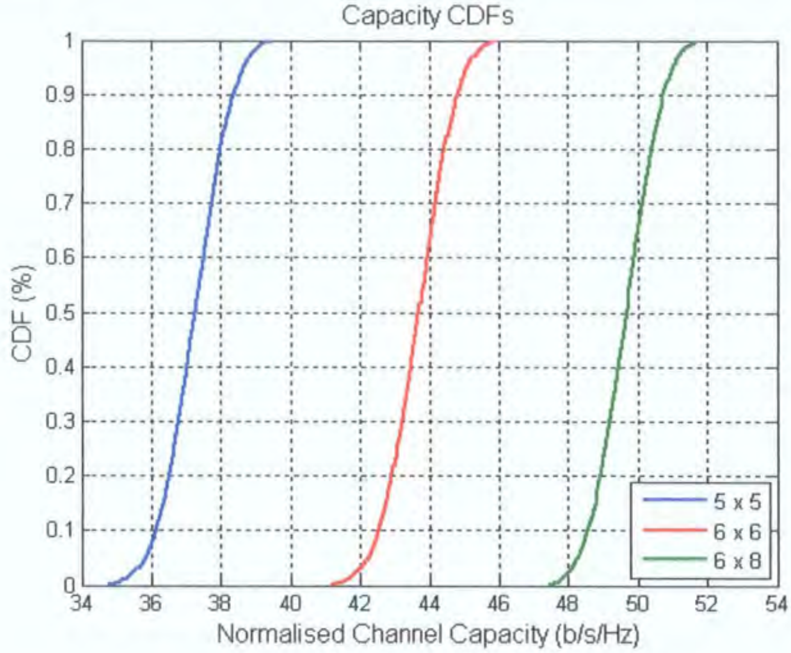

Figure 8.44: MIMO capacity CDFs for indoor 2.4 GHz ISM channels.

In addition to processing the data with full 240 MHz bandwidth, files were also examined using 5 MHz bandwidth sections. As might be expected, the results after averaging showed no significant increase or decrease in capacity. Figure 8.45 shows the fully computed channel capacities as a function of SNR from 1 – 45 dB.

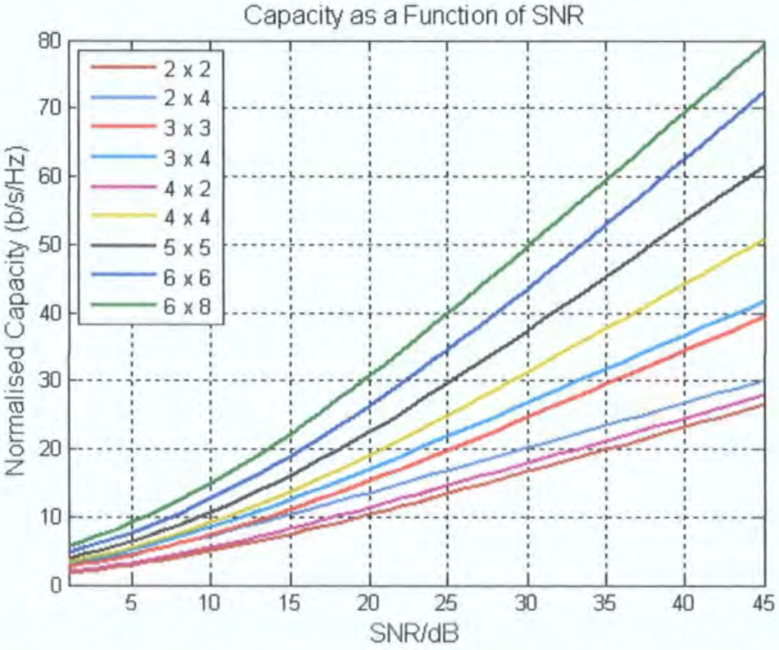

Figure 8.45: MIMO capacity vs. SNR for indoor 2.4 GHz ISM channels.

As noted previously, the majority of the measurement data were collected in non-LOS scenarios. The capacity results computed from this data could be modelled using the Normal distribution as shown in figure 8.46, which gives the PDF (density) plot of the measurement data per sweep for a 4 × 4 setup. Here the red line represents the normal fit (data fitting, mean = 31.207 and standard deviation = 0.856).

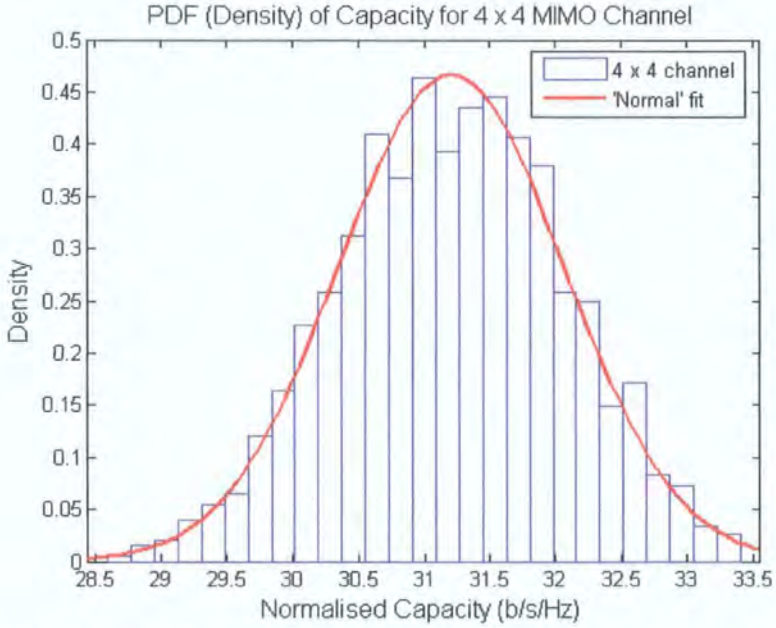

Figure 8.46: MIMO (4 × 4) PDF of capacity for non-LOS indoor 2.4 GHz ISM channels (SNR = 30 dB).

A limited number of higher Doppler files were also collected during this campaign in LOS conditions. Figure 8.47 shows the typical scattering functions for a 4 × 4 setup, where the transmitter was moving slowly towards the receiver. All the files collected under such scenarios showed greater than average capacity estimates. This concurs with the analysis of the BBC measurement data.

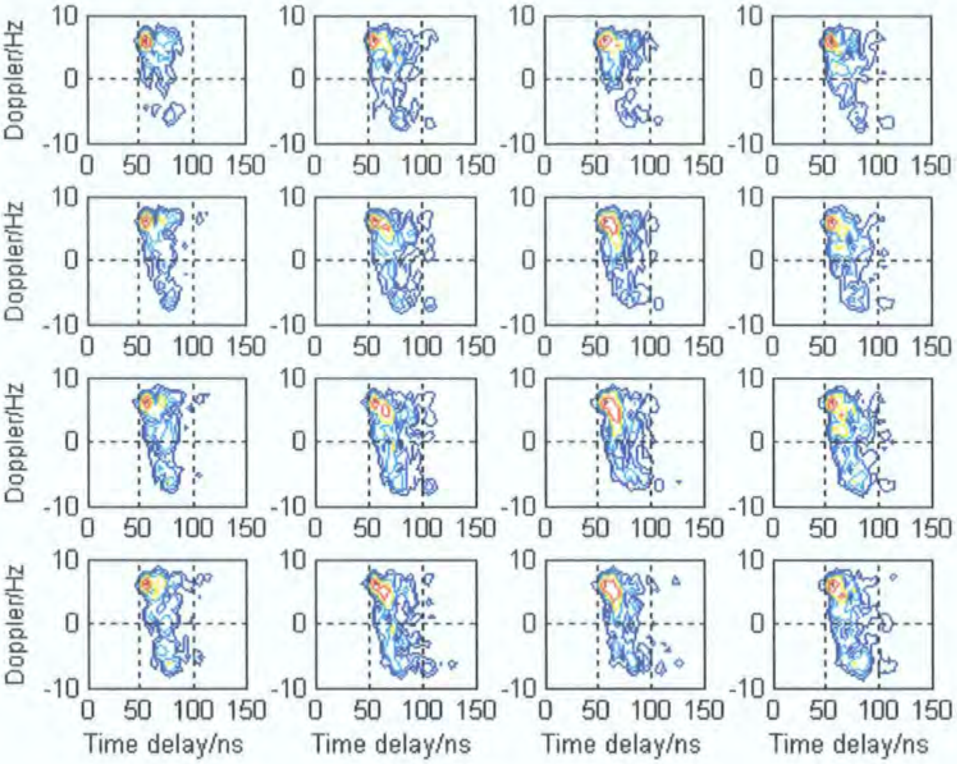

Figure 8.47: MIMO (4 × 4) high Doppler scattering function for indoor 2.4 GHz ISM channel.

8.4.3.1 The Effect of Antenna Spacing on Channel Capacity

The spacing between antenna elements in a MIMO communication system can affect the overall system throughput. In fact it is suggested that a larger than λ/2 inter-element spacing can be beneficial, since clearly a large separation for the antennas would result in less correlation and thus higher throughputs. Some researchers have suggested inter-element spacings as high as 10λ, although this would clearly be limited in a mobile radio system. In this section, 4 different antenna spacings are examined, namely λ/3, λ/2, λ, and 3λ/2. For these measurements, the receiver was placed in the Communications Laboratory within the School of Engineering, while the transmitter was moved around the school, floor 2a. Figure 8.48 shows the measurement results for 10 separate locations.

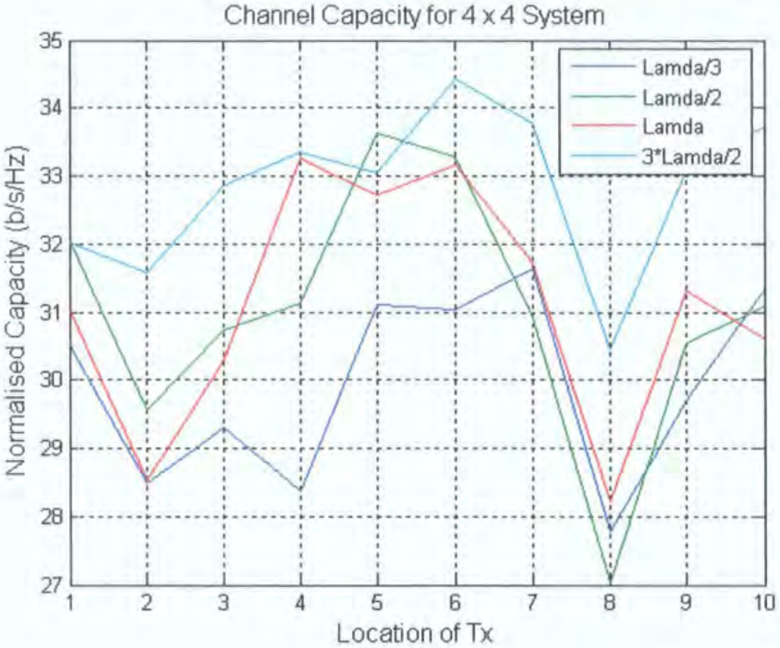

Figure 8.48: MIMO (4 × 4) capacity for different antenna spacings in indoor 2.4 GHz ISM channels.

The results suggest that the largest inter-element spacing shows the highest capacity estimates at almost all locations, but generally there is no significant difference in computed capacity between $\lambda/2$ and λ spaced arrays. Here, the difference between $3\lambda/2$ and $\lambda/3$ spaced arrays is shown to be between 2 - 5 b/s/Hz. It should be noted that the data presented here is limited, firstly by the low number of files collected and secondly by the positional errors of the arrays at each measurement location. The latter cannot be avoided due to practical measurement considerations.

It is also of interest to examine the number of estimated multipath components as a function of antenna spacing. Figure 8.49 shows the number of significant multipath components at each location for a 20dB threshold. In general, the number of paths found for each setup was similar. Although this is not conclusive, for this particular set of measurements, it was found that on average the highest number of paths was estimated at the smallest inter-element spacing. Clearly, this needs to be examined in more detail at larger inter-element spacings.

The transmit and receive array correlation coefficients for these data are also shown in figures 8.50 and 8.51, respectively. As in previous results, this shows that at locations where the transmit and receive correlation coefficients are collectively high, the throughput estimate is low.

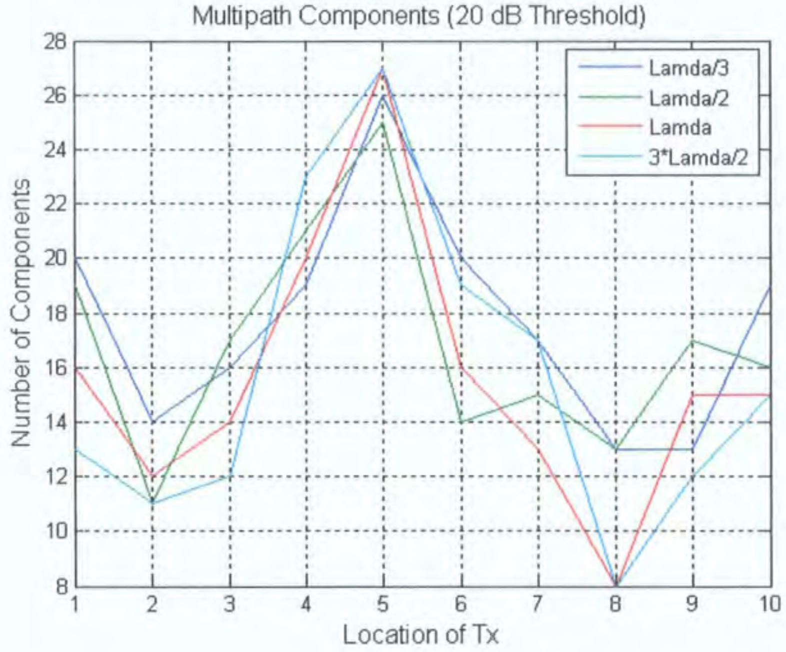

Figure 8.49: MIMO (4 × 4) resolved multipath components for different antenna spacings in indoor 2.4 GHz ISM channels.

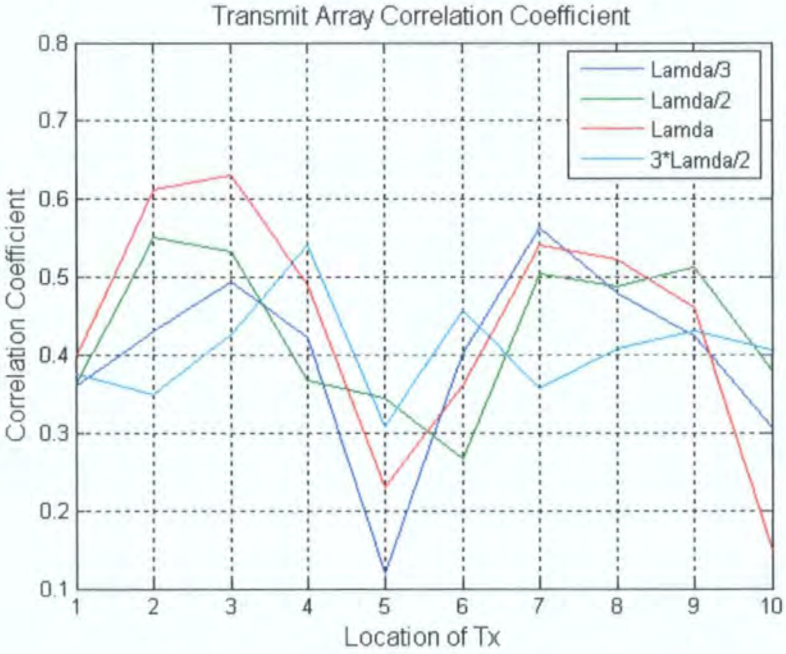

Figure 8.50: MIMO (4 × 4) transmit correlation coefficients for different antenna spacings in indoor 2.4 GHz ISM channels.

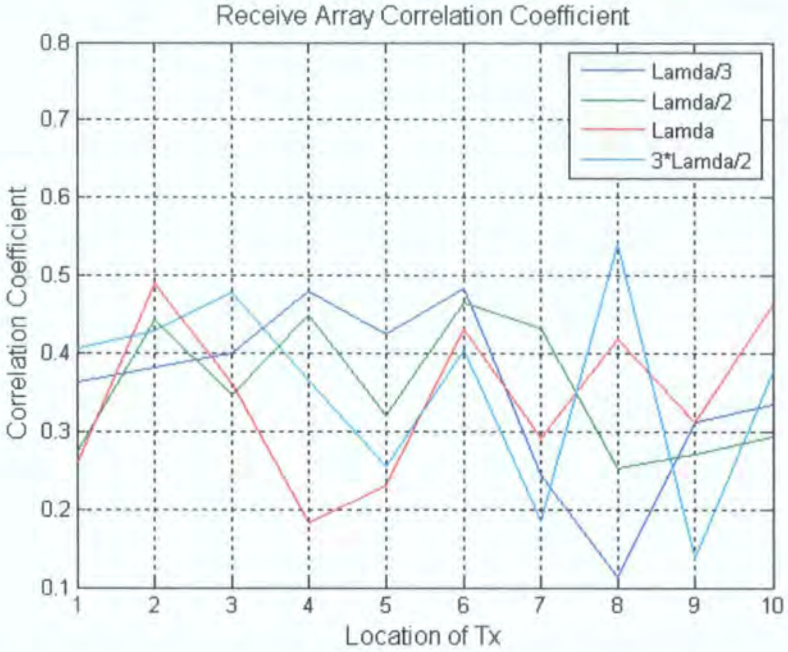

Figure 8.51: MIMO (4 × 4) receive correlation coefficients for different antenna spacings in indoor 2.4 GHz ISM channels.

8.5 Outdoor MIMO Channel Characterisation

Three sets of outdoor 4 × 8 non-LOS channel measurements were made around the Science Laboratories, University of Durham as described in section 8.2.2. All these measurements were carried out with 60 MHz system bandwidth in the UMTS-FDD uplink band. The main purpose of this campaign was to examine the effect of directional antennas on a MIMO link. In addition to this data, two sets of indoor 2 × 8 channel measurements were made to support the findings [11].

As described previously, three main types of antenna arrays were used during the campaign and these are listed below:

- Vertically polarised uniform linear dipole array (VPULDA).
- Vertically polarised directional linear patch array (VPDLPA).
- Vertically polarised directional circular patch array (VPDCPA).

For the outdoor 4 × 8 MIMO measurements, each data set was collected using one of the above listed arrays (with 4 elements) at the transmitter and an 8-element VPDCPA (45° beamwidth) at the receiver. The capacity CDFs of the three data sets are shown in figure 8.52 assuming 30 dB SNR.

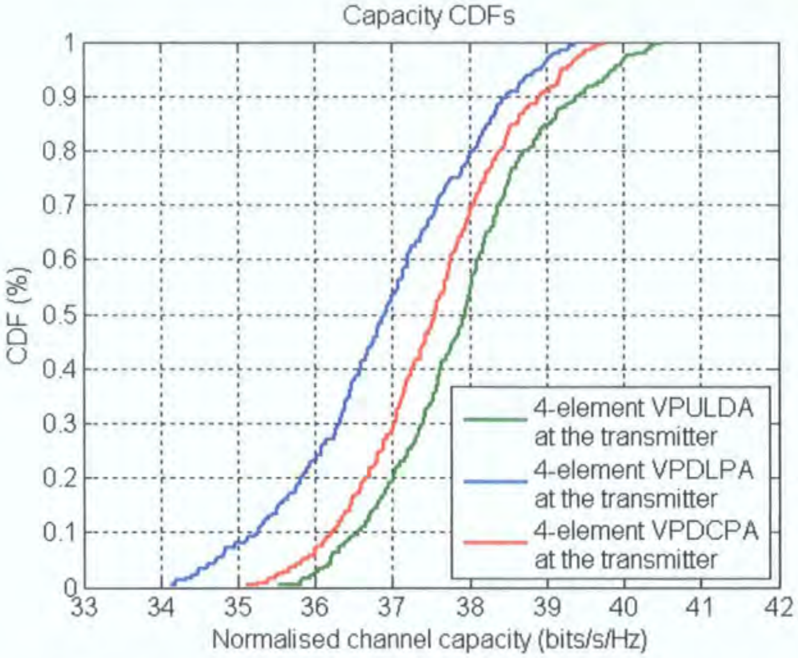

Figure 8.52: MIMO capacity CDFs for outdoor non-LOS UMTS channels.

Figure 8.52 shows that directionality at the transmitter can actually reduce the overall link capacity. In general, it is known that higher channel throughputs are expected in rich scattering MIMO channels. As a result, less channel scattering would be expected when directional antennas are employed at the transmitter as opposed to omnidirectional antennas. Hence in figure 8.52, the highest channel throughputs are achieved when employing a linear dipole array (VPULDA) at the transmitter, while the lowest capacity is achieved when employing a linear patch array (VPDLPA) at the transmitter, where the antennas are all pointing in one direction. The overall differences in figure 8.52 are not considerable, however, it does show that directionality at one (or both) link ends may be detrimental to the performance of a MIMO system. It should also be noted that the LOS capacity for these arrays (measured for outdoor channels) was typically reduced to ~ 25 b/s/Hz.

Figure 8.53 shows the measured capacity as a function of SNR. When comparing this to the IID model, it could be observed that at 30 dB SNR, the average capacity is ~ 88% of the IID case. The measurements carried out so far show that the outdoor environment in Durham gives more correlated channels than the indoor setups.

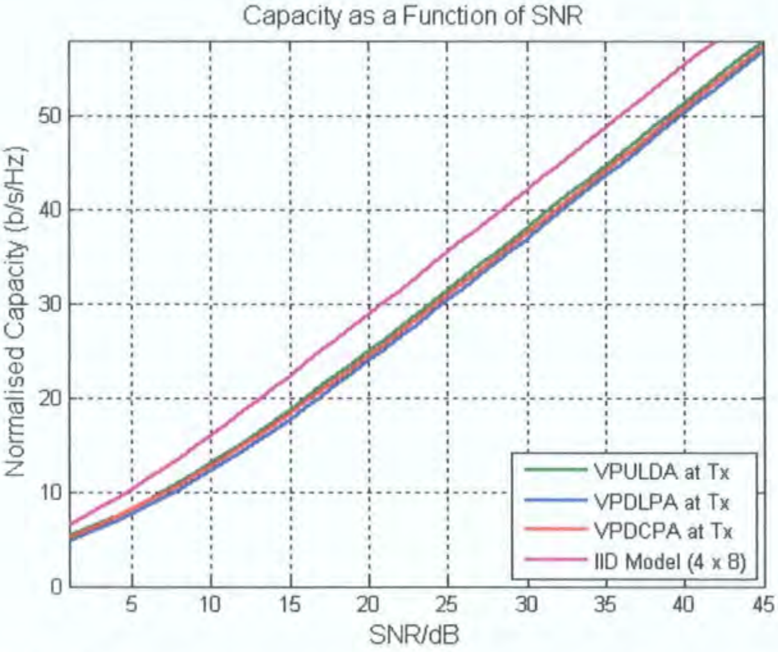

Figure 8.53: MIMO capacity vs. SNR for outdoor non-LOS UMTS channels.

In the second trial, measurements were collected for non-LOS indoor channels where high scattering would be expected. Here the transmitter-receiver separation was no more than 150 meters. For the measurements, a simple two dipole array (VPULDA) was used at the transmitter while two different 8-element arrays were used at the receiver. The aim here was to examine what effect directional antennas would have on the channel capacity when employed at the receiver side. The CDFs of the collected measurement results are shown in figure 8.54 for 30 dB SNR.

It can be observed from figure 8.54 that there is a marked improvement (less than 0.5 b/s/Hz) in the link capacity when a directional circular array is employed at the receiver end. The outcome of these results may suggest that there is less spatial correlation as a result of using the 8-element VPDCPA at the receiver side.

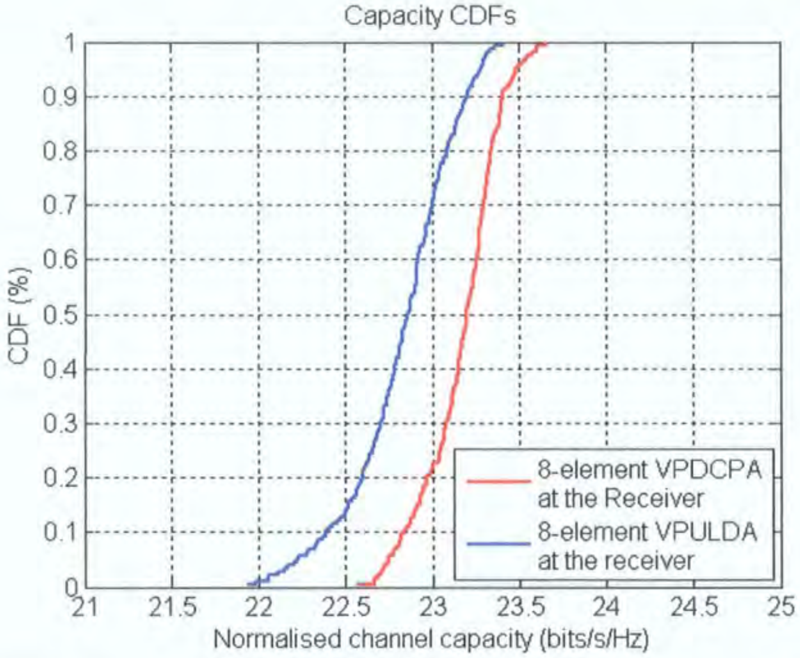

Figure 8.54: MIMO capacity CDFs for indoor non-LOS UMTS channels.

8.6 Frequency Fading Characteristics

There are a number of MIMO system applications which can be explored using the measurement data. MIMO systems are often implemented with OFDM (or OFDMA) air interface technology. Therefore, this section briefly presents data which describes the frequency selective fading for a range of indoor 4 × 4 array configurations.

In the frequency domain, the term LCR_f (frequency level crossing rate) gives the average number of crossings per Hz at which the transfer function crosses a threshold level in a positive direction. Similarly, ABF (average bandwidth of fades) is the mean value for the bandwidth over which the amplitude of the transfer function is below a specified threshold leve. Figure 8.55 shows the MIMO LCR_f (per element) for the 5.8 GHz measurements and figure 8.56 shows the ABF (per element). The results are summarised in tables 8.11 and 8.12 for different threshold levels.

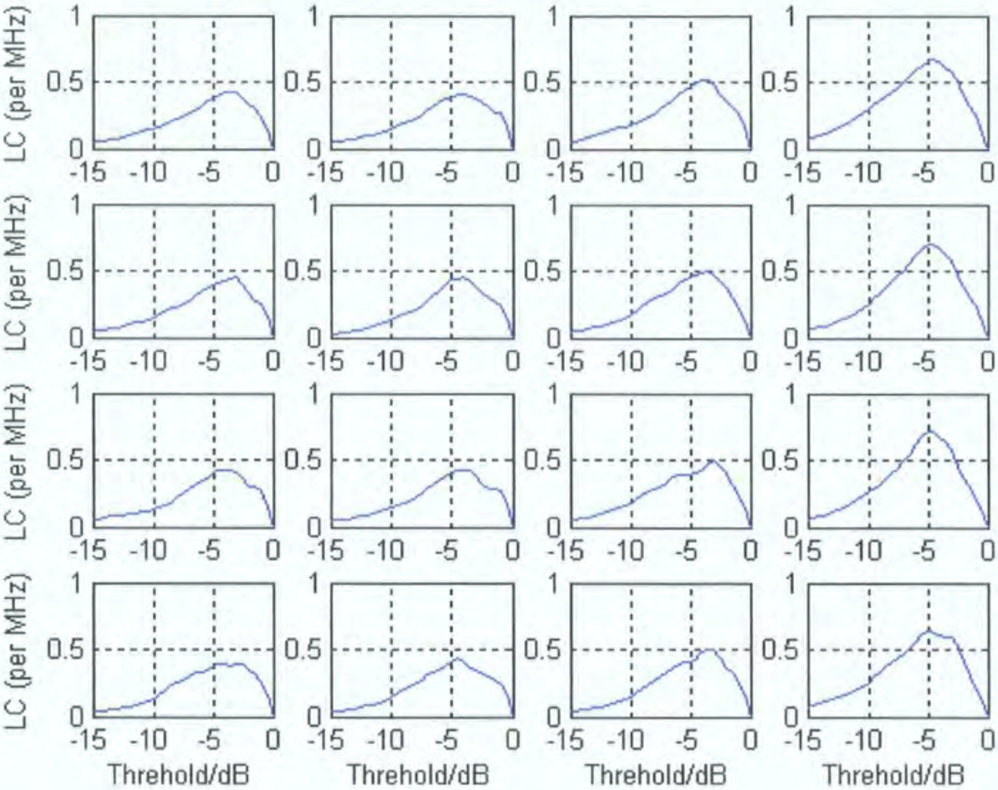

Figure 8.55: MIMO LCR_f for indoor BBC (5.8 GHz band) channels.

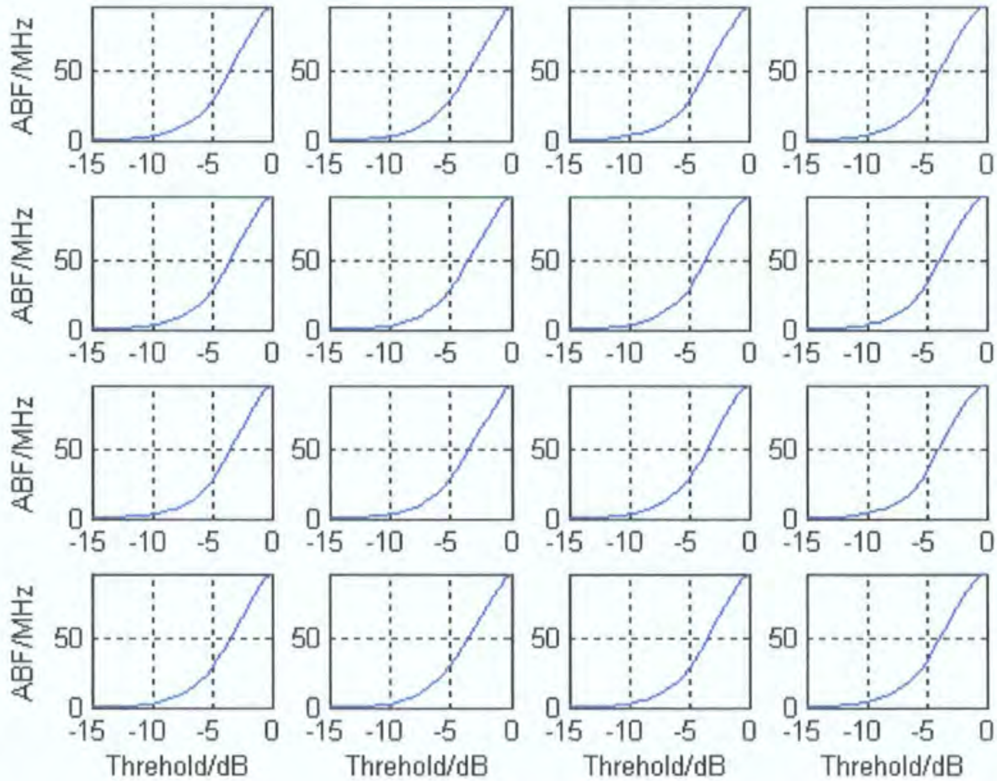

Figure 8.56: MIMO ABF for indoor BBC (5.8 GHz band) channels.

Level (dB)	UMTS-FDD (60 MHz)		2.4 GHz ISM (240 MHz)	
	LCR$_f$ (per MHz)	ABF (MHz)	LCR$_f$ (per MHz)	ABF (MHz)
-1	0.356	54.636	0.043	225.82
-2	0.397	45.944	0.077	199.27
-3	0.433	36.655	0.107	164.15
-4	0.423	27.961	0.124	127.02
-5	0.410	20.263	0.131	93.101
-6	0.367	13.928	0.126	65.403
-7	0.297	9.2364	0.114	44.402
-8	0.239	6.0963	0.097	29.449
-9	0.195	3.9275	0.082	19.348
-10	0.154	2.4924	0.067	12.591
-11	0.120	1.5839	0.055	8.1101
-12	0.096	1.0141	0.044	5.1627
-13	0.076	0.64116	0.034	3.2765
-14	0.059	0.40487	0.026	2.0771
-15	0.046	0.25439	0.020	1.3091

Table 8.11: Mean values of LCR$_f$ and ABF for UMTS and ISM measurements.

Level (dB)	2.25 GHz BBC (96 MHz)		5.8 GHz BBC (96 MHz)	
	LCR$_f$ (per MHz)	ABF (MHz)	LCR$_f$ (per MHz)	ABF (MHz)
-1	0.163	86.834	0.246	88.542
-2	0.237	72.947	0.347	74.712
-3	0.275	57.04	0.464	58.902
-4	0.287	41.961	0.490	43.087
-5	0.278	29.242	0.477	29.944
-6	0.242	19.491	0.420	19.989
-7	0.204	12.723	0.348	13.036
-8	0.168	8.1714	0.289	8.394
-9	0.134	5.1711	0.232	5.3154
-10	0.106	3.253	0.181	3.3539
-11	0.086	2.0412	0.141	2.1207
-12	0.068	1.2596	0.110	1.3352
-13	0.052	0.77709	0.084	0.84001
-14	0.039	0.48205	0.062	0.52919
-15	0.030	0.30079	0.046	0.3326

Table 8.12: Mean values of LCR$_f$ and ABF for BBC (dual band) measurements.

The results in table 8.11 show that the LCR_f is lower for the measurements carried out in the ISM band than those for the other campaigns. Table 8.12 shows the results for the BBC campaign, where a higher LCR_f was found for the upper measurement band (5.8 GHz). For the ABF results at -6 dB threshold level, the UMTS band showed around 14 MHz ABF (23%), 65 MHz (27%) for the ISM measurements, and just below 20 MHz (21%) for the BBC data. These parameters can be useful in assessing MIMO system performance for a given environment.

8.7 Summary and Conclusions

This chapter has presented various channel characteristics primarily for indoor MIMO links. The indoor measurement campaign has included the UMTS-FDD measurements, the BBC measurements, and the 2.4 GHz ISM band measurements. In addition to this, results were presented for outdoor MIMO channels around the University of Durham. The main focus for all the MIMO measurements has been to assess the link throughput and correlation characteristics. The results have included the assessment of channel capacity for LOS, OLOS, and non-LOS channels. Capacity has also been evaluated as a function of location, measurement time, system bandwidth (inherent to the results), SNR, antenna spacing and Doppler. In particular, it was shown that in some scenarios, Doppler could be beneficial to link capacity.

8.8 References

1. S. Salous, S. Feeney, N. Razavi-Ghods, R. Lewenz, "Measurements in the 2 - 6 GHz Band," XXVIIIth General Assembly of International Union of Radio Science (URSI GA 2005), New Delhi, India, 2005.
2. N. Razavi-Ghods, S. Salous, "Semi-Sequential MIMO Radio Channel Sounding," International Conference on Computing, Communications and Control Technologies (CCCT 2004), Austin, Texas, 2004.
3. M. Abdalla, "Directional Antenna Array for Channel Measurement System," Ph.D. Thesis, School of Electrical and Electronic Engineering, The University of Manchester, Manchester, UK, 2005.

4. M. A. Jenson, J. W. Wallace, "A Review of Antennas and Propagation for MIMO Wireless Communications," *IEEE Transactions on Antennas and Propagation*, vol. 52, pp. 2810-2824, 2004.
5. A. Paulraj, Nabar, R., Gore, D., *Introduction to Space-Time Wireless Communications*: Cambridge University Press, 2003.
6. J. P. Kermoal, L. Schumacher, K. I. Pedersen, P. E. Mogensen, F. Frederiksen, "A Stochastic MIMO Radio Channel Model with Experimental Validation," *IEEE Journal on Selected Areas in Communications*, vol. 20, pp. 1211-1226, 2002.
7. W. Weichselberger, M. Herdin, H. ¨Ozcelik, E. Bonek, "A Novel Stochastic MIMO Channel Model and its Physical Interpretation," International Symposium on Wireless Personal Multimedia Communications, Yokosuka, Japan, 2003.
8. B. T. Maharaj, W. Wallace, L. P. Linde, M. A. Jensen, "Frequency Scaling of Spatial Correlation from Co-located 2.4 and 5.2 GHz Wideband Indoor MIMO Channel Measurements," *IEE Electronics Letters*, vol. 41, pp. 336 - 337, 2005.
9. C. H. Y. Eugene, K. Sakaguchi, K. Araki, "Experimental and Analytical Investigation of MIMO Channel Capacity in an Indoor Line-of-Sight (LOS) Environment," 15th IEEE International Symposium on Personal, Indoor, and Mobile Radio Communications (PIMRC 2004), Barcelona, Spain, 2004.
10. H. Gokalp, "Characterisation of UMTS FDD Channels," Ph.D. Thesis, Dept. of Electrical Engineering and Electronics, UMIST, Manchester, UK, 2001.
11. N. Razavi-Ghods, M. Abdalla, S. Salous, "Characterisation of MIMO Propagation Channels Using Directional Antenna Arrays," IEE International Conference on 3G Mobile Communication Technologies (3G 2004), London, UK, 2004.

Chapter 9

Conclusions and Further Work

9.1 Conclusions

The various elements of multi-antenna radio channel characterisation have been discussed so far. A novel semi-sequential chirp sounding system was described in chapter 6. This involved the construction of four PLL synthesisers, two DDFS controller cards, two RF switch units, an RF up-converter (transmitter) and down-converter (receiver), and inter-digital band-pass filters for every sounder channel (a total of 10 filters). The transmitter was placed into a new 3U rack and the receiver into a 6U rack. The other components of the sounder such as receiver RF front-end cards, signal conditioning unit, synchronisation unit and data acquisition unit were developed by other workers. Various performance tests have been used to validate the operation of the system. This includes single-tone and two-tone tests. Sounder calibration data were also collected in order to compensate for the varying channel gains.

The semi-sequential sounder has been employed for various measurement campaigns which account to more than 700 measurement files corresponding to over 175,000 impulse responses. A relatively low number of indoor and outdoor files were collected for SIMO configurations described in chapter 7. The majority of the data have been collected for wideband indoor MIMO channels, particularly in the 2.4 GHz ISM band. Numerous algorithms have been developed in MATLAB software for data processing and analysis. These can be subdivided into three groups, namely: general processing based primarily on the FFT routine, MIMO data processing, and spatial array processing, such as SAGE and beamforming.

The SIMO 1 × 8 measurements (chapter 7) were used to analyse the spatio-temporal information in the channel. Initial FFT algorithms yielded impulse responses (or power delay profiles), transfer functions, and scattering functions.

The second part of this analysis examined spatial channel information using beamforming and SAGE. It was shown that in non-LOS scenarios, beamforming was not adequate in determining high accuracy DOA information. This was clearly a limitation which could be avoided with a more sophisticated estimation procedure as described for SAGE. Double directional (6 × 8 MIMO) data was also analysed primarily for azimuth DOA, and DOD estimation. In this case, the MIMO channel data were vectorised and the corresponding antenna calibration data were used to yield the spatial channel information. The beamforming technique was used mostly to validate the measurement data against SAGE. In all cases the DOA (and DOD) were evaluated based on the geometric location of the transmitter and the receiver before employing any type of array signal processing.

Various MIMO measurements were examined in chapter 8. The majority of the data were acquired for indoor non-LOS links. The first set of indoor measurements were for 2 × 2, 3 × 3, 4 × 4, and 2 × 8 UMTS-FDD (60 MHz bandwidth) uplink channels. Capacity results were shown for all the configurations and this was compared to the IID channel model with more than 90% fit at 30 dB SNR. At low SNRs of less than 10 dB it was shown that diversity gain is more prominent in the channel, whilst at higher SNR it was shown that better performance is available for the 3 × 3 array setup rather than the 2 × 8 setup due to multiplexing gain. It was shown through real channel measurements (using 10% outage capacity) that almost 3 times the data rate could be achieved for a high SNR 4 × 4 channel relative to a SISO system.

The BBC 4 × 4 data were used to compare two simultaneous measurement bands at 2.25 GHz and at 5.8 GHz. These data generally demonstrated higher thoughputs in the lower 2.25 GHz band. However, it was determined that the transmitter GaAs switch used in the semi-sequential MIMO system provided 10 dB lower isolation in the 5.8 GHz band as compared to the 2.25 GHz band. This explains the differences in the results. Since the antenna spacing was greater at the higher measurement band it would typically be expected that this band would provide more throughput. In order for the results to be comparable, measurements should be carried out using two separate switch matrices (running from the same control clock) which provide comparable isolation in both bands, meaning that correlation at the transmitter is similar. The isolation of the switch and the apparent correlation at the transmitter in the higher band is less prominent for highly correlated links.

Moreover, the data were described as LOS or obstructed LOS (OLOS). The results showed that high (much greater than SISO) capacities could be expected even in scenarios where the channel was highly correlated, which showed 2 times the SISO data rate for a 4 × 4 link at 30 dB SNR. For measurements where the transmitter was moved in order to create more channel Doppler, the capacity estimates were seen to increase due to the spatial variation of the MIMO matrix. As would be expected, these data also showed greater fluctuations in the capacity results as a function of time. Furthermore, Doppler had a greater affect at the 5.8 GHz band which resulted in higher throughputs. Time-variant analysis is important for adaptive (waterfilling) systems where some feedback and channel training information is required. For this reason, high Doppler channels would be problematic from a systems and signals perspective.

The final set of indoor measurements, which was by far the largest, examined MIMO channels in the 2.4 GHz ISM band with a wider bandwidth of 240 MHz. Here, measurements were carried out for many array configurations within the School of Engineering and capacity results were presented along with figures for array correlation, and number of multipath components. As the array at both ends of the channel increased in size, there was a general downward trend in the correlation calculated for the transmitter and receiver. This was due to the averaging being done over a much larger array. The mean estimate for the multipath components showed very similar results for all non-LOS environments.

The capacity results for the measurements were presented as CDF plots and as a function of SNR. These results were comparable to the previous measurements showing an increase in channel throughput as the array size increased at both ends of the link. Analysis of the higher Doppler files at this bandwidth showed very similar results to the BBC data, i.e. that capacity estimates were 2 – 3 b/s/Hz higher. In addition to this, 4 × 4 measurements were made with 4 different antenna spacings. The largest spacing of $3\lambda/2$ yielded the highest capacity estimates which would imply that less MIMO channel correlation is expected at a greater inter-element spacing, as would be expected.

Some MIMO measurement campaigns were also carried out for outdoor 4 × 8 links. Here, 3 array geometries were examined at the transmit end. In particular, it was shown that the lowest capacities were a result of directional antennas at the transmitter, where all the antennas had the same look angle. However, using a circular directional array at the receiver gave slightly higher throughput estimates than using a linear omni array. These data were acquired for indoor 2 × 8 MIMO links measured in the School of Engineering. When comparing the indoor data to the outdoor measurements, it was apparent that the indoor measurements showed a better fit to the IID model (greater than 90%). Furthermore, when computing capacity for different bandwidth sections (5 MHz), the capacity estimates were not significantly different. This infers that varying the processing bandwidth of the data does not result in significantly different capacity estimates.

The frequency fading characteristics of all three indoor measurement configurations were also presented. The results for the BBC data were similar for both bands, however the LCR_f was higher for the 5.8 GHz measurements. The UMTS-FDD downlink data and the ISM band data showed quite significant differences in both LCR_f and ABF.

In general, MIMO results were evaluated as a function of time, distance, bandwidth, location, SNR, antenna spacing, and Doppler, as well as the measurement environment (i.e. LOS, OLOS, non-LOS), where any MIMO link is a function of all the aforementioned parameters.

In summary, various aspects of MIMO (and SIMO) radio propagation channels have been explored in this thesis. Chapters 2 and 3 provided the background theory and literature review for multi-antenna propagation channels. In chapter 4, various spatial array processing tools were described, such as beamforming and SAGE. Chapter 5 examined the requirement for sounding systems and chapter 6 provided detailed systems level descriptions of the hardware developed. Finally, chapters 7 and 8 presented the measurement results and conclusions. Appendix 7 lists all the papers written during the course of this project.

9.2 Further Work

Although many MIMO measurements have been examined so far, there is undoubtedly further work which could be extremely valuable to the development of MIMO systems. In the first case, more system configurations can be examined to yield a particular set of results. For example, employing the sounder with greater system bandwidth would give higher resolution information in the time-delay domain.

This is particularly interesting for estimation of spatial parameters for indoor links. Furthermore, every location presents a different spatial environment and the data corresponds to a different local area. For MIMO measurements in both the 2.25 GHz band and the 5.8 GHz band, measurements should be carried out with separate switches for each band which provide similar isolation between the transmit chirps.

Since the sounder employs parallel receive channels, it is quite possible to connect each RF channel to a different sub-array. In other words, by using more RF switches, a 24 or 32 element array could be formed. The ultimate limit for spatial characterisation is the number of array elements. Even for very sophisticated super-resolution techniques, more elements in the array will result in a better spatial resolution.

In addition to more measurements using different sounder configurations, there are other software tools which could be developed to analyse the sounder data. For example PCA (Principle Component Analysis) could be employed for cluster analysis. Also, more MATLAB GUIs (Graphical User Interfaces) could be developed to aid with channel measurements and real-time analysis.

No real system or channel modelling has been presented in this thesis, since this is a project in itself. Developing a MIMO system simulator is a valuable task for the main reason that the channel measurements could be imported into the model for performance tests such as BER analysis. Furthermore the simulator could be used to evaluate channel models against the actual measurement data for various system configurations (number of antennas, modulation, space-time coding, etc.) The implementation of a MIMO-OFDM simulator in SIMULINK software would have obvious merits. Currently an OFDM system simulator has been developed by another worker, where the SISO radio channel is defined as a set of filters.

Appendix 1

Signal Processing in MATLAB

A1.1 SIMO Processing

Many programs were developed in MATLAB for computing different parameters for the SIMO/MIMO radio channel. Figure A1.1 shows the core processing used to extract SIMO delay/Doppler characteristics, such as power delay profiles, scattering functions, and time-variant transfer functions. A list of these programs is available on the accompanying CD-ROM, which includes algorithms used to extract delay spread, frequency fading statistics and a host of other parameters. A plotter GUI (Graphical User Interface) was also developed for processing raw data directly.

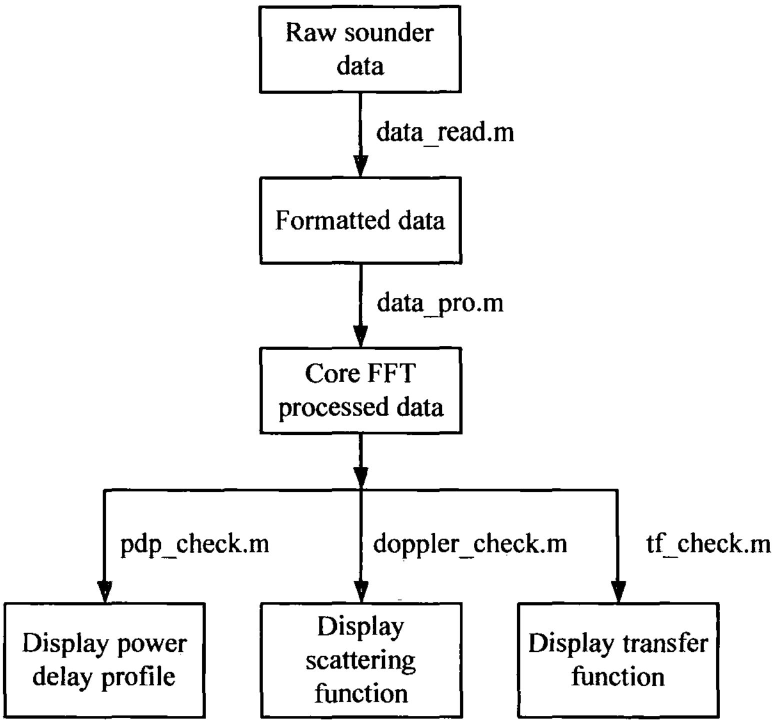

Figure A1.1: SIMO processing in MATLAB.

A1.2 MIMO Processing

Figure A1.2 shows the MIMO signal processing performed on the sounder data. The computed channel capacity results were often compared to the IID channel which was simulated using the normrnd() function. A MATLAB GUI was also developed to processed raw data directly (available on the accompanying CD-ROM).

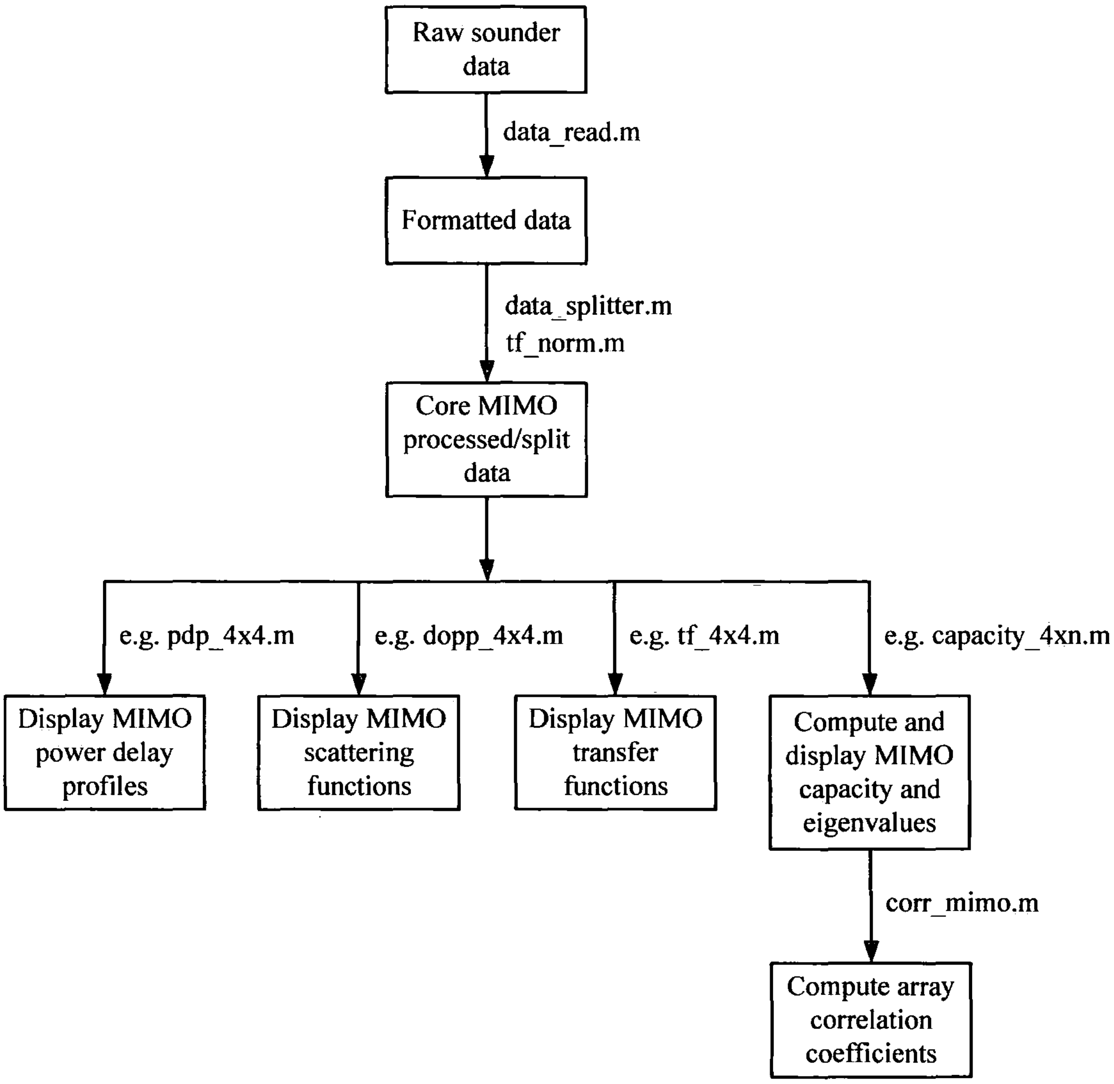

Figure A1.2: MIMO processing in MATLAB.

A1.3 Array Signal Processing

In order to estimate spatial channel information, both sounder measurement data and antenna calibration information was necessary. Figure A1.3 shows the array processing which can yield results using both the beamforming and the SAGE techniques. Although figure A1.3 illustrates the spatial processing for SIMO channels, the same core processing is applied to yield both DOA and DOD results.

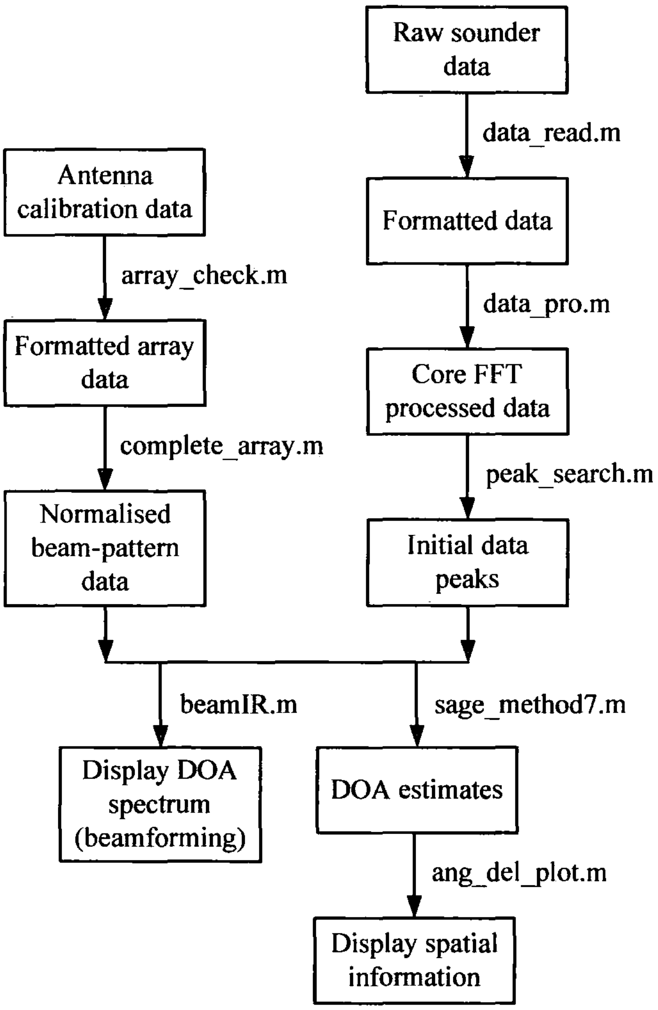

Figure A1.3: Spatial (DOA) processing in MATLAB.

Appendix 2

Microcontroller PLM Program

A2.1 Microcontroller Program for the Digital Controller

The microcontroller must be programmed to perform the IF to RF conversions, i.e., given the centre frequency, f_c, the SRF and the bandwidth, BW, the microcontroller must calculate f_1, Δf, and f_2. Two other parameters must be taken into account. The first is the minimum (set) frequency resolution of the DDFS, denoted by a factor, and the second is the update rate of the DDFS, F_{update}, which is determined by the frequency strobe used to latch the data into the DDFS. Of course the data in this case refers to the binary 24-bit parallel input that programs the DDFS to produce the frequency sweeping "chirp" signal. The other parameter to consider is the number of steps the DDFS takes to sweep from f_1 to f_2. This is simply determined by $F_{update}/Factor$. The microcontroller calculations are shown below:

Calculate Δf:

$$\Delta f = \frac{BW \times SRF}{F_{Update}} \cdot \frac{1}{Factor} \qquad \text{(A2.1)}$$

where the DDFS frequency resolution, *Factor*, is given by

$$Factor = \frac{F_{\max}(DDFS)}{2^n} = \frac{F_{\max}/4}{2^n} = \frac{400 \times 10^6}{2^n} \qquad \text{(A2.2)}$$

The maximum frequency output of the DDFS in this case is 400 MHz (for a 1.6 GHz reference). n denotes the number of data bits going into the DDFS and since n is equal to 24 bits, the DDFS factor is given as 23.84 Hz.

Calculate f_1:

$$f_1 = \left(f_c - \frac{BW}{2} \right) \times \frac{1}{Factor} \qquad \text{(A2.3)}$$

Calculate N:

$$N = \frac{F_{Update}}{SRF} \tag{A2.4}$$

where in theory: $N = BW/\Delta f = T/\Delta t$.

Calculate f_1:

$$f_2 = f_1 + N\Delta f = \left(f_c + \frac{BW}{2} \right) \times \frac{1}{Factor} \tag{A2.5}$$

The part of the PLM code that calculates the aforementioned values is given by the following. Note in this case F_{update} = 1.25 MHz and *Factor* = 23.84 Hz.

IF to RF conversion in the 89C52 microcontroller:

```
/* Calculate DF */
/* DF=(BW*SRF/UpdateRate)*(1/Factor) */

ACC = Load_32 (BW$2, BW$1);   /*  Load Bandwidth (2 words)    */
ACC = Mul_16 (SRF$1);         /*  multiply by SRF    */
ACC = Mul_16 (10486);
ACC = Mul_16 (4);
ACC = Div_16 (32);
ACC = Div_16 (39062); /*  i.e., 1/(UpdateRate* Factor) = 0.33555629.  */
/*  Factor = 23.8441.    */
DF = Low_16;
DF$L = LOW (DF);                 /*  Store DF    */
DF$H = HIGH (DF);


/*  calculate F1          */
/*  F1=(Fc-BW/2)*1 000 000   */

ACC = Load_32(Fc$2, Fc$1);
ACC = Mul_16(2);
ACC = Sub_32(BW$2, BW$1);
ACC = Mul_16(50);
F1$IF$L = Low_16;
F1$IF$H = High_16;
/*  F1$IF = (Fc * 100 - BW * 50) - LO$FCY */

ACC =  Load_32 (F1$IF$H, F1$IF$L);
ACC = Mul_16 (10000);    /* Final F1 is in Hz */
ACC = Div_16 (39062);
```

```
ACC = Mul_16 (10486);     /* Final F1 is in Hz */
ACC = Div_16 (32);
ACC = Mul_16 (5);
F1$1 = Low_16;
F1$2 = High_16;                /* F1 = ACC */


/*  calculate N, number of steps    */
N = 125;
ACC = Load_16 (N);
ACC = Mul_16 (10000);          /*  N=1250000/SRF  */
ACC = Div_16 (SRF$1);


/*  calculate F2 = F1 + N * DF      */
ACC = Mul_16 (DF);
ACC = Add_32 (F1$2,F1$1);  /*  ACC=F1+N*DF   */
F2$1 = Low_16;
F2$2 = High_16;                /*  F2 = ACC  */
```

Appendix 3

DDFS Programmer

A1.1 Digital Controller Board

The Schematic of the Digital controller board is shown in figure A3.1. This circuit was designed based on previous logic designs (Actel FPGA), all of which are well documented. In order to make the board operational, there was a special phase relationship between the onboard signals (phase reset, frequency strobe, and latch clock) which had to be adhered to. This was due to the required alignment of data between the digital controller board and the high performance DDFS, which had a problematic input interface. As a result, an additional circuit was implemented to provide this timing alignment, and this is shown in figure A3.2. It should be noted that all the PCB designs were done in Protel (99SE) software. These were saved as DDB files, which includes SCH, PCB and NET components. Figures A3.3 and A3.4 show the two layers of the digital controller board. Similarly, figures A3.5 and A3.6 show the two layers for the additional timing board.

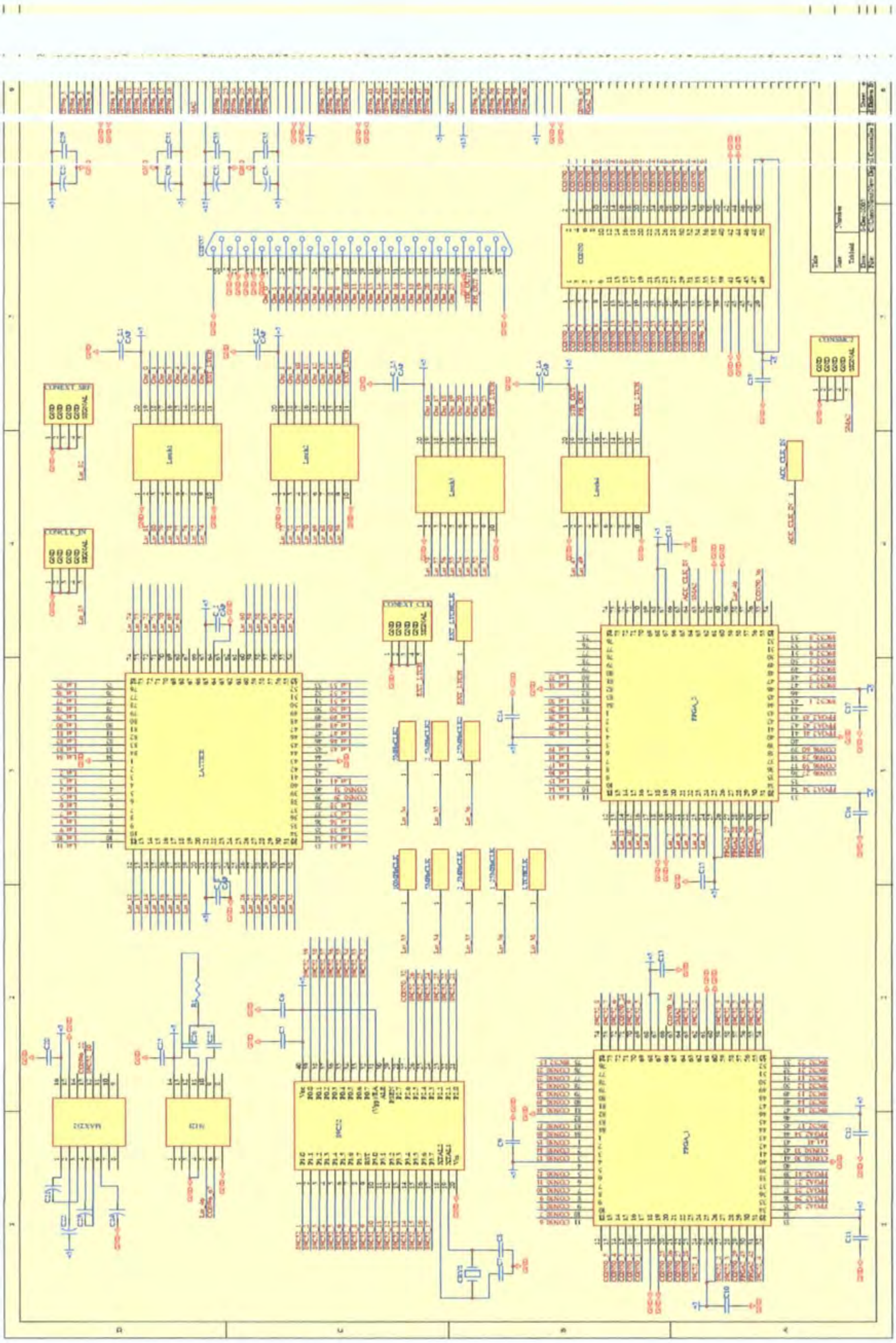

Figure A3.1: Schematic of digital controller board.

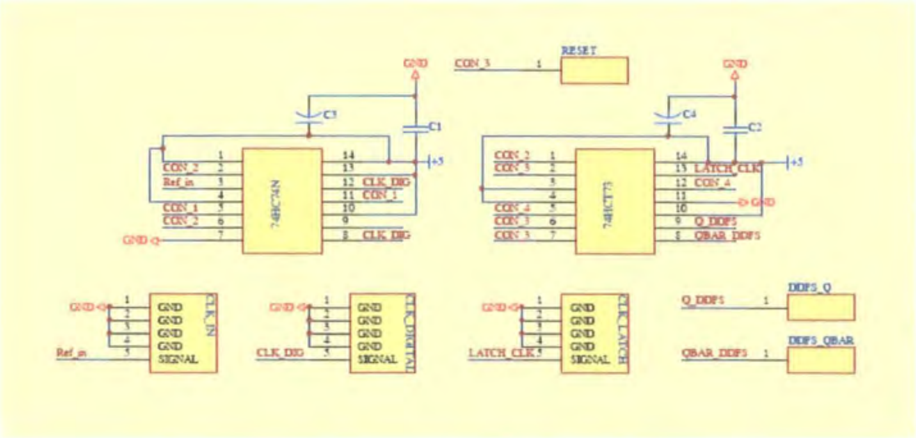

Figure A3.2: Schematic of Timing board.

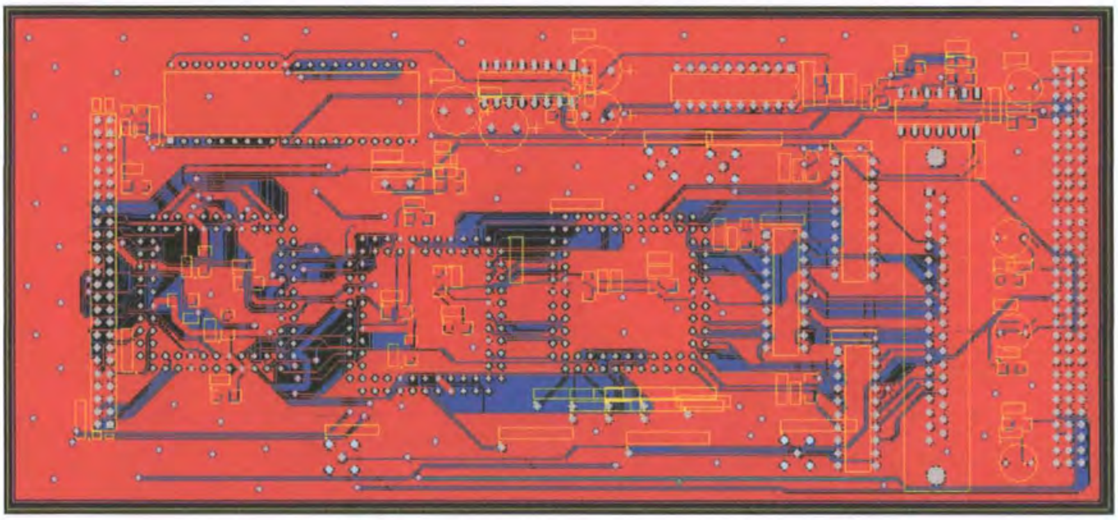

Figure A3.3: Top layer of digital controller board in Protel software.

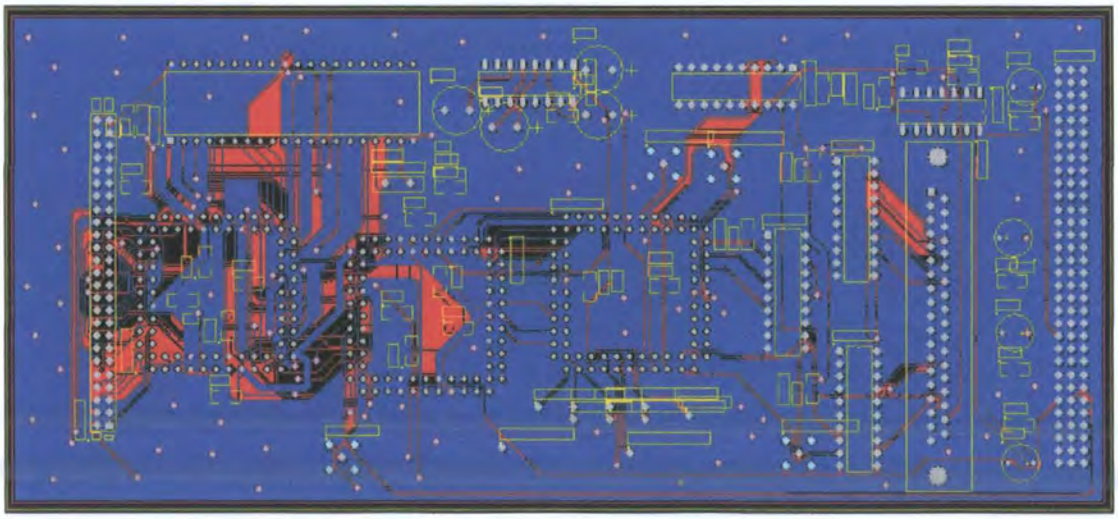

Figure A3.4: Bottom layer of digital controller board in Protel software.

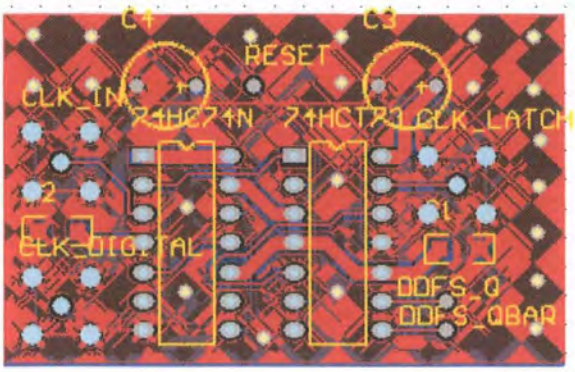

Figure A3.5: Top layer of timing board in Protel software.

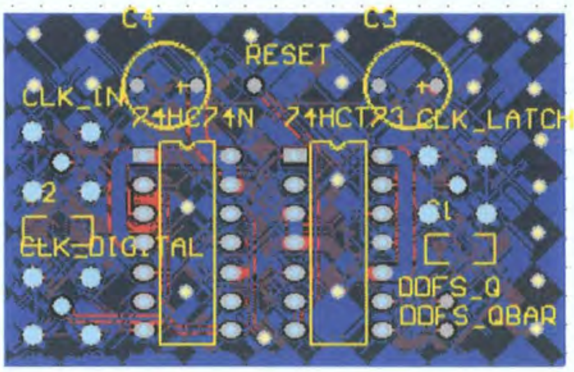

Figure A3.6: Bottom layer of timing board in Protel software.

Appendix 4

Antenna Switching Control

A4.1 Digital Design for Antenna Switching

The counters for the control FPGAs, which were used to switch the antennas at the transmitter, are shown in figure A4.1 for an 8-way configuration and figure A4.2 for a 5-way configuration. In general for a 1 × 8 switch, there are three control signals to distinguish between each antenna (QA, QB, and QC.) The software ispDesignExpert v8.0 was used to control the Lattice 1032E FPGAs. Here, the effective sampling rate is given by SRF/N, where N is the number of switching ports.

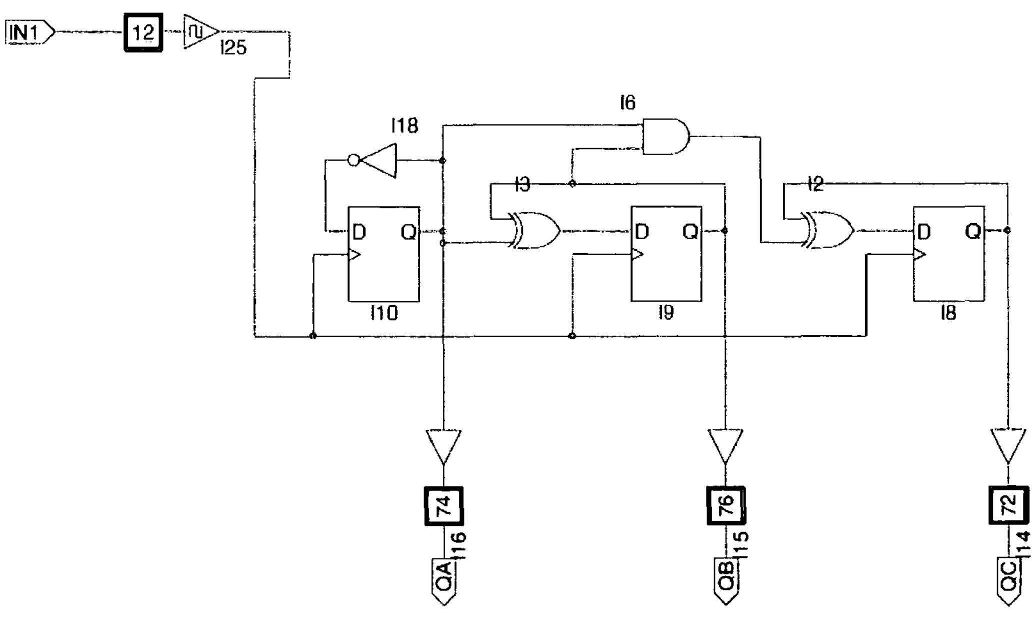

Figure A4.1: Antenna switching logic at the transmitter (8-way.)

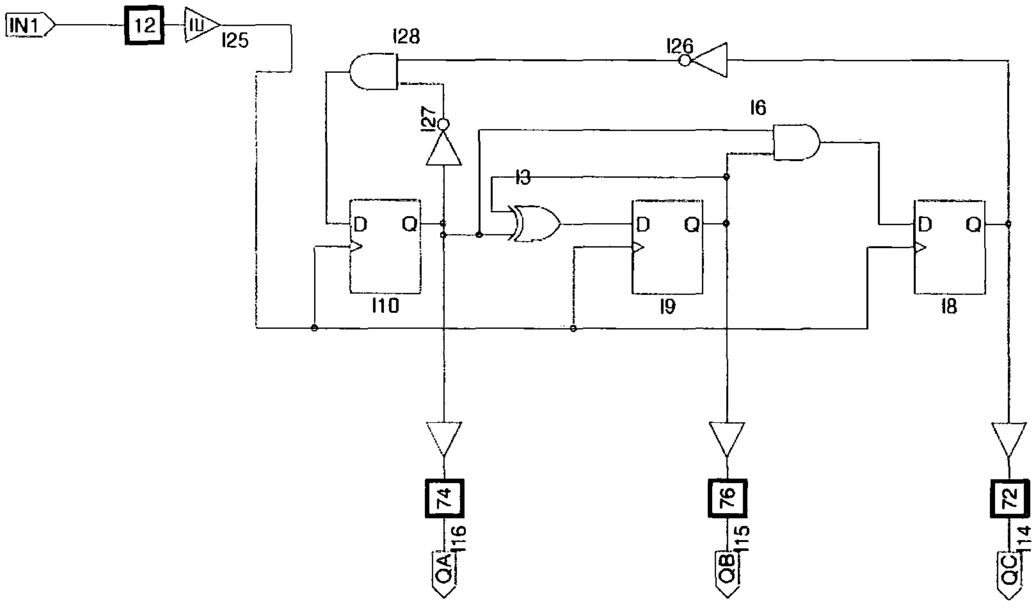

Figure A4.2: Antenna switching logic at the transmitter (5-way.)

Appendix 5
Inter-digital Filters

A5.1 Inter-digital Filter Design

This section describes an approximate design process for inter-digital (microwave cavity) band-pass filters based on the work by Matthaei, *et al.* [1]. These filters are reliable and offer excellent performance characteristics.

An inter-digital filter consists primarily of interleaved conducting rods sandwiched between two parallel conducting ground planes, normally with conductive plates along the sides (figure A5.1). The width of the filter is nominally one-quarter wavelength while the elements themselves are physically shorter and can be tuned by screws. Since the main dimension of these filters is directly related to one quarter of the physical wavelength at the frequency of interest (in the pass-band), building such a filter with air as the dielectric for frequencies much below the 70 cm amateur band would be problematic because of the sheer physical size. However, these filters are used for a wide range of frequencies and it is not uncommon to find an inter-digital filter for frequencies as high as 10 GHz and beyond.

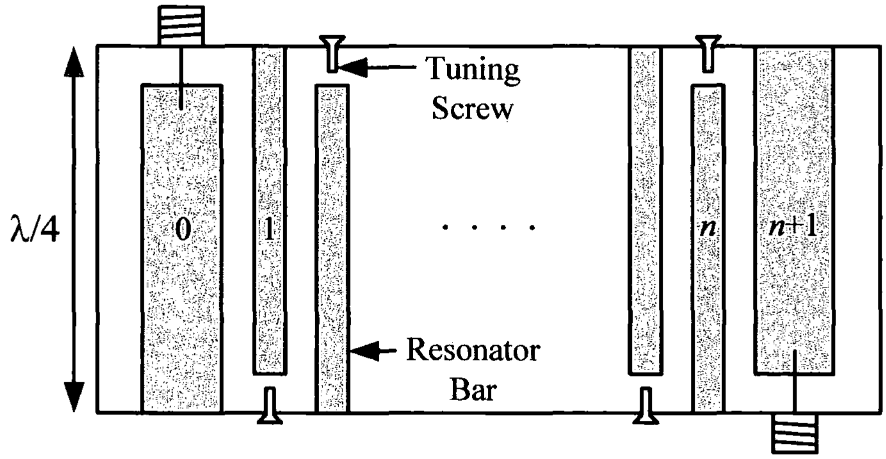

Figure A5.1: Illustration of a typical inter-digital band-pass filter with *n* reactive elements (i.e. *n* coupled ~ λ/4 resonators).

The structure shown in figure A5.1 consists of TEM-mode strip-line resonators between parallel ground planes. Coupling here is achieved by way of the fields fringing between adjacent resonator elements [1]. Lines 1 to *n* serve as resonators, while lines 0 and *n* + 1 operate as impedance-transforming sections and not as resonators. The electrical properties of such a structure are fundamentally characterised in terms of the self-capacitances, C_k, per unit length of each bar with respect to ground, and the mutual capacitances, $C_{k,k+1}$, per unit length between adjacent bars *k* and *k* + 1. This is represented in figure A5.2.

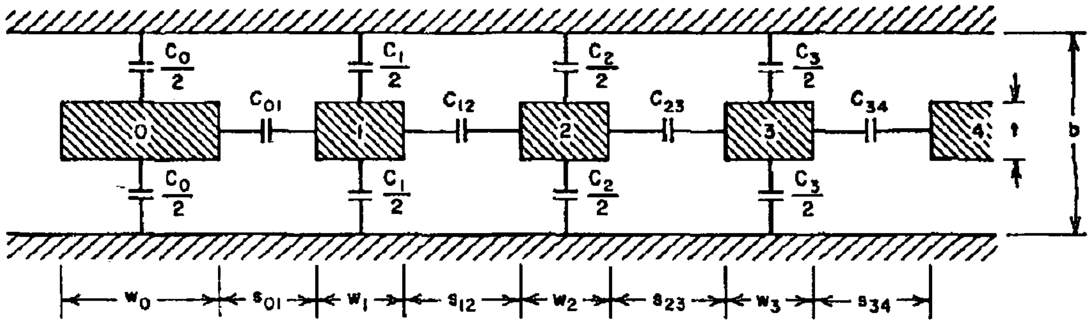

Figure A5.2: Cross section of an array of parallel-coupled lines such as those used in an inter-digital filter [2].

The coupled structure represented in figure A5.2 is not always highly accurate. However, it is generally difficult to provide exact analysis of the filter synthesis problem, therefore the synthesis procedure described will involve a number of simplifying approximations. The design procedures to follow are based on a low-pass to high-pass filter transformation which produces a band-pass filter with a total of *n* + 2 line elements [2].

The design equations discussed here are for filters where the bandwidth does not exceed 25% of the centre frequency. Because this is an approximate synthesis procedure, Matthaei, *et al.* [1] suggest a typical +7% bandwidth correction factor to overcome these approximations. Before describing the design formulas, it is critical to state the band-pass filter design parameters. Based on the out-of-band interference, more than ~ 40 dB of rejection is necessary for the UMTS frequencies. Since the sounding signal is wideband, a filter bandwidth of 335 MHz centred on 2.37 GHz should be quite adequate for most measurements around the 2.4 GHz ISM band. The choice of these parameters will be discussed later on.

Based on the aforementioned values, the practical design bandwidth, which includes the correction factor is ~ 358 MHz (335 MHz + 7%). This corresponds to start frequency, f_1 = 2191 MHz, and end frequency, f_2 = 2549 MHz. This gives a fractional bandwidth, W = $(f_2 - f_1)/fc \approx 0.15$. It should be noted that the normalised centre frequency here is given by

$$f_0 = \sqrt{f_1 f_2} \approx 2.363 \text{ GHz} \tag{A5.1}$$

The order of the filter (i.e. number of resonators) depends almost entirely on the required filter rejection characteristics. This steepness factor is defined by the ratio of stop-band bandwidth over pass-band bandwidth [3]. It is possible to identify a Chebyshev filter with 0.1 dB ripple, which requires a VSWR of 1.36, corresponding to ~ 16 dB return loss. By calculating the geometrically related stop-band pair for ≤ -40 dB rejection at frequencies below 2160 MHz, it is possible to define the number of filter poles. From the attenuation curves in [4], a Chebyshev filter with 0.1 dB ripple and 8 poles (n = 8) is shown to be quite adequate for these specifications. The selectivity factor for this filter is, $Q = f_0/(f_2 - f_1) \approx 6.6$.

A number of basic constants required for the computation of the filter parameters are listed below:

- $\varepsilon_r = 1$ (dielectric constant of air)
- $L = \lambda / 4 = c/\left(4 f_C\right) \approx 31.6$ mm
- $\theta_1 = \dfrac{\pi}{2}\dfrac{\omega_1}{\omega_0} = \dfrac{\pi}{2}\left(1 - \dfrac{W}{2}\right) = 1.452$ rad (or 83.202 degrees)
- $Y_A = 0.02$ mho (terminating line admittance $= 1/Z_A = 1/50$ ohms)

Here, ω_1 is the cutoff frequency (band-pass to low-pass transformation). The filter element values for a normalised Chebyshev ($g_0 = 1$, $\omega_1' = 1$) with 0.1 dB ripple and 8 poles is given by [1]

$$g_1 = 1.1897,\ g_2 = 1.4346,\ g_3 = 2.1199,\ g_4 = 1.6010,$$

$$g_5 = 2.1699,\ g_6 = 1.5640,\ g_7 = 1.9444,\ g_8 = 0.8778,\ g_9 = 1.3554$$

Now it is possible to compute the following quantities

$$\frac{J_{01}}{Y_A} = \frac{1}{\sqrt{g_0 g_1 \omega'_1}} \tag{A5.2a}$$

$$\left.\frac{J_{k,k+1}}{Y_A}\right|_{k=1 \text{ to } n-1} = \frac{1}{\omega'_1 \sqrt{g_k g_{k+1}}} \tag{A5.2b}$$

$$\frac{J_{n,n+1}}{Y_A} = \frac{1}{\sqrt{g_n g_{n+1} \omega'_1}} \tag{A5.2c}$$

Substituting the previously defined parameters into equation A5.2, yields

J_{01}/Y_A	0.9168
J_{12}/Y_A	0.7654
J_{23}/Y_A	0.5734
J_{32}/Y_A	0.5428
J_{45}/Y_A	0.5365
J_{56}/Y_A	0.5428
J_{67}/Y_A	0.5734
J_{78}/Y_A	0.7654
J_{89}/Y_A	0.9168

Table A5.1: Computed $J_{k,k+1}/Y_A$ filter quantities.

It can be observed that the values in table A5.1 show a basic symmetry. This is a property that is inherent to these types of filters and will be apparent for all the computed parameters. Further quantities to be calculated include

$$\left.N_{k,k+1}\right|_{k=1 \text{ to } n-1} = \sqrt{\left(\frac{J_{k,k+1}}{Y_A}\right)^2 + \left(\frac{\tan^2\theta_1}{4}\right)} \tag{A5.3}$$

$$M_1 = Y_A\left(\frac{J_{01}}{Y_A}\sqrt{h} + 1\right) \tag{A5.4a}$$

$$M_n = Y_A\left(\frac{J_{n,n+1}}{Y_A}\sqrt{h} + 1\right) \tag{A5.4b}$$

Substituting parameters into equation A5.3, gives

N_{12}	4.2640
N_{23}	4.2337
N_{34}	4.2297
N_{45}	4.2289
N_{56}	4.2297
N_{67}	4.2337
N_{78}	4.2640

Table A5.2: Computed $N_{k,k+1}$ filter quantities.

The parameter *h* in equation A5.4 is called the dimensionless admittance scale factor and is significant to all the filter computations. This parameter is directly related to the scale of the filter and even a small adjustment of this value will cause a significant change in the filter geometry. Practically, this factor should be treated as a design variable. In [1, 2], it is suggested that *h* should typically be chosen to make the quantity

$$\left.\frac{2C_{k-1,k}}{\varepsilon}+\frac{C_k}{\varepsilon}+\frac{2C_{k,k+1}}{\varepsilon}\right|_{\substack{k=n/2 \text{ for } n \text{ even} \\ =(n+1)/2 \text{ for } n \text{ odd}}} \approx 5.4 \qquad \text{(A5.5)}$$

where ε is the dielectric constant, C_k/ε are the normalised self-capacitances per unit length for the line elements, and $C_{k,k+1}/\varepsilon$ (and $C_{k-1,k}/\varepsilon$) are the normalised mutual capacitances per unit length between adjacent line elements (see figure A5.2). These capacitances need to be defined before solving for *h*. The normalised self-capacitances, C_k/ε, are given by

$$\frac{C_0}{\varepsilon}=\frac{376.7}{\sqrt{\varepsilon_r}}\left[2Y_A-M_1\right] \qquad \text{(A5.6a)}$$

$$\frac{C_1}{\varepsilon}=\frac{376.7}{\sqrt{\varepsilon_r}}\left[Y_A-M_1+hY_A\left[\frac{\tan\theta_1}{2}+\left(\frac{J_{01}}{Y_A}\right)^2+N_{12}-\frac{J_{12}}{Y_A}\right]\right] \qquad \text{(A5.6b)}$$

$$\left.\frac{C_k}{\varepsilon}\right|_{k=2 \text{ to } n-1}=\frac{376.7}{\sqrt{\varepsilon_r}}hY_A\left[N_{k-1,k}+N_{k,k+1}-\left(\frac{J_{k-1,k}}{Y_A}\right)-\left(\frac{J_{k,k+1}}{Y_A}\right)\right] \qquad \text{(A5.6c)}$$

$$\frac{C_n}{\varepsilon}=\frac{376.7}{\sqrt{\varepsilon_r}}\left[Y_A-M_1+hY_A\left[\frac{\tan\theta_1}{2}+\left(\frac{J_{n,n+1}}{Y_A}\right)^2+N_{n-1,n}-\frac{J_{n-1,n}}{Y_A}\right]\right] \tag{A5.6d}$$

$$\frac{C_{n+1}}{\varepsilon}=\frac{376.7}{\sqrt{\varepsilon_r}}\left[2Y_A-M_n\right] \tag{A5.6e}$$

The normalised mutual capacitances, $C_{k,k+1}/\varepsilon$, are given by

$$\frac{C_{01}}{\varepsilon}=\frac{376.7}{\sqrt{\varepsilon_r}}\left[M_1-Y_A\right] \tag{A5.7a}$$

$$\left.\frac{C_{k,k+1}}{\varepsilon}\right|_{k=1\text{ to }n-1}=\frac{376.7}{\sqrt{\varepsilon_r}}hY_A\left(\frac{J_{k,k+1}}{Y_A}\right) \tag{A5.7b}$$

$$\frac{C_{n,n+1}}{\varepsilon}=\frac{376.7}{\sqrt{\varepsilon_r}}\left[M_n-Y_A\right] \tag{A5.7c}$$

By substitution of parameters C_{34}, C_4 and C_{45} from equations (A5.6) and (A5.7) into equation (A5.5), *h* could be solved as

$$K_A=\frac{376.7}{\sqrt{\varepsilon_r}}\left[2Y_A\left(\frac{J_{34}}{Y_A}\right)\right]+$$

$$+\frac{376.7}{\sqrt{\varepsilon_r}}Y_A\left[N_{34}+N_{45}-\left(\frac{J_{34}}{Y_A}\right)-\left(\frac{J_{45}}{Y_A}\right)\right]+\frac{376.7}{\sqrt{\varepsilon_r}}\left[2Y_A\left(\frac{J_{45}}{Y_A}\right)\right] \tag{A5.8}$$

$$\therefore h=5.4/K_A=0.0751 \tag{A5.9}$$

Now that *h* has been found, it is possible to compute the values in equation A5.4, as

M_1	0.0250
M_2	0.0250

Table A5.3: Computed M_1 and M_8 filter quantities.

Computation of equations (A5.6) and (A5.7) using all the above defined parameters, yields

C_0/ε	5.6405
C_1/ε	2.9380
C_2/ε	4.0531
C_3/ε	4.1597
C_4/ε	4.1778
C_5/ε	4.1778
C_6/ε	4.1597
C_7/ε	4.0531
C_8/ε	2.9380
C_9/ε	5.6406

Table A5.4: Computed C_k/ε filter quantities.

C_{01}/ε	1.8935
C_{12}/ε	0.4334
C_{23}/ε	0.3247
C_{34}/ε	0.3073
C_{45}/ε	0.3038
C_{56}/ε	0.3073
C_{67}/ε	0.3247
C_{78}/ε	0.4334
C_{89}/ε	1.8934

Table A5.5: Computed $C_{k,k+1}/\varepsilon$ filter quantities.

A convenient t/b ratio can now be defined (refer to figure A5.2). Using a thickness, $t = 4.7$ mm and height, $b = 12$ mm, for aluminium is practical. This yields a convenient t/b ratio of ~ 0.4. Using Getsinger's chart [5], shown in figure A5.3, and the mutual (inter-bar) capacitances in table A5.5 for rectangular bars (denoted as $\Delta C/\varepsilon$), it is possible to determine the inter-bar spacings, from the s/b ratios. This is shown in table A5.6. Table A5.6 also includes the normalised even-mode fringing capacitances, C'_{fe}/ε, which are derived from the same chart, shown in figure A5.3.

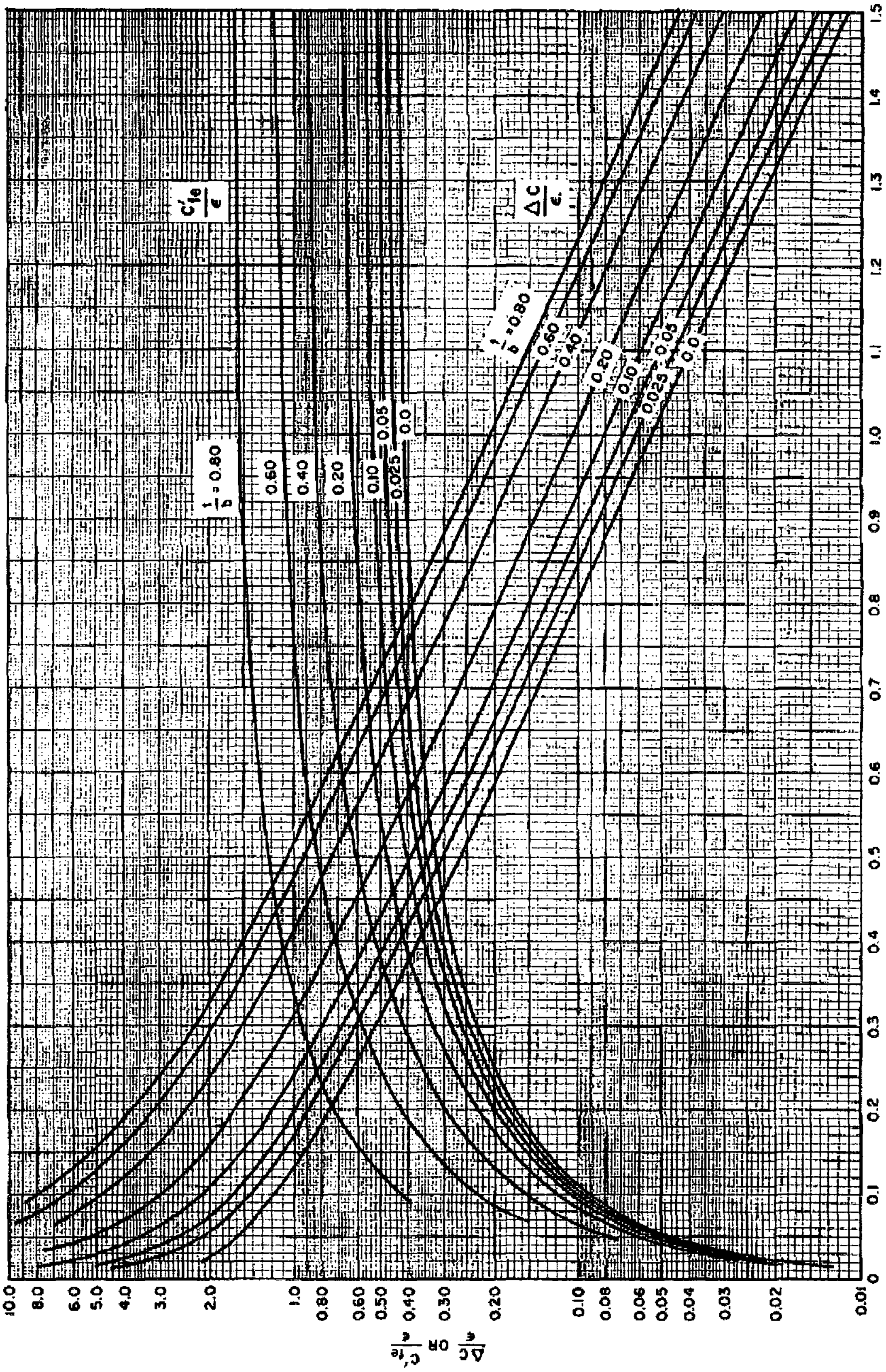

Figure A5.3: Fringing capacitances for coupled rectangular bars [5].

Spacing (k, k+1)	$\Delta C/\varepsilon$	s/b	S (mm)	$C'_{fe(k,k+1)}/\varepsilon$
01	1.8935	0.2460	2.9520	0.3480
12	0.4334	0.6570	7.8840	0.7030
23	0.3247	0.7470	8.9640	0.7500
34	0.3073	0.7670	9.2040	0.7600
45	0.3038	0.7690	9.2280	0.7610
56	0.3073	0.7670	9.2040	0.7600
67	0.3247	0.7470	8.9640	0.7500
78	0.4334	0.6570	7.8840	0.7030
89	1.8934	0.2460	2.9520	0.3480

Table A5.6: Filter inter-bar spacing, S, and C'_{fe}/ε values based on figure A5.3.

It should be noted that the inter-bar spacing, S, shown in table A5.6 represents the computed values according to the aforementioned equations. However, according to [1], a reduction of ~ 20% in the inter-bar spacing was applied to alter the coupling between the terminations and the first resonator on each end of the filter. This resulted in a reduction in the VSWR across the whole band which would correspond to smaller ripples in the pass-band. Therefore, these corrections were applied to the 8-pole inter-digital filter discussed here.

Another parameter which should be defined before working out the widths of the rectangular bars (resonators), is the fringing capacitance, C'_f/ε, for an isolated bar. From Getsinger's chart (figure A5.4), this is shown to be 0.905 for a t/b value of ~ 0.4. The width of the rectangular bars is given by [1, 2]

$$\frac{w_k}{b}=\frac{1}{2}\left(1-\left(\frac{t}{b}\right)\right)\left[\frac{1}{2}\left(\frac{C_k}{\varepsilon}\right)-\left(\frac{C'_f}{\varepsilon}\right)-\left(\frac{C'_{fe(k,k+1)}}{\varepsilon}\right)\right]\Bigg|_{k=0 \text{ or } k=n+1} \qquad \text{(A5.10a)}$$

$$\frac{w_k}{b}=\frac{1}{2}\left(1-\left(\frac{t}{b}\right)\right)\left[\frac{1}{2}\left(\frac{C_k}{\varepsilon}\right)-\left(\frac{C'_{fe(k-1,k)}}{\varepsilon}\right)-\left(\frac{C'_{fe(k,k+1)}}{\varepsilon}\right)\right]\Bigg|_{k=1 \text{ to } n} \qquad \text{(A5.10b)}$$

The computed bar widths are shown in table A5.7. It should be notes that in case the width of the bars is too small (i.e. $w_k/b \leq 0.35(1-t/b)$), an empirical correction formula is provided in [1, 2]

$$\frac{w'}{b}=\frac{0.07\left(1-\frac{t}{b}\right)+\frac{w}{b}}{1.2} \qquad \text{(A5.11)}$$

where *w* is the uncorrected bar width and *w*' is the corrected width.

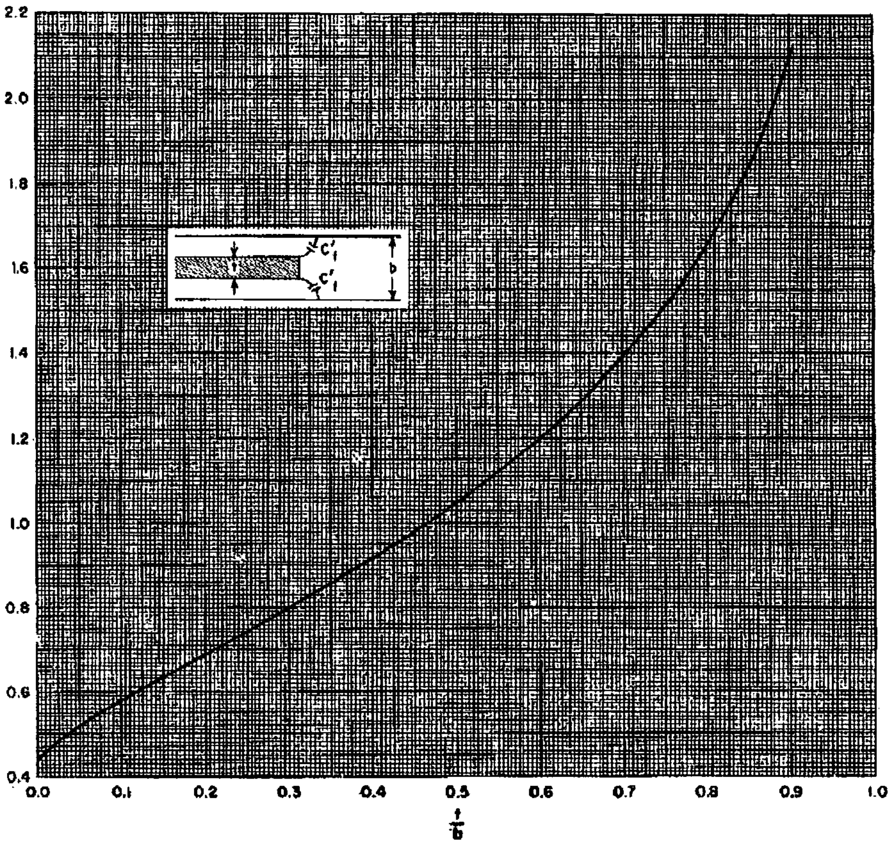

Figure A5.4: Fringing capacitance for an isolated rectangular bar [5].

Element (k)	w_k/b	w_k (mm)	w'_k (mm)
0	0.4767	5.7205	-
1	0.1271	1.5257	1.69727
2	0.1744	2.0934	2.17032
3	0.1733	2.0799	2.15912
4	0.1727	2.0729	2.15327
5	0.1727	2.0729	2.15326
6	0.1733	2.0799	2.15909
7	0.1744	2.0934	2.17031
8	0.1271	1.5258	1.69732
9	0.4767	5.7206	-

Table A5.7: Filter bar width, w_k, and corrected width, w'_k (if required).

The procedures shown here are all approximations of the filter synthesis problem. They are at best a practical solution to the design of inter-digital band-pass filters. When developing these filters, it is often useful to be able to change particularly the spacing between the terminating bar (impedance-transforming sections at each end of the filter) and the first resonator bar. As noted previously, this often reduces the VSWR across the band and therefore allows better matching of the filter ports (to 50 ohms). Also, it is quite sensible to permit the RF signal to typically occupy the middle 80% of the filter band as to avoid high group delay [1].

A5.2 Filter Geometry

A mechanical drawing of the inter-digital band-pass filter is shown in figure A5.5. The filter was made as 3 main pieces, which included 2 different rectangular plates and a centre piece. All the filters were cut on a C & C machine within the school's own mechanical workshop.

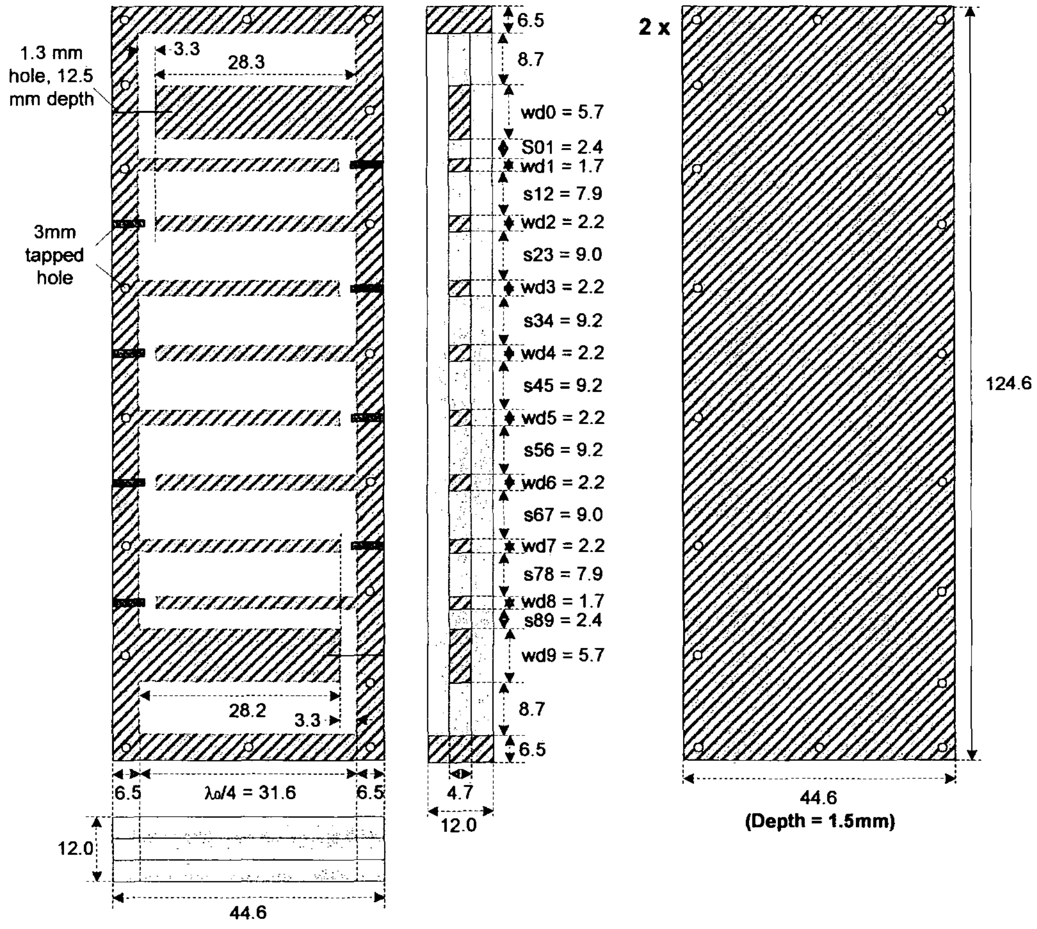

Figure A5.5: Mechanical drawing of inter-digital band-pass filter.

A5.3 MATLAB Program

The following program was written in MATLAB to compute the filter parameters and give the coordinates for the C & C machine.

```
% Design for 8-pole Chebyshev (0.1 dB ripple) bandpass filter
% Change g for other ripple factors and subsequently t, b, Ck_eps,
% Cf_eps, and Cefk_eps. This program is written with minimum number
% of loops for simplicity.

format long;
fc = 2370; % centre frequency in MHz
BW_ideal = 335; % ideal bandwidth in MHz (should not exceed 25%)
CF = 0.07; % correction factor
BW = floor(BW_ideal + CF*BW_ideal); % practical design bandwith
w = BW/fc; % fractional bandwidth
if w >= 0.25 disp('Bandwidth is too large'); end;

f1 = fc - BW/2;
f2 = fc + BW/2;
disp(sprintf('\nCentre frequency = %d MHz, bandwidth = %d MHz',fc,BW));
disp(sprintf('\nFractional bandwidth = %0.3f\n',w));

% Normalisation & filter selection
VSWR = 1.36; % required for 16 dB RL
RL = (VSWR - 1)/(VSWR + 1);
lamda = 3e8/(fc*1e6);
% For filter selection look at Zverev page 84
BW_40dB = 420; % stopband bandwidth
As = BW_40dB/BW; % steepness factor = BW_40dB/BW_3dB
n = 8;
Q = round(fc/BW); % selectivity factor
disp(sprintf('\n... 0.1 dB ripple Chebyshev with %d poles, Q = %d ...',n,Q));
disp(sprintf('\nReturn Loss = %0.2f dB (VSWR = %0.2f)',20*log10(RL),VSWR));

% 0.1 dB Chebyshev pole locations (8th order)
% Williams 3rd Ed., page 11.19 (not required for calculations)
P = [0.3058 0.1952i; 0.2592 0.5558i; 0.1732 0.8319i; 0.0608 0.9812i];

% basic constants, Matthaei, Young, and Jones
er = 1;
phi1 = (pi/2)*(1 - w/2);
YA = 0.020; % mho, terminating line admittance (= 1/ZA = 1/50ohms)
g0 = 1; w1 = 1;
g = [1.1897 1.4346 2.1199 1.6010 2.1699 1.5640 1.9444 0.8778 1.3554];
% g is the element values for normalised Chebyshev (g(0)=1, w1'=1)
% Matthaei, Young, and Jones, page 100.

% Design parameters
J01 = YA/sqrt(g0*g(1)*w1);
J12 = YA/(w1*sqrt(g(1)*g(2)));
J23 = YA/(w1*sqrt(g(2)*g(3)));
J34 = YA/(w1*sqrt(g(3)*g(4)));
J45 = YA/(w1*sqrt(g(4)*g(5)));
J56 = YA/(w1*sqrt(g(5)*g(6)));
J67 = YA/(w1*sqrt(g(6)*g(7)));
J78 = YA/(w1*sqrt(g(7)*g(8)));
```

```
J89 = YA/(w1*sqrt(g(8)*g(9)));
% [J01 J12 J23 J34 J45 J56 J67 J78 J89]'/YA

N12 = sqrt((J12/YA).^2 + ((tan(phi1)).^2)/4);
N23 = sqrt((J23/YA).^2 + ((tan(phi1)).^2)/4);
N34 = sqrt((J34/YA).^2 + ((tan(phi1)).^2)/4);
N45 = sqrt((J45/YA).^2 + ((tan(phi1)).^2)/4);
N56 = sqrt((J56/YA).^2 + ((tan(phi1)).^2)/4);
N67 = sqrt((J67/YA).^2 + ((tan(phi1)).^2)/4);
N78 = sqrt((J78/YA).^2 + ((tan(phi1)).^2)/4);

% calculation of h (dimensionless admittance scale factor
% ref: formula 11 in Matthaei, "Interdigital Band-Pass Filters",
% IRE Trans. Microwave Theory and Techniques, November 1962.
% for n = 8, k = n/2 = 4:
A = 2*(376.7*YA*(J34/YA)/sqrt(er)) + ((376.7/sqrt(er))*YA*(N34 + N45 ...
   - (J34/YA) - (J45/YA))) + 2*(376.7*YA*(J45/YA)/sqrt(er));
h = 5.4/A; % this is a factor that can be treated as a design variable
%h = 0.088; % practical scaling. If h changes, then change mutual Capacitances
disp(sprintf('\nDimensionless admittance scale factor: h = %0.3f',h));

M1 = YA*[(J01/YA)*sqrt(h) + 1];
M8 = YA*[(J89/YA)*sqrt(h) + 1];

% Calculations of element capacitances - refer to fig 7 in Matthaei paper
% Normalised self capacitances Ck/eps per unit length (line elements)
C0_eps = (376.7/sqrt(er))*[2*YA - M1];
C1_eps = (376.7/sqrt(er))*[YA - M1 + h*YA*((tan(phi1))/2 + (J01/YA).^2 ...
   + N12 - (J12/YA))];
C2_eps = (376.7*h*YA/sqrt(er))*[N12 + N23 - (J12/YA) - (J23/YA)];
C3_eps = (376.7*h*YA/sqrt(er))*[N23 + N34 - (J23/YA) - (J34/YA)];
C4_eps = (376.7*h*YA/sqrt(er))*[N34 + N45 - (J34/YA) - (J45/YA)];
C5_eps = (376.7*h*YA/sqrt(er))*[N45 + N56 - (J45/YA) - (J56/YA)];
C6_eps = (376.7*h*YA/sqrt(er))*[N56 + N67 - (J56/YA) - (J67/YA)];
C7_eps = (376.7*h*YA/sqrt(er))*[N67 + N78 - (J67/YA) - (J78/YA)];
C8_eps = (376.7/sqrt(er))*[YA - M8 + h*YA*((tan(phi1))/2 + (J89/YA).^2 ...
   + N78 - (J78/YA))];
C9_eps = (376.7/sqrt(er))*[2*YA - M8];
% [C0_eps C1_eps C2_eps C3_eps C4_eps C5_eps C6_eps C7_eps C8_eps C9_eps]'

% Normalised mutual capacitances Ck/eps per unit length (adjacent lines)
C01_eps = (376.7/sqrt(er))*[M1 - YA];
C12_eps = (376.7*h*YA/sqrt(er))*(J12/YA);
C23_eps = (376.7*h*YA/sqrt(er))*(J23/YA);
C34_eps = (376.7*h*YA/sqrt(er))*(J34/YA);
C45_eps = (376.7*h*YA/sqrt(er))*(J45/YA);
C56_eps = (376.7*h*YA/sqrt(er))*(J56/YA);
C67_eps = (376.7*h*YA/sqrt(er))*(J67/YA);
C78_eps = (376.7*h*YA/sqrt(er))*(J78/YA);
C89_eps = (376.7/sqrt(er))*[M8 - YA];
Mutual_Interbar_Capacitances = ...
   [C01_eps C12_eps C23_eps C34_eps C45_eps C56_eps C67_eps C78_eps C89_eps]'

% Choosing the t/b curve to be ~0.4 (from Matthaei, Young, and Jones)
t = 4.7; b = 12; % dimensions in mm
disp(sprintf('\nt = %0.1f mm, b = %0.1f mm, t/b = %0.2f mm\n',t,b,t/b));

% Using Getsinger's chart and the mutual (interbar) capacitances for
% rectangular bars we can calculate the s/b ratio (assuming b = 12mm).
% Figure 3, Getsinger, "Coupled Rectangular Bars Between Parallel Plates",
```

```
% IRE Trans. Microwave Theory and Techniques, January 1962.

% after looking up the s/b values, we can determine the bar spacings
disp('... Using Getsingers data values (from graph) ... ');
s01 = 0.246*b;
s12 = 0.657*b;
s23 = 0.747*b;
s34 = 0.767*b;
s45 = 0.769*b;
s56 = 0.767*b;
s67 = 0.747*b;
s78 = 0.657*b;
s89 = 0.246*b;

% according to Matthaei, Young and Jones, page 622, a reduction of ~20%
% in spacing was applied to alter the coupling between the terminations
% and the first resonator on each end. This reduces the VSWR across the
% whole band which is necessary for smaller ripples in the passband
shim = s01*0.2;
s01 = s01 - shim; % practical reduction in the spacings
s89 = s89 - shim;

% from the same graph, the normalised even-mode fringing capacitances are:
Cfe01_eps = 0.348;
Cfe12_eps = 0.703;
Cfe23_eps = 0.750;
Cfe34_eps = 0.760;
Cfe45_eps = 0.761;
Cfe56_eps = 0.760;
Cfe67_eps = 0.750;
Cfe78_eps = 0.703;
Cfe89_eps = 0.348;

Cf_eps = 0.905; % from figure 5 in Getsinger's paper (reading off t/b value)
% this is the normalised fringing capacitance for the bars at each end

% from the above parameters we determine the rectangular bar widths
wd0_b = (1/2)*(1-t/b)*(0.5*C0_eps - Cf_eps - Cfe01_eps);
wd1_b = (1/2)*(1-t/b)*(0.5*C1_eps - Cfe01_eps - Cfe12_eps);
wd2_b = (1/2)*(1-t/b)*(0.5*C2_eps - Cfe12_eps - Cfe23_eps);
wd3_b = (1/2)*(1-t/b)*(0.5*C3_eps - Cfe23_eps - Cfe34_eps);
wd4_b = (1/2)*(1-t/b)*(0.5*C4_eps - Cfe34_eps - Cfe45_eps);
wd5_b = (1/2)*(1-t/b)*(0.5*C5_eps - Cfe45_eps - Cfe56_eps);
wd6_b = (1/2)*(1-t/b)*(0.5*C6_eps - Cfe56_eps - Cfe67_eps);
wd7_b = (1/2)*(1-t/b)*(0.5*C7_eps - Cfe67_eps - Cfe78_eps);
wd8_b = (1/2)*(1-t/b)*(0.5*C8_eps - Cfe78_eps - Cfe89_eps);
wd9_b = (1/2)*(1-t/b)*(0.5*C9_eps - Cf_eps - Cfe89_eps);

% wd0_b = wd0_b + shim/b; % Empirical correction from decreasing s01 & s89
% wd9_b = wd9_b + shim/b;

cor = input('\nDo you want to apply bar correction (1==Yes, 2==No): \n\nAnswer = ');
if cor == 1
  if wd0_b < 0.35*(1-t/b)
    wd0_b = (0.07*(1-t/b)+wd0_b)/1.2; % Correction in Matthaei
    val = wd0_b/(1-t/b);
    disp(sprintf('\nCorrection for bar 0,(w/b)/(1-t/b) = %0.3f',val));
  end
  if wd1_b < 0.35*(1-t/b)
    wd1_b = (0.07*(1-t/b)+wd1_b)/1.2; % Correction in Matthaei
```

```
        val = wd1_b/(1-t/b);
        disp(sprintf('Correction for bar 1,(w/b)/(1-t/b) = %0.3f',val));
    end
    if wd2_b < 0.35*(1-t/b)
        wd2_b = (0.07*(1-t/b)+wd2_b)/1.2; % Correction in Matthaei
        val = wd2_b/(1-t/b);
        disp(sprintf('Correction for bar 2,(w/b)/(1-t/b) = %0.3f',val));
    end
    if wd3_b < 0.35*(1-t/b)
        wd3_b = (0.07*(1-t/b)+wd3_b)/1.2; % Correction in Matthaei
        val = wd3_b/(1-t/b);
        disp(sprintf('Correction for bar 3,(w/b)/(1-t/b) = %0.3f',val));
    end
    if wd4_b < 0.35*(1-t/b)
        wd4_b = (0.07*(1-t/b)+wd4_b)/1.2; % Correction in Matthaei
        val = wd4_b/(1-t/b);
        disp(sprintf('Correction for bar 4,(w/b)/(1-t/b) = %0.3f',val));
    end
    if wd5_b < 0.35*(1-t/b)
        wd5_b = (0.07*(1-t/b)+wd5_b)/1.2; % Correction in Matthaei
        val = wd5_b/(1-t/b);
        disp(sprintf('Correction for bar 5,(w/b)/(1-t/b) = %0.3f',val));
    end
    if wd6_b < 0.35*(1-t/b)
        wd6_b = (0.07*(1-t/b)+wd6_b)/1.2; % Correction in Matthaei
        val = wd6_b/(1-t/b);
        disp(sprintf('Correction for bar 6,(w/b)/(1-t/b) = %0.3f',val));
    end
    if wd7_b < 0.35*(1-t/b)
        wd7_b = (0.07*(1-t/b)+wd7_b)/1.2; % Correction in Matthaei
        val = wd7_b/(1-t/b);
        disp(sprintf('Correction for bar 7,(w/b)/(1-t/b) = %0.3f',val));
    end
    if wd8_b < 0.35*(1-t/b)
        wd8_b = (0.07*(1-t/b)+wd8_b)/1.2; % Correction in Matthaei
        val = wd8_b/(1-t/b);
        disp(sprintf('Correction for bar 8,(w/b)/(1-t/b) = %0.3f',val));
    end
    if wd9_b < 0.35*(1-t/b)
        wd9_b = (0.07*(1-t/b)+wd9_b)/1.2; % Correction in Matthaei
         val = wd9_b/(1-t/b);
        disp(sprintf('Correction for bar 9,(w/b)/(1-t/b) = %0.3f\n',val));
    end
else
    disp('  ');
    disp('No bar correction applied');
end

w_e = 6.5;
W = [wd0_b*b wd1_b*b wd2_b*b wd3_b*b wd4_b*b wd5_b*b wd6_b*b wd7_b*b...
    wd8_b*b wd9_b*b]'
s_s = 7.5 + 1.1639; % Standard spacing plus practical value
S = [s01 s12 s23 s34 s45 s56 s67 s78 s89]'
width_t = (lamda/4)*1e3 + 2*w_e;
length_t = sum(W) + sum(S) + 2*w_e + 2*s_s;
c_w = width_t/2; c_l = length_t/2;
res = (lamda/4)*1e3;
res_gap = 0.1*res;
% res_gap = (res - 0.12*res)*0.12; % ~12% of actual resonator length
real_scale_factor = 2*C34_eps + C4_eps + 2*C45_eps;
```

```
disp(sprintf('\nReal scale factor = %0.3f (relative to 5.4)\n',...
   real_scale_factor));

disp(sprintf('\nWidth edge = %0.1f mm, resonator start gap = %0.1f mm',...
   w_e,s_s));
disp(sprintf('\nTotal width = %0.4f mm, total length = %0.4f mm',...
   width_t,length_t));
disp(sprintf('\nResonator (lamda/4) = %0.4f mm, resonator gap = %0.4f mm',...
   res,res_gap));
disp(sprintf('\nCentre width = %0.4f mm, centre length = %0.4f mm\n',c_w,c_l));

format short
Spacing_Centres = [w_e+s_s/2; w_e+s_s+W(1)+S(1)/2;w_e+s_s+W(1)+...
   S(1)+W(2)+S(2)/2; w_e+s_s+W(1)+S(1)+W(2)+S(2)+W(3)+S(3)/2;...
   w_e+s_s+W(1)+S(1)+W(2)+S(2)+W(3)+S(3)+W(4)+S(4)/2; w_e+s_s+...
   W(1)+S(1)+W(2)+S(2)+W(3)+S(3)+W(4)+S(4)+W(5)+S(5)/2; w_e+s_s+...
   W(1)+S(1)+W(2)+S(2)+W(3)+S(3)+W(4)+S(4)+W(5)+S(5)+W(6)+S(6)/2;...
   w_e+s_s+W(1)+S(1)+W(2)+S(2)+W(3)+S(3)+W(4)+S(4)+W(5)+S(5)+...
   W(6)+S(6)+W(7)+S(7)/2; w_e+s_s+W(1)+S(1)+W(2)+S(2)+W(3)+S(3)+...
   W(4)+S(4)+W(5)+S(5)+W(6)+S(6)+W(7)+S(7)+W(8)+S(8)/2; w_e+s_s+...
   W(1)+S(1)+W(2)+S(2)+W(3)+S(3)+W(4)+S(4)+W(5)+S(5)+W(6)+S(6)+...
   W(7)+S(7)+W(8)+S(8)+W(9)+S(9)/2;w_e+s_s+W(1)+S(1)+W(2)+S(2)+...
   W(3)+S(3)+W(4)+S(4)+W(5)+S(5)+W(6)+S(6)+W(7)+S(7)+W(8)+S(8)+...
   W(9)+S(9)+W(10)+s_s/2]

Bar_Centres = [w_e+s_s+W(1)/2; w_e+s_s+W(1)+S(1)+W(2)/2; w_e+s_s+...
   W(1)+S(1)+W(2)+S(2)+W(3)/2; w_e+s_s+W(1)+S(1)+W(2)+S(2)+W(3)+...
   S(3)+W(4)/2; w_e+s_s+W(1)+S(1)+W(2)+S(2)+W(3)+S(3)+W(4)+S(4)+...
   W(5)/2; w_e+s_s+W(1)+S(1)+W(2)+S(2)+W(3)+S(3)+W(4)+S(4)+W(5)+...
   S(5)+W(6)/2; w_e+s_s+W(1)+S(1)+W(2)+S(2)+W(3)+S(3)+W(4)+S(4)+...
   W(5)+S(5)+W(6)+S(6)+W(7)/2; w_e+s_s+W(1)+S(1)+W(2)+S(2)+W(3)+...
   S(3)+W(4)+S(4)+W(5)+S(5)+W(6)+S(6)+W(7)+S(7)+W(8)/2; w_e+s_s+...
   W(1)+S(1)+W(2)+S(2)+W(3)+S(3)+W(4)+S(4)+W(5)+S(5)+W(6)+S(6)+...
   W(7)+S(7)+W(8)+S(8)+W(9)/2; w_e+s_s+W(1)+S(1)+W(2)+S(2)+W(3)+...
   S(3)+W(4)+S(4)+W(5)+S(5)+W(6)+S(6)+W(7)+S(7)+W(8)+S(8)+W(9)+...
   S(9)+W(10)/2]
```

A5.4 Anilam Program

Once the filter parameters were defined in MATLAB, they were verified with Solid Works CAD package. Finally a program was written in Anilam (m program) to control the cutting of the filters on the C & C machine with 4 separate tool changes. This program (see below) instructs the machine on the length, width and depth to be removed from the aluminium slab.

```
Dim Abs
Tool# 1
Feed 100.0
RectPock   XCenter 22.6556 YCenter 22.27 StartHgt 3.000 Length 2.3616 Width 31.54 ZDepth -4.700
Ccw DepthCut 0.500 FinStock 0.100
RectPock   XCenter 102.7091 YCenter 22.27 StartHgt 3.000 Length 2.3616 Width 31.54 ZDepth -
4.700 Ccw DepthCut 0.500 FinStock 0.100
Rapid      Z 20.000
```

```
Rapid    X 300.000
Rapid    Z 64.400
Tool# 2
Feed 200.0
RectPock   XCenter 10.83190 YCenter 22.27 StartHgt 3.000 Length 8.6639 Width 31.54 ZDepth -
4.700 Ccw DepthCut 0.500 FinStock 0.100
RectPock   XCenter 114.5328 YCenter 22.27 StartHgt 3.000 Length 8.6639 Width 31.54 ZDepth -
4.700 Ccw DepthCut 0.500 FinStock 0.100
RectPock   XCenter 29.4756 YCenter 22.27 StartHgt 3.000 Length 7.884 Width 31.54 ZDepth -4.700
Ccw DepthCut 0.500 FinStock 0.100
RectPock   XCenter 95.8890 YCenter 22.27 StartHgt 3.000 Length 7.884 Width 31.54 ZDepth -4.700
Ccw DepthCut 0.500 FinStock 0.100
RectPock   XCenter 40.0700 YCenter 22.27 StartHgt 3.000 Length 8.964 Width 31.54 ZDepth -4.700
Ccw DepthCut 0.500 FinStock 0.100
RectPock   XCenter 85.2947 YCenter 22.27 StartHgt 3.000 Length 8.964 Width 31.54 ZDepth -4.700
Ccw DepthCut 0.500 FinStock 0.100
RectPock   XCenter 51.3131 YCenter 22.27 StartHgt 3.000 Length 9.204 Width 31.54 ZDepth -4.700
Ccw DepthCut 0.500 FinStock 0.100
RectPock   XCenter 74.0516 YCenter 22.27 StartHgt 3.000 Length 9.204 Width 31.54 ZDepth -4.700
Ccw DepthCut 0.500 FinStock 0.100
RectPock   XCenter 62.6823 YCenter 22.27 StartHgt 3.000 Length 9.228 Width 31.54 ZDepth -4.700
Ccw DepthCut 0.500 FinStock 0.100
Rapid    Z 20.000
Rapid    X 300.000
Rapid    Z 89.346
Tool# 3
Feed 150.0
RectPock   XCenter 17.8193 YCenter 8.03 StartHgt 3.000 Length 9.600 Width 3.06 ZDepth -4.700
Ccw DepthCut 0.500 FinStock 0.100
RectPock   XCenter 25.1850 YCenter 36.51 StartHgt 3.000 Length 7.000 Width 3.06 ZDepth -4.700
Ccw DepthCut 0.500 FinStock 0.100
RectPock   XCenter 34.5028 YCenter 8.03 StartHgt 3.000 Length 9.000 Width 3.06 ZDepth -4.700
Ccw DepthCut 0.500 FinStock 0.100
RectPock   XCenter 45.6315 YCenter 36.51 StartHgt 3.000 Length 9.000 Width 3.06 ZDepth -4.700
Ccw DepthCut 0.500 FinStock 0.100
RectPock   XCenter 56.9917 YCenter 8.03 StartHgt 3.000 Length 9.000 Width 3.06 ZDepth -4.700
Ccw DepthCut 0.500 FinStock 0.100
RectPock   XCenter 68.3730 YCenter 36.51 StartHgt 3.000 Length 9.000 Width 3.06 ZDepth -4.700
Ccw DepthCut 0.500 FinStock 0.100
RectPock   XCenter 79.7331 YCenter 8.03 StartHgt 3.000 Length 9.000 Width 3.06 ZDepth -4.700
Ccw DepthCut 0.500 FinStock 0.100
RectPock   XCenter 90.8618 YCenter 36.51 StartHgt 3.000 Length 9.000 Width 3.06 ZDepth -4.700
Ccw DepthCut 0.500 FinStock 0.100
RectPock   XCenter 100.1797 YCenter 8.03 StartHgt 3.000 Length 7.000 Width 3.06 ZDepth -4.700
Ccw DepthCut 0.500 FinStock 0.100
RectPock   XCenter 107.5454 YCenter 36.51 StartHgt 3.000 Length 9.600 Width 3.06 ZDepth -4.700
Ccw DepthCut 0.500 FinStock 0.100
Rapid    Z 20.000
Rapid    X 300.000
Rapid    Z 68.595
Tool# 4
PeckDrill  ZDepth -11.000 StartHgt 3.000 ReturnHgt 25.000 Peck 1.000
Rapid    X 3.250 Y 3.250
Rapid    X 3.250 Y 22.27
Rapid    X 3.250 Y 41.26
Rapid    X 18.3193 Y 41.26
Rapid    X 34.5028 Y 41.26
Rapid    X 56.9917 Y 41.26
Rapid    X 79.7331 Y 41.26
Rapid    X 95.8890 Y 41.26
```

```
Rapid    X 122.1100 Y 41.26
Rapid    X 122.1100 Y 22.27
Rapid    X 122.1100 Y 3.250
Rapid    X 107.0454 Y 3.250
Rapid    X 90.8618 Y 3.250
Rapid    X 68.3730 Y 3.250
Rapid    X 45.6315 Y 3.250
Rapid    X 29.4756 Y 3.250
DrillOff
Rapid    Z 20.000
Rapid    X 300.000
Rapid    Z 57.851
* Tool# 2
* Feed 200.0
* RectPock   XCenter 62.6824 YCenter 22.27 StartHgt 2.000 Length 112.3648 Width 31.54 ZDepth -
3.830 Ccw DepthCut 1.500 FinStock 0.100
* Rapid    Z 20.000
* Rapid    X 300.000
* Rapid    Z 89.346
* Tool# 4
* PeckDrill  ZDepth -3.500 StartHgt 3.000 ReturnHgt 25.000 Peck 1.000 Feed 40.0
* Rapid    X 24.6850 Y 2.350
* Rapid    X 45.6315 Y 2.350
* Rapid    X 68.3730 Y 2.350
* Rapid    X 90.8618 Y 2.350
* Rapid    X 100.9654 Y 2.350
* Rapid    X 107.0454 Y 2.350
Rapid    X 113.1254 Y 2.350
DrillOff
Rapid    X 300.000
Rapid    Z 57.851
EndMain
```

A5.5 Filter Rejection

The primary purpose of the filters was to reduce the interference from the UMTS-FDD downlink band. Figure A5.6 shows this band measured on an Agilent E4407B Analyzer (with 28 dB input gain) within the School of Engineering, University of Durham. Here, at least 3 operators are visible.

Figure A5.7 shows the measured nominal response of an inter-digital filter made within the school. The characteristic behaviour of the filter, in particular the bandwidth and the centre frequency match the design parameters defined at the start of this section. Here the blue curve shows the transmission across the filter and the red curve denotes the return-loss performance. The return-loss characteristics could be improved; however the limitations inherent in machining these filters mean that there are errors in the cutting parameters, which ultimately result in mismatches. Most importantly, the filters provide more than 30 dB of rejection in the downlink band.

Figure A5.6: Spectrum plot of UMTS-FDD downlink band for indoor environment.

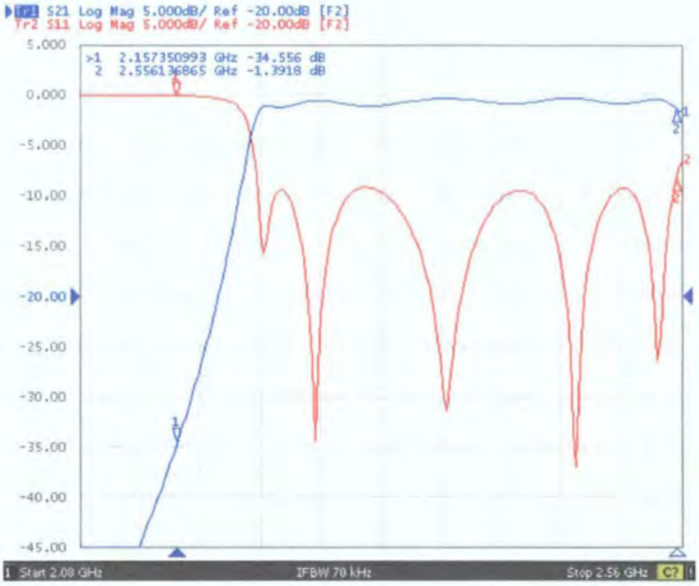

Figure A5.7: Inter-digital band-pass filter response.

A5.6 References

1. G. Matthaei, L. Young, E.M.T. Jones, *Microwave Filters, Impedance-matching Networks, and Coupling Structures*. Norwood: Artech House, 1980.
2. G. L. Matthaei, "Interdigital Band-Pass Filters," *IEEE Transactions on Microwave Theory and Techniques*, vol. 10, pp. 479-491, 1962.

3. A. B. Williams, F. J. Taylor, *Electronic Filter Design Handbook*, 3 ed: McGraw-Hill, 1995.
4. A. I. Zverev, *Handbook of Filter Synthesis*: John Wiley & Sons, 1967.
5. W. J. Getsinger, "Coupled Rectangular Bars Between Parallel Plates," *IEEE Transactions on Microwave Theory and Techniques*, vol. 10, pp. 65 - 72, 1962.

Appendix 6

PLL Synthesisers

A6.1 PLL Synthesisers

The block diagram of a basic PLL (phase-locked loop) synthesiser is shown in figure A6.1. A PLL circuit with a division ratio of N behaves as a frequency multiplier to the reference signal (with frequency f_{ref}).

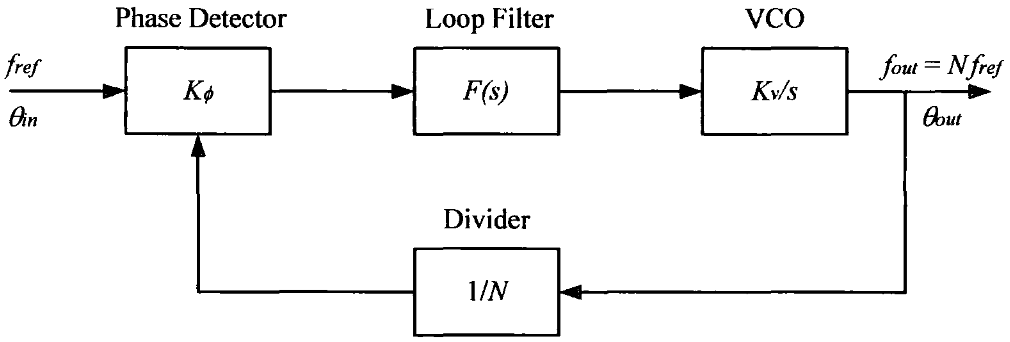

Figure A6.1: Block diagram of Basic PLL synthesiser.

In figure, A6.1, K_v is the VCOs gain factor (sensitivity) in radians/second/volt, K_ϕ is the phase detector gain factor in mA/radians, and $F(s)$ represents the Laplace transform of the filter response in time. Here, the phase detector compares the phase of the reference signal, θ_{in}, against the phase, θ_{out}, of the VCO output and produces a voltage proportional to the difference, θ_{in} - θ_{out}. This voltage is then sent through a loop filter (low-pass filter) to suppress the high frequency ripple and noise. The result is called the error voltage, which is applied to the control input of the VCO in order to adjust its frequency, f_{out}, towards the desired signal (synchronised with the input reference). The division ratio, N, determines the output frequency for a given reference frequency, so that $f_{out} = N \times f_{ref}$.

The design of the loop filter is vital in achieving the desired PLL characteristics, given the transfer functions of the VCO and the phase detector. In general, the loop is required to be stable and should attenuate phase noise contributions from the reference and the VCO. In this loop, noise contributions from the reference are low-pass filtered, while that of the VCO are high-pass filtered. Thus, the optimum loop filter bandwidth is a compromise between suppressing the VCO noise and the reference noise. A third order loop filter (recommended in the SP8855E data sheet) is used in the PLL. The diagram of this circuit is shown in figure A6.2.

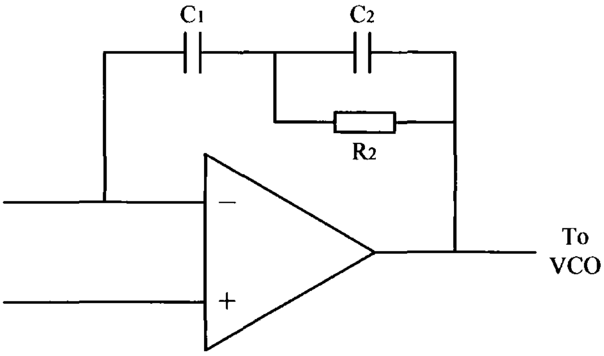

Figure A6.2: Third-order loop filter.

Generally, third-order filter configurations, such as that shown in figure A6.2 give better results than the more commonly used second-order because the reference sidebands are reduced. In order to design this filter, three time-constants of the loop need to be determined, where

$$\tau_1 = C_1 \tag{A6.1}$$

$$\tau_2 = R_2(C_1 + C_2) \tag{A6.2}$$

$$\tau_3 = C_2 R_2 \tag{A6.3}$$

These equations are

$$\tau_1 = \frac{K_\phi K_v}{N\omega_n^2}\left[\frac{1+\omega_n^2\tau_2^2}{1+\omega_n^2\tau_3^2}\right]^{1/2} \tag{A6.4}$$

$$\tau_2 = \frac{1}{\omega_n^2\tau_3} \tag{A6.5}$$

$$\tau_3 = \frac{-\tan\phi_0 + \dfrac{1}{\cos\phi_0}}{\omega_n} \tag{A6.6}$$

where ω_n is the natural loop frequency (bandwidth), and ϕ_0 is the phase margin, which is typically ~ 45°. Here, K_ϕ is represented as the phase comparator current setting in mA/radian, typically given as 6.3mA/2π for the SP8855E synthesiser. The aforementioned formulas need to be solved in reverse order, i.e. $\tau_3 \rightarrow \tau_2 \rightarrow \tau_1$, to find the values of the circuit component C1, C2, and R2 in figure A6.2.

A6.2 Performance Considerations

A variety of factors affect the performance of a PLL synthesiser, namely phase margin, damping and phase noise. The phase margin is generally defined as the difference between 180° and the phase of the open loop transfer function. A larger phase margin corresponds to a more stable PLL loop, however, a larger phase margin also slows the loop response, increases the sidebands at the output, and reduces the noise suppression capability of the VCO [1]. In general a phase margin of ~ 45° seems to provide a good compromise.

The noise sources in a PLL circuit include the phase detector, loop filter, VCO, division counter and the reference signal. In practical circuits, part of the reference source will always leak through the phase detector, resulting in undesirable sidebands due to the frequency modulation. The noise in the loop increases as a function of the division factor, *N*. Therefore, it is preferable to have a low division factor (possible with a higher reference frequency) in order decrease the noise contribution due to the reference and divider.

As noted earlier, the loop acts as a low pass filter against the reference noise, therefore by decreasing the loop filter bandwidth, better reference noise suppression could be achieved. However, a wider loop bandwidth corresponds to a better noise suppression capability for the VCO. Therefore, the optimum loop bandwidth is a compromise between the noise contributions from the VCO and the reference.

The noise contribution of the phase detector acts in the same way as the reference but the contribution is divided by the square of the phase detector gain, $(K_\phi)^2$. The loop filter's noise contribution is also divided by the square of this gain. A higher phase detector gain could be used to minimise the noise contributions of the phase detector and the loop filter.

It should be noted that the phase noise characteristics of the PLL plays a significant role in determining the performance of the sounder such as the instantaneous dynamic range and the measured Doppler resolution. Therefore, it is important to design a synthesiser with good phase noise performance. Analysis of PLL synthesisers is found in numerous books and papers, including [2-5].

A6.3 Synthesiser Design

This section briefly describes the PLL synthesisers implemented for the channel sounder. A total of four synthesisers ere required, two of which operate at 1.6 GHz (DDFS) and the other two provide the source signal for the RF up-converter and down-converter. The design of these PLLs is almost identical, except for the VCOs and loop-filter parameters. The basic block diagram of the PLL using the Zarlink SP8855E synthesiser is shown in figure A6.3. For the DDFS PLLs the Micronetics M3500C-1324T VCO part was used, while the RF PLLs used the M3500C-2032T VCO part.

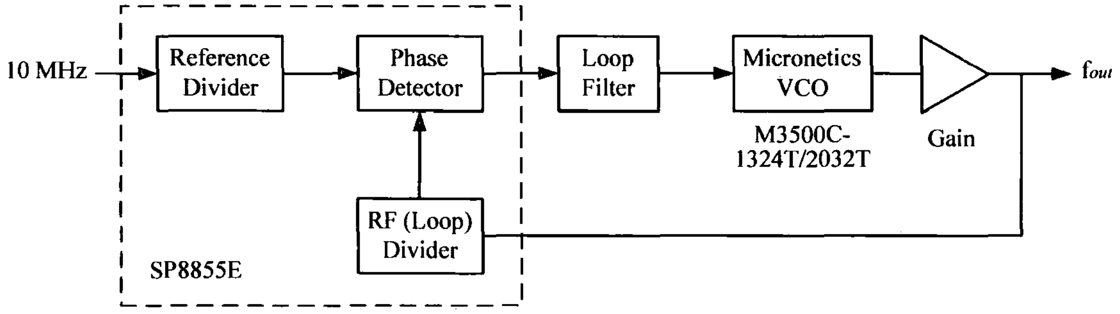

Figure A6.3: Block diagram of PLL synthesiser with 10 MHz reference.

In figure A6.3, the gain block is represented by the Mini-Circuits ERA-5SM monolithic broadband amplifier. This is required to provide a sufficient output signal. The reference is provided by the rubidium and can be either a sine or square wave signal. The SP8855 has a programmable phase detector gain, typically defined as 1 mA/radian (6.3mA/2π). The RF and reference division ratios, the phase detector gain and direction of the loop, can all be set by (parallel) programming switches. Here, a 14-bit word is allocated to set the RF division ratio and a 10-bit word is used for the reference division ratio. The layout of the programming switches, corresponding to the pin numbers are provided in the SP8855E data sheet.

The output of the phase detector is a series of pulses at the reference frequency. Thus, when there is a phase error, the pulse width varies depending on the phase difference. The charge pump circuit in the SP8855E converts these pulses into adjustable current pulses. The current pulses are filtered, amplified, and subsequently fed into the VCO's tuning port in order to reduce the phase error. This is done to achieve phase lock. When the loop is locked, the pulses become very narrow [1]. More detail about the synthesiser operation and programming is given in the application sheet.

Using the PLL design parameters, it is possible to compute the value of the components used in the loop filter. Table A6.1 shows the PLL parameters used for the DDFS PLL, while table A6.2 gives the parameters for the RF PLL.

Synthesised frequency (optimum)	1600 MHz
Reference frequency	10 MHz
RF division ratio	160 (× 2)
Reference division ratio	2
Natural loop frequency, ω_n (optimum)	80 kHz
VCO gain factor, K_v	$2\pi \times 92$ MHz/Volt
Phase margin, ϕ_0	50
Phase comparator current	6.3 mA
Phase detector gain factor, K_ϕ	1 mA

Table A6.1: DDFS PLL parameters used in the loop filter design.

Synthesised frequency (optimum)	2350 MHz
Reference frequency	10 MHz
RF division ratio	235 (× 2)
Reference division ratio	2
Natural loop frequency, ω_n (optimum)	90 kHz
VCO gain factor, K_v	$2\pi \times 115$ MHz/Volt
Phase margin, ϕ_0	50
Phase comparator current	6.3 mA
Phase detector gain factor, K_ϕ	1 mA

Table A6.2: RF PLL parameters used in the loop filter design.

Substituting these values into the filter equations, gives time constants

	τ_1	τ_2	τ_3
DDFS PLL	1.97×10^{-8}	5.47×10^{-6}	7.24×10^{-7}
RF PLL	1.32×10^{-8}	4.86×10^{-6}	6.44×10^{-7}

Table A6.3: Computed loop filter time constants.

The time constants in table A6.3 correspond to the following loop filter components (table A6.4). This table represents the computed components values, while those in the parentheses are the preferred values.

	C_1	C_2	R_2
DDFS PLL	19.7 nF (10 nF || 10 nF)	3.0 nF (1.5 nF || 1.5 nF)	240.8 Ω (240 Ω)
RF PLL	13.2 nF (10 nF || 3.3 nF)	2.0 nF (1 nF || 1 nF)	318.1 Ω (300 Ω + 18 Ω)

Table A6.4: Computed loop filter component values.

A6.4 Construction of PLLs

Each PLL was built as shown in figure A6.4. The main board was places in a metal box, with a fan placed on the lid of the box in order to cool the synthesiser. The 10 MHz reference was provided via the SMC connector and cable shown and the RF (synthesised) output was provided using a SMA connector. The actual unit was provided with 12V, 15V and ground, however the onboard voltage of 5V and 12V was provided by the two regulators. As well as using a high frequency supply filter on board, good grounding was also practiced. The 16-way connector on the board was used to program the synthesiser part (Zarlink SP8855E) with the DIL switches available on the front panel (taking into account the reference division factor.)

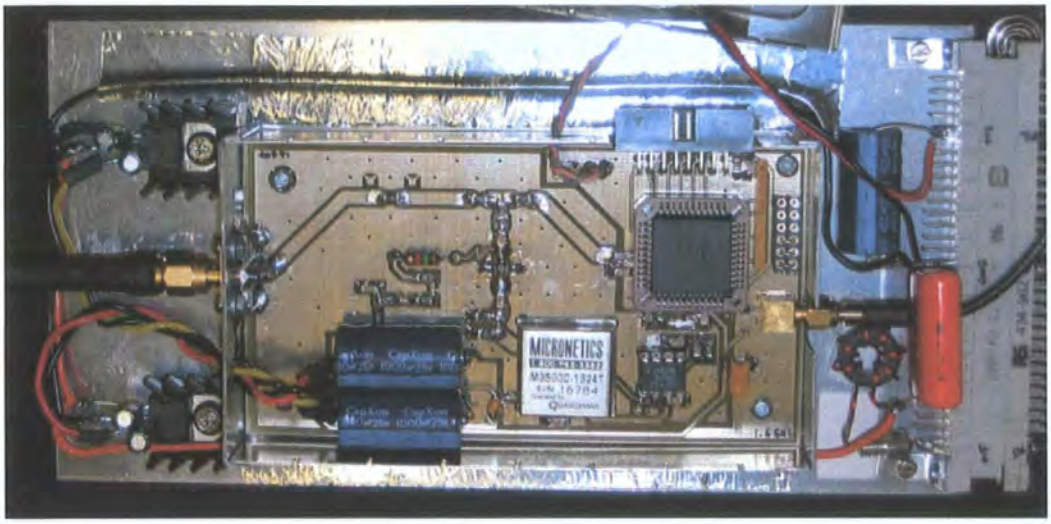

Figure A6.4: PLL synthesiser construction.

A6.5 Phase Noise Performance

It is important to have satisfactory phase noise performance from the PLLs, since this affects the overall system range and resolution. Figures A6.5 and A6.6 show the close-in phase at 1.6 GHz and 2.16 GHz, respectively. Figure A6.7 shows a plot of the measured phase noise on a spectrum analyzer (Agilent E4407B Analyzer) at various offsets from the carrier. Here, the RF PLLs were measured at 2.16 GHz, since this carrier was used for many of the MIMO measurements.

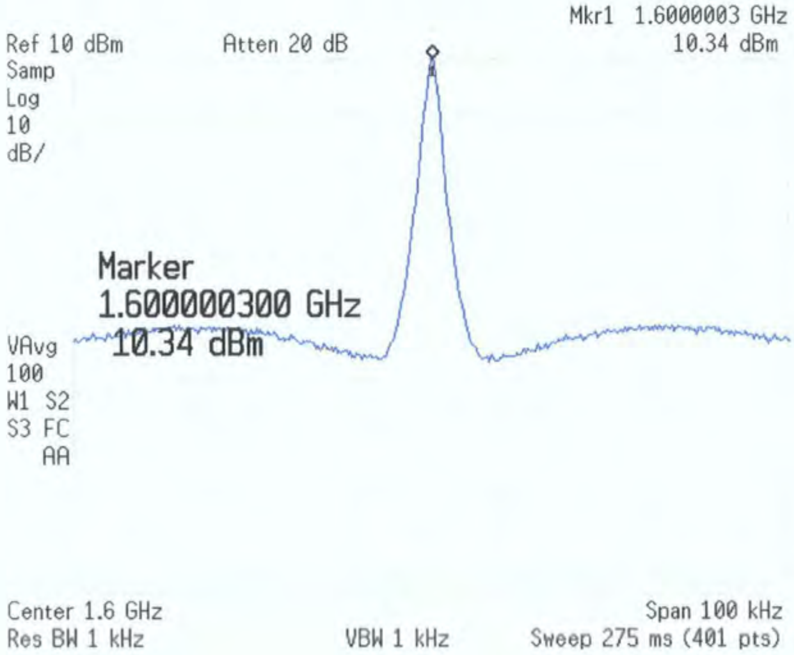

Figure A6.5: DDFS PLL close in phase noise.

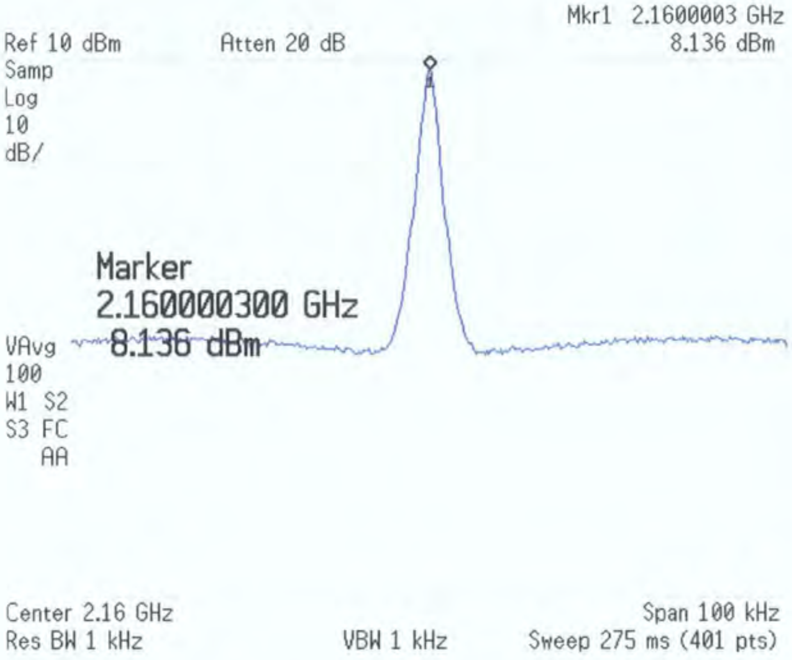

Figure A6.6: RF PLL (2.16 GHz) close in phase noise.

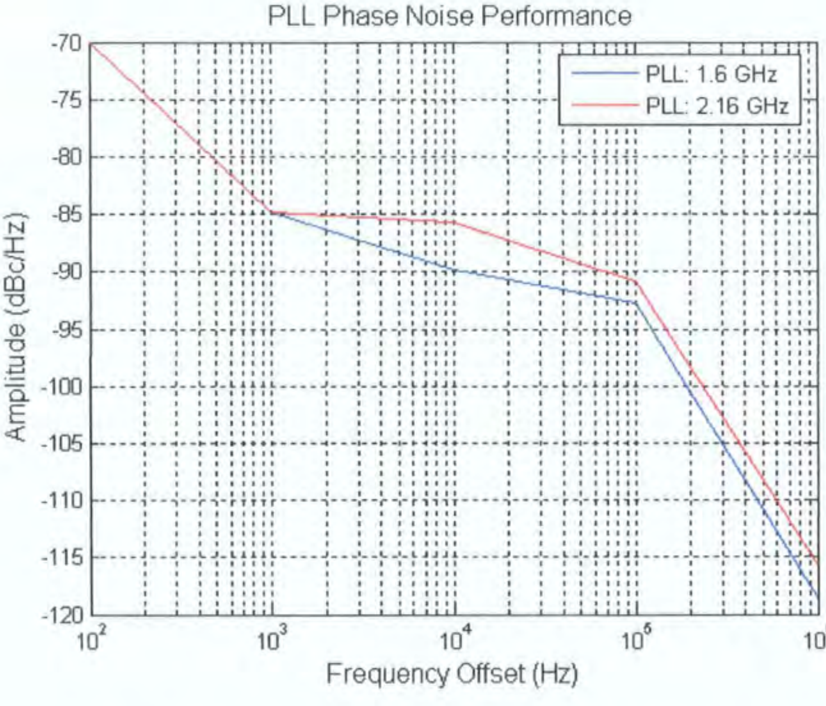

Figure A6.7: Measured PLL phase noise performance.

Figure A6.7 shows that the phase noise at 1 kHz offset from the carrier is -85 dBc/Hz and is less than -90 dBc/Hz at 100 kHz offset. Although these PLLs are more than adequate for the applications mentioned in this chapter, there is certainly room for improvement for future synthesisers and this could be achieved in a number of ways. The most likely way of reducing the phase noise from these synthesisers is to reduce the division ratio. A larger *N* implies that there is greater contribution of reference noise and other noise sources related to this ratio. These synthesisers were built with a reference division ratio of 2 resulting in a reference clock of 5 MHz, meaning that the overall RF division factor was doubled. This could infer up to 6 dB (20 Log10 *N*) worst phase noise performance. Therefore, a division ratio of 1 is possibly a more appropriate choice.

A6.6 References

1. H. Gokalp, "Characterisation of UMTS FDD Channels," Ph.D. Thesis, Dept. of Electrical Engineering and Electronics, UMIST, Manchester, UK, 2001.
2. A. B. Przedpelski, "Analyze, Don't Estimate, Phase-Lock-Loop Performance of Type-2, Third-Order Systems," *Electronic Design*, vol. 26, 1978.
3. R. E. Best, *Phase-Locked Loops: Design, Simulation, and Applications*, 5 ed: McGraw-Hill, 2003.
4. J. A. Crawford, *Frequency Synthesizer Design Handbook*: Artech House, 1994.
5. W. P. Robins, *Phase Noise in Signal Sources: Theory and Applications (IEE Telecommunications Series)*: Peter Peregrinus, 1984.

Appendix 7
Publications

A7.1 List of Publications

The following is a list of publications for conferences and journals during the course of the project. A number of these papers are provided in electronic format on the accompanying CD-ROM.

1. M.Matthaiou, N. Razavi-Ghods, D.I. Laurenson, and S. Salous, Frequency Correlation of an Indoor MIMO Channel, presented at European Conference on Antennas and Propagation (EuCAP 2006), Nice, France, November 2006.
2. M.Matthaiou, N. Razavi-Ghods, D.I. Laurenson, and S. Salous, Dual Frequency MIMO Measurements in the 2.26-2.5GHz Band, presented at International Symposium on Wireless Communication Systems (ISWCS 2006), Valencia, Spain, September 2006.
3. S. M. Feeney, N. Razavi-Ghods, and S. Salous, Experimental 60 GHz Wideband Channel Sounder, presented at IEE Seminar on Ultra Wideband Systems, Technologies and Applications, Savoy Place, London, UK, April 2006.
4. M.Matthaiou, N. Razavi-Ghods, D.I. Laurenson, and S. Salous, Dual Frequency MIMO Measurements in the 2.26-2.5GHz Band, presented at NEWCOM Dept. 2 Workshop, Sophia Antipolis, France, April 2006
5. S. Salous, P. Filippidis, R. Lewenz, I. Hawking, N. Razavi-Ghods, and M. Abdallah, Parallel Receiver Channel Sounder for Spatial and MIMO Characterisation of the Mobile Radio Channel, *IEE Proceedings on Communication*, vol. 152 (6), pp. 912-918, December 2005.
6. S. Salous, S. Feeney, N. Razavi-Ghods and R. Lewenz, Measurements in the 2 – 6 GHz Band, presented at XXVIIIth General Assembly of International Union of Radio Science (URSI GA 2005), New Delhi, India, October 2005.

7. S. Salous, S. Feeney, N. Razavi-Ghods and M. Abdalla, Sounders for MIMO Channel Measurements, presented at European Signal Processing Conference (EUSIPCO 2005), Antalya, Turkey, September 2005.
8. N. Razavi-Ghods and S. Salous, Experimental Characterisation of Indoor Multi-Element Array Propagation Channels, presented at Signal Processing for Wireless Communications (SPWC 2005), London, UK, June 2005.
9. M. Abdalla, N. Razavi-Ghods and S. Salous, Performance Evaluation of Sector Antenna Arrays for Angle of Arrival Estimation, presented at International Symposium on Antenna Technology and Applied Electromagnetics (ANTEM 2005), Saint-Malo, France, June 2005.
10. N. Razavi-Ghods, M. Abdalla and S. Salous, Characterisation of MIMO Propagation Channels Using Directional Antenna Arrays, presented at IEE International Conference on 3G Mobile Communication Technologies (3G 2004), London, UK, October 2004.
11. N. Razavi-Ghods and S. Salous, Semi-Sequential MIMO Radio Channel Sounding, presented at International Conference on Computing, Communications and Control Technologies (CCCT 2004), Austin, Texas, August 2004.
12. N. Razavi-Ghods and S. Salous, Semi-Sequential MIMO Channel Measurements in Indoor Environments, TD(04) 079, presented at COST273 meeting, Gothenburg, Sweden, June 2004.
13. N. Razavi-Ghods and S. Salous, Sequential MIMO Sounder Architecture for Mobile Radio Channel Characterisation, presented at National URSI symposium, Leeds, UK, July 2003.

A7.2 Other Outputs

1. N. Razavi-Ghods, Characterisation of Wideband Indoor MIMO Channels, to be presented at Durham University Research Day, School of Engineering, Durham, UK, June 2006.
2. S. Feeney, and N. Razavi-Ghods, Ultra Wideband 60 GHz Channel Sounder and MIMO Sounding, presented at 4th Annual Wireless Broadband Forum (Exhibition), Hinxton Hall Conference Centre, Cambridge, UK, November 2005.

3. N. Razavi-Ghods, Experimental Characterisation of MIMO Indoor Channels, presented at Durham University Research Day, School of Engineering, Durham, UK, June 2005.
4. N. Razavi-Ghods, and S. Feeney, High Resolution Chirp Sounder, presented at Durham University Regional Event (Exhibition) - Excellence Working for the Region, Newcastle, UK, June 2005.
5. S. Feeney, N. Razavi-Ghods, and S. Salous, Wideband Radio Channel Sounder, presented at 3rd Annual Wireless Broadband Forum (Exhibition), Hinxton Hall Conference Centre, Cambridge, UK, November 2004.
6. N. Razavi-Ghods and S. Salous, Characterisation of MIMO Propagation Channels, presented at Durham University Research Day, School of Engineering, Durham, UK, June 2004.